University of Southampton

Faculty of Engineering and Physical Sciences

School of Engineering

Control of 3D Sound Scattering based on Decomposition into Spherical Harmonic Components

DOI: https://doi.org/10.5258/SOTON/T0045

by

Mihai Orita

MEng Acoustical Engineering

ORCiD: 0000-0001-7307-0497

Thesis for the degree of Doctor of Philosophy

July 2021

University of Southampton

Abstract

Faculty of Engineering and Physical Sciences

School of Engineering

Doctor of Philosophy

Control of 3D Sound Scattering based on Decomposition into Spherical Harmonic Components

by

Mihai Orita

This thesis explores the active control of sound scattering from finite 3D structures using series of spherical harmonic components to describe the involved physical quantities. The investigation is theoretically focused and attempts to establish a framework for modelling complicated 3D sound scattering behaviour. An idealized approach is first explored where all variations of relevant physical quantities are known at all moments in time. This involves solving partial differential equations for an exterior impedance boundary-value problem and is done for two different models surrounded by an idealized fluid. One model is the uniform, locally-reacting impedance sphere, which is characterized by a radial wave impedance on the separation boundary that does not change with frequency, does not exhibit modes of dynamic motion, and is independent at each point on the boundary from all other points on the boundary. The other model is the thin, uniform, empty, elastic spherical shell based on Love`s first approximation and is characterized by a wave impedance on the separation boundary that has the opposite three properties of the previous model. Idealized active control approaches based on spherical harmonic components are explored for the two scenarios when using a small number of secondary control sources to suppress the scattered sound. For simplicity, the incidence that produces the scattering is chosen as a single monochromatic plane-wave. The common constraint of 'least mean squares' minimization is used for the scattered sound power. Predictions are realized for the scattering behaviour before and after power minimization using the spherical harmonic components, specifically at low frequencies, where the chosen active control produces the most significant suppression. These predictions confirm that the minimization with one or two control sources is similar to completely cancelling the first and, respectively, first two most dominant spherical harmonic components of the scattered sound in which the secondary also couples the best. The next component in the sequence is left as a residual after control, either enhanced or suppressed. With more control parameters to optimize, increasingly more of the dominant components in the scattering can be suppressed, depending on the order in the sequence of which is most dominant and coupled best into. A practical-oriented control approach is also explored, which relies on measurements of the incidence plus scattering at discrete locations, but on no prior knowledge of the scattering. This takes the form of velocity feedback control and is based on Bobrovnitskii`s method for modelling scattering, but translated to modal components, i.e. the spherical harmonics, rather than elemental components in space. Such active control is found to change the loaded impedance of the shell when excited with forces and measured with velocity sensors. The first few structural resonances can be dampened using this approach, which results in some reduction of the scattered sound at these frequencies.

Table of Contents

Table of Tables

Table of Figures

Research Thesis: Declaration of Authorship

Print name:

Title of thesis:

I declare that this thesis and the work presented in it are my own and has been generated by me as the result of my own original research.

I confirm that:

1. This work was done wholly or mainly while in candidature for a research degree at this University;
2. Where any part of this thesis has previously been submitted for a degree or any other qualification at this University or any other institution, this has been clearly stated;
3. Where I have consulted the published work of others, this is always clearly attributed;
4. Where I have quoted from the work of others, the source is always given. With the exception of such quotations, this thesis is entirely my own work;
5. I have acknowledged all main sources of help;
6. Where the thesis is based on work done by myself jointly with others, I have made clear exactly what was done by others and what I have contributed myself;
7. Parts of this work have been published as:

    - [Invited Talk] Mihai Orita, Stephen Elliott, and Jordan Cheer. Spherical harmonic formulations for passive and active control of acoustic scattering around the sphere. Abstract submitted for the 176th Meeting of the Acoustical Society of America, published as conference proceedings in the Journal of the Acoustical Society of America 144, 1757 (2018). Oct. 2018.
    - [Conference paper] Mihai Orita, Stephen Elliott, and Jordan Cheer. "Tonal active control of the power scattered by locally-reacting spheres using a small number of radiators near the surface: active control of scattering". In: Proceedings of the 23rd International Congress Acoustics, integrating 4th EAA Euroregio 2019: Session 01 A - Physical aspects for active control of noise and vibration. Deutsche Gesellschaft fur Akustik, Sept. 2019, pp. 69–76.
    - [Journal paper] Stephen Elliott, Mihai Orita, and Jordan Cheer. "Active control of the sound power scattered by a locally-reacting sphere". In: Journal of the Acoustical Society of America 147.3 (Mar. 2020), pp. 1851–1862.

- [Peer-reviewed conference paper] Mihai Orita, Stephen Elliott, and Jordan Cheer. “Active control of sound scattering from a uniform impedance sphere: power minimization versus backscattering cancellation”. In: Proceedings of the 27th International Congress on Sound and Vibration (ICSV27). 11-16 July 2021.
- [Peer-reviewed conference paper] Stephen Elliott, Mihai Orita, and Jordan Cheer. “A modal approach to acoustic scattering and its active control”. In: Proceedings of the 27th International Congress on Sound and Vibration (ICSV27). 11-16 July 2021.

Signature: .... Date:...........................

Acknowledgements

Completing a PhD has played a crucial part in the evolution of myself as a person and in the evolution of my professional expertise. This endeavor would have not been possible without the help and guidance received from a number of people.

I would like to first express my sincere gratitude to my two supervisors, Prof Stephen J Elliot and Dr Jordan Cheer. Both were very supportive throughout my PhD, from university bureaucracy to certain personal struggles, from guiding me to develop my general skills to helping me understand complicated scientific principles. Both my supervisors were very patient and accommodating when it came to my style of work, as well as gave me plenty of room to pursue my own scientific ideas. I would like to offer them my sincere thanks for all the important knowledge they have passed on to me.

I gratefully acknowledge the funding of my PhD by the UK Defence Science and Technology Laboratory (Dstl). Furthermore, I would like to offer my special thanks to Dr John Smith from Dstl for his continued guidance and invaluable insight throughout the duration of the project.

I would also like to thank my internal examiners, Prof Filippo Fazi and Prof Stephen Daley, for all the important feedback and suggestions provided during my PhD progression reviews.

I am deeply grateful to Dr Alan McAlpine for all the discussions about and help with advanced mathematical concepts.

I would like to offer my special thanks to my friend and colleague Francesco D'Amore for all his advice and counsel, as well as for all the good conversations we exchanged.

I would like to express my sincere gratitude to my colleagues Charlie House, Daniel Wallace, Joe Tan, Mattia dal Borgo, and to the university admin, library, and teaching staff, in particular, to Harriet Gemmell, Katie Rouse, Stephen Wakeling, Lee Chisman, Jacqueline Bonnin, Laura Duncan. All their help and support that were integral to the success of my PhD.

Last but not least, a special thanks to all the people that maintain and/or provide answers on sites such as the MATLAB forum, the Stack Exchange forums, Wikipedia and Wolfram MathWorld. All these were essential tools that aided my learning and understanding of certain topics in mathematics and programming.

Definitions and Abbreviations

Mathematical symbols	
$\mathbb{Z}$, $\mathbb{Z}^*$	The set of integer numbers, respectively, the set of integer numbers without zero
$\mathbb{R}$, $\mathbb{R}^*$	The set of real numbers, respectively, the set of real numbers without zero
$\mathbb{C}$, $\mathbb{C}^*$	The set of complex numbers, respectively, the set of complex numbers without zero
i	Imaginary unit number, $i = \sqrt{-1}$
D_+ , D_-	Only positive and, respectively, only negative elements in a set D
$\in$	‘belongs to’ operator
$f: D \rightarrow C$	Function f defined over domain D to co-domain C
$\mathcal{C}_{n,m}$	Modal coefficients of degree $n \in \mathbb{Z}_+$ and order $\lvert m \rvert \leq n$ in series decomposition
$\mathcal{W}_{n,m}$	Frequency weighting of modal coefficient of degree $n \in \mathbb{Z}_+$ and order $\lvert m \rvert \leq n$
$x^{(n,m)}$	Superscript in parentheses denotes additional indexing
Mathematical operators	
$\bar{z}$	Complex conjugate of number $z \in \mathbb{C}$
$\mathrm{Re}\{z\}$	The real part of complex number $z \in \mathbb{C}$
$\mathrm{Im}\{z\}$	The imaginary part of complex number $z \in \mathbb{C}$
$\tilde{f}$	A time-varying physical quantity $f(t)$ evaluated at a single frequency
$\mathcal{L}\{\}$, $\mathcal{L}^{-1}\{\}$	Operator $\mathcal{L}$ and the corresponding inverse operator $\mathcal{L}^{-1}$
$\mathcal{F}\{\}$, $\mathcal{F}^{-1}\{\}$	The direct and, respectively inverse Fourier Transform operators
$\frac{d^n}{dx^n}\{\}$	The total derivative operator with respect to variable x, applied $n \in \mathbb{Z}_+^*$ times
$\frac{\partial^n}{\partial x^n}\{\}$	The partial derivative operator with respect to variable x, applied $n \in \mathbb{Z}_+^*$ times
$f'(ka)$	First derivative of function $f(ka)$ with respect to the variable (ka)

$\int_D dx\{\}$	The integral operator over set D with respect to variable $x \in D$
$O(f(x))$	'Big O notation'; denotes limiting behaviour which takes the form of $f(x)$
Special functions	
$\delta(x-y)$	Dirac delta function. It is equal to ∞ when $x = y$ and to zero otherwise
$\delta_{n,m}$	Kronecker delta function. It is equal to 1 when $n = m$ and to zero otherwise
$j_n(x)$	Spherical Bessel function of the first kind, order $n \in \mathbb{Z}$ and argument $x \in \mathbb{R}$
$n_n(x)$	Spherical Bessel function of the second kind, order $n \in \mathbb{Z}$ and argument $x \in \mathbb{R}$
$h_n^{(1)}(x)$	Spherical Hankel function of the first kind, order $n \in \mathbb{Z}$ and argument $x \in \mathbb{R}$
$h_n^{(2)}(x)$	Spherical Hankel function of the second kind, order $n \in \mathbb{Z}$ and argument $x \in \mathbb{R}$
$Y_{n,m}(\theta, \varphi)$	Spherical harmonic of degree $n \in \mathbb{Z}_+$, order $\lvert m\rvert \leq n$, and arguments $\theta \in [0; \pi/2]$ and $\varphi \in [0; 2\pi)$
$P_n(x)$	Legendre polynomial of degree $n \in \mathbb{Z}$, and argument $x \in [-1; 1]$
$P_n^m(x)$	Associated Legendre function of degree $n \in \mathbb{Z}$ and order $\lvert m\rvert \leq n$, $x \in [-1; 1]$
Vector fields and operations	
$\vec{x}$	$\vec{x} = [x\ y\ z]^{\mathrm{T}}$ is the position vector in 3D Cartesian coordinates
f_x, f_y, f_z	Cartesian components of function $f(\vec{x})$
$\vec{r}$	$\vec{r} = [r\ \theta\ \varphi]^{\mathrm{T}}$ is the position vector in 3D spherical coordinates
f_r, f_θ, f_φ	Spherical polar coordinate components of function $f(\vec{r})$
$\vec{n}$	Vector outward normal to an enclosed surface
$\hat{x}$, $\hat{r}$, $\hat{n}$	Unit vectors in the corresponding directions
$f(\vec{x}), f(\vec{r})$	Scalar field $f: \mathbb{R}^3 \to \mathbb{R}^3$, domain and co-domain are both the set of position vectors of all points in 3D space
$\vec{f}(\vec{x}), \vec{f}(\vec{r})$	Vector field of $\vec{f}: \mathbb{R}^3 \to \mathbb{R}^3$, domain is the set of position vectors of all points in 3D space, and co-domain is vectors originating from each point in domain
$\vec{f}_x, \vec{f}_y, \vec{f}_z\ (\vec{x})$	Components of 3D vector field $\vec{f}(\vec{x})$ along Cartesian directions $\hat{x}$, $\hat{y}$, $\hat{z}$

∇	The Del operator
∇f	The gradient of the scalar function f
$\nabla^2 f$	The Laplacian of the scalar function f
Matrix algebra	
$\mathbf{A}$	Bolded quantities denote matrices that are not vectors in physical space
$\widetilde{\mathbf{A}}$	Matrix (not vectors in space) where elements belong to the frequency domain
$\breve{\mathbf{A}}$	Matrix (not vectors in space) where elements belong to the modal domain
$\mathbf{A}^{\mathrm{T}}$	Transpose of matrix $\mathbf{A}$
$\mathbf{A}^{\mathrm{H}}$	$\mathbf{A}^{\mathrm{H}} = \overline{(\mathbf{A}^{\mathrm{T}})}$ is the Hermitian transpose of matrix $\mathbf{A}$
$\mathbf{A}^{-1}$	Inverse of matrix $\mathbf{A}$
$\mathbf{I}$	Identity matrix, $I_{nm} = \delta_{nm}$
Physical quantities	
a	Radius of spherical surface $[\mathrm{m}]$
t	Time $[\mathrm{s}]$
ω	Angular frequency $[\mathrm{rads\ s^{-1}}]$
k	Angular wavenumber $[\mathrm{rads\ m^{-1}}]$
ka	Normalized frequency relative to radius of spherical surface []
c	Speed of sound in a medium $[\mathrm{m\ s^{-1}}]$
ρ	Density of a medium $[\mathrm{kg\ m^{-3}}]$
S	Surface area $[\mathrm{m^2}]$
V	Volume $[\mathrm{m^3}]$
E	Young`s modulus $[\mathrm{Pa}]$
ν	Poisson`s ratio []
p_0, c_0, ρ_0	Ambient pressure, speed of sound and density in a static isotropic gas/fluid
γ	Adiabatic constant in a static isotropic gas/fluid

p	Acoustic pressure (scalar field) $[\mathrm{Pa}]$
$\vec{u}$	Acoustic velocity (vector field) $[\mathrm{m\ s^{-1}}]$
$\vec{w}(\vec{r})$	Deflection vector filed in 3D space $[\mathrm{m}]$
$\vec{w}_\varphi(\vec{r})$	Tangential component of deflection vector along direction φ $[\mathrm{m}]$
$\vec{w}_\theta(\vec{r})$	Tangential component of deflection vector along direction θ $[\mathrm{m}]$
$\vec{w}_r(\vec{r})$	Radial component of deflection vector $[\mathrm{m}]$ (has direction of $\hat{n}$ and $\hat{r}$)
q	Volume flow rate (volume velocity) $[\mathrm{m^3\ s^{-1}}]$
Z	Wave impedance, i.e. ratio between magnitude of pressure and magnitude of velocity in a given direction, calculated at a point $[\mathrm{Rayl} = \mathrm{Pa} \cdot \mathrm{m\ s^{-1}}]$
ζ	Wave impedance normalized by the characteristic impedance of the wave propagation medium []
A	Wave admittance $[1/\mathrm{Rayl}]$
W	Radiated sound power [W]
Π	Normalized radiated sound power []
$f_\infty(\vec{x})$	Far-field behaviour of function $f(\vec{x})$
$f_\Theta(\vec{x})$	Far-field directivity pattern of function $f(\vec{x})$
Θ	Normalized far-filed directivity pattern []
Special superscripts and subscripts	
$f_i(\vec{x},t)$, $\mathcal{C}_{n,m}^{(i)}$	Quantities corresponding to incident disturbance
$f_s(\vec{x},t)$, $\mathcal{C}_{n,m}^{(s)}$	Quantities corresponding to scattering in medium exterior to scattering object
$f_{\mathbb{1}}(\vec{x},t)$, $\mathcal{C}_{n,m}^{(\mathbb{1})}$	Quantities corresponding to the primary in the control problem
$f_{\mathbb{2}}(\vec{x},t)$, $\mathcal{C}_{n,m}^{(\mathbb{2})}$	Quantities corresponding to the secondary in the control problem
$f_t(\vec{x},t)$, $\mathcal{C}_{n,m}^{(t)}$	Quantities corresponding to the overall behaviour in medium exterior to scattering object
$f_c(\vec{x},t)$, $\mathcal{C}_{n,m}^{(c)}$	Quantities corresponding to behaviour after active control was applied

$f_{\triangleright}(\vec{x},t)$, $\mathcal{C}_{n,m}^{(\triangleright)}$	Quantities corresponding to waves converging to the origin
$f_{\triangleleft}(\vec{x},t)$, $\mathcal{C}_{n,m}^{(\triangleleft)}$	Quantities corresponding to waves diverging from the origin
$\mathcal{C}_{n,m}^{(\mathbb{C})}$, $\mathcal{C}_{n,m}^{(\mathbb{R})}$	Quantities corresponding to series decomposition based on complex-valued, or real-valued, spherical harmonic basis functions

Chapter 1 Introduction

We humans have been around on planet Earth for some time, and we have progressively come to possess more and more knowledge about our surroundings. From using our senses to notice that a human body floats in a bath of water or that an apple falls from a tree in a certain way, to building advanced tools that have allowed us to discover the microscopic and astronomic worlds beyond those senses, humans have conquered many of nature`s puzzles. And the fundamental building blocks that form the pillars of this pursuit for understanding generally comprise a phenomenon, i.e. an entity that generates information, an observer, i.e. an entity that can receive information, and a method for interpreting information that was observed.

Reality and existence seem to revolve around the creation and transmission of information. If no information is generated, then no observation can take place. Likewise, if there is no way for the information corresponding to a phenomenon to reach an observer (e.g. hill obstructing radio antenna) or if the observer does not have the means to receive that information (e.g. a microscope or a telescope), then the occurrence of the initial phenomenon remains unknown to them, as if it never happened. Further still, even if received, information must still be interpreted by the observer, for example, humans can see that the clear sky is blue during the day, but further insight is required into the meaning of what blue is. A crucial concept for understanding the observation and interpretation of physical phenomena is the wave.

A wave is defined as the oscillatory behaviour of a physical entity as time progresses, or, in other words, the motion of a physical entity varying periodically from one side to the other of a mean position. Mathematically, a wave can be described using a sinusoidal function of time and position in space. Under certain conditions, elaborate physical behaviour can be described mathematically as a combination of waves, which was demonstrated by the famous work of Fourier and its consequent developments. This is done by expressing a complicated function of time as a sum of sinusoidal components of time corresponding to all possible periods of oscillations, called frequencies. Each sinusoid is weighted in the sum by a scaling factor that results from the inherent nature of the initial complicated function. Since its inception, this method of interpreting elaborate physical behaviour based on decomposing it into a spectrum of well-defined, simple components has paved the way for subsequent scientific discovery, and is currently used beyond just sinusoidal functions of time in applications ranging from nuclear physics, to dynamics of engineering structures, and to image processing.

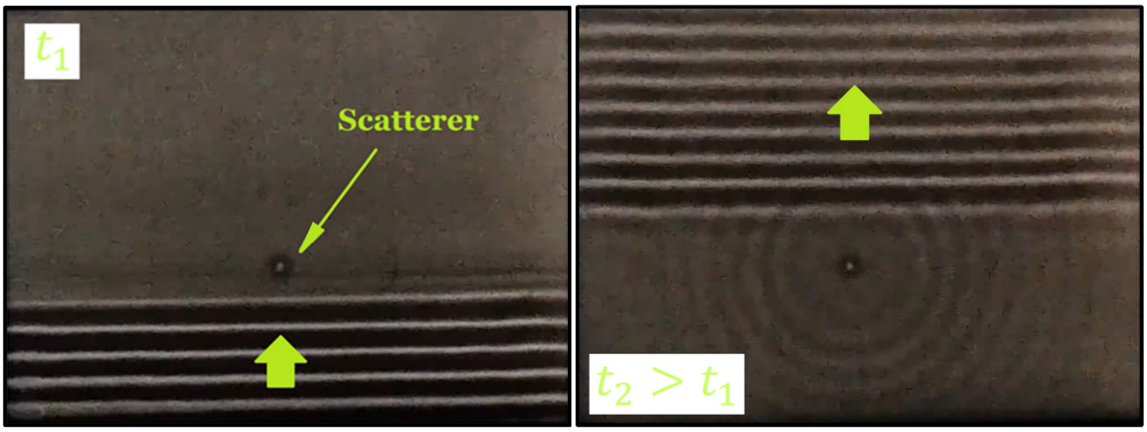

Figure 1-1 Short-duration mechanical disturbance containing single-frequency plane-wave on surface of water that approaches and interacts with round obstacle of small size relative to the wavelength of the disturbance. Two frames shown, an early one (at time t_1) and a later one (at time t_2), from video recording [2] of water wave experiments in ripple tank.

Wave behaviour innately has energy associated with it, whether it be nuclear, electro-magnetic, thermal, mechanical or gravitational. Some waves, for example those that constitute sound or light, can propagate and ’carry’ energy across distance and time under certain circumstances. However, from a more abstract perspective, travelling waves are not just carriers of energy but are also carriers of information corresponding to the phenomena that generated them. Likewise, all the interactions a travelling wave has along its path with other entities creates new sources of information. This can be observed in Figure 1-1, which shows the interaction between mechanical waves travelling on the surface of water towards a small, round obstacle, which was recorded during a ripple tank experiment. The initial disturbance (incidence), composed of a single-frequency plane-wave, reflects back from and diffracts around the obstacle while putting it in mechanical motion, thus creating new behaviour in the initial propagating medium, which is denoted as scattering. The nature of the scattering is governed by the physical properties of the obstacle, the water and their physical connection, as well as by the size of the obstacle relative to the size of the spatial variations corresponding to the frequencies of oscillation in the initial disturbance, which are denoted as wavelengths. At certain frequencies, a finite-sized object can be put into large amounts of motion called resonances depending on its material properties, which in turn would drastically change the generated scattering.

Scattering can play a crucial role in the transmission of information to an observer and, hence, the detection of a phenomenon. This is demonstrated very well by light, which represents a propagating oscillation of particles called photons, and the workings of human sight. In the presence of a light source such as the Sun, objects on the planet Earth interact with this light and scatter it to be picked up and interpreted by human eyes, resulting in the visual images that humans perceive. The colours are perceptual representations of the different frequency components which make up the oscillations of the particles in light. In the absence of light on Earth, humans perceive pitch black as nothing would be visible; however, this does not fully happen as light from the Sun still reaches the planet as very low-intensity scattering from other cosmic bodies such as the Moon. Furthermore, a human that is blind cannot be aware that the Sun exists through interpreting sources of light, but can reach that awareness from receiving, interpreting, and contextualizing other types of information, such as temperature changes between night and day or explanations from other humans.

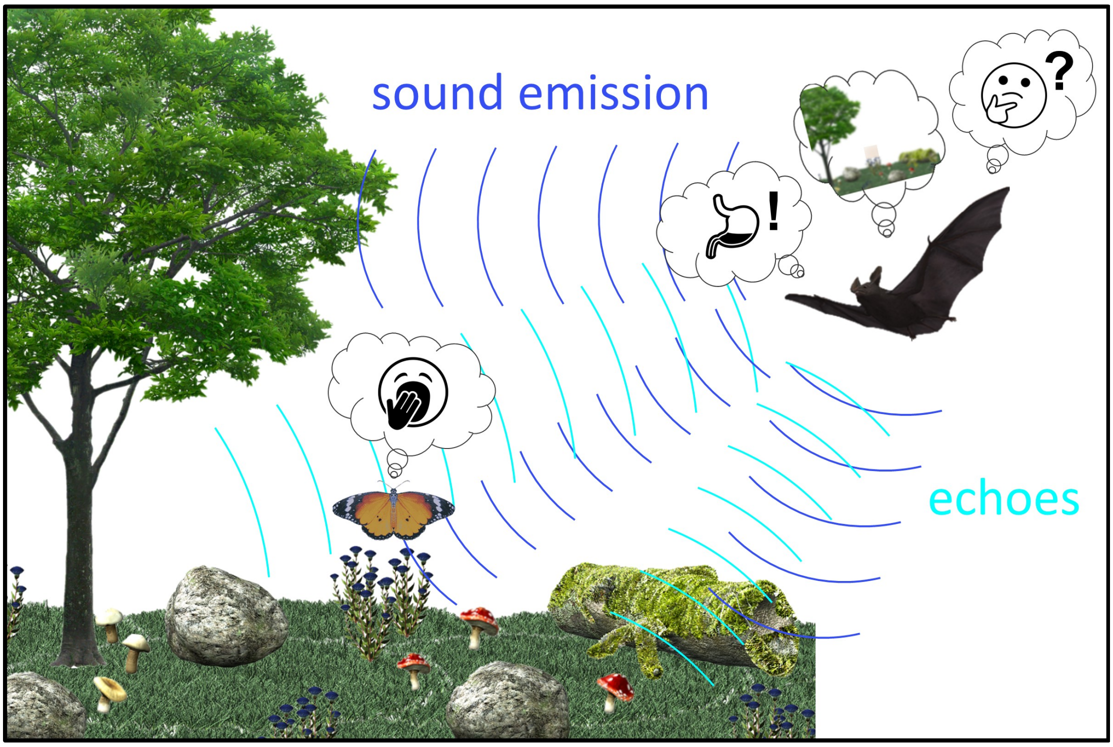

Figure 1-2 Bat using echolocation to find prey in the form of a species of butterfly (Danaus chrysippus). Structure of butterfly wings absorbs the sound waves helping it avoid detection [1]. Graphical elements for icons, bat, butterfly, and natural environment used from [3].

Another example is echolocation, where certain animals such as dolphins and bats have respective anatomical features that produce and detect ultrasound (high frequencies), which represents a propagating mechanical oscillation of matter (well-defined mass and volume). Monitoring the echoes (reflections) produced by objects given a certain emitted sound allows these animals to have an extra sense of their surrounding environment. Furthermore, certain species of moths and butterflies have evolved to counteract the echolocation properties of their main predator - bats (see Figure 1-2). Recent studies have found that geometrical patterns in the wing structure of these insects allow them to absorb up to approximately 70% of the ultrasound frequencies specifically emitted by the bats that hunt them, frequencies which play no role in the hearing or any other function of the insects [1]. This significantly decreases the amount of scattering from the prey and, thus, increases the chance of it being undetected.

The cases described above show that the game of generating and detecting information is prevalent in the natural world. The presence of an object can be hidden to an observer by completely suppressing any scattering behaviour that is generated by it. Alternatively, the scattering behaviour can be significantly altered to render the observer either unable to adequately detect/interpret this information, or make them perceive an illusion. Furthermore, representing and analysing elaborate behaviour based on simple components such as waves can play a very important role in this game of hide and seek. However, when it comes to humans, mastering the understanding behind such phenomena and concepts does not represent the finish line.

Beyond the pursuit for knowledge, we humans also strive to manipulate and control our surroundings like no other creature on planet Earth. This has pushed us towards great achievements where we have conquered immense obstacles and adverse circumstances, for example, the realization of planes, rockets, tunnels that cross mountain ranges, and dams that harness the motion of rivers. Thus, an interesting question can be brought forward. Can humans interfere with reality to make things seem as they are not? Or, more specifically, can additional intervention make some random scattering object interact with incoming physical phenomena or their components such that the object is made to appear as something else or non-existent to an observer?

1.1 Acoustic scattering and cloaking: an overview

Mechanical wave motion represents the oscillatory variation with space and time of matter that has been disturbed from rest. When describing the matter as a continuum, the motion at each point in it is represented through macroscopic physical quantities such as force, pressure, displacement, velocity, acceleration, stress, and strain. Mechanical waves cannot occur in a vacuum and can travel through mediums. The propagation manifests either as a fluid/solid going through cycles of compression - extension in the same direction as that of travel, or as a solid going through cycles of deformation in the direction perpendicular to that of travel.

When a finite or infinite-sized entity made of matter, fluid or solid, is mechanically excited with a force, the resulting motion is governed by the mechanical properties of the matter making up the object and any other matter surrounding the entity. The amount of opposition to motion generated by the propagation medium in response to the force is described through the concept of impedance. Impedance is a physical quantity used to measure opposition, and, in the case of mechanical waves, it is typically defined at a point in space as the ratio between the magnitude of the applied force and the magnitude of a quantity representing the generated motion, such as velocity in a given direction, for example.

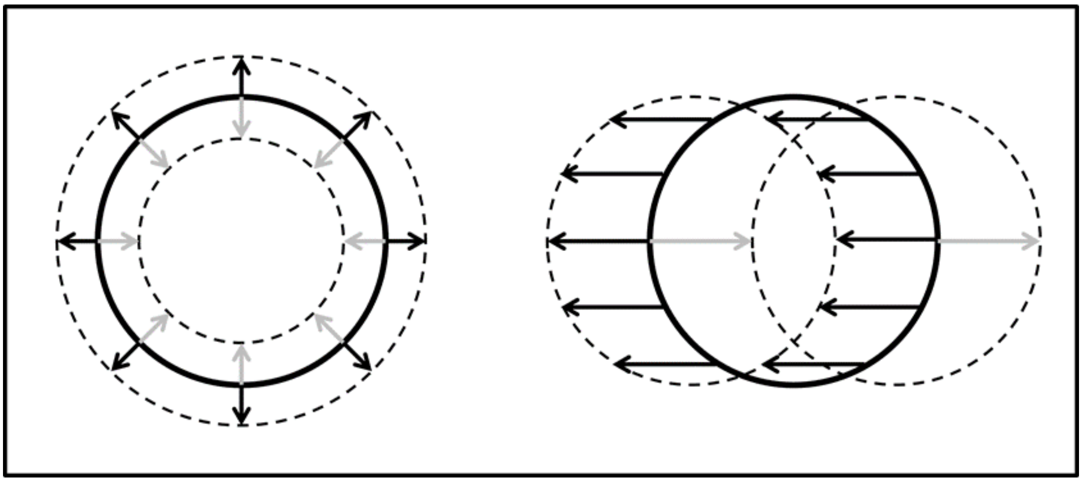

Figure 1-3 2D view of 3D spherical boundary (solid line) either: moving in all outward/inward directions by the same amount – breathing mode (left), or moving back and forth on a single axis – translational mode (right). Lamb [4] shows that, at low frequencies, when a scattering body surrounded by a fluid does not compress or translate in the same way as the same volume of fluid occupying its space, these two modes appear.

Following the line of thought used in the concept of Fourier analysis, but applied to variations with space rather than time, the elaborate motion of the entity can be described as the combination of an infinite number of well-defined, simple functions of space, under certain assumptions. One set/spectrum of such shapes is denoted as the modes of motion and represents the spatial variations the entity is most likely to exhibit when moving as a result of its geometry and mass distribution. Depending on other material properties, some of the modes can be resonant and display a large amount of motion when excited with a force of specific characteristics, such as frequency of oscillation. For some entities, the motion of some modes is interconnected to that of others; however, under certain assumptions such as linearity, any set of modes can be mathematically mapped to another set of fixed velocity distributions that move independently from each other [5-7]. This can be done both for an object that creates outward propagating motion, such as a piston or scatterer, and an object generating motion within an enclosed volume, such as air in a room or duct. Two common example of independent mode shapes are a finite 3D object moving by the same amount in all directions of 3D space or the whole object moving backwards and forwards on a single axis, as shown in Figure 1-3.

At fundamental level, sound is a mechanical wave; however, not all mechanical waves are denoted as sound. This label is interconnected with the capability of the human ears and brain to detect and, respectively, interpret mechanical motion in atmospheric air. What is labelled as sound represents very small pressure variations of specific frequencies about the mean atmospheric one. These variations span between a lower threshold and upper (pain) threshold that are smaller than the mean atmospheric pressure at sea level by approximately five billion times and, respectively, five hundred times. Also, for a healthy, young human adult, the frequency range of these variations is approximately 20 Hz to 20 kHz; anything higher or lower is not detectable by the human ear, with the latter being perceived as mechanical motion of the human body.

An important special case of physical behaviour is a linear process, for which superposition applies. During a such a process, the ‘cause’ is scaled by a constant amount in order to generate the ‘effect’, i.e. the variations of the involved physical quantities. Furthermore, the overall outcome of multiple linear operations acting on a set of circumstances is the direct sum between all individual operations. Linear processes are prevalent in the physical world, one example being most of the phenomena that involve the generation, transmission, and human perception of sound on a day-to-day basis. For sound waves in particular, linearity means that the shape of the corresponding spatial-temporal variations of physical quantities are preserved. In other words, a linear process does not alter the frequency of an oscillation or the shape of a modal pattern of motion, thus, making it easier to model mathematically, to obtain physical insight, and to manipulate in practice.

1.1.1 Acoustic cloaking and its applications

Just like other waves, propagating sound interacts with objects made of matter to produce scattering. Acoustic scattering is an important physical phenomenon in multiple scientific applications, such as ultrasonic- based imaging [8], shaping the acoustic environments in rooms [9, 10], the effects of scattering from the human head and body on perceived sound [11, 12]. The suppression of sound scattering relative to an observer detecting it is denoted as acoustic cloaking and it has specific purpose in several practical applications (see Figure 1-4).

In architectural and room acoustics, the cloaking of certain building structural elements such as columns, balconies and rafters can prevent them from altering the acoustic environment in an undesirable way. Thus, the sound quality requirements are effectively separated from the structural design requirements.

Anechoic chambers are rooms designed to mimic an infinitely large sound propagation volume, in other words, an acoustic environment unaffected by the presence of the room. This is typically achieved through special design of the room walls and lining them with acoustic absorptive material. However, the status-quo for this approach only achieves anechoic conditions in a limited frequency range. In particular, very low frequency resonances associated with the dimensions of the room volume are still able to form. At these low frequencies, external energy can be introduced in the room via loudspeakers to give the walls a degree of acoustic invisibility.

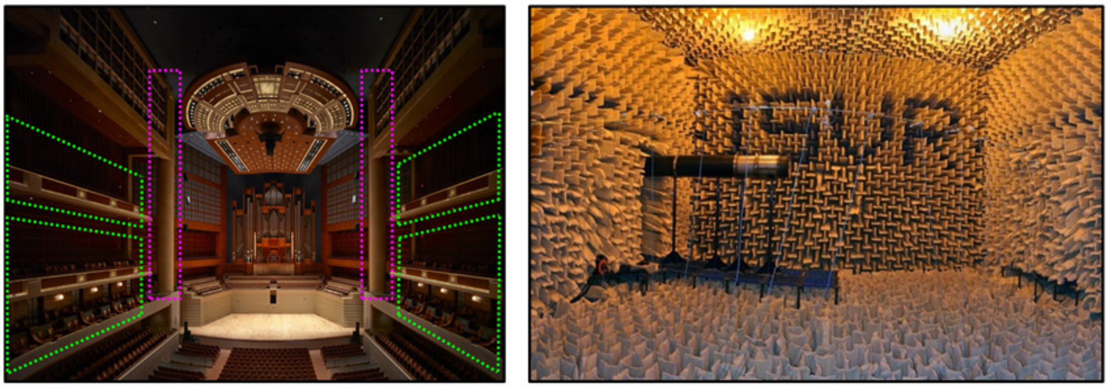

Figure 1-4 Applications of acoustic cloaking: making the columns in concert halls and auditoria to be sound transparent (image of Hartington Auditorium, Nebraska shown from [13]), and addressing low frequency room modes in anechoic chambers by making their walls sound transparent (image of large anechoic chamber at the University of Southampton, England, United kingdom).

1.1.2 Acoustic cloaking strategies

Systems that suppress sound scattering have been researched for many years, but in recent times, the focus has been on such systems that counteract the overall scattering behaviour rather than specific aspects like backscattering reflections or the shadow due to diffraction. The reasoning behind this is that detection methods have become more and more sophisticated, as seen, for example, in the advancements of ultrasound tomography [14]. The current literature on sound scattering suppression highlights different ways of approaching and solving this problem, which can be categorised into:

- passive control methods, i.e. manipulate the scattering behaviour by introducing no external energy,
- active control methods, i.e. manipulate the scattering behaviour by using additional external energy,
- hybrid control methods, i.e. an optimized combination of passive and active methods for a given set of circumstances.

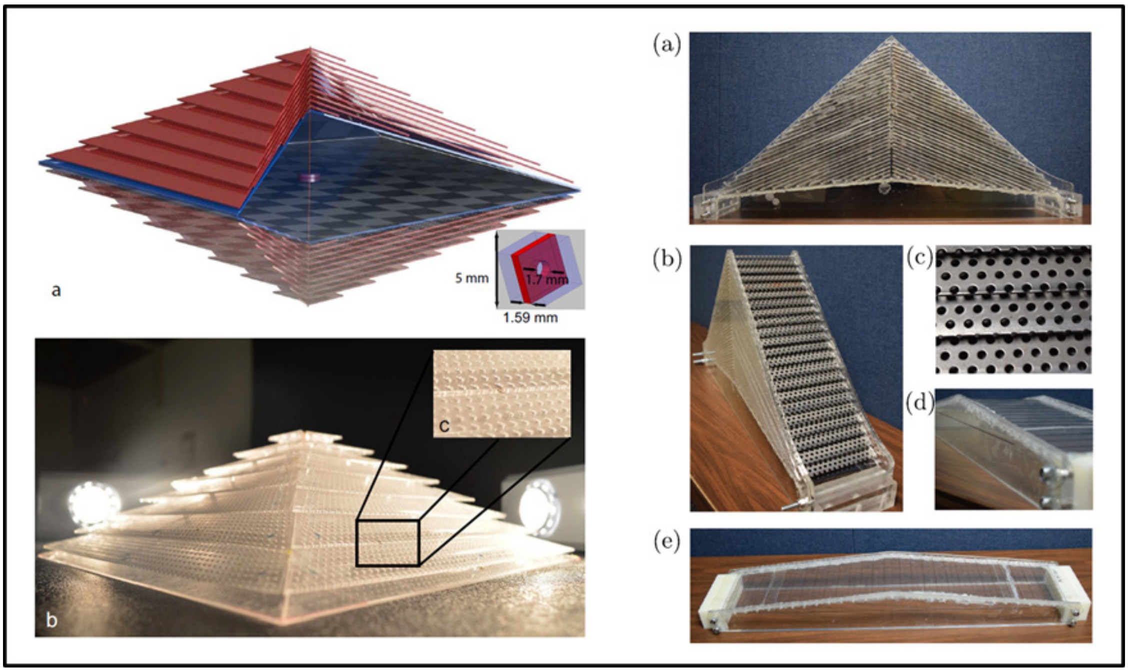

Figure 1-5 Metamaterial-based 3D acoustic ground cloaks achieved and tested in practice. Images recreated from [15] and [16] on the left and, respectively, right.

The first in the above list involves optimizing characteristics such as geometrical features and material properties of the scatterer, its boundary and/or its immediate surroundings. For example, certain shapes or geometrical feature can produce less sound scattering than others, as seen in [17]. However, relying on shape optimization as a solution introduces an extra requirement when designing the object or requires the modification of an existing object that may not allow any alteration. Likewise, objects with certain material properties scatter less when situated in a medium of certain material properties, as observed from comparing the results in the works [18-22]. Extra layers of new material can also be added around an obstacle to change its scattering characteristics [23], which is not as drastic of an approach as modifying the actual design of the object. However, the properties of currently available traditional engineering materials limit the achievement of scattering suppression when it comes to either simple types of incident spatial motion, or a broad range of small wavelength (high frequencies) incident motion. Therefore, more recent research of passive methods has focused on surrounding the scatterer with layers/coatings of metamaterial designs. These materials exhibit geometrical structures of subwavelength scale that result in effective macro properties which are not typically encountered in nature and can lead to significantly less generated sound scattering [14]. Two current practical examples of 3D acoustic cloaks made out of metamaterials can be found in [15, 16]. These are illustrated in Figure 1-5. Results from simulations and experiments show that these designs can provide cloaking over a broadband range of frequencies that covers, in some cases, all directions of arrival; however, this is possible only for very specific types of initial disturbances or may rely on the presence of the ground. Thus, some of the current practical examples are not a robust solution to changes of the circumstances.

A completely different method of overcoming the control performance shortcomings of traditional materials is represented by the second item in the above list. Active control is achieved in practice by positioning sensors in the vicinity of or on the scatterer to capture extra information that is used to govern the action of additional generators of sound (secondary sources) placed in the scenario, as seen in Figure 1-6. These generators can be loudspeakers around the scatterer or devices on its surface that govern its motion (actuators), for example, and their action is typically governed through an optimization algorithm. A mathematical ideal exists where, given certain constraints such as linearity, secondary sound that completely cancels the scattering produced by a given incidence impinging on a given obstacle can always be derived. This concept is based on the work of Malyuzhinets, Jessel and Mangiante from the 1960s and 1970s, as summarized in [24]. However, this ideal requires the sensors and the secondary sources to measure or act over a continuous surface enclosing the volume of the scatterer and to be acoustically transparent, which are both not reasonable requirements to achieve in practice. Therefore, a more feasible employed approach minimizes the effects of scattering using only a discrete number of sensors and sources that exhibit their own effects on the overall behaviour just by being present in the scenario. This method has been demonstrated for acoustic cloaking in simulations [25-33] as well as in practice [34-37]. However, arrangements that are discrete inherently offer restricted spatial information and regions of manipulation compared to their continuous counterparts, which leads to limitations on the working range of frequencies and achievable performance. Sensors or sources cannot be placed either to close or too far from each other as they would not be able to accurately capture or generate motion which varies over very large distances (low frequencies) or, respectively, over very small distances (high frequencies). Furthermore, active control based on discrete arrangements are generally found to give performance over a frequency range depending on the number of used sources. A small number of these only produces suppression at lower frequencies, where the spatial variations of motion are not complicated [24].

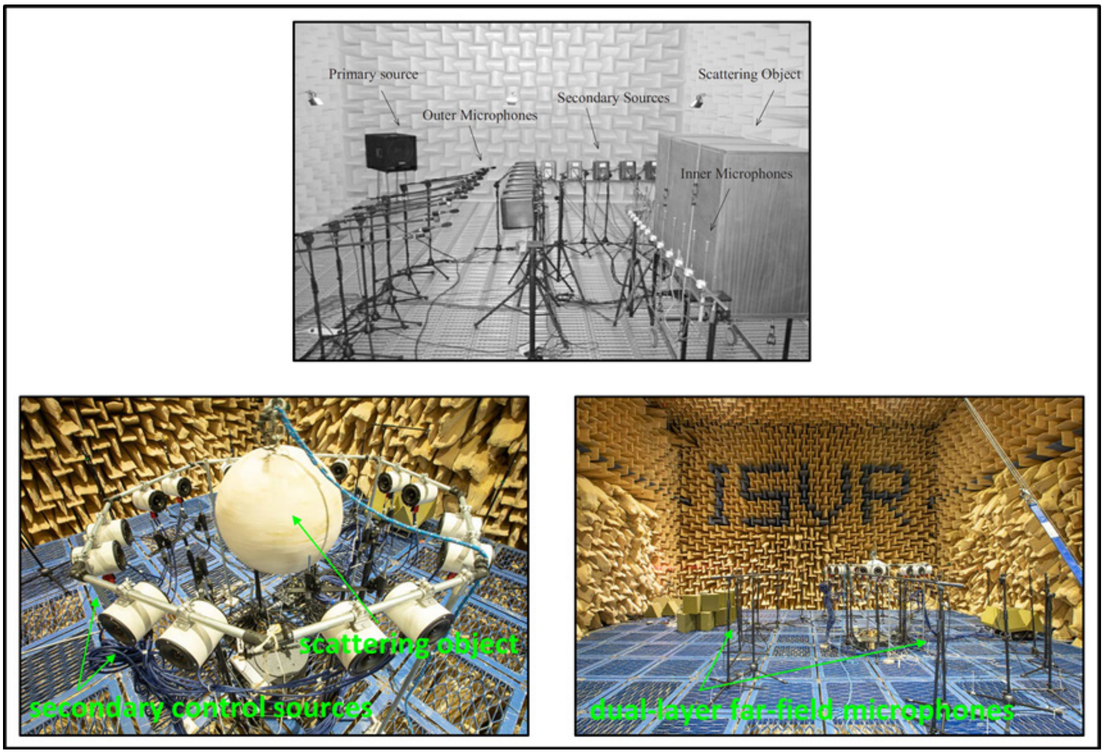

Figure 1-6 Acoustic cloaking of 3D scatterers based on active control arrangements realized and tested in practice. Images recreated from [34] on the top and, respectively, [37] on the bottom.

The choices of how, when and where the additional energy is introduced in a scenario are crucial aspects that dictate the outcome of an active control system. In Figure 1-1, the initial disturbance is of short duration, which results in the reflection and diffraction being visually distinguishable in the image. An initial disturbance that persists for a long duration combines with the scattering, leading to the generation of regions of constructive and destructive interference around the obstacle, depending on the frequencies involved. Placing secondary control sources in the regions where destructive interference naturally occurs would not result in a good scattering suppression performance, for example. Also, the incidence mixes with the generated scattering gradually over time as it goes around the geometry of the obstacle based on the propagation speed of the waves. Thus, an active control system intended to work in real-time would need the abilities to capture information and to manipulate the circumstances in a timely manner as events are occurring. One strategy to achieve real-time acoustic cloaking requires prior understanding of how a known incidence generates scattering from a known obstacle, which can be obtained from offline measurements [34, 35], computer-simulated models [38], or virtual sensing estimations [36]. Then, that information can be used to directly derive the ideal practical counteraction of the secondary sources in real-time. However, such strategies are not robust to changes of the scattering object, the surrounding medium, or the incidence. One real-time strategy that does not require prior knowledge of scattering circumstances involves using the secondary sources to create a zone of quiet in the vicinity of the obstacle without creating any effect outside of it, as shown in the works of [27, 28, 30, 32, 39]. In this way, the incidence and scattering are reduced together near the object, which results in minimizing the effect of the scattering further away from the obstacle. A third potential real-time strategy requiring no prior knowledge is represented by separation methods of incoming and outgoing waves relative to a coordinate system. Such methods have been explored when it comes to isolating and then suppressing the effect of the incoming reflection off of a room`s walls due a primary noise source [40-45]. But these methods have not investigated in relation to acoustic cloaking.

The third item included in the list is the potential synergy of passive and active scattering control techniques. In the literature, some theoretical concepts have been proposed where the scatterer is surrounded with non-metamaterial layers of optimized material properties that also have an active system integrated within them [46]. Strategies for enhancing acoustic metamaterial designs with active control have also been considered, though this has not been explored for the purpose of cloaking. One of this strategies consists of incorporating tiny loudspeakers and microphones as part of the subwavelength periodic structure, which effectively allows another level of control in shaping the macro-behaviour of such structural patterns [47, 48]. This approach has been shown in practice to widen the gaps in the low frequency range over which passive metamaterials offer significant attenuation. Another strategy is concerned with designing the periodic structure with the ability to actively adapt its repeating physical dimensions depending on the given circumstances and requirements; however, this method is currently only conceptual as it is very elaborate to realize in practice.

1.1.3 Previously studied scatterers

The predominant part of the literature on acoustic cloaking and scattering control discussed in the above paragraphs focuses on a specific set of circumstances. Firstly, both passive and active methods have been studied significantly more across time for simple geometries of 1D and 2D rather than 3D – for example, reflection of acoustic plane-waves at the termination in an impedance tube and, respectively, in a 2D duct. When it comes to 3D scatterers, the focus of the passive and active research has been on plates and cylinders [49-52], due to their use in the construction of room walls, aeroplane fuselage and submarine hulls. However, these have been studied from the perspective of idealized mathematical models, such as very thin plates and infinite length cylinders, which simplify the problem, essentially, to a 2D case and only allow limited prediction of the practical physical behaviour. In particular, the active scattering control from structures which truly have three dimensions has not been researched as extensively compared to the idealized plates and cylinders.

Secondly, the study of acoustically cloaking moving scatterers or scatterers in fluid flow is a very recent area of research with few examples of work [42, 53, 54]. Such two types of motion can significantly complicate the problem as they inherently make the scenario non-reciprocal and cause a shifting of the frequencies perceived at a stationary observer position (Doppler shift). Reciprocity is the property where the wave motion generated by a stationary emitter at a stationary receiver remains the same if the positions of the two were switched.

Thirdly, the processes considered in the scattering control problem are linear, which extends to the most commonly used active control algorithms being tonal-based (at single frequency) [51]. The linearity property significantly simplifies the mathematical modelling, practical realization, and outcome analysis of an active control scenario.

1.1.4 Modelling techniques for acoustic scattering and cloaking

The most common mathematical method of modelling the physical behaviour of a phenomenon such as mechanical motion is in the form of equations involving single- or multi-variable continuous functions corresponding to variations of physical quantities with respect to other physical quantities. Such equations often contain derivatives of functions (partial differential equations) or integration of functions (integral equations). When it comes to modelling motion that generates sound, the most common considered functions are the acoustic pressure and acoustic displacement or velocity or acceleration at a point in a fluid continuum, or the stress and strain at a point in the structure of a solid. These quantities vary with position in space and time – and consequently frequency through Fourier analysis.

There are many diverse methods to establish equations characterizing linear physical phenomena and there are multiple different ways to solve them. Some methods are concerned with solving for continuous functions and others with solving only over a discrete set of values. In the case of the latter, equations can typically be written as operations between finite-sized matrices and then solved by employing techniques from matrix algebra. In certain scenarios, an equation that characterizes physical phenomena may consist of elaborate operations such as differentiation and integration, which makes obtaining solutions not straightforward. Such operations may not be simply calculated without some form of numerical approximation, e.g. finite differences for estimating derivatives and the trapezium rule for estimating integrals.

The variation of a function with time can be studied at a finite number of instances, which can be a good representation if there is no significant variation over the smallest interval between two instances. Also, an infinite set of positions in space can be discretized into subsets of finite-sized spatial elements, as used in finite element methods, boundary element methods and lumped-parameter models. Furthermore, when expressing complicated linear functions as the combination between an infinite number of other functions with more simple variations, it may not be practical to calculate or manipulate all possible components. For example, when using Fourier analysis on a function of time, only a finite set of frequencies can be considered, leading to an approximation. As another example, only a finite number of modal patterns of motion can be considered for describing a variation in space.

In linear acoustics, the overall behaviour of sound waves generated in a medium exterior to an obstacle due to its interaction with an incoming incident disturbance is modelled as the direct sum of:

- the incidence, i.e. the motion in the medium exterior to the obstacle as if the obstacle is not present, and
- the scattering, i.e. the new motion in the exterior medium generated solely from the incident disturbance putting the obstacle in motion.

An active control system generates its own additional motion in the medium outside the obstacle, which is denoted as the secondary and adds up directly to the previous two. The primary is the name given to the physical behaviour (motion) that is controlled, which can be either the incidence, the scattering, or their combination.

Both continuous and discrete mathematical models for describing the linear scattering control problem have been significantly studied in the literature from as early as the 1800s [55, 56]. Discrete model can either involve the elemental approach of dividing space into finite-sized chunks, or the modal approach of considering a set of fixed velocity distributions to describe the motion. However, there is no unified method or framework that encompasses all approaches, as certain shapes of scatterers or certain frequency ranges of interest require very different modelling techniques. An overview of the principal methods for expressing sound scattering in linear acoustics is contained in [38]. In addition to these, the more recent elemental approach of Bobrovnitskii based on finite-sized impedance matrices of the media involved in the scattering problems is worth highlighting [57-59]. All these techniques ultimately establish a linear relation between the incidence and the produced scattering based on the properties of the media involved.

When it comes to active control of sound and vibration, the most prevalent method is to use a discrete number of sources to suppress motion at a discrete number of positions, due to its practicality. By extension, it is most common to use approaches such as modal analysis to model the quantities involved in the control algorithms rather than use their individual components in the algorithm. Modal active control has been researched previously, for example in [49-51], and spherical harmonics have been used to simulate the primary and secondary involved in active control of sound [60]. However, manipulating the simple spatially variating components individually with the control algorithm has not been extensively researched for 3D sound scattering. Such a tactic has been explored significantly in the area of 3D sound field reproduction and recording, with works such as [61-64].

1.2 Scientific contributions of this thesis

The spherical harmonic functions are a set of spatial variation patterns commonly used in the recording and reproduction of 3D sound, as well as in applications such as illumination procedures within graphical design software, gravitational fields of planets, electromagnetic wave emission and reception, and quantum mechanics of atomic orbitals. These functions can be observed in Figure 1-7 for the first few indices (l, m), where degree $l \in \mathbb{Z}_+$ and order $m \in \mathbb{Z}_+$, $|m| \leq l$, govern the variation with elevation angle θ and, respectively, azimuthal angle φ. The spherical harmonics are encountered as the components of the infinite series solution to the Helmholtz equation expressed in a spherical coordinate system (see Appendix A), which is used to describe sound wave propagation in an idealized fluid. Spherical harmonics also appear in the solutions to equations illustrating the mechanical motion of solid spherical structures [65, 66] and form the set of radiation modes for certain spherical structures [67]. The variations of the first four spherical harmonics are associated with the breathing mode and translational modes along the Cartesian axes depicted in Figure 1-3.

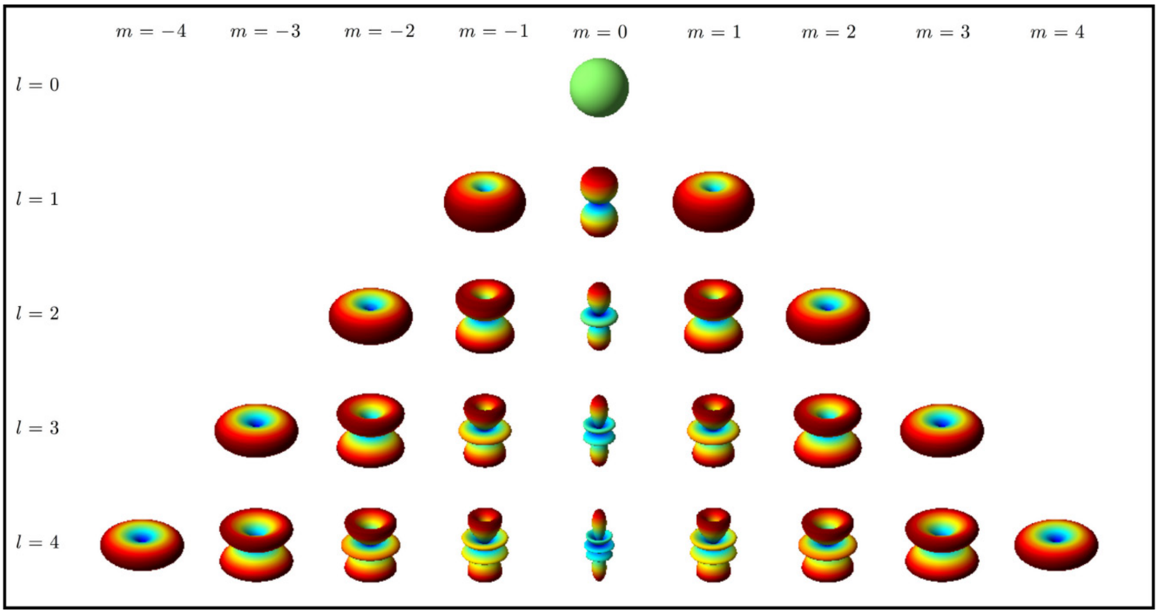

Figure 1-7 Complex-valued spherical harmonic functions, depicted for the first few indices (l, m), recreated from [68]. The degree $l \in \mathbb{Z}_+$ and order $m \in \mathbb{Z}_+$, $|m| \leq l$, govern the variation with elevation angle θ and, respectively, azimuthal angle φ. In the 3D plot, the radial distance corresponds to magnitude of the function, and the colourmap corresponds to the real part of the function.

The topic of the current thesis involves the passive and active control of 3D acoustic scattering from structures, in particular, the construction of mathematical models based on spherical harmonic series decompositions to describe such control problems. The main goal of the work was to obtain better insight on the physics of 3D acoustic scattering and its manipulation, and, ultimately, to create a basis for implementing a real-time acoustic scattering control procedure in a real-world scenario.

The work detailed in this thesis produces several scientific contributions to the research area in question. Firstly, an attempt is made to create a mathematical framework for approaching the modelling of the 3D sound scattering problem that brings together some of the principal methods used before in the literature. In particular, modelling the scenario based on orthogonal series decomposition is detailed, then extended to application in active control algorithms to ultimately exemplify passive and centralized, tonal, active control results for two simple geometries. The two geometries are a uniform, spherical impedance boundary surrounded by a fluid and a thin, uniform, empty, elastic spherical shell in a fluid.

Secondly, further physical insight is obtained about 3D sound scattering in the two sets of circumstances described above, which are traditional examples previously studied in the literature. Expressions based on spherical harmonics series are derived in place of the Legendre polynomial series, as used in the current literature to describe the simplified axisymmetric geometry of a sphere. In addition, the low frequency and resonant asymptotic behaviour of the scattering are predicted and exemplified before and after active control for different impedances and material properties of the two types of spherical surfaces, which goes beyond the present literature. Furthermore, the optimal choice of such properties for the passive and hybrid control is studied using parameter searches in computer simulations.

Thirdly, global active control algorithms based on minimizing the contributions of the components in an orthogonal series decomposition of a quantity are studied and are shown to be equivalent to the traditional method of ’least-mean squares’ minimization of the power associated with said quantity. Due to the complexity of the 3D problem, regional active control in a single far-field direction is also studied and compared to the global approach for some examples, using spherical harmonic series still. Furthermore, simple feedforward as well as feedback control system arrangements are investigated, with a focus on the latter, which has not been explored in the current literature for 3D scattering control.

Fourthly, the practical considerations of realizing a real-time active control system based on orthogonal series decomposition of the involved sound fields are discussed. Specific placement of control sensors and control sources in a feedforward arrangement such as described above is shown to resolve some of the obstacles of practical implementation.

Lastly, all theoretical models used for this work have been simulated in MATLAB by truncating infinite series of spherical harmonic components. The written code is generalized to cover the multiple different notation conventions used in separate parts of the literature and is also optimized to produce results in a timely manner all the way up to the complicated 3D variations of physical quantities.

1.3 Methodology used for this thesis

The methodology of approaching the research covered in this thesis was based on the design and implementation hierarchy discussed in classic textbooks covering active control of sound, such as [24] and [51]. This hierarchy consists of starting with the analysis of the control performance when using idealized secondary sources, such as point-monopoles and point-forces, when perfect sensing can be achieved at any point in space. Afterwards, the effects of practical limitations on the sensing are explored, for example, non-ideal source and sensor positioning, causality, averaging over space and time, non-linearity, measurement error, and randomness. The last stage involves the experimental validation of the active control system where its performance is verified given secondary sources that have practical limitations.

The work detailed in this thesis focused specifically on the initial two stages described above, where the goal was to develop theoretical models and gain further physical insight on the problem of active control of 3D acoustic scattering. Furthermore, this work relied on using spherical harmonic series decomposition of the involved acoustic pressures and velocities to achieve the intended goal, due to the prevalence of this tactic in the existing literature on 3D sound recording and reproduction, and due to the chosen geometries for study.

The investigation revolved around the sphere as a scatterer due to it being a symmetric and smooth 3D shape that has not been extensively studied before in terms of sound scattering control. The properties are desirable for a goal such as obtaining further in- sight on physical problems, while also bringing some mathematical modelling advantages. To further keep the circumstances simple, only linear and reciprocal processes were considered, such that the chosen spherical shapes of study were surrounded by a fluid that is stationary (no fluid flow), isentropic (reversible and adiabatic thermo- dynamic processes), isotropic (uniform bulk modulus and ambient density over the occupied volume), satisfies the perfect gas law, and exhibits no viscosity (no internal energy losses due to friction). The last property means any tangential motion of the spherical surface is uncoupled from the motion of the fluid.

The first studied modelled consisted of a uniform, locally-reacting impedance sphere, which is equivalent to a scattering surface satisfying the classic Dirichlet, Neumann or Robin boundary conditions. The second studied modelled was that of a thin, uniform, empty, elastic spherical shell based on Love`s first approximation, as described in [65]. This model can be conceptualized as a dynamic structure exhibiting membrane and flexural motion that has resonances and anti-resonances. The two geometries essentially represent a simplified problem of an impedance condition on a boundary, where the inside of the scatterer does not exist. The impedance in the first model is a constant value, while the one in the second is a modal-dependent and frequency-dependent function with poles and zeros.

In terms of active control, the general modelling framework was written in a general way in order to accommodate different types of tonal primary disturbances and secondary control sources. In the presented examples, a single monochromatic plane- wave is chosen as the incidence such that the 3D behaviour is somewhat simplified and easier to interpret before and after control. Point-monopoles and point-forces on and around the spherical surface were used as secondary sources in order to better represent what can be achieved in practice with current technology. The incidence and the secondary sources are placed on the z-axis of a coordinate system originating in the centre of the sphere, which only activates a set of spherical harmonics of certain indices, thus, facilitating the analysis and interpretation of results.

The ’least-mean squares’ minimization of scattered power, a conceptual measure, is used as a global active control strategy due to its prevalence in the traditional literature and its expression as an easily solvable quadratic equation. The regional active control is exemplified for a single far-field direction such that it can be easily compared with the power criterion and such that complicated near-field variations are avoided.

The results for the feedforward active control arrangements are based on always being able to individually measure the incidence and the scattering, thus it is the best possible representation of the control performance where the scattering is the primary disturbance. Global versus regional control is only studied and exemplified from this perspective of best possible outcomes. The feedback control arrangement is used to exemplify a non-ideal outcome of control performance from a control system that can be potentially realized to work in real-time. In this scenario, the primary is represented by the total field before control, i.e. the combination of the incidence and the scattering. Furthermore, the feedback arrangement is not illustrated for an impedance sphere due to its effect being only a change of the impedance value which can, alternatively, be done as a passive process.

1.4 Contents of this thesis

The current chapter details the full context of the thesis, and this specific section further illustrates how the contents of the work associated with this thesis are structured. In Chapter 2, the idealized theoretical models for describing the problem of controlling 3D acoustic scattering and, respectively, the active control of this problem, from the perspective of using continuous functions and their descriptions in terms of infinite series of spherical harmonics. This chapter contains general mathematical tools and procedures required for the purpose in question. Further modelling strategies are presented in Chapter 3, which account for certain practical limitations arising from realizing a real-time active control system based on orthogonal series decompositions.

The theoretical models and general results from the previous two chapters are exemplified for two specific geometries – the impedance sphere and the thin spherical shell – in the following four chapters. These were simulated with a finite number of spherical harmonic components in the series representations. Chapter 4 and Chapter 6 are studies of the sound radiation and scattering involving the impedance sphere and, respectively, the thin spherical shell. They illustrate some example sound fields which are later used as either the primary or secondary in the active control problem and its analysis. This analysis is done in Chapter 5 and Chapter 7 for the impedance sphere and, respectively, the thin spherical shell. All these four chapters show how the sound scattering problem and its active control changes depending on the impedance and material properties of the scatterer relative to its surrounding medium.

Finally, conclusions are drawn in Chapter 8, followed by a discussion of avenues for potentially extending the work of this thesis in future research. The work presented in this thesis that has been previously published is listed in the ‘Declaration of Authorship’ section found at the beginning of the document. The MATLAB programs used to obtain the results presented in this thesis are listed in Appendix I and are submitted together with the document as the dataset identified by https://doi.org/10.5258/SOTON/D2174.

Chapter 2 Idealized Theoretical Modelling of Sound Scattering and Its Control

This chapter is concerned with presenting the general theoretical modelling approach used in the examples contained in subsequent chapters, when it comes to describing the 3D sound wave propagation involved in acoustic scattering and its active control. This is based on partial differential equations (PDEs) of three spatial dimensions and of time, where the focus is on exterior impedance boundary-value problems based on spherical coordinates. Furthermore, ’idealized’, in this context, refers to this chapter covering mathematical aspects rather than any practical considerations; in other words, all relevant physical behaviour is known as all times and can be expressed as continuous mathematical functions.

The content in this chapter is predominantly reproduced from existing literature but re-packaged in a consistent framework that is suitable for approaching the research question of the thesis. General building blocks for modelling physical behaviour with PDEs are first presented. These building blocks are then used to represent 3D sound scattering and the secondary sources used to control it under the most fundamental circumstances, and facilitate the investigation and discussion approached in later chapters. Special consideration is given to aspects such as the wave impedance on the scattering surface, the characteristic acoustic impedance of the propagation medium, and the effect of scatterer size relative to the wavelength sound scattering behaviour in different frequency ranges. These are crucial considerations in the subsequent problem of actively controlling the 3D sound scattering.

2.1 Modelling 3D physical behaviour with partial differential equations

Partial differential equations relate single- or multi- variate differentiable functions to their total or partial derivatives of different orders. These participants in the PDE can correspond to the different variations created due to a physical phenomenon. Mathematical functions have domains, i.e. the set of values the variables in the function can take, and co-domains, i.e. the set of values resulting from applying the function to the values in the domain. All the functions involved in a PDE that describe physical behaviour commonly have the same domain and co-domain, which govern the solutions of PDEs.

Furthermore, functions representing physical variations can take the form of a scalar field, f , or a vector field, $\vec{f}$. The first represents behaviour where domain and co-domain are comprised of number values, for example, ambient pressure at different positions in a fluid such as air. The latter represents behaviour where either the domain, the co-domain, or both consist of number values, each associated with a direction, i.e. vectors. For example, the mechanical oscillatory motion (vibration) in void of a solid cylindrical beam manifests as an amount as well as in a direction depending on the acting forces, at any point along the bar and at any given time. A scalar field can be transformed into a vector field via a mathematical operation and vice-versa, plus, both types can appear in PDEs describing physical phenomena at the same time. For example, the vibration of the bar when surrounded by air can be modelled as a mathematical relation between the vector field corresponding to the rate of change of the bars momentum (its mass times its velocity) with time, and the vector field corresponding to the mechanical forces acting on the bar. The scalar field describing the ambient pressure of the surrounding air contributes to the latter as a dynamically impeding radial force acting uniformly around the diameter of the cylinder.

The common independent variables involved in describing physical phenomena are time and position in space, either of which can be modelled as having a finite, semi-infinite, or infinite domains and co-domains of values. Variations with time can be mapped to the frequency domain via the Fourier Transform, under certain assumptions. The work in this thesis is focused on three spatial dimensions and harmonic variations at a single frequency. Complex numbers in the co-domain of any used function are strictly related to the Fourier Transform and have no association with spatial vectors. The imaginary parts of these complex numbers correspond to shifts in time when mapped back to the time domain, thus, they represent no dissipation of energy – reactive rather than resistive in response to mechanical motion.

2.1.1 Homogeneous and inhomogeneous PDEs

Creating an imbalanced state within a set of circumstances generates a phenomenon. There are two fundamental ways in which this can be achieved: change of initial conditions or introducing additional energy. The first of the two involves setting the initial circumstances such that there is an inherent imbalance of energy at time $t = 0$ and then letting the physics manifest with no additional influence as time progresses. For example, pulling a string fixed between two points and then letting it go to vibrate until rest. At mathematical level, this translates in the other variables of the functions involved in the governing PDE having a specific set of values at time $t = 0$, and in the described variation of physical quantities equating to zero as a state of no variation is eventually reached. Such governing PDEs are denoted as homogeneous.

The second way of realizing an imbalanced state is to continuously influence the physics within a domain with additional energy, denoted as a ‘forcing term’. For example, when having a string fixed between two points, moving the whole assembly up and down continuously with the same force sets the string in harmonic motion. Generally, when creating mathematical models of physical phenomena, forcing terms appear as functions that replace the zero in a homogeneous PDE, turning it into an inhomogeneous one. Solutions of inhomogeneous PDEs exist depending on the nature of the given equation and are, typically, related in some way to the solutions of the homogeneous version of the initial PDE. When using the solution to a homogeneous PDE as a forcing term, the resulting inhomogeneous PDE is guaranteed to be solvable.

2.1.2 Linearity. Reciprocity

A wide span of physical phenomena can be modelled using linear PDEs under certain constraints. A PDE is deemed linear if all involved functions and corresponding derivatives are linear and have corresponding coefficients (factors) that can only be dependent on independent variables of the existing functions. In other words, two involved functions and/or derivatives cannot appear together in a product. Any linear combinations of solutions to a linear PDE is also a solution.

Another special case of physical circumstances is represented by reciprocity. A simple example of reciprocity is represented by the experiment of two communicating vessels being filled with fluid; the fluid level equalizes in the same way regardless of the liquid being poured in one vessel or the other. When it comes to a homogeneous or inhomogeneous PDE describing physical behaviour, under reciprocity, the PDE solution at an evaluation point A in the domain when an initial condition or a forcing term exists at point B of the domain is the same as the PDE solution at evaluation point B when the same initial condition or forcing terms exists at point A.

2.1.3 Building blocks for modelling with PDEs

The work in this thesis is concerned with linear and reciprocal mechanical motion in three spatial dimensions that varies harmonically at a single frequency. The spatial variations can appear as scalar fields (e.g. pressure, kinetic energy) or vector fields (e.g. force, displacement, velocity, acceleration) with domains and co-domains containing only real values. The variation with time is always a scalar field with a domain containing real values and co-domain containing values that can be complex-valued.

The infinite set of all positions in 3D space is represented mathematically by $\mathbb{R}^3$ in Cartesian coordinates (see Appendix A) and can be divided into subsets of finite or semi-infinite size to describe geometries with finite features. These abstract delimitations can be chosen to either intersect or not and can be the domains of different PDEs at the same time. The corresponding co-domains in such PDEs are typically $\mathbb{R}^3$.

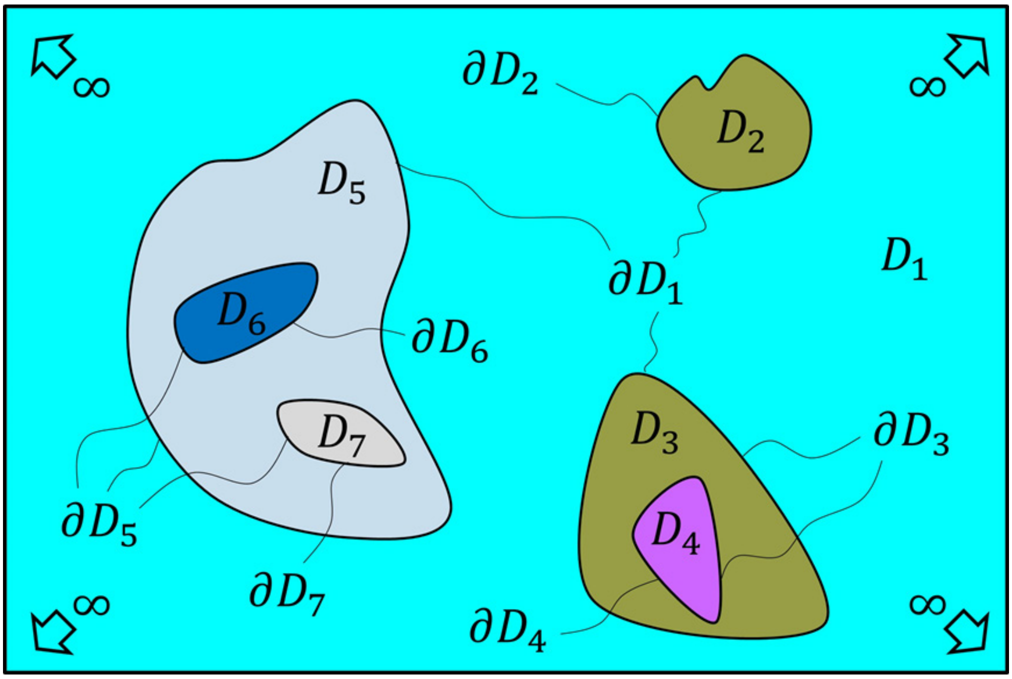

Figure 2-1 2D view of dividing infinite 3D space, $\mathbb{R}^3$, into multiple non-intersecting subsets, D_{1-7}, illustrated as different colors, where D_1 extends to infinity and D_{2-7} are closed sets.

Let there be a division of 3D infinite space where all subsets do not intersect with each other, but one can be completely enclosed by another, as exemplified in Figure 2-1. In physical terms, this representation corresponds to non-intersecting volumes of matter that undergo physical phenomena governed by different PDEs, where the involved boundaries between different volumes do not allow any transfer of matter. Any subset in the division does not cease to exist, such that any physical object cannot be destroyed. Also, any existing subset cannot form new subdivisions, in other words, matter does not suffer changes of state or catastrophic failures.

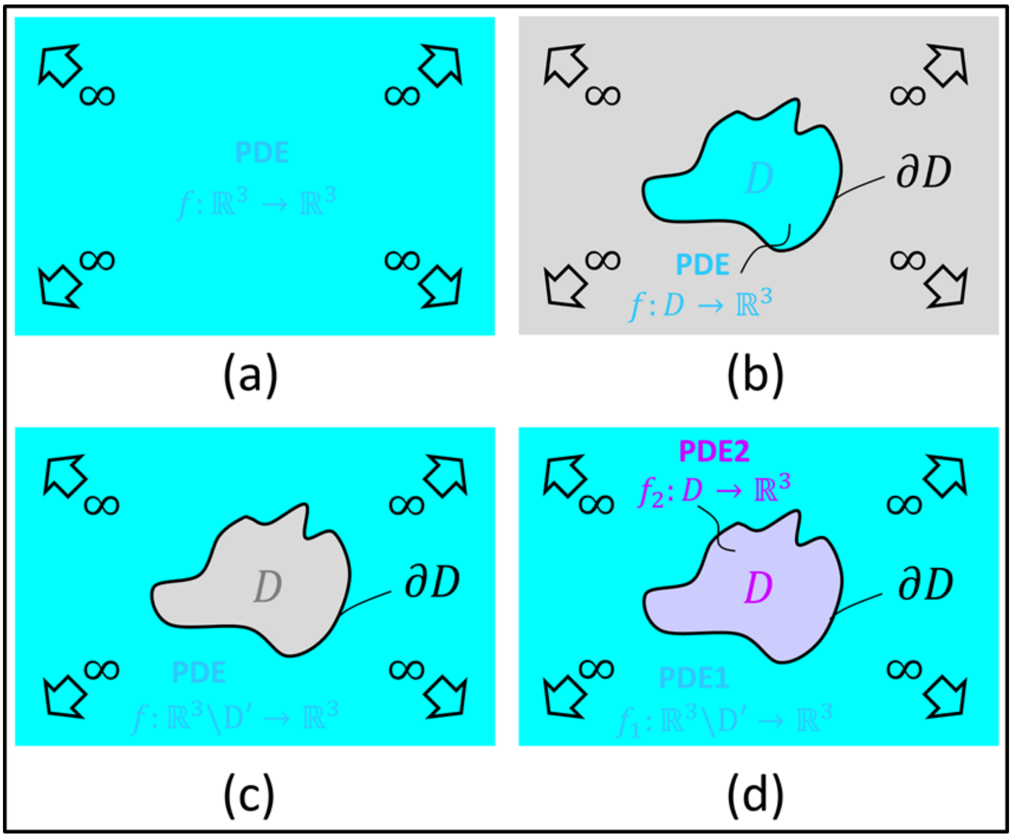

Figure 2-2 2D view of 3D building blocks for modelling with PDEs: the free-field problem (a), the interior boundary-value problem (b), the exterior boundary-value problem (c), and the transmission boundary-value problem (d), where $D' = D \cup \partial D$.

Under the constraints presented in the above paragraph, physical scenarios characterized by complicated geometries exhibiting mechanical motion can be modelled using a set of basic building blocks. These are the free-field problem, the interior boundary- value problem, the exterior boundary-value problem, and the transmission boundary- value problem, which are shown in Figure 2-2. The free-field represents the infinite set of 3D positions, which is used as the domain and co-domain of functions involved in a single linear and reciprocal PDE that can be homogeneous or inhomogeneous. The chosen geometry brings no additional constraints to the PDE and, thus, potentially allows for a diversity of solutions. However, additional constraints may be required to restrict the solutions only to those that describe physical behaviour. For example, the Sommerfeld radiation condition for the Helmholtz equation (detailed in later sections) ensures that, in an infinite medium, energy cannot propagate as sound waves from infinite distance back to an observer.

For modelling classical mechanical motion, the domain in Figure 2-2a represents an infinite continuum of matter respecting the laws of classical mechanics, in particular, the conservation of momentum or Newton`s second law. This law can be interpreted as a description of how matter impedes motion based on its macroscopic properties inherited from its molecular structure. The governing PDE obtained from the fundamental law relates the force vector field $\vec{F}: \mathbb{R}^4 \to \mathbb{R}^4$, i.e. the action, to the corresponding displacement vector field $\vec{w}: \mathbb{R}^4 \to \mathbb{R}^4$, i.e. the reaction. The first function is once integrable with respect to position in space ($\mathbb{R}^3$). The latter function is twice differentiable with respect to time to allow the existence of velocity and acceleration, and once differentiable with respect to position in space ($\mathbb{R}^3$). After mapping to the frequency domain, the force and displacement vector fields become $\tilde{\vec{F}}: \mathbb{R}^3 \to \mathbb{R}^3$ and, respectively, $\tilde{\vec{w}}: \mathbb{R}^3 \to \mathbb{R}^3$, where the notation $\tilde{w}$ denotes a quantity at a single frequency and domains/co-domains are the positions in space ($\mathbb{R}^3$).

The interior and exterior boundary-value problems are free-field problems that have been additionally constrained by the presence of a given set $D \subsetneq \mathbb{R}^3$ and its border ∂D. The domain of the governing PDE is restricted to D without its border for the interior problem (see Figure 2-2b), and to $\mathbb{R}^3 \setminus (D \cup \partial D)$ for the exterior problem (see Figure 2-2c). An additional constraint on the functions involved in the PDE is defined specifically on ∂D, which further restricts the possible solutions of the equivalent free- field linear PDE to only those of specific behaviour imposed by the boundary condition. This constraint is denoted as a boundary condition. For a given type of problem, the sets that are not part of the domain, $\mathbb{R}^3 \setminus (D \cup \partial D)$ and, respectively D, correspond to no function and do not affect the nature of the PDE or of the boundary condition.

The physical interpretation the two scenarios described above are an enclosed volume of matter and, respectively, a semi-infinite volume of matter enclosing a pocket of vacuum, where matter does not transfer through the boundary ∂D. The regions of space which are not part of the domain are equivalent to regions of vacuum that do not affect the matter or the boundary in any way. In reality, this last condition is an idealization, especially in the case of the exterior problem. This is because a volume of matter left in void, or a region of void left enclosed by matter, change their circumstance based on the static internal forces within the matter. The work in this thesis is focused on motion due to dynamic rather than static forces, therefore, the static effects on the regions of vacuum due to the adjacent matter are ignored.

The border ∂D can be set in mechanical motion, thus the boundary condition must still respect the momentum equation relating a displacement vector field due to an applied force vector field and must not render the associated PDE unsolvable. These vector fields must also be differentiable and integrable a number of times with respect to position in space and/or time, as for the free-field problem. The momentum equation is commonly used as the boundary condition on ∂D, i.e. the capability of the boundary to impede and-redirect mechanical motion. From this perspective, the boundary-value problems can be conceptualized as the equivalent of additional sources of energy (forcing terms) present in a free-field problem that create very specific physical behaviour in certain regions of space.

The transmission problem is the combination of an interior boundary-value problem and an exterior boundary-value problem that share the same border, ∂D, between exterior and interior domains (see Figure 2-2d). Each domain can be governed by a different PDE. Such PDEs commonly share the same physical quantities between the two domains, quantities which are then inherited in the and the boundary conditions on ∂D. In physical terms, this scenario corresponds to a finite volume of some matter enclosed within a semi-infinite volume of some different or the same matter. No transfer of matter occurs between the two volumes and each volume can potentially undertake different physical phenomena. However, the separate physical behaviour in the interior and exterior are related in certain regards due to their shared border. Again, the idealized case is considered where the static forces due to mechanical material properties within each region of matter are ignored, and the focus is dynamic forces. Given the force vector field $\vec{F}_1: \mathbb{R}^4 \to \mathbb{R}^4$ and displacement vector field $\vec{w}_1: \mathbb{R}^4 \to \mathbb{R}^4$ in the exterior domain, and the force vector field $\vec{F}_2: \mathbb{R}^4 \to \mathbb{R}^4$ and displacement vector field $\vec{w}_2: \mathbb{R}^4 \to \mathbb{R}^4$ in the interior domain, the force and displacement on the boundary are the combination of $\vec{F}_1$ and $\vec{F}_2$, and, respectively, $\vec{w}_1$ and $\vec{w}_2$. These vector fields must also be differentiable and integrable a number of times with respect to position in space and/or time, as for the free-field problem. Also, the boundary condition on ∂D has to respect the momentum equation; however, the nature of this geometry leads to certain problems when mathematical modelling, such as the discontinuity on ∂D for interior and exterior version of a function [69], and the undampened natural resonances of the interior volume creating singularities in the solutions of the exterior problem [70].

As a building block, the transmission boundary-value problem can be extended to create a scenario such as that in Figure 2-1 by taking the semi-infinite region of matter and then introducing additional finite-sized volumes of different or the same matter that do not intersect with each other. Each volume can be governed by a different PDE and each separating boundary can have a different constraint. In this way, an elaborate environment of different objects with different geometries can be modelled; however, the task becomes more complicated.

In the following section of this chapter, the building blocks presented above are used to model the 3D sound scattering problem and its active control using a spherical coordinate system. Specifically, the sound radiation and scattering in a fluid with desirable properties is considered, which can predict to some extent situations such as human perception of sound travelling in air. As such, the main focus of the modelling work revolves around the 3D Helmholtz equation and its solutions, which are first covered for the free-field problem and then restricted to the exterior boundary-value problem to represent 3D sound scattering from a single spherical boundary. Under a spherical co- ordinate system, the working solutions take the form of infinite series expansions of spherical harmonics components (see Figure 1-7), which are modal patterns of sound radiation for spherical scatterers, as is discussed in future chapters. The momentum equation is used as the constraint on this boundary, which leads to mathematical formulations based on impedances to acoustic wave motion. For the two models of sound scatterer considered in later chapters, these impedances can vary with frequency, can vary with modal index, can exhibit poles, and can exhibit zeroes.

2.2 Modelling free-field propagation of 3D sound waves in spherical coordinates

2.2.1 The wave and momentum equations for 3D acoustic waves

Let there be a free-field fluid that is stationary (no fluid flow), is isentropic (reversible and adiabatic thermodynamic processes), satisfies the ideal gas law, and exhibits no viscosity (no internal energy losses due to friction). Let the fluid also be homogeneous, i.e. properties such as its bulk modulus and ambient density are uniform over the whole occupied space. A mechanical wave propagating through such a medium satisfies conservation of momentum, i.e. Euler`s linearized momentum equation [71]

$$\nabla p + \rho_0 \frac{\partial \vec{u}}{\partial t} = 0\,, \tag{2.1}$$

as well as the linearized homogeneous wave equation [71]

$$\nabla^2 p - \frac{1}{c_0^2}\frac{\partial^2 p}{\partial t^2} = 0\,, \tag{2.2}$$

in terms of the acoustic pressure scalar field $p(\vec{r})\colon \mathbb{R}^4 \to \mathbb{R}^4$, or

$$\nabla^2 \vec{u} - \frac{1}{c_0^2}\frac{\partial^2 \vec{u}}{\partial t^2} = 0\,, \tag{2.3}$$

in terms of the acoustic velocity vector field $\vec{u}(\vec{r})\colon \mathbb{R}^4 \to \mathbb{R}^4$. p and $\vec{u}$ are both functions of position in space and time t, where the del operator ∇ and the Laplacian ∇^2 describe the variation in space with respect to the used coordinate system (see Appendix A). The quantity $c_0 = \sqrt{\gamma p_0/\rho_0}$ represents the ambient speed of sound, where p_0 is the ambient pressure in the fluid, ρ_0 is the ambient density of the fluid and γ is the adiabatic constant of the fluid.

Equation (2.1) relates each of the three components in the vector field for acoustic velocity to one of the three components in the spatial gradient of the scalar field for acoustic pressure. In future parts of the thesis, this result is used to define boundary conditions based on wave impedance for the surface of a 3D sound scatterer. Only the radial component of the velocity and, hence, of the radial pressure gradient, are later considered, as these two quantities act on the normal direction relative to the surface of the obstacle. This is done because the chosen fluid exhibits no viscosity, such that it does not couple with the motion of the scattering surface in other spatial directions.

2.2.2 The frequency domain and the 3D Helmholtz equation

The wave equation (2.2) is expressed in the time-domain, and can be transformed to the frequency-domain with the Fourier Transform [71, 72]

$$\tilde{F}(\omega) = \mathcal{F}\{f(t)\} = \int_{-\infty}^{\infty} dt \left\{ f(t) \cdot e^{-i\omega t} \right\}, \tag{2.4}$$

and, then back to the time-domain with the Inverse Fourier Transform

$$f(t) = \mathcal{F}^{-1}\{\tilde{F}(\omega)\} = \frac{1}{2\pi} \int_{-\infty}^{\infty} d\omega \left\{ \tilde{F}(\omega) \cdot e^{i\omega t} \right\}. \tag{2.5}$$

It is important to emphasize that different definitions of the Fourier Transform are used in certain research fields. Maintaining Parseval`s identity, a normalization factor of $1/\sqrt{2\pi}$ can be used in front of both direct and inverse transformations instead of just a factor of $1/(2\pi)$ in front of the inverse one. Also, the $\mathcal{F}\{\}$ can be defined with a factor of $e^{i\omega t}$, as in [73], instead of $e^{-i\omega t}$, as in [71], which leads to a sign change in front of Euler`s momentum equation (2.1) and the time-dependency of a steady-state sound field at a single frequency being expressed as $\tilde{F}(\omega) \cdot e^{-i\omega t}$ instead of the $\tilde{F}(\omega) \cdot e^{i\omega t}$ used throughout this thesis. Furthermore, this discrepancy also establishes the convention for representing travelling waves either converging or diverging relative to the origin of the coordinate system. For definition (2.4), waves whose spatial variation behaves as $e^{-ik|\vec{r}|}$ or $e^{-i\vec{k}\cdot\vec{x}}$ are moving away from the origin, while those that behave as $e^{+ik|\vec{r}|}$ or $e^{+i\vec{k}\cdot\vec{x}}$ are moving towards the origin.

Assuming steady-state and no further transient effects, the Fourier Transform is applied to (2.2). Using the fact that a double derivative in time translates into a factor of $-\omega^2$ emerging in front, yields the homogeneous Helmholtz equation

$$\nabla^2\tilde{p} + k^2\tilde{p} = 0\,, \tag{2.6}$$

written in terms of the frequency-domain of the acoustic pressure, $\tilde{p}$. This can also be used on the linearized version of Euler`s momentum equation, (2.1), to obtain

$$\nabla\tilde{p} = -ik\rho_0 c_0\,\tilde{\vec{u}}\,. \tag{2.7}$$

2.2.3 General solutions to the 3D Helmholtz equation

The homogeneous wave equation (2.2) and homogeneous Helmholtz equation (2.6) in spherical coordinates (r, θ, φ) are expressed as [71]

$$\left[\frac{1}{r^2}\frac{\partial}{\partial r}\left(r^2\frac{\partial p}{\partial r}\right) + \frac{1}{r^2\sin\theta}\frac{\partial}{\partial\theta}\left(\sin\theta\frac{\partial p}{\partial\theta}\right) + \frac{1}{r^2\sin^2\theta}\frac{\partial^2 p}{\partial\varphi^2}\right] - \frac{1}{c_0^2}\frac{\partial^2 p}{\partial t^2} = 0\,, \tag{2.8}$$

In the time domain, and, respectively, [20]

$$\left[\frac{1}{r^2}\frac{\partial}{\partial r}\left(r^2\frac{\partial\tilde{p}}{\partial r}\right) + \frac{1}{r^2\sin\theta}\frac{\partial}{\partial\theta}\left(\sin\theta\frac{\partial\tilde{p}}{\partial\theta}\right) + \frac{1}{r^2\sin^2\theta}\frac{\partial^2\tilde{p}}{\partial\varphi^2}\right] + k^2\tilde{p} = 0\,, \tag{2.9}$$

in the frequency domain, both of which also hold for the acoustic velocity vector field in place of acoustic pressure scalar field. Using separation of variables or methods based on Kirchhoff-Helmholtz integrals, at a single frequency, equation (2.9) has the general solutions [71]

$$\tilde{p}(\vec{r}) = \sum_{n=0}^{\infty}\sum_{m=-n}^{n}\left[\tilde{\mathcal{A}}_{n,m}^{(\mathbb{C})}\, j_n(kr) + \tilde{\mathfrak{B}}_{n,m}^{(\mathbb{C})}\, n_n(kr)\right] Y_{n,m}^{(\mathbb{C})}(\theta,\varphi)\,, \tag{2.10}$$

with

$$\tilde{\mathcal{A}}_{n,m}^{(\mathbb{C})}\, j_n(kr) + \tilde{\mathfrak{B}}_{n,m}^{(\mathbb{C})}\, n_n(kr) = \int_0^{\pi}\sin\theta\, d\theta\int_0^{2\pi} d\varphi\,\left\{\tilde{p}(\vec{r})\,\bar{Y}_{n,m}^{(\mathbb{C})}(\theta,\varphi)\right\}, \tag{2.11}$$

for standing waves, and

$$\tilde{p}(\vec{r}) = \sum_{n=0}^{\infty} \sum_{m=-n}^{n} \left[\tilde{\mathcal{C}}_{n,m}^{(\mathbb{C})} h_n^{(1)}(kr) + \widetilde{\mathfrak{D}}_{n,m}^{(\mathbb{C})} h_n^{(2)}(kr)\right] Y_{n,m}^{(\mathbb{C})}(\theta, \varphi)\,, \tag{2.12}$$

with

$$\tilde{\mathcal{C}}_{n,m}^{(\mathbb{C})} h_n^{(1)}(kr) + \widetilde{\mathfrak{D}}_{n,m}^{(\mathbb{C})} h_n^{(2)}(kr) = \int_0^{\pi} \sin\theta \, d\theta \int_0^{2\pi} d\varphi \, \left\{\tilde{p}(\vec{r}) \, \bar{Y}_{n,m}^{(\mathbb{C})}(\theta, \varphi)\right\}, \tag{2.13}$$

for travelling waves. Both (2.10) and (2.12) are expressed in the frequency-domain by omitting a $e^{i\omega t}$ factor, which would vanish under the Fourier Transform. For a given value of n, there are n terms corresponding to the negative values of m, n terms corresponding to the positive values of m, and a $m = 0$ term, thus $2n + 1$ terms in total. Also, for a truncation degree $n = N$ there are $(N + 1)^2$ terms with degree $n \leq N$ in the overall summation.

The j_n and n_n are spherical Bessel functions of the first and second kind, respectively, while $h_n^{(1)}$ and $h_n^{(2)}$ are spherical Hankel functions of the first and second kind, respectively. These describe the dependence of the sound waves with radial distance away from the origin of the coordinate system and are detailed in Appendix D. The $\tilde{\mathcal{A}}_{n,m}^{(\mathbb{C})}$, $\widetilde{\mathfrak{B}}_{n,m}^{(\mathbb{C})}$, $\tilde{\mathcal{C}}_{n,m}^{(\mathbb{C})}$, and $\widetilde{\mathfrak{D}}_{n,m}^{(\mathbb{C})}$ are sets of complex-valued spherical harmonic coefficients that are typically frequency-dependent and that fully describe the free-field sound waves under specified circumstances, such as an additional boundary condition or additional sound sources. It is important to highlight that superscript $\mathbb{C}$ of these coefficients denotes that they correspond to the complex-valued spherical harmonics, specifically.

The orthonormal functions $Y_{n,m}^{(\mathbb{C})}(\theta, \varphi)$ are the complex-valued spherical harmonics of degree n and order m, and they define the azimuthal and co-elevation dependence of the sound waves. Spherical harmonics are fixed spatial patterns on a virtual sphere centred at the origin of the coordinate system. They are depicted in Figure 1-7 for the first few indices and are detailed in Appendix B. It is important to comment that different disciplines use different definitions for the spherical harmonics. In this work, the chosen version includes the Condon-Shortley phase, i.e. an extra $(-1)^m$ factor, which is added in the formulation of the associated Legendre functions. Said definition is the one utilized in [71]. Furthermore, there are also real-valued versions of the spherical harmonics, which are covered in Appendix C, but not used in this work. The formulations (2.10) and (2.12) are denoted as spherical harmonic decompositions or expansions in terms of spherical harmonics because the functions $Y_{n,m}^{(\mathbb{C})}(\theta, \varphi)$ are considered the basis functions of the series. The expressions (2.11) and (2.13) arise as a result of the orthonormality of the spherical harmonics.

The spherical Bessel functions and the spherical harmonics are dimensionless quantities. The first of the two are power series expansions of the argument kr which is dimensionless (as seen in Appendix D). The latter of the two are linear combinations of different powers of sine and cosine functions with arguments θ and φ. Because of this, the units of the physical quantities expressed as a series of spherical harmonics are given by the sets of coefficients.

For a given coordinate system, a traveling sound wave can either converge towards or diverge outwards, relative to the origin. For the time-frequency convention $e^{i\omega t}$, at a single frequency, a converging wave $\tilde{p}_{\triangleright}(\vec{r})$ that satisfies (2.6) takes the form [71]

$$\tilde{p}_{\triangleright}(\vec{r}) = \sum_{n=0}^{\infty} \sum_{m=-n}^{n} \tilde{\mathcal{A}}_{n,m}^{(\mathbb{C})}\, j_n(kr)\, Y_{n,m}^{(\mathbb{C})}(\theta,\varphi)\,, \tag{2.14}$$

with

$$\tilde{\mathcal{A}}_{n,m}^{(\mathbb{C})}\, j_n(kr) = \int_0^{\pi} \sin\theta\, d\theta \int_0^{2\pi} d\varphi\, \left\{\tilde{p}_{\triangleright}(\vec{r})\, \bar{Y}_{n,m}^{(\mathbb{C})}(\theta,\varphi)\right\}, \tag{2.15}$$

and a diverging solution $\tilde{p}_{\triangleleft}(\vec{r})$ that satisfies (2.6) takes the form [71]

$$\tilde{p}_{\triangleleft}(\vec{r}) = \sum_{n=0}^{\infty} \sum_{m=-n}^{n} \tilde{\mathcal{D}}_{n,m}^{(\mathbb{C})}\, h_n^{(2)}(kr)\, Y_{n,m}^{(\mathbb{C})}(\theta,\varphi)\,, \tag{2.16}$$

with

$$\tilde{\mathcal{D}}_{n,m}^{(\mathbb{C})}\, h_n^{(2)}(kr) = \int_0^{\pi} \sin\theta\, d\theta \int_0^{2\pi} d\varphi\, \left\{\tilde{p}_{\triangleleft}(\vec{r})\, \bar{Y}_{n,m}^{(\mathbb{C})}(\theta,\varphi)\right\}, \tag{2.17}$$

The latter must also satisfy the Sommerfeld radiation condition, [20]

$$\lim_{|\vec{r}|\to\infty} \left\{ |\vec{r}| \left(\frac{\partial \tilde{p}_{\triangleleft}(\vec{r})}{\partial |\vec{r}|} + ik\, \tilde{p}_{\triangleleft}(\vec{r}) \right) \right\} = 0\,, \tag{2.18}$$

which translates into the sound pressure tending to zero at infinite distance away from the origin, such that it is impossible to have any acoustic energy travelling back to the origin from this distance.

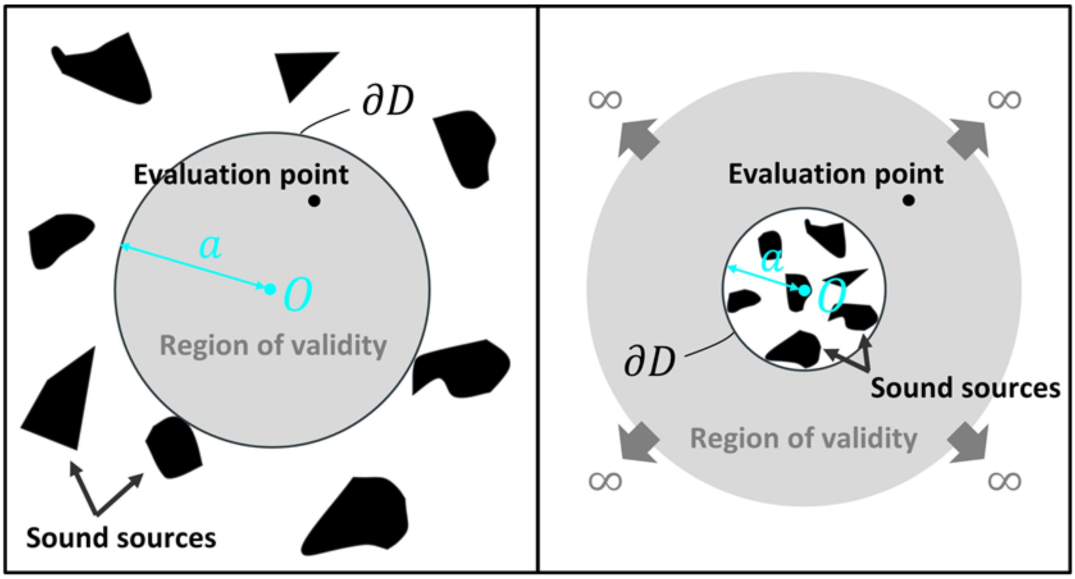

Figure 2-3 2D view of 3D regions of validity for a converging traveling wave solution (left) and a diverging travelling wave solution (right) of the 3D Helmholtz equation, relative to the origin O of the coordinate system. Spherical region of volume D, boundary ∂D, and radius a used as reference. No sound sources present inside D on the left, and outside $D \cup \partial D$ on the right.

A converging wave solution (2.14) represents the case where all acoustic sources are situated outside a bounded spatial region of validity centred at the origin, while a diverging wave solution represents the case where all sources of sound are enclosed by a half-bounded spatial region of validity that extends towards infinity and is centred at the origin, as seen in Figure 2.3. The terms corresponding to $n_n(kr)$, $h_n^{(1)}(kr)$ and $h_n^{(2)}(kr)$ from (2.10) and (2.12) are ignored when expressing (2.14) in order to avoid a singularity at the origin. These functions tend to $-\infty$ as r tends to zero (see Appendix D). For expressing (2.16), this is not an issue as the origin is excluded. $n_n(kr)$, $h_n^{(1)}(kr)$ and $h_n^{(2)}(kr)$ all satisfy the Sommerfeld condition, but $\tilde{\mathcal{D}}_{n,m}^{(\mathbb{C})}\, h_n^{(2)}(kr)$ is used in expressing the solution instead of $\tilde{\mathcal{A}}_{n,m}^{(\mathbb{C})}\, j_n(kr) + \tilde{\mathfrak{B}}_{n,m}^{(\mathbb{C})}\, n_n(kr)$ for convenience.

Taking (2.14) and (2.16), differentiating them once with respect to r, and then applying Euler`s momentum equation (2.7), leads to the radial component of the acoustic velocity vector field [71]

$$\tilde{u}_{\mathrm{r},\rhd}(\vec{r}) = \frac{i}{\rho_0 c_0} \sum_{n=0}^{\infty} \sum_{m=-n}^{n} \tilde{\mathcal{A}}_{n,m}^{(\mathbb{C})} \frac{dj_n(kr)}{d(kr)} Y_{n,m}^{(\mathbb{C})}(\theta, \varphi)\,, \tag{2.19}$$

for the converging wave solution, and

$$\tilde{u}_{r,\triangleleft}(\vec{r}) = \frac{i}{\rho_0 c_0}\sum_{n=0}^{\infty}\sum_{m=-n}^{n} \tilde{\mathcal{D}}_{n,m}^{(\mathbb{C})}\, \frac{dh_n^{(2)}(kr)}{d(kr)}\, Y_{n,m}^{(\mathbb{C})}(\theta,\varphi)\,, \tag{2.20}$$

for the diverging wave solution. From this point forward in the thesis, h_n is used to denote $h_n^{(2)}$, and $h_n'(kr)$, $j_n'(kr)$ are used to denote $dh_n^{(2)}(kr)/\, d(kr)$, $dj_n(kr)/\, d(kr)$

2.2.4 Spherical wave spectra

If the acoustic pressure or acoustic velocity is known on a virtual sphere of radius $r = r_0$ in the free-field fluid, the subsequent acoustic pressure and acoustic velocity at any other point $r < r_0$ or $r > r_0$ can be derived based on spherical wave spectra of a converging wave solution or, respectively, a diverging wave solution. A spherical wave spectrum corresponding to a spherical harmonic series expansion is the equivalent of the frequency spectrum corresponding to a Fourier Transform of a function varying with time, i.e. the set of components with associated coefficients that combine to describe a more elaborate function.

From (2.14), (2.15) and (2.19) the spherical wave spectrum of a converging wave solution is [71]

$$\tilde{p}_{\triangleright}(r,\theta,\varphi) = \sum_{n=0}^{\infty}\frac{j_n\,(kr)}{j_n\,(kr_0)}\sum_{m=-n}^{n} Y_{n,m}^{(\mathbb{C})}(\theta,\varphi)\int_{\Omega'} d\Omega' \left\{\tilde{p}_{\triangleright}(r_0,\theta',\varphi')\cdot \bar{Y}_{n,m}^{(\mathbb{C})}(\theta',\varphi')\right\}\,, \tag{2.21}$$

for the acoustic pressure, and

$$\begin{split}\tilde{u}_{\mathrm{r},\triangleright}(r,\theta,\varphi) = \frac{i}{\rho_0 c_0}\sum_{n=0}^{\infty}\frac{j_n'(kr)}{j_n\,(kr_0)}\sum_{m=-n}^{n} Y_{n,m}^{(\mathbb{C})}(\theta,\varphi)\int_{\Omega'} d\Omega' \Big\{\tilde{u}_{\mathrm{r},\triangleright}(r_0,\theta',\varphi') \\ \cdot \bar{Y}_{n,m}^{(\mathbb{C})}(\theta',\varphi')\Big\}\,,\end{split} \tag{2.22}$$

for the acoustic velocity. From (2.16), (2.17) and (2.20) the spherical wave spectrum of a diverging wave solution is given by [71]

$$\tilde{p}_{\triangleleft}(r,\theta,\varphi) = \sum_{n=0}^{\infty}\frac{h_n\,(kr)}{h_n\,(kr_0)}\sum_{m=-n}^{n} Y_{n,m}^{(\mathbb{C})}(\theta,\varphi)\int_{\Omega'} d\Omega' \left\{\tilde{p}_{\triangleleft}(r_0,\theta',\varphi')\cdot \bar{Y}_{n,m}^{(\mathbb{C})}(\theta',\varphi')\right\}\,, \tag{2.23}$$

for the acoustic pressure, and

$$\tilde{u}_{r,\lhd}(r,\theta,\varphi) = \frac{i}{\rho_0 c_0}\sum_{n=0}^{\infty}\frac{h_n'(kr)}{h_n\,(kr_0)}\sum_{m=-n}^{n} Y_{n,m}^{(\mathbb{C})}(\theta,\varphi)\int\limits_{\Omega'} d\Omega'\left\{\tilde{u}_{r,\lhd}(r_0,\theta',\varphi') \cdot \bar{Y}_{n,m}^{(\mathbb{C})}(\theta',\varphi')\right\}, \quad (2.24)$$

for the acoustic velocity, where the pair (θ',φ') in the integrals represents a set of angles around the sphere different from (θ,φ), and $\int_{\Omega'} d\Omega'\{\} = \int_0^{\pi}\sin\theta\, d\theta \int_0^{2\pi} d\varphi\,\{\}$ is a compact way to express the derivation across a spherical surface of unit radius.

The acoustic wave impedance in a direction of acoustic motion is defined as the ratio between the acoustic pressure and the norm of the acoustic velocity in that direction, i.e. a measure of how acoustic motion due to an excitation is impeded. Only radial acoustic velocity is considered in the free-field fluid due to it having no viscosity, as previously described. Therefore, from (2.21) and (2.22), the acoustic wave impedance of the free-field fluid in response to a travelling sound wave converging to the origin is expressed as

$$\tilde{z}_n^{(\rhd)} = i\rho_0 c_0 \frac{j_n\,(ka)}{j_n'(ka)}, \quad (2.25)$$

on a virtual sphere of radius $r = a$, for each spherical harmonic degree (mode) n. Likewise, from (2.23) and (2.24), the acoustic wave impedance of the free-field fluid in response to a travelling sound wave diverging to the origin is expressed as

$$\tilde{z}_n^{(\lhd)} = -i\rho_0 c_0 \frac{h_n\,(ka)}{h_n'(ka)}, \quad (2.26)$$

on a virtual sphere of radius $r = a$, for each spherical harmonic degree (mode) n.

2.2.5 The far-field. Radiated power

A sound wave diverging away from the origin in the free-field fluid gets attenuated with distance as more and more matter has to be set in motion, i.e. due to spreading in space. This is reflected in the Sommerfeld radiation condition. As r increases, the associated acoustic pressure eventually becomes proportional to $1/r$ depending on the frequency and the properties of the fluid. This region of space where the variation with r exhibits this behaviour is denoted as the far-field. In contrast, the region of proximity around the origin, denoted as the near-field, is characterized by the spherical Hankel function of the second kind, which has complicated behaviour around the origin, as seen in Appendix D.

The far-field behaviour of the acoustic pressure $\tilde{p}(\vec{r})$ of a diverging wave is given by [71]

$$\tilde{p}_{\infty}(\vec{r}) = \lim_{r\to\infty} \tilde{p}_{\triangleleft}(\vec{r}) = \frac{e^{-ikr}}{kr} \sum_{n=0}^{\infty} \sum_{m=-n}^{n} i^{n+1}\, \tilde{\mathcal{D}}_{n,m}^{(\mathbb{C})}\, Y_{n,m}^{(\mathbb{C})}(\theta,\varphi) \ , \tag{2.27}$$

and is discussed more rigorously in [74], where aspects such as convergence of this series expansion are covered. Because the asymptotic behaviour of $h_n(kr)$ at large arguments is not uniform with respect to n (see Appendix D), it cannot be used individually for each term in the summation of (2.16) to prove (2.27). A different approach is necessary, which is presented in [74] for the complex-valued spherical harmonics.

The directivity pattern of the acoustic pressure is defined as [71]

$$\tilde{p}_{\Theta}(\theta,\phi) = \frac{r}{e^{-ikr}}\, \tilde{p}_{\infty}(\vec{r}) = \frac{1}{k} \sum_{n=0}^{\infty} \sum_{m=-n}^{n} i^{n+1}\, \tilde{\mathcal{D}}_{n,m}^{(\mathbb{C})}\, Y_{n,m}^{(\mathbb{C})}(\theta,\varphi) \,, \tag{2.28}$$

and represents the angular dependence of the far-field acoustic pressure $\tilde{p}_{\infty}$, which is maintained in this region of space regardless of radial position. Using the approach from [74], the far-field of the acoustic velocity can be written as

$$\tilde{u}_{r,\infty}(\vec{r}) = \lim_{r\to\infty} \tilde{u}_{\mathrm{r},\triangleleft}(\vec{r}) = \frac{i}{\rho_0 c_0} \frac{e^{-ikr}}{kr} \sum_{n=0}^{\infty} \sum_{m=-n}^{n} i^{n+1} \sum_{m=-n}^{n} \tilde{\mathcal{D}}_{n,m}^{(\mathbb{C})}\, Y_{n,m}^{(\mathbb{C})}(\theta,\varphi) \ , \tag{2.29}$$

with the corresponding directivity pattern

$$\tilde{u}_{r,\Theta}(\theta,\phi) = \frac{r}{e^{-ikr}}\, \tilde{u}_{r,\infty}(\vec{r}) = \frac{1}{k} \frac{i}{\rho_0 c_0} \sum_{n=0}^{\infty} \sum_{m=-n}^{n} i^{n+1}\, \tilde{\mathcal{D}}_{n,m}^{(\mathbb{C})}\, Y_{n,m}^{(\mathbb{C})}(\theta,\varphi) \,. \tag{2.30}$$

The sound intensity is defined as the acoustic energy flux per unit area exhibited in the direction normal to a surface. This quantity is a vector field that varies with time and its instantaneous value at a given point in space is $I(t) = p(t) \cdot u(t)$. In the frequency domain, the time-averaged acoustic intensity, at a single frequency, becomes [71]

$$\vec{\tilde{I}}_{avg}(\vec{r}) = \frac{1}{2} \operatorname{Re}\{ \tilde{p}(\vec{r}) \cdot \bar{\tilde{u}}_r(\vec{r})\} \,. \tag{2.31}$$

Let there be an acoustic pressure generated outside of a virtual sphere of radius a, centred at the origin of the coordinate system. The region outside $r = a$ represents the region of validity for the diverging wave solution to the 3D Helmholtz equation. The acoustic power radiated from the virtual sphere is defined as the component of the time-averaged acoustic intensity that is outward normal to the surface, integrated over the surface [71]. The outward normal component of $\vec{\bar{\tilde{I}}}_{avg}(\vec{r})$ is its radial one, which corresponds to $\tilde{u}_{\mathrm{r}}(\vec{r})$, thus, the radiated sound power at a single frequency is

$$\widetilde{W} = \frac{1}{2}\int_{0}^{\pi} \sin\theta \, d\theta \int_{0}^{2\pi} d\varphi \left\{ a^2 \, \mathrm{Re}\{\tilde{p}(a,\theta,\varphi) \cdot \bar{\tilde{u}}_r(a,\theta,\varphi)\} \right\} . \tag{2.32}$$

By using relations (2.33) and (2.20) in (2.32), after doing some algebraic manipulation involving the Wronskian relation (see Appendix D), the dot product between the two double summations corresponding to the acoustic pressure and, respectively, to the conjugate of the radial acoustic velocity reduces to just the coefficients $\widetilde{\mathcal{D}}^{(\mathbb{C})}_{n,m}$, so [71]

$$\widetilde{W} = \frac{1}{2\rho_0 c_0 k^2} \sum_{n=0}^{\infty} \sum_{m=-n}^{n} \left|\widetilde{\mathcal{D}}^{(\mathbb{C})}_{n,m}\right|^2 . \tag{2.33}$$

The radiated power is a quantity that does not depend on position in space, such that $\widetilde{W}$ calculated using relation (2.31) at a different radius $r > a$ and is the same as (2.33). In addition, it is worth mentioning that each coefficient of the spherical harmonic decomposition is shown in (2.33) to have an individual contribution to the overall radiated power due to their orthogonality. The result can be interpreted as the spherical harmonics of a spherical surface being the modal patterns of acoustic radiation from that surface, where these modal patterns are decoupled from one another and radiate without influencing one another.

2.2.6 Special solutions to the 3D Helmholtz equation

Two special solutions that satisfy the 3D Helmholtz equation (2.6) are represented by a monochromatic acoustic plane-wave and an acoustic point-monopole source. These are used as the primary and secondary in the later chapters exemplifying 3D acoustic scattering and its active control due to their well-understood and simplified behaviour.

Let there be a monochromatic acoustic plane-wave of magnitude $\tilde{\mathcal{P}}_{pw}$ propagating in the direction $(\theta_{pw}, \varphi_{pw})$ relative to the origin. The spherical harmonic expansions of the generated acoustic pressure is [71, 72]

$$\tilde{p}_{pw}(\vec{r}) = \tilde{\mathcal{P}}_{pw}\, e^{\pm i\, \vec{k}_{pw}\cdot\vec{x}} = \sum_{n=0}^{\infty} \sum_{m=-n}^{n} \tilde{C}_{n,m}^{(\mathbb{C})}\; j_n(kr)\; Y_{n,m}^{(\mathbb{C})}(\theta,\varphi)\,, \tag{2.34}$$

and that of the generated radial acoustic velocity is [71]

$$\tilde{u}_{r,pw}(\vec{r}) = \frac{i}{\rho_0 c_0} \sum_{n=0}^{\infty} \sum_{m=-n}^{n} \tilde{C}_{n,m}^{(\mathbb{C})}\, j_n'(kr)\; Y_{n,m}^{(\mathbb{C})}(\theta,\varphi)\,, \tag{2.35}$$

where

$$\tilde{C}_{n,m}^{(\mathbb{C})} = 4\pi\, \tilde{\mathcal{P}}_{pw}\, (\pm i)^n\, \bar{Y}_{n,m}^{(\mathbb{C})}(\theta_{pw}, \varphi_{pw})\,, \tag{2.36}$$

and

$$\vec{x} = \begin{bmatrix} x \\ y \\ z \end{bmatrix} = \begin{bmatrix} r\ \sin\theta\ \cos\varphi \\ r\ \sin\theta\ \sin\varphi \\ r\ \cos\theta \end{bmatrix}, \quad \vec{k}_{pw} = k\, \hat{k}_{pw} = k \begin{bmatrix} \sin\theta_{pw}\ \cos\varphi_{pw} \\ \sin\theta_{pw}\ \sin\varphi_{pw} \\ \cos\theta_{pw} \end{bmatrix}. \tag{2.37}$$

In the time-frequency convention of this work, the ‘minus’ and ’plus’ signs correspond to plane-waves moving away from or towards the origin, respectively. It is worth mentioning that (2.34) takes the form of a converging solution (2.14) with a region of validity over all space. The plane-wave, which is an idealization of physical behaviour, travels over all space while maintaining constant magnitude, thus it cannot satisfy the Sommerfeld condition and cannot be described as a diverging wave solution, even when it is outgoing away from the origin. From (2.34), it can be observed that the expansion of the plane-wave always takes the form of a converging solution.

Let there be a monochromatic acoustic point-monopole of volumetric source strength $\tilde{q}_{pm}$ situated at position $(r_{pm}, \theta_{pm,}\varphi_{pm})$ away from the origin of the coordinate system $(r_{pm} \neq 0)$. The spherical harmonic expansion of the generated acoustic pressure is given by [71, 74]

$$\tilde{p}_{pm}(\vec{r}) = \begin{cases} \tilde{q}_{pm} \displaystyle\sum_{n=0}^{\infty} \sum_{m=-n}^{n} \tilde{C}_{n,m}^{(\mathbb{C})}\; j_n(kr)\; Y_{n,m}^{(\mathbb{C})}(\theta,\varphi)\ , & r < r_{pm} \\ \tilde{q}_{pm} \displaystyle\sum_{n=0}^{\infty} \sum_{m=-n}^{n} \tilde{C}_{n,m}^{(\mathbb{C})}\, h_n^{(2)}(kr)\, Y_{n,m}^{(\mathbb{C})}(\theta,\varphi)\ , & r > r_{pm} \end{cases}. \tag{2.38}$$

and that of the generated radial acoustic velocity is given by [71, 74]

$$\tilde{u}_{r,pm}(\vec{r}) = \begin{cases} \tilde{q}_{pm} \dfrac{i}{\rho_0 c_0} \displaystyle\sum_{n=0}^{\infty} \sum_{m=-n}^{n} \tilde{C}_{n,m}^{(\mathbb{C})} \; j_n'(kr) \; Y_{n,m}^{(\mathbb{C})}(\theta, \varphi) \ , & r < r_{pm} \\ \tilde{q}_{pm} \dfrac{i}{\rho_0 c_0} \displaystyle\sum_{n=0}^{\infty} \sum_{m=-n}^{n} \tilde{C}_{n,m}^{(\mathbb{C})} \, h_n'(kr) \, Y_{n,m}^{(\mathbb{C})}(\theta, \varphi) \ , & r > r_{pm} \end{cases} , \tag{2.39}$$

where

$$\tilde{C}_{n,m}^{(\mathbb{C})} = \begin{cases} k^2 \rho_0 c_0 \, h_n^{(2)}(k r_{pm}) \, \bar{Y}_{n,m}^{(\mathbb{C})}(\theta_{pm}, \varphi_{pm}), & r < r_{pm} \\ k^2 \rho_0 c_0 \, j_n(k r_{pm}) \, \bar{Y}_{n,m}^{(\mathbb{C})}(\theta_{pm}, \varphi_{pm}), & r > r_{pm} \end{cases} . \tag{2.40}$$

It can be observed from the above that a point-monopole source is defined differently in the regions inside and outside the circle of radius r_{pm}. This is a consequence of the coordinate system not being centred at the position of the point-monopole, which results in two regions of validity each described by converging wave behaviour and, respectively, diverging wave behaviour.

2.3 Modelling 3D sound scattering in spherical coordinates

2.3.1 Sound scattering modelled as superposition

In acoustics, the problem of scattering from a finite object of volume V, enclosed by surface S, is modelled as a wave freely propagating through a medium outside of V that impinges on the boundary and suffers reflections, diffraction, absorption and/or transmission into V depending on the given circumstances. Under the assumption of linearity and by the Huygens-Fresnel principle, each infinitesimally small point on S acts as a radiator in response to the interaction with the energy transported by the initial wave and the combined contributions of all points form a new sound field in the exterior of volume V and, respectively, in the interior of volume V. Therefore, using the frequency-domain representation, [71], it is said that

$$\tilde{p}_t = \tilde{p}_i + \tilde{p}_s \ . \tag{2.41}$$

The ideal cloak must achieve $\tilde{p}_s = 0$ in all directions such that $\tilde{p}_t = \tilde{p}_i$. As such, in an ideal scenario where all involved physical variations are always known, the scattering represents the primary disturbance that must be cancelled.

In practice, an ideal cloak may be difficult to achieve and the effectiveness of hiding the obstacle will always depend on the strategy used to search for its presence. Therefore, it is desirable to assess cloaking performance based on how much of $\tilde{p}_s$ is suppressed. One such criterion is represented by the radiated scattered power as it quantifies the overall rate of change of energy. This is a quantity that is invariant with position, therefore it is quite convenient to use in calculations and to measure/manipulate in practice. However, one downside is that $\tilde{p}_s$ generally has complicated variations in space, both with angular position and with radial position (near-field and far-field). Using a global criterion such as radiated power hinders the potential efficiency of addressing certain regions of space through different methods in order to achieve cloaking. Another downside is that scattered sound power is a conceptual, not an actual physical quantity, as it relies on the ability to take the information of the total physical behaviour and subtract from it the behaviour if the incidence to obtain the `scattering information'.

2.3.2 Scattering as an exterior impedance boundary-value problem

The exterior impedance boundary-value problem from Figure 2-2c is the fundamental building block that can be used to model sound scattering from a single object surrounded by a fluid. In this model, the sound scattering due to a given incidence acting on the obstacle is governed only by the physical properties of the separation boundary, which must satisfy (2.7). The interior of the object is considered voided.

As explained previously, the incident pressure field must take the form of a converging solution, thus let the incident pressure field be expressed as (2.14). Also, the scattered pressure field must take the form of a radiating solution, thus let the scattered field pressure field be expressed as (2.16). Taking all the above definitions into considerations, at a single frequency, the total field in the fluid before any control is

$$\tilde{p}_t(\vec{r}) = \tilde{p}_i(\vec{r}) + \tilde{p}_s(\vec{r}) = \sum_{n=0}^{\infty} \sum_{m=-n}^{n} \left[\tilde{C}_{n,m}^{(i,\mathbb{C})}\, j_n(kr) + \tilde{C}_{n,m}^{(s,\mathbb{C})}\, h_n(kr) \right] Y_{n,m}^{(\mathbb{C})}(\theta,\varphi). \tag{2.42}$$

Considering the total pressure on the surface of the scatterer, applying (2.7) at $r = a$ for the radial component and performing some algebraic manipulation leads to [65]

$$\frac{\tilde{C}_{n,m}^{(s,\mathbb{C})}}{\tilde{C}_{n,m}^{(i,\mathbb{C})}} = -\frac{j_n(ka) + i\dfrac{\tilde{Z}_n}{\rho_0 c_0} j_n'(ka)}{h_n(ka) + i\dfrac{\tilde{Z}_n}{\rho_0 c_0} h_n'(ka)} = -\frac{j_n'(ka)}{h_n'(ka)} + \frac{\rho_0 c_0}{(ka)^2 [h_n'(ka)]^2 \big(\tilde{Z}_n + \tilde{z}_n\big)}\ . \tag{2.43}$$

where $\tilde{Z}_n$ is the modal wave impedance on the surface of the scatterer, and $\tilde{z}_n$ is the free-field impedance or radiation loading of the fluid, given by (2.26). The total field is then equal to

$$\tilde{p}_t(\vec{r}) =$$

$$= \sum_{n=0}^{\infty} \sum_{m=-n}^{n} \tilde{C}_{n,m}^{(i,\mathbb{C})} \left[j_n(kr) - h_n(kr) \frac{j_n(ka) + i \frac{\tilde{Z}_n}{\rho_0 c_0} j_n'(ka)}{h_n(ka) + i \frac{\tilde{Z}_n}{\rho_0 c_0} h_n'(ka)} \right] Y_{n,m}^{(\mathbb{C})}(\theta, \varphi) \,. \tag{2.44}$$

The above relations relate the spherical harmonic coefficients $\tilde{C}_{n,m}^{(i,\mathbb{C})}$ that uniquely define the incident field to the spherical harmonic coefficients $\tilde{C}_{n,m}^{(s,\mathbb{C})}$ that uniquely define the corresponding scattered field. As long as the incident field coefficients are known, the scattered field coefficients can be derived with knowledge of the impedances of $\tilde{Z}_n + \tilde{z}_n$, which effectively governs the motion of the fluid-loaded spherical scattering surface.

2.3.3 Asymptotic behaviour in different frequency ranges

Expression (2.43) highlights that the variation with normalized frequency ka of the ratio coefficients between spherical harmonic coefficients of the scattering and of the incidence is given by a ratio of spherical Bessel and Hankel functions. For a fixed n, the coefficients with the same index m exhibit the same relation with ka. The asymptotic behaviour of the ratio at low frequencies, i.e. when $ka \ll 1$, otherwise known in the literature as the 'Rayleigh region', is discussed in [75] for different cases of constant surface impedance. However, this reference uses the opposite time-frequency convention from that employed in this work and, also, defines the acoustic impedance of the scattering surface normalized by the characteristic acoustic impedance of the surrounding medium as $\tilde{\zeta}_n = \tilde{Z}_n/(i\rho_0 c_0)$ rather than the $\tilde{\zeta}_n = \tilde{Z}_n/(\rho_0 c_0)$ used in this thesis. By combining the different asymptotic behaviours of the spherical Bessel and Hankel functions, which are discussed in Appendix D, it is obtained that

$$\frac{j_n(ka) + i\tilde{\zeta}_n\, j_n'(ka)}{h_n(ka) + i\tilde{\zeta}_n\, h_n'(ka)} \approx \begin{cases} \dfrac{(ka)^2 \left(1 - \tilde{\zeta}_n\, ika/3\right)}{\tilde{\zeta}_n + ika}, & n = 0 \\ i \left[\dfrac{2^n n!}{(2n)!}\right]^2 \dfrac{(ka)^{2n+1}}{(2n+1)} \dfrac{-ika + \tilde{\zeta}_n n}{ika + \tilde{\zeta}_n (n+1)}, & n > 0 \end{cases}, \tag{2.45}$$

without taking into consideration any variation of the impedance ζ_n with frequency or n. If ζ_n does vary with frequency and n, the asymptotic behaviour can be obtained by further manipulating (2.45).

2.4 Modelling active control of 3D sound scattering in spherical coordinates

2.4.1 Active control modelled as superposition

Using the same conceptual approach as in the previous section, an additional sound field is now considered alongside the previous incident and scattered pressure fields. For tonal active control, the new total pressure becomes

$$\tilde{p}_t = \tilde{p}_i + \tilde{p}_s + \tilde{p}_{\mathbb{2}} \,. \tag{2.46}$$

where $\tilde{p}_{\mathbb{2}}$ is the additional secondary pressure. The ideal suppression of the scattering, i.e. cloaking, is achieved when $\tilde{p}_{\mathbb{1}} + \tilde{p}_{\mathbb{2}} = \tilde{p}_s + \tilde{p}_{\mathbb{2}} = 0$ and $\tilde{p}_t = \tilde{p}_i$.

Assuming there are D incident waves that scatter from the spherical obstacle and each one creates a scattered field with coefficients $\tilde{\alpha}_{n,m}^{(\mathbb{C},d)}$, $d \in \{1, 2, 3 \cdots D\}$, then by linear superposition the primary field is

$$\tilde{p}_{\mathbb{1}}(\vec{r}) = \tilde{p}_s(\vec{r}) = \sum_{d=1}^{D} \sum_{n=0}^{\infty} \sum_{m=-n}^{n} \tilde{\alpha}_{n,m}^{(\mathbb{C},d)} \, Y_{n,m}^{(\mathbb{C})}(\theta, \varphi) = \sum_{n=0}^{\infty} \sum_{m=-n}^{n} \tilde{C}_{n,m}^{(\mathbb{C},\mathbb{1})} \, h_n(kr) \, Y_{n,m}^{(\mathbb{C})}(\theta, \varphi) \;. \tag{2.47}$$

Likewise, for the secondary field, let there be L control sources with the coefficients $\tilde{\beta}_{n,m}^{(\mathbb{C},l)}$, $l \in \{1, 2, 3 \cdots L\}$ and corresponding control parameters $\tilde{q}_l$, such that

$$\tilde{p}_{\mathbb{2}}(\vec{r}) = \sum_{l=1}^{L} \sum_{n=0}^{\infty} \sum_{m=-n}^{n} \tilde{q}_l \, \tilde{\beta}_{n,m}^{(\mathbb{C},l)} \, Y_{n,m}^{(\mathbb{C})}(\theta, \varphi) = \sum_{n=0}^{\infty} \sum_{m=-n}^{n} \tilde{q}_l \tilde{C}_{n,m}^{(\mathbb{C},\mathbb{2})} \, h_n(kr) \, Y_{n,m}^{(\mathbb{C})}(\theta, \varphi) \;. \tag{2.48}$$

Combining the scattering and the secondary control field leads to

$$\begin{aligned} \tilde{p}_{\mathbb{1}}(\vec{r}) + \tilde{p}_{\mathbb{2}}(\vec{r}) &= \sum_{n=0}^{\infty} \sum_{m=-n}^{n} \left(\tilde{C}_{n,m}^{(\mathbb{C},\mathbb{1})} + \tilde{Q}_q \tilde{C}_{n,m}^{(\mathbb{C},\mathbb{2})} \right) h_n(kr) \, Y_{n,m}^{(\mathbb{C})}(\theta, \varphi) = \\ &= \sum_{n=0}^{\infty} \sum_{m=-n}^{n} \left(\sum_{d=1}^{D} \tilde{\alpha}_{n,m}^{(\mathbb{C},d)} + \tilde{Q}_l \sum_{l=1}^{L} \tilde{\beta}_{n,m}^{(\mathbb{C},l)} \right) Y_{n,m}^{(\mathbb{C})}(\theta, \varphi) \,, \end{aligned} \tag{2.49}$$

which is still the form of a diverging wave solution with the new coefficients $\tilde{C}_{n,m}^{(\mathbb{C},\mathbb{1})} + \tilde{Q}_l \tilde{C}_{n,m}^{(\mathbb{C},\mathbb{2})}$.

Using the above formulations, it can be deduced that the total radiated sound power after control is

$$\widetilde{W}_t = \frac{1}{2\rho_0 c_0 k^2} \sum_{n=0}^{\infty} \sum_{m=-n}^{n} \left| \tilde{C}_{n,m}^{(\mathbb{C},\mathbb{1})} + \tilde{Q}_l \tilde{C}_{n,m}^{(\mathbb{C},\mathbb{2})} \right|^2 . \tag{2.50}$$

This can be expanded into

$$\begin{aligned} \widetilde{W}_t = \frac{1}{2\rho_0 c_0 k^2} \Bigg[& \sum_{n=0}^{\infty} \sum_{m=-n}^{n} \left| \tilde{C}_{n,m}^{(\mathbb{C},\mathbb{1})} \right|^2 + \sum_{n=0}^{\infty} \sum_{m=-n}^{n} \left| \tilde{C}_{n,m}^{(\mathbb{C},\mathbb{2})} \right|^2 \\ & + \sum_{n=0}^{\infty} \sum_{m=-n}^{n} \left(\tilde{C}_{n,m}^{(\mathbb{C},\mathbb{1})} \right) \cdot \overline{\left(\tilde{Q}_l \, \tilde{C}_{n,m}^{(\mathbb{C},\mathbb{2})} \right)} + \sum_{n=0}^{\infty} \sum_{m=-n}^{n} \overline{\left(\tilde{C}_{n,m}^{(\mathbb{C},\mathbb{1})} \right)} \cdot \left(\tilde{Q}_l \tilde{C}_{n,m}^{(\mathbb{C},\mathbb{2})} \right) \Bigg] . \end{aligned} \tag{2.51}$$

Relation (2.51) highlights the fact that there are three types of components that contribute to the power after control. The first and second double summations represent the power of the primary in the absence of the secondary and, respectively, the power of the secondary in the absence of the primary. These are always real and positive quantities. The last two double summations represent the cross-coupling, i.e. the outcome of the primary and secondary both being present and interacting with each other. Individually, they can be complex with negative values of real and imaginary parts; however, summed up together always results in a real number. In general, adding the primary pressure to the secondary pressure does not translate in the overall power being additive. This is because of the cross-coupling, which can either reduce or increase the sum of the independent powers radiated by the primary and, respectively, secondary, on their own. When the primary field and/or the secondary field consist of the superposition of many fields, each one will couple in its own way with all the others, including the ones from the other field.

2.4.2 Control constraint: power minimization

In practice, the total scattered sound power after control expressed as a series expansion is truncated up to N terms such that it can be calculated and manipulated. The choice of N dictates the amount of spatial precision that can be represented by the decomposition, as the spherical harmonic functions of higher indices described more complicated spatial variations. In practice, the truncation value is generally chosen based on the shortest wavelength of interest.

Let the truncated spherical harmonics expansion of the total power after control be denoted as

$$\widetilde{W}_t = \frac{1}{2\rho_0 c_0 k^2} \sum_{n=0}^{N} \sum_{m=-n}^{n} \left| \tilde{C}_{n,m}^{(\mathbb{C},\mathbb{1})} + \tilde{Q}_l \tilde{C}_{n,m}^{(\mathbb{C},\mathbb{2})} \right|^2 . \tag{2.52}$$

This can also be written as $J = 2\rho_0 c_0 k^2 \widetilde{W}_t = \breve{\mathbf{e}}^{\mathrm{H}}\breve{\mathbf{e}}$ using the matrix equation $\breve{\mathbf{e}} = \breve{\mathbf{d}} + \breve{\mathbf{B}} \cdot \breve{\mathbf{q}}$, where the $(N+1)^2$ by 1 column vector $\breve{\mathbf{d}}$ contains the coefficients in the primary arranged in the order

$$\breve{\mathbf{d}} = \left[\tilde{C}_{0,0}^{(\mathbb{C},\mathbb{1})}, \tilde{C}_{1,-1}^{(\mathbb{C},\mathbb{1})}, \tilde{C}_{1,0}^{(\mathbb{C},\mathbb{1})}, \tilde{C}_{1,1}^{(\mathbb{C},\mathbb{1})} \cdots \tilde{C}_{N,-N}^{(\mathbb{C},\mathbb{1})} \cdots \tilde{C}_{N,0}^{(\mathbb{C},\mathbb{1})} \cdots \tilde{C}_{N,N}^{(\mathbb{C},\mathbb{1})}\right]^{\mathrm{T}},$$

each column of the of the $(N+1)^2$ by L matrix $\breve{\mathbf{B}}$ contains the coupling coefficients $\tilde{C}_{n,m}^{(\mathbb{C},\mathbb{2})}$ of the secondary arranged in the same order, the L by 1 column vector $\breve{\mathbf{q}} = [q_1, q_2, q_3 \cdots q_L]^{\mathrm{T}}$ contains the adjustable control parameters (modal control signals), and $(N+1)^2$ by 1 column vector $\breve{\mathbf{e}}$ contains the combination after control of coefficients between primary and scaled secondary at each index, i.e. $\tilde{C}_{n,m}^{(\mathbb{C},\mathbb{1})} + \tilde{Q}_l \tilde{C}_{n,m}^{(\mathbb{C},\mathbb{2})}$.

Solving the quadratic equation to obtain the set of parameters $\breve{\mathbf{q}}$ that best minimizes the cost function $J = \breve{\mathbf{e}}^{\mathrm{H}}\breve{\mathbf{e}}$ represents the least-mean squares minimization, which is a common control strategy. The practical outcome of this is that the scattered sound power, a global measure, is minimized. For an overdetermined system ($E > L$), the optimal control parameters required to minimize J in a 'least-mean squares sense' are [76]

$$\breve{\mathbf{q}}_{\mathrm{opt}} = -\left[\breve{\mathbf{B}}^{\mathrm{H}}\breve{\mathbf{B}}\right]^{-1}\breve{\mathbf{B}}^{\mathrm{H}}\breve{\mathbf{d}}\ , \qquad (2.53)$$

under the assumption that $\breve{\mathbf{B}}^{\mathrm{H}}\breve{\mathbf{B}}$ is positive definite matrix, which leads to the minimum value of the cost function being

$$J_{min} = \breve{\mathbf{d}}^{\mathrm{H}}\left[\mathbf{I} - \breve{\mathbf{B}}\left[\breve{\mathbf{B}}^{\mathrm{H}}\breve{\mathbf{B}}\right]^{-1}\breve{\mathbf{B}}^{\mathrm{H}}\right]\breve{\mathbf{d}}\,. \qquad (2.54)$$

As described in [76], the way in which the minimum of $J = \breve{\mathbf{e}}^{\mathrm{H}}\breve{\mathbf{e}}$ is reached depends solely on the $\breve{\mathbf{B}}$, and the location of that minimum in the domain of the cost function is dependent on both $\breve{\mathbf{B}}$ and $\breve{\mathbf{d}}$.

In the case of a fully-determined system ($E = L$) , there is still a minimum for the quadratic cost function which is unique if $\breve{\mathbf{B}}^{\mathrm{H}}\breve{\mathbf{B}}$ is positive definite [76]. However, the expressions from the over-determined case simplify. While this situation yields $J_{min} = 0$ after optimization, there is still an inherent risk that the outcome may not be the same for the positions other than the chosen sensors location. Said risk is also present for the over-determined system. For the under- determined scenario ($E < L$) , $\breve{\mathbf{B}}^{\mathrm{H}}\breve{\mathbf{B}}$ cannot be positive definite and becomes singular, resulting in the inexistence of an unique solution to the minimization problem [76]. The problem can still be solved using different special approaches, one of which is represented by regularisation, where the control effort $\breve{\mathbf{q}}^{\mathrm{H}}\breve{\mathbf{q}}$ is minimized alongside the error $J = \breve{\mathbf{e}}^{\mathrm{H}}\breve{\mathbf{e}}$ and the new cost function is given by

$$J = \breve{\mathbf{e}}^{\mathrm{H}}\breve{\mathbf{e}} + \beta\, \breve{\mathbf{q}}^{\mathrm{H}}\breve{\mathbf{q}}\,, \tag{2.55}$$

where β is a regularisation parameter. The optimal modal control signals then become [76]

$$\breve{\mathbf{q}}_{\mathrm{opt}} = -\left[\breve{\mathbf{B}}^{\mathrm{H}}\breve{\mathbf{B}} + \beta\mathbf{I}\right]^{-1}\breve{\mathbf{B}}^{\mathrm{H}}\breve{\mathbf{d}}\,. \tag{2.56}$$

The control strategy described so far has several inherent disadvantages, the main one being that the spatial domain is being discretised into a finite number of positions when it comes to both the control sources and locations to be controlled. Firstly, this introduces spatial aliasing as the wavelength of the acoustic wave under consideration becomes comparable with the relative distance between these positions. Secondly, there is also the possibility for the chosen arrangement of secondary source and control locations to not be the best option for achieving control of the given scenario. For example, a pressure sensor can be placed in a region where the magnitude of the pressure field is already very low before any control, thus resulting in less benefit after control than could be achieved. Also, a source can be placed in a region where it does not couple very well with the primary and, thus, would not be able to contribute adequately to the control. In practice, convenient placement of sensors and secondary sources can either be identified by trial and error, or by modelling the circumstances of the application and then using mathematical techniques to optimize the locations.

2.4.3 Control minimization: single far-field direction cancellation

The parameter that optimizes the secondary can alternatively be constrained to produce regional control of the sound pressure in a specific spatial region. For example, in the far-field, one control source can be used to perfectly cancel the pressure at one angular position (θ_c, φ_c) corresponding to one direction relative to the origin of the coordinate system. In this scenario, using (2.47) and (2.48) with $L = 1$, and taking their far-field equivalents as shown in (2.27), yields the scattered pressure after control as

$$\tilde{p}_{\infty}^{(c)}(\vec{r}) = \tilde{p}_{\mathbb{1},\infty}(\vec{r}) + \tilde{p}_{\mathbb{2},\infty}(\vec{r}) = \frac{e^{-ikr}}{kr}\sum_{n=0}^{\infty} i^{n+1} \sum_{m=-n}^{n} \left(\tilde{C}_{n,m}^{(\mathbb{C},\mathbb{1})} + \tilde{q}\, \tilde{C}_{n,m}^{(\mathbb{C},\mathbb{2})}\right) Y_{n,m}^{(\mathbb{C})}(\theta,\varphi)\,, \tag{2.57}$$

which can be further expressed as a normalized far-field directivity of the pressure in the form

$$\widetilde{\Theta}_c(\theta,\phi) = \frac{1}{a}\,\frac{r}{e^{-ikr}}\,\tilde{p}^{(c)}_{\infty}(\vec{r}) = \frac{1}{ka}\sum_{n=0}^{\infty} i^{n+1} \sum_{m=-n}^{n} \left(\tilde{C}^{(\mathbb{C},\mathbb{1})}_{n,m} + \tilde{q}\;\tilde{C}^{(\mathbb{C},\mathbb{2})}_{n,m}\right) Y^{(\mathbb{C})}_{n,m}(\theta,\varphi)\,. \qquad (2.58)$$

The optimal source strength for completely cancelling $\widetilde{\Theta}_c(\theta,\phi)$ in direction (θ_c,φ_c) is then

$$\tilde{q}_{opt} = -\left[\sum_{n=0}^{\infty} i^{n+1} \sum_{m=-n}^{n} \tilde{C}^{(\mathbb{C},\mathbb{1})}_{n,m}\, Y^{(\mathbb{C})}_{n,m}(\theta_c,\varphi_c)\right] \Bigg/ \left[\sum_{n=0}^{\infty} i^{n+1} \sum_{m=-n}^{n} \tilde{C}^{(\mathbb{C},\mathbb{2})}_{n,m}\, Y^{(\mathbb{C})}_{n,m}(\theta_c,\varphi_c)\right]. \qquad (2.59)$$

2.5 Chapter summary

In the current chapter, a framework has been established for modelling the 3D scattering of acoustic travelling waves from an obstacle surrounded by an idealized fluid and for the active control of said scattering. This has been done using, predominantly, material reproduced from existing literature that has been repackaged in a consistent way. The contents of this chapter are employed in the later parts of the thesis as a toolbox for exploring the research question at a theoretical level.

Although the research contributions of the current work are in the form of theoretical analysis and modelled results, some consideration is given to the potential practical limitations of realizing an active control system for the 3D sound scattering from an object. These limitations are discussed in the following chapter and are used as a guide for the modelling work that is later presented in Chapter 4, Chapter 5, Chapter 6 and Chapter 7.

Chapter 3 Practical-Oriented Modelling of Sound Scattering and Its Control

The current chapter explores the challenges of transitioning the theoretical models discussed in the previous chapters into a practical working system. Firstly, the measurement of the sound scattering phenomenon is discussed, in particular, when it comes to capturing spherical harmonic components in real-time. The theoretical strategies for the frequency domain that are presented in Chapter 2 rely on the circumstances achieving a steady-state; however, a practical active control system is required to act accordingly to situational changes as time progresses, especially when performing the act of cloaking. Secondly, limitations are explained for using representations of spherical harmonics, in particular, when describing multiple sound fields at the same time, i.e. the scattering (the primary) and the secondary. Lastly, a specific modelling approach from the literature is presented. This relies on the work of Bobrovnitskii and can overcome some of the practical challenges covered in the previous sections.

3.1 Sensing sound scattering phenomena

3.1.1 Capturing spherical harmonic information for active control

Employing active control in a given situation implies gathering information about the situation such that the involved phenomena can be manipulated. However, information such as the spherical harmonic components of a physical quantity is a mathematical abstraction which is obtained in practice by performing measurements of that quantity in a specific way and then further processing the captured data. As such, this procedure is limited by the number and capabilities of the available sensing devices, as well as the causality of implemented system.

When it comes to sound fields, there are two types of fundamental sensor designs that can be generally realized in practice: a pressure microphone and a pressure gradient microphone. The first of the two senses in an omnidirectional pattern equivalent to the radiation of a point-monopole. The latter of the two consists of placing two pressure microphones very close to each other, resulting in directivity patterns equivalent to the radiation of two point-monopoles in close proximity to each other. This includes the figure-of-eight pattern associated with a dipole and the cardioid pattern. Both these designs are limited when it comes to the 3D spatial information they can discern. Accurately measuring sound fields with more complicated spatial pressure variations patterns requires more than one instance of the previously mentioned designs, arranged in different combinations.

It can be observed from Figure 1-7 that as the degree n of a spherical harmonic increases, the function has more and more complicated variations with angular position on a virtual sphere. From the literature on measuring and reproducing 3D sound fields, it is known that $(N + 1)^2$ omnidirectional loudspeakers or microphones are required to create or capture, respectively, the spherical harmonic components of a sound field up to the degree N [77]. When it comes to implementing active control, this limitation is inherited. Even more so, the active control system is comprised of both sensors and sources, thus, the constraint applies in two separate cases.

However, active tonal control with a small number of sources produces benefit when the frequency is low and no improvement in the high frequency regime, as mentioned in [24]. Furthermore, the results in [78] suggest that there is a relation between the spherical harmonic coefficients in the expansion and the wavelength relative to the size of the scattering object. This is because, at low values of ka, where the spatial variations of a sound field occur over a relatively large distance, only the first few spherical harmonic terms contribute in the expansion. Furthermore, as the spatial variations of the field occur over smaller and smaller distance, more and more spherical harmonic terms are present simultaneously in the expansion, such that the series becomes more difficult to compute and methods such as series based on the Watson Transform are required [38, 65]. Considering all of these aspects, it can be said that active controllers based on spherical harmonic series representations are most advantageous when using a small number of sensors and secondary sources to suppress in the low frequency regime.

As an example, let only the monopole-like $n = 0$ term and the dipole-like $n = 1$ terms oriented along the Cartesian axes be considered in the spherical harmonics series. These are expected to be most dominant at low frequencies. Using the constraint described previously, at least four omnidirectional sensors and at least four omnidirectional sources are needed for an active control system. Ideally, each of the two array types would be positioned uniformly on a virtual sphere [77]. The number ‘four’ can be further reduced depending on the circumstances of the situation. If the scenario was such that only the $n = 0$ term and one specific $n = 1$ term were always contributing in the series, then the number ‘four’ could be reduced to ‘two’.

In addition to the practical limitations on number and position of sensors/sources, capturing spherical harmonic information also is constrained by causality. Obtaining the spherical harmonic components of a sound pressure field in practice requires measurement and processing of data from locations on a virtual spherical surface, or at least an enclosed 3D surface. In real-time, as an individual acoustic wave travels towards such a virtual surface, it does not immediately create sound pressure data at all sensor positions, unless it arrives on the virtual surface simultaneously from all directions. In all other scenarios, time must pass before all sensors have measured some signal corresponding to the initial wave, from which the spherical harmonic component information can then be processed. This time delay makes the real-time control of the initial wave based on spherical harmonic components not viable, as any manipulation relies on the knowledge of what the spherical harmonic components are. Furthermore, additional time delay is introduced when a scatterer is present inside the sensing surface, as it takes time for the incident wave to reach the obstacle, interact with, and then reach all sensors after the interaction.

As an example, the practical approach used in [34, 35] for real-time control of 3D sound scattering relies on relating the incident or total sound pressure to the scattered pressure. This relationship can typically be mapped to the corresponding spherical harmonic components of each quantity. These components can be measured and manipulated without issues, given the appropriate arrangements of sensors and secondary sources. However, due to all the aspects presented in the previous paragraph, the re-mapping would not lead to a causal system, thus preventing the achievement of real-time from this method.

3.1.2 Isolating the scattered field from the total field in real-time

The behaviour in the region exterior to a scattering obstacle is comprised of both incident and scattered sound fields, at steady-state. For cloaking, the interest is only controlling the scattered field without affecting the incident field. However, placing sensors in the region outside the obstacle or on its surface captures the total field. There is no way to avoid this outcome just by placing the sensors and sources of the control system in different arrangements; a distinct way of approaching the problem is required.

One approach for directly obtaining sound scattering data is to perform measurements both in the presence and in the absence of the scatterer, under the same set of circumstances, as done in [34, 35]. In anechoic conditions, with the obstacle absent, impulse responses or transfer functions can be measured between acoustic sources generating signals such as white noise or a frequency sweep, and a discrete set of sensor positions outside the volume that would have been occupied by the obstacle. This data corresponds to the incidence and, with a proper regularization strategy, can be processed to obtain inverse filters that map any measurements of total pressure in the presence of the obstacle to the scattering it produces, at any sensing position in its exterior. These filters can then be convolved in real-time with the measurements of total pressure at discrete locations on a virtual sphere surrounding the obstacle to account for any incoming incidence. With the scatterer, sensors and secondary sources all present, impulses responses or transfer functions are also capture in the absence of the incidence between each source and sensor. These are used in a real-time optimization process of the source signals such as steepest descent. The overall tactic presented in this paragraph is limited by the fact that it depends on capturing the initial data for the incidence. In practice, this offline measurement may not be possible, or it may be rendered useless by changes of circumstances, such as significant fluctuations of sound speed in exterior medium. Therefore, the tactic is not ideal.

A second approach is illustrated in Figure 3-1, on the left, and is similar to the previous one, but relies on the domain exterior to the scattering obstacle being coupled with the interior one. In this scenario, the scattered field is directly related to the sound field generated inside the object. Therefore, a layer of sensors is placed in the interior domain to capture the scattered field and a second layer of sensors is placed outside, surrounding the obstacle, for minimizing the pressure with the aid of control sources. The real-time limitation of this method is that the incident field first passes through the outside layer of sensors, then it takes time to reach the interior layer.

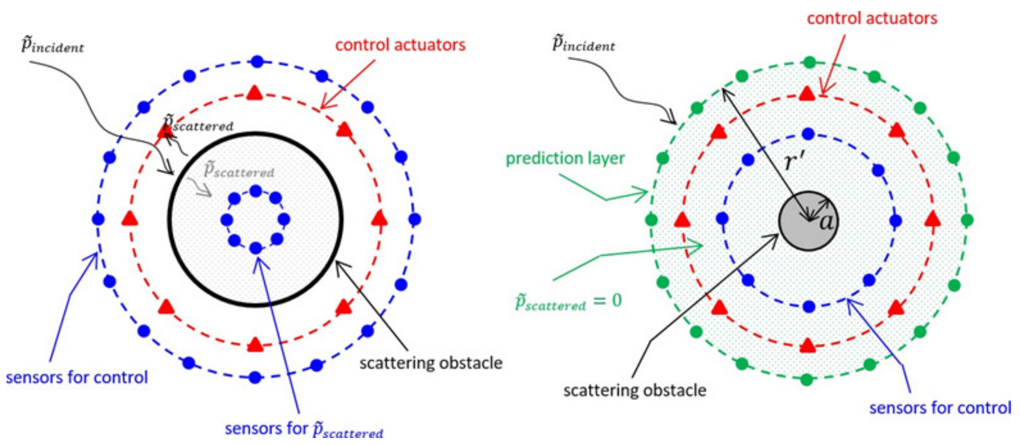

Figure 3-1 Illustration of two arrangements for isolating the scattered field from the total field generated around an obstacle, such that it can be controlled by an active system. On the left, the method relies on the scattering object being flexible and enclosing a volume, such that internal sensors can be used. On the right, the method relies on cancelling the scattering before it can reach and contaminate an exterior sensing layer that captures the incidence [79-82].

A third potential strategy is highlighted in the recent work done at the Immersive Boundary Conditions Laboratory at ETH Zurich [79-82]. This method relies on capturing the incident field as it first reaches an external layer of sensors surrounding the scatterer and then using that information to actively cancel the scattering artefacts before they can reach back to this initial layer to contaminate it. In other words, on the layer at distance r', the pressure is always the incident one, and in the annular region between r' and a, the total pressure is measured at a second layer of sensors surrounding the obstacle. A prediction of what the incident pressure is at this second layer is performed in real-time from the measurements on the initial layer through extrapolating a Kirchhoff-Helmholtz integral. This prediction is then subtracted from the measurements at the second layer such that the scattering is left isolated. Ultimately, the contribution of the isolated scattering data is controlled through secondary sources placed in the annular region between r' and a. The real-time limitations of this strategy are the computational cost of performing the prediction in the interval before the scattering can reach the external layer of sensors, and the pre-calibration needed to account for the sound propagation properties inside the annular region.

It is important to note that the strategies discussed in the previous paragraphs do not consider the requirement to capture spherical harmonic components of a sound field in real-time. Further development is required to obtain a solution for such a task. One possible way of approaching the problem is to further explore strategies for separating the converging, i.e. the incidence, and the diverging, i.e. the scattering, waves relative to a virtual surface enclosing the scatterer [40-45]. These methods have been previously studied for sound field reproduction and active control of sound within rooms, i.e. enclosed environments, and they may potentially be repurposed active control of scattering produced in the exterior of obstacles. Another way of tackling the manipulation of spherical harmonic components in real-time is presented in the following subsection as a preliminary concept.

3.1.3 A preliminary concept for solving the sensing challenges

An enclosing surface of sensors cannot be avoided for measuring the spherical harmonic information of a sound field. Thus, a potential option for achieving real-time 3D cloaking of a scatterer is to design sensing layers surrounding it that have a number of enclosed sensing regions. Each region would be approximately associated with a direction of arrival and combined they would form themselves a layer that encircles the object. The tactic is illustrated in Figure 3-2 for virtual spherical regions and it relies on the same principles as those in the work from ETH Zurich, that was

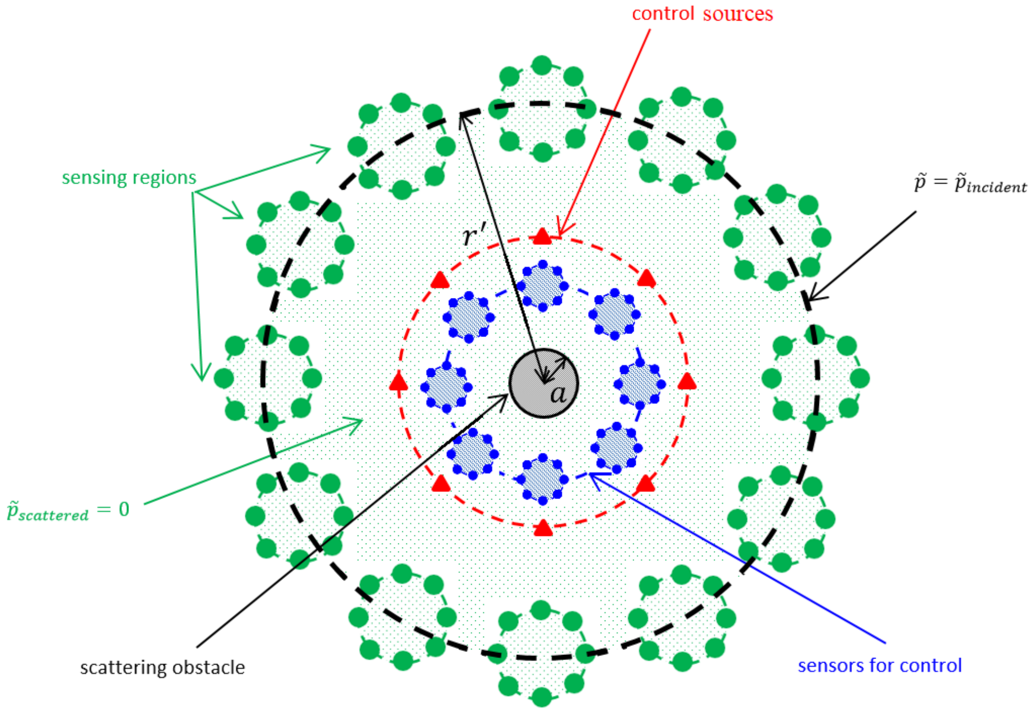

Figure 3-2 Illustration of a preliminary practical concept for achieving real-time 3D acoustic cloaking based on spherical harmonic components. A virtual sphere of radius r' encloses the scattering obstacle and contains a number of spherical regions of smaller radius on it. The smaller spheres are sensing regions that capture the incident field in the form of spherical harmonic components. In the annular region between r' and a, the scattered pressure is maintained zero with the aid of an active control system comprised of a second sensing layer and secondary sources. The second sensing layer is also subdivided into spherical regions. The incident components measured on the surface at r' are used to make a prediction of the incident components on the surface of control sensors and then isolate it from the scattering components. The isolated scattering components are then targeted for control with the secondary sources.

described in the previous subsection. The ring of sensing spheres around the object is equivalent to the external layer from which p_i is predicted, and a sensor-source arrangement for active control is positioned inside the region between the prediction layer and the obstacle. The layer of sensors for control is also subdivided into spherical sensing regions. The prediction layer and the layer for control measure the spherical harmonic components of p_i and, respectively, p_t, at each corresponding spherical subdivision. A procedure would have to be devised for using the data captured from each of these subdivisions to obtain a prediction of the spherical harmonic components of p_i at the control sensors situated between r' and a. This might potentially require cross-talk cancellation methods implemented between regional virtual spheres on the same layer.

A number of limitations can be identified for the approach described above. Firstly, two different instances of discretization are employed. For an individual regional sensing sphere, the number of sensors is finite, thus, the highest order of spherical harmonic that can be manipulated is constrained. Furthermore, for each overall sensing layer, there are a finite number of spheres that can be placed surrounding the scattering object. This translates into spatial discretization, where certain directions of arrival may be captured inaccurately. Secondly, each sensing sphere inherits the $(N + 1)^2$ limitation of manipulating the spherical harmonic components. This has the potential to increase the number of required sensors by an exaggerated amount if both spatial resolution and harmonic content resolution are required to be high.

3.2 Limitations of minimizing spherical harmonic coefficient contribution to the power

As seen in the previous section, realizing the control system in practice relies heavily on reducing the number of sensors and secondary sources that are used, while still obtaining benefit after control. However, this also reduces the number of components in the truncated spherical harmonic representations that can be gathered in a practical scenario for the primary and, respectively, secondary. As such, it may become not be possible to use strategies based on spherical harmonics due to truncation error. The number of spherical harmonic components required to accurately represent a physical quantity can vary with frequency, depending on the nature of the quantity, as can be observed in [83, 84]. Typically, to describe a higher frequency requires more spherical harmonic components in the series summation. This variation with frequency can be different between the representation of the primary and that of the secondary. For accuracy up to a given frequency limit, out of the two different truncation values required by the primary and, respectively, by the secondary, the lower one may be chosen, then used at all frequencies in the working range. This sacrifices some of the high frequency accuracy of the quantity for which more spherical harmonic terms are necessary. The sacrifice may not be important if the chosen truncation value is high enough to create the error in a regime of frequencies where a strategy such as tonal control already does not produce any benefit due to the finite number of used sensors and secondary sources.

3.3 Bobrovnitskii`s modelling approach

Bobrovnitskii [57-59] introduced an impedance-based approach to the analysis of sound scattering by assuming that the surface of the scattering body was divided into many discrete elements, which are assumed to be small compared with a wavelength in the surrounding fluid. If the pressure and velocity over the surface are instead expressed in terms of a modal expansion, an entirely analogous analysis of scattering can be formulated [85]. Assuming tonal excitation proportional to $e^{i\omega t}$, the vectors of complex total modal pressures and total modal velocities on the surface of the scattering body are denoted $\breve{\mathbf{p}}_t$ and $\breve{\mathbf{v}}_{t,}$ where $\breve{\mathbf{v}}_t$ is measured normal and outward with respect to the surface. Each of these vectors is made up of contributions from the sound field incident on the scattering body, and contributions from the scattered sound field, so that $\breve{\mathbf{p}}_t$ can be written as $\breve{\mathbf{p}}_i$ plus $\breve{\mathbf{p}}_s$ and $\breve{\mathbf{v}}_t$ as $\breve{\mathbf{v}}_i$ plus $\breve{\mathbf{v}}_s$. Three input impedance matrices are then defined, which are the in-vacuo structural impedance matrix of the scattering body, $\breve{\mathbf{Z}}_B$, the impedance matrix of the internal volume of the scattering body if filled with the surrounding fluid, $\breve{\mathbf{Z}}_I$, and the outward radiation impedance matrix into the surrounding fluid, $\breve{\mathbf{Z}}_R$, so that

$$\breve{\mathbf{p}}_t = -\breve{\mathbf{Z}}_B \cdot \breve{\mathbf{v}}_t \,, \qquad \breve{\mathbf{p}}_i = -\breve{\mathbf{Z}}_I \cdot \breve{\mathbf{v}}_i \,, \qquad \breve{\mathbf{p}}_s = \breve{\mathbf{Z}}_R \cdot \breve{\mathbf{v}}_s \;. \tag{3.1}$$

Using simple manipulations of the defining equations above, the vector of scattered surface pressures, $\breve{\mathbf{p}}_s$, can be expressed in terms of the vector of incident surface pressures, $\breve{\mathbf{p}}_i$, as [57-59]

$$\breve{\mathbf{p}}_s = \left[\left(\breve{\mathbf{Y}}_R + \breve{\mathbf{Y}}_B\right)^{-1} \cdot \left(\breve{\mathbf{Y}}_I - \breve{\mathbf{Y}}_B\right)\right] \cdot \breve{\mathbf{p}}_{\boldsymbol{i}} = \breve{\mathbf{R}}_1 \cdot \breve{\mathbf{p}}_{\boldsymbol{i}} \;, \tag{3.2}$$

and in terms of the vector of total surface pressures $\breve{\mathbf{p}}_t$ as

$$\breve{\mathbf{p}}_s = \left[\left(\breve{\mathbf{Y}}_I + \breve{\mathbf{Y}}_R\right)^{-1} \cdot \left(\breve{\mathbf{Y}}_I - \breve{\mathbf{Y}}_B\right)\right] \cdot \breve{\mathbf{p}}_{\boldsymbol{t}} = \breve{\mathbf{R}}_2 \cdot \breve{\mathbf{p}}_{\boldsymbol{t}} \;. \tag{3.3}$$

where the admittance matrices $\breve{\mathbf{Y}}_B$, $\breve{\mathbf{Y}}_R$ and $\breve{\mathbf{Y}}_I$ are the inverses of the impedance matrices $\breve{\mathbf{Z}}_B$, $\breve{\mathbf{Z}}_R$ and $\breve{\mathbf{Z}}_I$, assuming that these matrices are non-singular. The matrices $\left(\breve{\mathbf{Y}}_R + \breve{\mathbf{Y}}_B\right)$ and $\left(\breve{\mathbf{Y}}_I + \breve{\mathbf{Y}}_R\right)$ are also assumed to be non-singular. Under the conditions of linearity and reciprocity, the matrices $\breve{\mathbf{Y}}_B$, $\breve{\mathbf{Y}}_R$ and $\breve{\mathbf{Y}}_I$ are symmetric, and when all the processes involved are passive, their real parts are positive definite. The latter condition leads to all their associated impulse responses being causal. It is important to note that despite being formulated in terms of the in-vacuo structural response of the body, the loading of the fluid on the structure, as well as the sound scattering, are all accounted for in equation (3.3).

These impedance matrices are fully populated in the original formulation using elemental radiators, but each could be diagonalised by choosing a modal expansion involving either the structural modes of the body, for $\breve{\mathbf{Z}}_B$, the interior acoustic modes of the space, for $\breve{\mathbf{Z}}_I$, or the radiation modes, for $\breve{\mathbf{Z}}_R$. The eigenvectors of any of the three impedance matrices could thus potentially be used to define this modal expansion. However, for certain cases, such as that of the scattering from a thin, uniform, empty spherical shell in a semi-infinite fluid, an expansion in terms of spherical harmonics diagonalises all three impedance matrices. This expansion is truncated here to $N = N'$ terms, so that the pressure and velocity on the surface of the sphere are

$$\tilde{p}(\theta,\varphi) = \sum_{n=0}^{N\prime} \sum_{m=-n}^{n} \breve{p}(n,m)\, Y_{n,m}^{(\mathbb{C})}(\theta,\varphi)\,, \tag{3.4}$$

$$\tilde{v}(\theta,\varphi) = \sum_{n=0}^{N\prime} \sum_{m=-n}^{n} \breve{v}(n,m)\, Y_{n,m}^{(\mathbb{C})}(\theta,\varphi)\,, \tag{3.5}$$

where $Y_{n,m}^{(\mathbb{C})}(\theta,\varphi)$ is the complex spherical harmonic of index (n,m) and $\breve{p}(n,m)$ and $\breve{v}(n,m)$ denote the modal amplitudes. The vectors of $(N' + 1)^2$ modal pressures and velocities are then defined as

$$\breve{\mathbf{p}} = [\breve{p}(0,0)\ \ \breve{p}(1,-1)\ \ \breve{p}(1,0)\ \ \breve{p}(1,1) \ldots \breve{p}(N',-N') \ldots \breve{p}(N',0) \ldots \breve{p}(N',N')]^{\mathrm{T}}\,, \tag{3.6}$$

$$\breve{\mathbf{v}} = [\breve{v}(0,0)\ \ \breve{v}(1,-1)\ \ \breve{v}(1,0)\ \ \breve{v}(1,1) \ldots \breve{v}(N',-N') \ldots \breve{v}(N',0) \ldots \breve{v}(N',N')]^{\mathrm{T}}. \tag{3.7}$$

3.3.1 Active feedforward formulation

A frequency domain feedforward control formulation can be used to calculate the optimal performance of an array of secondary sources in minimizing the scattered power, assuming knowledge of the incident and scattered fields. This allows evaluation of the best possible performance with a given number of secondary sources, without having to be concerned with the sensing of the reference or of the error signals, or with the implementation of a practical controller, and so can be used as the first step in a hierarchical design approach for active control [24, 51].

Let there be L secondary sources on the surface of the scatterer, each of which has a magnitude $\tilde{f}_l$ acting at (θ_l, φ_l) that generates a modal pressure of $\breve{\mathbf{B}} \cdot \breve{\mathbf{p}}_c$ [65], where $\breve{\mathbf{p}}_c = \left[\tilde{f}_1,\ \tilde{f}_2,\ \tilde{f}_3 \ldots\ \tilde{f}_L\right]^{\mathrm{T}}$ is the vector of L modal control signals corresponding to each source, and $\breve{\mathbf{B}}$ is equal to

$\breve{\mathbf{Z}}_B\left[\breve{\boldsymbol{Z}}_{\boldsymbol{B}} + \breve{\boldsymbol{Z}}_{\boldsymbol{R}}\right]^{-1}$ times the $(N' + 1)^2$ by L matrix $\mathbf{S}$, where the l-th column of $\mathbf{S}$ has elements of $\bar{Y}_{n,m}^{(\mathbb{C})}(\theta_l, \varphi_l)$. It is assumed that $\left(\breve{\boldsymbol{Z}}_{\boldsymbol{B}} + \breve{\boldsymbol{Z}}_{\boldsymbol{R}}\right)$ is non-singular.

The total field after control is

$$\breve{\mathbf{p}}_{sc} = \breve{\mathbf{p}}_s - \breve{\mathbf{B}} \cdot \breve{\mathbf{p}}_c \ . \tag{3.8}$$

The scattered power after control is given by

$$\widetilde{W}_{sc} = \frac{a^2}{2} \mathrm{Re}\{\breve{\mathbf{p}}_{sc}^{\mathrm{H}} \cdot \breve{\mathbf{v}}_{sc}\} = \frac{a^2}{2} \breve{\mathbf{p}}_{sc}^{\mathrm{H}} \cdot \mathrm{Re}\{\breve{\mathbf{Y}}_R\} \cdot \breve{\mathbf{p}}_{sc} \ , \tag{3.9}$$

since $\breve{\mathbf{v}}_{sc}$ is given by $\breve{\mathbf{Y}}_R \cdot \breve{\mathbf{p}}_{sc}$, which is a quadratic function of $\breve{\mathbf{p}}_c$. The scattered pressure can thus be minimized by the vector of control sources given by [76]

$$\begin{aligned} \breve{\mathbf{p}}_c^{(\mathrm{opt})} &= \left[\breve{\mathbf{B}}^{\mathrm{H}} \cdot \mathrm{Re}\{\breve{\mathbf{Y}}_R\} \cdot \breve{\mathbf{B}}\,\right]^{-1} \cdot \breve{\mathbf{B}}^{\mathrm{H}} \cdot \mathrm{Re}\{\breve{\mathbf{Y}}_R\} \cdot \breve{\mathbf{R}}_1 \cdot \breve{\mathbf{p}}_{\boldsymbol{i}} = \\ &= \left[\breve{\mathbf{B}}^{\mathrm{H}} \cdot \mathrm{Re}\{\breve{\mathbf{Y}}_R\} \cdot \breve{\mathbf{B}}\,\right]^{-1} \cdot \breve{\mathbf{B}}^{\mathrm{H}} \cdot \mathrm{Re}\{\breve{\mathbf{Y}}_R\} \cdot \breve{\mathbf{R}}_2 \cdot \breve{\mathbf{p}}_t \ , \end{aligned} \tag{3.10}$$

where equations (3.2) and (3.3) are used to relate $\breve{\mathbf{p}}_s$ to $\breve{\mathbf{p}}_i$ and, respectively, $\breve{\mathbf{p}}_s$ to $\breve{\mathbf{p}}_t$. The procedure described by equations (3.1) – (3.9) also holds for incident, scattered and total pressures on a virtual sphere away from the scattering surface.

In practice, a simple experiment can be performed to validate the feedforward control strategy described above by ignoring some of the real-time measurement limitations and following the procedure from [34, 35]. For air as the propagation medium, a spherical scatterer would be placed in an anechoic chamber. The needed size of the obstacle would be governed by the frequency range of interest. For a given choice of incident wave to test, one or multiple loudspeakers can be placed around the scatterer with the sole purpose of generating this disturbance. However, the space in between these loudspeakers and the obstacle must allow for the appropriate placement of sensors and secondary sources for the control system. In the first instance, the experiment can use only a small number of devices for active control. The $n = 0$ and all $n = 1$ spherical harmonic components can be measured and manipulated with only four microphones and four secondary loudspeakers, each arranged in a tetrahedron on the same virtual sphere surrounding the scatterer. The microphones would ideally be placed in the far-field and the control loudspeakers between the sensors and the obstacle. This is done in order to eliminate unwanted effects at certain frequencies due to scatterer proximity, and to simplify the variation with radial distance in the spherical harmonic representation. However, being in the far-field at high frequencies may require sensor locations that are very far away from the obstacle, and forces the loudspeakers that generate the incidence to be far away as well.

Given the practical arrangement described in the first paragraph, the scatterer would be first removed, and all other devices left present. Using only the loudspeakers designated for the incidence and the sensors, impulse responses or transfer functions between the incidence and each microphone position would be captured. This data would be processed offline into spherical harmonic components, and then used to obtain filters that map the spherical harmonic components of the total pressure that would be created in the presence of the obstacle, to those of the scattered pressure, for any given incidence. This procedure is similar to that used in [34, 35], but done for spherical harmonic components, and is equivalent to obtaining $\breve{\mathbf{R}}_2$ in (3.3) from experimental data. All devices are left present such that any scattering that they produce is accounted for when creating the filters. Secondly, with the scatterer and all other devices present, the impulse responses or transfer functions between each secondary source and sensor would be measured, without the incidence being generated, and then processed into spherical harmonic components. This procedure would be equivalent to obtaining $\breve{\mathbf{B}}$ in (3.7). Again, all the devices are left present such that any scattering they produce is accounted for when capturing data.

Ultimately, the information processed to obtain $\breve{\mathbf{R}}_2$ and $\breve{\mathbf{B}}$ can be used in (3.7) – (3.9) to obtain the optimal loudspeaker signals $\breve{\mathbf{p}}_c^{(\mathrm{opt})}$ that minimize the spherical harmonic components of the scattering. These signals would then be used in the experimental arrangement with all devices and scatterer present, as well as with the incidence turned out and at steady-state. The microphones would now capture the optimized outcome, which can be later processed for an evaluation of the control performance. It is important to stress that this proposed procedure is not adaptive to changes of circumstances and does not achieve real-time.

3.3.2 Active feedback formulation

The effect of active feedback control on a scattering sphere in a fluid is shown in the physical arrangement example from Figure 3-3a. The signals from E discrete velocity sensors are fed to L internal point force actuators via a feedback controller matrix, $\mathbf{H}$. The effect of such a controller on the modal velocity in response to a general modal pressure excitation is shown in Figure 3-3b.

The vector of the overall modal velocities in response to a general vector of an overall modal pressures is

$$\breve{\mathbf{v}} = -\breve{\mathbf{Y}}_B \cdot \breve{\mathbf{p}}\,. \tag{3.11}$$

In the presence of active control with any array of internal point-force sources, as for feedforward control, the modal pressures acting on the shell are modified, such that

$$\breve{\mathbf{v}} = -\breve{\mathbf{Y}}_B \cdot (\breve{\mathbf{p}} - \mathbf{S} \cdot \breve{\mathbf{p}}_c)\ . \tag{3.12}$$

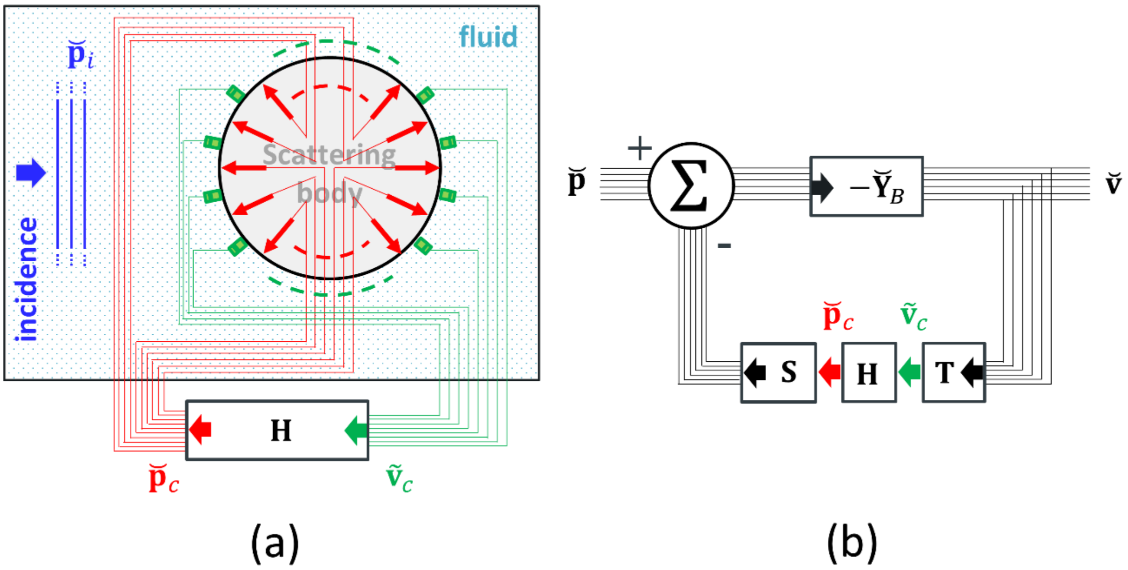

Figure 3-3 Feedback control using secondary point-force actuators driven by the measured velocities at discrete sensors on the surface of the scatterer (a), and the block diagram of the equivalent modal feedback system (b).

For the feedback arrangement shown in Figure 3-3a, the secondary forces, i.e. the secondary, are related in the feedback to the velocities at the E sensor positions, $\tilde{\mathbf{v}}_c$, i.e. the primary, via the feedback controller $\mathbf{H}$, so that

$$\breve{\mathbf{p}}_c = \mathbf{H} \cdot \tilde{\mathbf{v}}_c, \quad \tilde{\mathbf{v}}_c = \mathbf{T} \cdot \breve{\mathbf{v}}\ , \tag{3.13}$$

where $\breve{\mathbf{v}}$ is the vector of modal velocities, and $\mathbf{T}$ is a E by $(N' + 1)^2$ transformation matrix, which, from equation (3.5), has elements of the form $Y_{n,m}^{(\mathbb{C})}(\theta_e, \varphi_e)$. Thus,

$$\breve{\mathbf{v}} = -\breve{\mathbf{Y}}_B(\,\breve{\mathbf{p}} - \mathbf{S} \cdot \mathbf{H} \cdot \mathbf{T} \cdot \breve{\mathbf{v}})\,, \tag{3.14}$$

and, so,

$$\breve{\mathbf{v}} = -\left(\mathbf{I} + \breve{\mathbf{Y}}_B \cdot \mathbf{S} \cdot \mathbf{H} \cdot \mathbf{T}\right)^{-1} \cdot \breve{\mathbf{Y}}_B \cdot \breve{\mathbf{p}}\,, \tag{3.15}$$

The modal pressure can be expressed as

$$\breve{\mathbf{p}} = -\breve{\mathbf{Z}}_B \cdot \left[\mathbf{I} + \breve{\mathbf{Y}}_B \cdot \mathbf{S} \cdot \mathbf{H} \cdot \mathbf{T}\right] \cdot \breve{\mathbf{v}} = -\breve{\mathbf{Z}}_B^{(cl)} \cdot \breve{\mathbf{v}}\ , \tag{3.16}$$

where $\breve{\mathbf{Z}}_B^{(cl)}$ is the overall modal impedance of the scatterer with closed-loop feedback control, which can be written as

$$\breve{\mathbf{Z}}_B^{(cl)} = \breve{\mathbf{Z}}_B + \mathbf{S} \cdot \mathbf{H} \cdot \mathbf{T}\ . \tag{3.17}$$

Although $\breve{\mathbf{Z}}_B$ is diagonal for a spherical harmonic expansion, the matrix $\mathbf{S} \cdot \mathbf{H} \cdot \mathbf{T}$ is generally not diagonal. Nevertheless, the matrix $\breve{\mathbf{Z}}_B^{(cl)}$ can now be used instead of $\breve{\mathbf{Z}}_B$ in equation (3.5) to give the vector of scattered modal pressures after feedback control in terms of the vector of incident modal pressures, and, hence, the scattered power after control can be calculated using equation (3.9).

In the absence of an incident field, the matrix of ‘plant’ responses, $\mathbf{G}_c$, between the point-force actuators and the discrete velocity sensors is

$$\breve{\mathbf{v}}_c = \mathbf{T} \cdot \left[\breve{\mathbf{Z}}_B + \breve{\mathbf{Z}}_R\right]^{-1} \cdot \mathbf{S} \cdot \breve{\mathbf{p}}_c = \mathbf{G}_c \cdot \breve{\mathbf{p}}_c\ , \tag{3.18}$$

since the force actuators must overcome both the impedance of the scattering surface and the radiation impedance. If there are the same number of actuators as sensors and they are collocated, then $\mathbf{S}$ is equal to $\mathbf{T}^{\mathrm{H}}$, which leads to

$$\mathbf{G}_c = \mathbf{T} \cdot \left[\breve{\mathbf{Z}}_B + \breve{\mathbf{Z}}_R\right]^{-1} \cdot \mathbf{T}^{\mathbf{H}}, \tag{3.19}$$

an entirely passive modal representation. The stability of the closed-loop system is thus guaranteed provided the feedback gain matrix, $\mathbf{H}$, is also passive [86, 87].

Several designs of feedback controller are possible. The simplest is decentralised local velocity feedback, for which $\mathbf{H}$ is equal to $\gamma\mathbf{I}$, where γ is the gain of each local feedback loop. A more selective approach to implementing the feedback controller is to make it modal [52], so that for the collocated case

$$\mathbf{H} = \boldsymbol{\Psi} \cdot \boldsymbol{\Omega} \cdot \boldsymbol{\Psi}^{\mathrm{H}}\ , \tag{3.20}$$

where, for $L < (N' + 1)^2$, $\boldsymbol{\Psi}$ is a matrix of mode shapes at the transducer locations for a subset of the spherical harmonics, and $\boldsymbol{\Omega}$ is the diagonal matrix of modal velocity feedback gains. In the limiting case, where it is assumed that there are as many actuators and sensors as there are modes, $L = E = (N' + 1)^2$, and assuming that the transducers are collocated and positioned so as to actuate and sense all of the modes such that $\mathbf{T}^{\mathrm{H}}$ is a good approximation to the identity matrix, then perfect control of all the modes would be possible. In this case, the closed-loop impedance of the spherical surface could, in principal, be set equal to the input impedance of the volume of the scattering body filled with fluid, $\breve{\mathbf{Z}}_I$, so that the scattering would be completely suppressed [57, 58]. Setting equation (3.17) equal to $\breve{\mathbf{Z}}_I$ in this case leads to the feedback controller having the form

$$\mathbf{H} = \mathbf{T} \cdot \left(\breve{\mathbf{Z}}_I - \breve{\mathbf{Z}}_B\right) \cdot \mathbf{T}^{\mathrm{H}} \,. \tag{3.21}$$

In practice, a simple experiment can be performed to validate the velocity feedback control strategy described above and illustrated in Figure 3-3a. For air as the propagation medium, a spherical scatterer would be placed in an anechoic chamber. The needed size of the obstacle would be governed by the frequency range of interest. For a given choice of incident wave to test, one or multiple loudspeakers can be placed around the scatterer with the sole purpose of generating this disturbance. However, the space in between these loudspeakers and the obstacle must allow for the appropriate placement of sensors and secondary sources for the control system. In the first instance, the experiment can use only a small number of devices for active control. The $n = 0$ and all $n = 1$ spherical harmonic components can be measured and manipulated with only four sensors and four secondary actuators, each arranged in a tetrahedron on the surface of the scatterer. The sensors and actuators would have to measure velocity and respectively, generate a force, in the direction normal to the spherical surface. With the incidence turned, the measurements of total velocity on the surface of the scatterer are fed back through the controller $\mathbf{H}$ to optimize the actuator signals. This controller can be computer capable of digital processing and real-time playback. The matrices $\mathbf{S}$ and $\mathbf{T}$ are obtained from the knowledge of the seniors and actuator positions but are only required for understanding the outcome of the control and, hence, for choosing the controller $\mathbf{H}$. Optimization of $\mathbf{H}$ requires further processing steps, and can be done either adaptively, in real-time, or offline.

3.3.3 The use of zero-valued spherical harmonic components when inverting

The modal strategies outlined in subsection 3.3.1 and subsection 3.3.2 use the spherical harmonic components of all degrees n and orders m, for a given truncation value N. However, the placement of sound sources relative to the coordinate system and, hence, to the scatterer, can lead to certain spherical harmonic functions always being zero. In turn, the corresponding spherical harmonic terms in the series representations of the primary and/or the secondary are always zero. This property is later used for the investigations in Chapter 4 – Chapter 7 of the thesis.

The zero-valued spherical harmonic components are an important consideration when computing results for the previously mentioned active control strategies, specifically when doing matrix inversions. For feedforward control, this operation is required when obtaining the optimal parameters of the secondary sources in the minimization problem from equation (3.10). For feedback control, matrix inversion is used when computing the quantity $\mathbf{G}_c$ in equation (3.18), which leads to the open-loop and closed-loop response. Furthermore, whether the used set of spherical harmonic components has non-contributing, zero-valued elements plays a role in the choice of feedback controller $\mathbf{H}$.

For a given placement of sound sources relative to the scatterer, if the zero-valued spherical harmonic components are known, it may be convenient to not include them in the matrices when performing computations. This would eliminate any potential issues that may arise from inverting sparse matrices. Furthermore, if the computational procedure introduces slight error in the spherical harmonic components that should be zero, not including them prevents these errors affecting the inversion. The tactic described in this paragraph is employed when computing the active control results from Chapter 5 and Chapter 7 which illustrate an ideal placement of secondary sources relative to the incidence and scatterer.

3.4 Chapter summary

This chapter has reviewed two types of potential approaches to the practical implementation of an active system to control 3D sound scattering based on decomposition into series of spherical harmonic components. The first involves arrays of sensors and secondary acoustic sources placed away from the surface of the scatterer, where scattering suppression is achieved by directly manipulating the motion of the fluid. The second involves arrays of sensors and actuators on the surface of the scattering obstacle and employs feedback to change the dynamic response of this obstacle in order to alter the scattering it produces. The time constraints of the research project prevented a detailed experimental investigation of all these approaches and allowed only the theoretical study of velocity feedback control for the 3D sound scattering from an elastic spherical shell, which is presented in Chapter 7.

Chapter 4 Sound Scattering and Radiation: The Uniform Impedance Sphere in a Fluid

This chapter explores the mathematical modelling for scattering from and radiation in the vicinity of a uniform impedance sphere surrounded by a fluid (see Figure 4-1). This scenario represents the exterior boundary-value problem with a fixed radial wave impedance $\tilde{Z}$ on the scattering surface. This impedance has no dependence on frequency or modal index n and is locally-reacting. The last property translates in the behaviour at one position on the surface being independent of the behaviour at all other positions on the surface. The physics in the domain inside the spherical surface are considered to not alter the condition on the separation boundary, such that they can be ignored in the study of scattering.

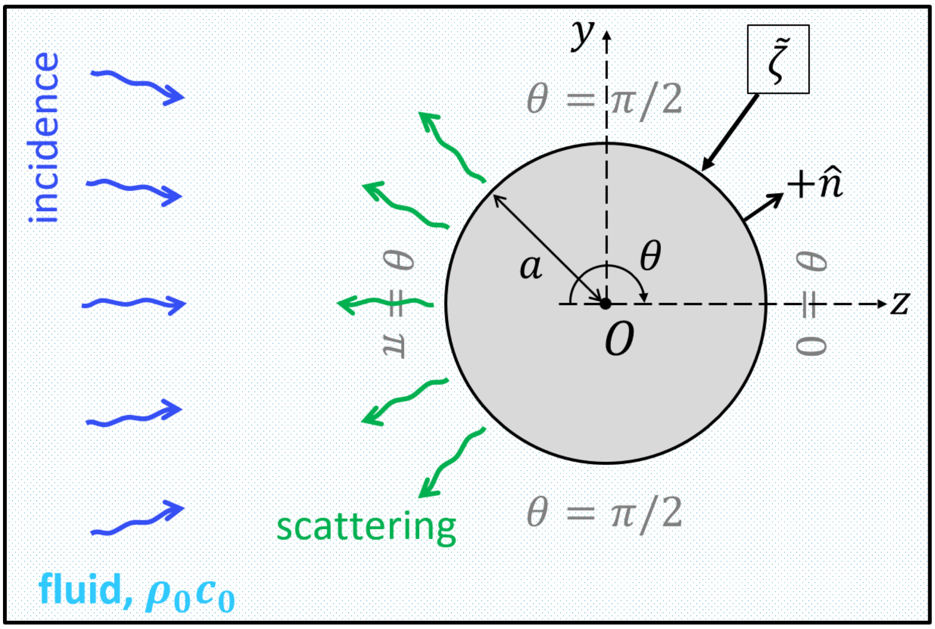

Figure 4-1 Diagram of geometry and circumstances studied in this chapter, i.e. 3D sound scattering from uniform impedance sphere in a fluid, shown as slice along yz-plane.

Classic solutions to the Helmholtz equation, such as a plane-wave and a point-monopole, are exemplified when enforcing a condition on the spherical boundary. The scenarios discussed here correspond with the passive case where no active control is considered. These scenarios are used in the following as either the primary or the secondary to exemplify the effects of active controlling the sound scattering from the uniform impedance sphere.

The asymptotic behaviour at low normalized frequency is analysed for the exemplified cases of scattering and radiation. This is the region in frequency where active control is expected to provided performance when using a practical small number of control source, as explained in classic active control textbooks [24, 51].

The investigation described in the paragraphs above is performed for three cases of locally-reacting impedance on the scattering surface. The first is a rigid (or acoustically hard) sphere, where $\tilde{Z}$ is considerably larger than the characteristic impedance of the surrounding medium, $\rho_0 c_0$. The second is an acoustically soft sphere, where $\tilde{Z}$ is close to zero. And the third is the case of a sphere where $\tilde{Z} = \rho_0 c_0$, i.e. the locally-reacting impedance, which acts on the radial direction, is matched to the impedance of the surrounding medium. This last case is denoted as 'radially-matched'.

4.1 General formulation for scattering of a point-monopole source by the sphere

Let there be a theoretical point-monopole with acoustic strength $\tilde{q}$ situated at position (r', θ', φ') away from an impedance sphere of radius a, centred at the origin of the coordinate system. The inequalities $r' \geq a$ and $r \geq a$ thus hold. This situation represents a scattering problem, where the incident field is given by

$$\tilde{p}_i(\vec{r}) = k^2 \rho_0 c_0 \, \tilde{q} \sum_{n=0}^{\infty} \sum_{m=-n}^{n} j_n(kr_<) \, h_n(kr_>) \, Y_{n,m}^{(\mathbb{C})}(\theta, \varphi) \, \bar{Y}_{n,m}^{(\mathbb{C})}(\theta', \varphi') \, , \tag{4.1}$$

at the evaluation point (r, θ, φ), following expression (2.38), where $r_< = \min(r, r')$ and $r_> = \max(r, r')$. In other words,

$$\tilde{p}_i(\vec{r}) = \begin{cases} k^2 \rho_0 c_0 \tilde{q} \displaystyle\sum_{n=0}^{\infty} \sum_{m=-n}^{n} j_n(kr') \, h_n(kr) \, Y_{n,m}^{(\mathbb{C})}(\theta, \varphi) \, \bar{Y}_{n,m}^{(\mathbb{C})}(\theta', \varphi') \, , & r > r' \\ k^2 \rho_0 c_0 \tilde{q} \displaystyle\sum_{n=0}^{\infty} \sum_{m=-n}^{n} h_n(kr') \, j_n(kr) \, Y_{n,m}^{(\mathbb{C})}(\theta, \varphi) \, \bar{Y}_{n,m}^{(\mathbb{C})}(\theta', \varphi') \, , & r < r' \end{cases} , \tag{4.2}$$

with its corresponding radial velocity taking the form of (2.39). The scattered pressure field, $\tilde{p}_s(\vec{r})$, is represented by the solution to the exterior problem (2.16) and has the corresponding radial velocity (2.20).

The radial pressure gradients of the incident and scattered fields are expressed, respectively, as

$$\frac{\partial \tilde{p}_i}{\partial r}(\vec{r}) = \begin{cases} k^3 \rho_0 c_0\, \tilde{q} \displaystyle\sum_{n=0}^{\infty} \sum_{m=-n}^{n} h_n'(kr)\, j_n(kr')\, Y_{n,m}^{(\mathbb{C})}(\theta,\varphi)\, \bar{Y}_{n,m}^{(\mathbb{C})}(\theta',\varphi')\,, & r > r' \\ k^3 \rho_0 c_0\, \tilde{q} \displaystyle\sum_{n=0}^{\infty} \sum_{m=-n}^{n} j_n'(kr)\, h_n(kr')\, Y_{n,m}^{(\mathbb{C})}(\theta,\varphi)\, \bar{Y}_{n,m}^{(\mathbb{C})}(\theta',\varphi')\,, & r < r' \end{cases}, \qquad (4.3)$$

and

$$\frac{\partial \tilde{p}_s}{\partial r}(\vec{r}) = k \sum_{n=0}^{\infty} \sum_{m=-n}^{n} \tilde{D}_{n,m}^{\mathbb{C}}\, h_n'(kr)\, Y_{n,m}^{(\mathbb{C})}(\theta,\varphi)\,, \qquad (4.4)$$

Let the surface $r = a$ be considered, which respects the $r < r'$ condition. Using the lower expression in (4.3) and, respectively, expression (4.4) within (2.7) relates the velocities of the incidence and, respectively, the scattering to their corresponding pressure gradients, on the considered surface. These gradients are then used together with the pressures to obtain

$$\tilde{\zeta} k \sum_{n=0}^{\infty} \sum_{m=-n}^{n} k^2 \rho_0 c_0\, \tilde{q}\, j_n'(ka)\, h_n(kr')\, Y_{n,m}^{(\mathbb{C})}(\theta,\varphi)\, \bar{Y}_{n,m}^{(\mathbb{C})}(\theta',\varphi') + \tilde{D}_{n,m}^{\mathbb{C}}\, h_n'(ka)\, Y_n^m(\theta,\varphi) =$$

$$= ik \sum_{n=0}^{\infty} \sum_{m=-n}^{n} k^2 \rho_0 c_0\, \tilde{q}\, j_n(ka)\, h_n(kr')\, Y_{n,m}^{(\mathbb{C})}(\theta,\varphi)\, \bar{Y}_{n,m}^{(\mathbb{C})}(\theta',\varphi') + \tilde{D}_{n,m}^{\mathbb{C}}\, h_n(ka)\, Y_n^m(\theta,\varphi)\,,$$

where $\tilde{\zeta} = \tilde{Z}/(\rho_0 c_0)$ is the surface impedance normalized by the characteristic acoustic impedance of the exterior propagation medium.

Using the orthogonality of the spherical harmonics, the double summation signs in the above equation can be eliminated. Thus,

$$\tilde{\zeta}\, k^3 \rho_0 c_0\, \tilde{q}\, j_n'(ka)\, h_n(kr')\, Y_{n,m}^{(\mathbb{C})}(\theta',\varphi')^* + \tilde{\zeta} k\, \tilde{D}_{n,m}^{\mathbb{C}}\, h_n'(ka) =$$

$$= ik^3 \rho_0 c_0\, \tilde{q}\, j_n(ka)\, h_n(kr')\, Y_{n,m}^{(\mathbb{C})}(\theta',\varphi')^* + ik\, \tilde{D}_{n,m}^{\mathbb{C}}\, h_n(ka) =>$$

$$=> \tilde{D}_{n,m}^{\mathbb{C}}\, k\big[ih_n(ka) - \tilde{\zeta} h_n'(ka)\big] = -k^3 \rho_0 c_0\, \tilde{q}\, h_n(kr')\, Y_{n,m}^{(\mathbb{C})}(\theta',\varphi')^*\, \big[\, ij_n(ka) - \tilde{\zeta} j_n'(ka)\big] =>$$

$$=> \widetilde{D}^{\mathbb{C}}_{n,m} = -k^2 \rho_0 c_0\, \tilde{q}\, h_n(kr')\, \frac{j_n(ka) + i\tilde{\zeta} j_n'(ka)}{i h_n^{(2)}(ka) + i\tilde{\zeta} h_n'(ka)}\, \bar{Y}^{(\mathbb{C})}_{n,m}(\theta',\varphi') \ . \tag{4.5}$$

For convenience, the ratio of spherical Bessel and Hankel functions of ka is denoted as

$$\widetilde{\mathcal{W}}_n(\tilde{\zeta}, ka) = \frac{j_n(ka) + i\tilde{\zeta} j_n'(ka)}{h_n(ka) + i\tilde{\zeta} h_n'(ka)} \ . \qquad (4.8) \ (4.6)$$

Using (4.5) , the scattered pressure field is given by

$$\tilde{p}_s(\vec{r}) = -k^2 \rho_0 c_0\, \tilde{q} \sum_{n=0}^{\infty} \sum_{m=-n}^{n} \widetilde{\mathcal{W}}_n\, h_n(kr)\, h_n(kr')\, Y^{(\mathbb{C})}_{n,m}(\theta,\varphi)\, \bar{Y}^{(\mathbb{C})}_{n,m}(\theta',\varphi') \, , \tag{4.7}$$

where the arguments of $\widetilde{\mathcal{W}}_n$ are omitted, and the total pressure field is given by

$$\tilde{p}_t(\vec{r}) = \begin{cases} k^2 \rho_0 c_0 \tilde{q} \sum_{n=0}^{\infty} \sum_{m=-n}^{n} \left[j_n(kr') - \widetilde{\mathcal{W}}_n\, h_n(kr') \right] h_n(kr)\, Y^{(\mathbb{C})}_{n,m}(\theta,\varphi)\, \bar{Y}^{(\mathbb{C})}_{n,m}(\theta',\varphi') \, , r > r' \\ k^2 \rho_0 c_0 \tilde{q} \sum_{n=0}^{\infty} \sum_{m=-n}^{n} \left[j_n(kr) - \widetilde{\mathcal{W}}_n\, h_n(kr) \right] h_n(kr')\, Y^{(\mathbb{C})}_{n,m}(\theta,\varphi)\, \bar{Y}^{(\mathbb{C})}_{n,m}(\theta',\varphi') \, , r < r' \end{cases} ,$$

where the modal frequency weighting of the radiation is defined as

$$\widetilde{\mathcal{W}}_n^{(pm)}\left(r', \tilde{\zeta}, ka\right) = \begin{cases} (ka)^2 \left[j_n(kr') - \widetilde{\mathcal{W}}_n\, h_n(kr') \right], & r > r' \\ -(ka)^2 \widetilde{\mathcal{W}}_n h_n(kr'), & r < r' \end{cases} , \tag{4.9}$$

with the first expression represents the combination of direct and scattering radiation, and the second relation represents the scattering, all of which are diverging waves.

When it comes to radiated sound power, the known spherical harmonic coefficients (4.9) can be substituted back into (2.33), where the closure relation of the functions (see Appendix B) leads to the scattered sound power being

$$\widetilde{W}_s = \frac{1}{2\rho_0 c_0 k^2} \sum_{n=0}^{\infty} \sum_{m=-n}^{n} \left| k^2 \rho_0 c_0\, \tilde{q}\, h_n(kr')\, \frac{j_n(ka) + i\tilde{\zeta} j_n'(ka)}{h_n(ka) + i\tilde{\zeta} h_n'(ka)}\, \bar{Y}^{(\mathbb{C})}_{n,m}(\theta',\varphi') \right|^2 =$$

$$= \frac{k^2 \rho_0 c_0\, |\tilde{q}|^2}{2} \sum_{n=0}^{\infty} \left| h_n(kr')\, \frac{j_n(ka) + i\tilde{\zeta} j_n'(ka)}{h_n(ka) + i\tilde{\zeta} h_n'(ka)} \right|^2 \sum_{m=-n}^{n} \left| \bar{Y}^{(\mathbb{C})}_{n,m}(\theta',\varphi') \right|^2$$

$$= \frac{k^2 \rho_0 c_0\, |\tilde{q}|^2}{8\pi} \sum_{n=0}^{\infty} (2n+1) \left| h_n(kr')\, \widetilde{\mathcal{W}}_n \right|^2 \, , \tag{4.10}$$

and the total radiated sound power (direct radiation plus scattering) being

$$\widetilde{W}_t = \frac{1}{2\rho_0 c_0 k^2} \sum_{n=0}^{\infty} \sum_{m=-n}^{n} \left| k^2 \rho_0 c_0 \, \tilde{q} \left[j_n(kr') - \widetilde{\mathcal{W}}_n \, h_n(kr') \right] \bar{Y}^{(\mathbb{C})}_{n,m}(\theta', \varphi') \right|^2 =$$

$$= \frac{k^2 \rho_0 c_0 \, |\tilde{q}|^2}{2} \sum_{n=0}^{\infty} \left| j_n(kr') - \widetilde{\mathcal{W}}_n \, h_n(kr') \right|^2 \sum_{m=-n}^{n} \left| \bar{Y}^{(\mathbb{C})}_{n,m}(\theta', \varphi') \right|^2$$

$$= \frac{k^2 \rho_0 c_0 \, |\tilde{q}|^2}{8\pi} \sum_{n=0}^{\infty} (2n+1) \left| j_n(kr') - \widetilde{\mathcal{W}}_n \, h_n(kr') \right|^2 \; . \qquad (4.11)$$

It is important to note that the above expressions do not have any dependence on angular position or radial position of the point-monopole. This is to be expected as the radiated power is a quantity invariant in space. Furthermore, the expression highlights that radiated power also does not depend on whether the real or complex spherical harmonics were used in the expansion.

4.2 Scattering of a monochromatic plane-wave by the sphere

4.2.1 Coefficients in spherical harmonic expansion

In expression (4.8), allowing the radial position of the point-monopole to tend to infinity leads to the spherical harmonic expansion of a plane-wave, in a similar fashion to what is presented in Appendix I. Using that derivation, it is obtained that for a monochromatic plane-wave of magnitude $\tilde{\mathcal{P}}_i$ arriving from the incidence angles (θ_i, φ_i) , the scattering coefficients are

$$\widetilde{D}^{(\mathbb{C},pw)}_{n,m} = -\tilde{\mathcal{P}}_i \, 4\pi \, i^n \, \bar{Y}^{(\mathbb{C})}_{n,m}(\theta_i, \varphi_i) \, \frac{j_n(ka) + i\tilde{\zeta} j_n'(ka)}{h_n(ka) + i\tilde{\zeta} h_n'(ka)} = -\tilde{\mathcal{P}}_i \, 4\pi \, i^n \, \widetilde{\mathcal{W}}_n \, \bar{Y}^{(\mathbb{C})}_{n,m}(\theta_i, \varphi_i) \, , \qquad (4.12)$$

where the ratio dependent on spherical Bessel and Hankel functions is the same as $\widetilde{\mathcal{W}}_n$ in (4.6) .

It is important to note that in (4.12) the denominator $h_n(ka) + i\tilde{\zeta} \, h_n'(ka)$ is never zero, so it is possible to write $\widetilde{D}^{(\mathbb{C},pw)}_{n,m}$ in terms of a ratio. This is not straightforward to prove analytically, however, it has been checked to be the case via numerical computation in MATLAB.

4.2.2 Asymptotic behaviour of coefficients with ka

Expression (4.5) highlights that the variation with ka of the spherical harmonic coefficients $\widetilde{D}_{n,m}^{(\mathbb{C},pw)}$ is given by the modal frequency weighting, $\widetilde{\mathcal{W}}_n(\tilde{\zeta}, ka)$, from (4.6). For a fixed n , the coefficients with the same index m exhibit the same relation with the normalized frequency. The only dependence on m of the modal coefficient is given by $\bar{Y}_{n,m}^{(\mathbb{C})}(\theta_i, \varphi_i)$. The magnitude of $\widetilde{\mathcal{W}}_n$ is plotted in Figure 4-2 for a rigid ($\tilde{\zeta} = 100$), soft ($\tilde{\zeta} = 0.01$) and radially-matched ($\tilde{\zeta} = 1$) spheres, when $n \in \{0,1,2\}$. Approximate values of the normalized impedance were chosen for the soft and rigid spheres, which are normally $\tilde{\zeta} = 0$ and, respectively, $\tilde{\zeta} = +\infty$, in order to avoid some practical and numerical limitations, as will become apparent in section 4.3 . The results in Figure 4-2 are indistinguishable from those of the corresponding cases $\tilde{\zeta} = 0$ and $\tilde{\zeta} = +\infty$, in the used normalized frequency range ka. Where soft and rigid are mentioned further in this thesis, it is referred to results computed for $\tilde{\zeta} = 0.01$ and $\tilde{\zeta} = 100$, unless specifically stated otherwise.

It can be concluded from the above-mentioned results that for a fixed value of ka , the coefficients with the lowest n are the most dominant when ka is close to zero, and as ka increases to higher values, the contributions of more and more orders of $\widetilde{\mathcal{W}}_n$ become significant. Generally, the $n = 0$ coefficient is the most dominant at low ka, with the exception of the rigid sphere, which has the same variation for $\widetilde{\mathcal{W}}_0$ and, respectively, $\widetilde{\mathcal{W}}_1$.

The asymptotic behaviour of $\widetilde{\mathcal{W}}_n$ when $ka \ll 1$, otherwise known in the literature as the 'Rayleigh region', is discussed in the paper [75] for the three cases of surface impedance. In this paper, such formulations are demonstrated for $\widetilde{\mathcal{W}}_0$ and $\widetilde{\mathcal{W}}_n$ for a soft, hard and a general uniform, locally-reacting impedance. However, the time-frequency working convention is opposite from that used in this work and $\tilde{\zeta}$, the normalized impedance, is used to denote $\tilde{Z}/(i\rho_0 c_0)$ rather than $\tilde{Z}/(\rho_0 c_0)$. The expressions in question from [75] are arranged and presented in Table 4-1 using the current convention. These can be obtained by combining the asymptotic behaviours of the spherical Bessel and Hankel functions at low argument, which are discussed in Appendix D. They are also simplified for when the value of ka is very close to zero (see Table 4-2), which are then applied to $\widetilde{\mathcal{W}}_n$ and to the coefficients $\widetilde{D}_{n,m}^{(\mathbb{C},pw)}$ for each impedance surface. This asymptotic behaviour is shown in the plots in Figure 4-2 to demonstrate the limiting behaviour.

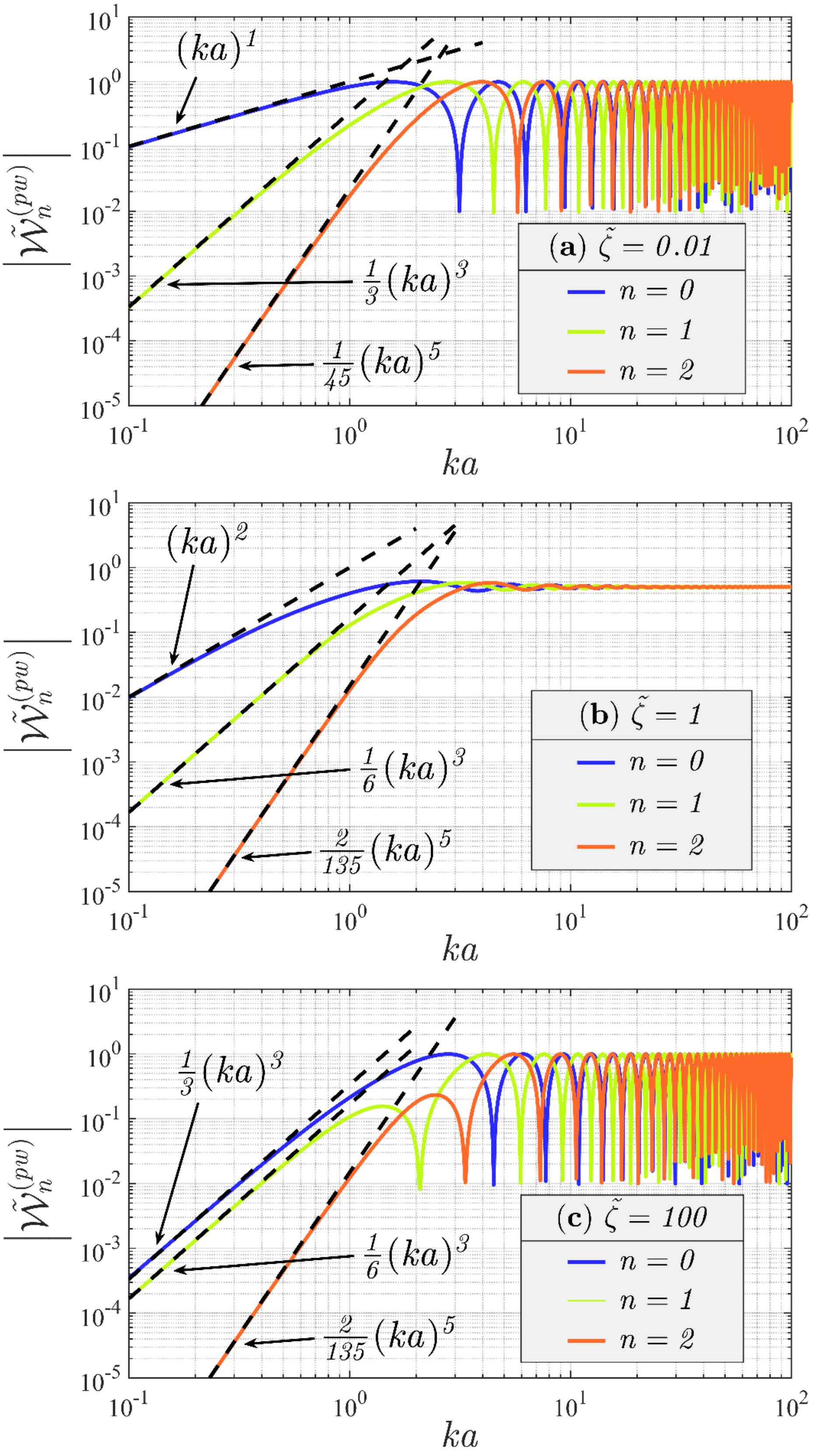

Figure 4-2 Modal frequency weightings $\widetilde{\mathcal{W}}_n^{(pw)} = \widetilde{\mathcal{W}}_n$ of scattered sound field due to a plane incident wave for the soft $\tilde{\zeta} = 0.01$ (a), radially-matched $\tilde{\zeta} = 1$ (b), and hard $\tilde{\zeta} = 100$ (c) spheres.

The results in Table 4-1 echo all the conclusions found when plotting $\widetilde{\mathcal{W}}_n$ for the first few orders. The most general forms of the relationships consist of the product between an amplitude dependent on n and ka as a power dependent on n. Thus, the $\widetilde{\mathcal{W}}_n$ of lowest n are dominant in magnitude for a fixed value of the normalized frequency. Also, the $n = 1$ component is just as significant as the $n = 0$ one for the rigid case only. It is also important to highlight that $\widetilde{\mathcal{W}}_0$ for the hard sphere and $\widetilde{\mathcal{W}}_1$ for the soft sphere have the same limiting behaviour. In actuality, these weightings of the two different spheres are equal for all values of ka , which can be proven with the definitions from Appendix D.

As pointed out in [75], if $|\tilde{\zeta}| \gg ka$, i.e. as the magnitude of the impedance rises closer and closer towards infinity, the formulation of $\widetilde{\mathcal{W}}_n$ for a general uniform, locally-reacting impedance becomes that of the rigid one. Indeed, in the expression for $\widetilde{\mathcal{W}}_0$ and $\widetilde{\mathcal{W}}_1$ from the first column in Table 4-1, the terms with a factor of $\tilde{\zeta}$ from the nominators and the denominators become dominant as $\tilde{\zeta}$ approaches $+\infty$, thus implying to the corresponding expressions of the hard sphere.

As a result of all the aspects discussed above, in the expressions for the far-field scattered pressure, the behaviour of the spherical harmonic series in the 'Rayleigh region' is equivalent to the most dominant term of the summation, i.e. the $n = 0$ term, for the soft and radially-matched spheres. As the surface impedance approaches infinity and when the sphere is rigid, the $n = 1$ terms need to be also considered.

$ka \ll 1$	$\widetilde{\mathcal{W}}_n^{(pw)}\,(\tilde{\zeta}, ka)$	$\widetilde{\mathcal{W}}_n^{(pw)}\,(100, ka)$	$\widetilde{\mathcal{W}}_n^{(pw)}\,(0.01, ka)$
$n = 0$	$\frac{(ka)^2\left(1 - \tilde{\zeta}\, ika/3\right)}{\tilde{\zeta} + ika\, e^{-ika}}$	$\frac{-i}{3}\,(ka)^3$	$-ika\, e^{ika}$
$n = 1$	$i\,\frac{(ka)^3}{3}\,\frac{-ika + \tilde{\zeta}}{ika + 2\tilde{\zeta}}$	$\frac{i}{6}\,(ka)^3$	$\frac{-i}{3}\,(ka)^3$
$n \geq 1$	$i\left[\frac{2^n n!}{(2n)!}\right]^2 \frac{(ka)^{2n+1}}{(2n+1)}\,\frac{-ika + \tilde{\zeta} n}{ika + \tilde{\zeta}(n+1)}$	$i\left[\frac{2^n n!}{(2n)!}\right]^2 \frac{n\,(ka)^{2n+1}}{(n+1)(2n+1)}$	$-i\left[\frac{2^n n!}{(2n)!}\right]^2 \frac{(ka)^{2n+1}}{(2n+1)}$

Table 4-1 Asymptotic behaviour of modal frequency weightings $\widetilde{\mathcal{W}}_n^{(pw)}$ when $ka \ll 1$, calculated for different regimes of $\tilde{\zeta}$. Expressions are obtained for $n = 0$ and for $n \geq 1$. All expression above omit a factor of $1 + O(k^2 a^2)$.

$ka \ll 1$	$\widetilde{\mathcal{W}}_n^{(pw)}\,(100, ka)$	$\widetilde{\mathcal{W}}_n^{(pw)}\,(1, ka)$	$\widetilde{\mathcal{W}}_n^{(pw)}\,(0.01, ka)$
$n = 0$	$\frac{-i}{3}(ka)^3$	$(ka)^2$	$-i(ka)^1$
$n = 1$	$\frac{i}{6}(ka)^3$	$\frac{i}{6}(ka)^3$	$\frac{-i}{3}(ka)^3$
$n = 2$	$\frac{2i}{135}(ka)^5$	$\frac{2i}{135}(ka)^5$	$\frac{-i}{45}(ka)^5$

Table 4-2 Asymptotic behaviour of modal frequency weightings $\widetilde{\mathcal{W}}_n^{(pw)}$ when $ka \ll 1$, calculated for different regimes of $\tilde{\zeta}$. Expressions are obtained for $n = 0, 1, 2$.

4.2.3 Scattered field and total field expressed in terms of spherical harmonics

Substituting the calculated coefficients (4.12) back into the representation of the diverging wave from subsection 2.2.3 leads to the spherical harmonic decomposition of the scattered pressure

$$\tilde{p}_s(\vec{r}) = \tilde{\mathcal{P}}_i \sum_{n=0}^{\infty} \sum_{m=-n}^{n} -4\pi i^n \frac{j_n(ka) + i\tilde{\zeta}\, j_n{}'(ka)}{h_n(ka) + i\tilde{\zeta}\, h_n'(ka)}\, h_n(kr) Y_{n,m}^{(\mathbb{C})}(\theta, \varphi)\, \bar{Y}_{n,m}^{(\mathbb{C})}(\theta_i, \varphi_i)\,. \qquad (4.13)$$

By combining (2.34) and (4.13) , the total sound field due to scattering is

$$\tilde{p}_t(\vec{r}) =$$

$$= \tilde{\mathcal{P}}_i \sum_{n=0}^{\infty} \sum_{m=-n}^{n} 4\pi\, i^n \left[j_n(kr) - \frac{j_n(ka) + i\tilde{\zeta}\, j_n{}'(ka)}{h_n(ka) + i\tilde{\zeta}\, h_n'(ka)}\, h_n(kr) \right] Y_{n,m}^{(\mathbb{C})}(\theta, \varphi)\, \bar{Y}_{n,m}^{(\mathbb{C})}\,. \qquad (4.14)$$

To demonstrate the essential aspects of the scattering scenario under discussion,

- contour plots of the instantaneous, total pressure field on the yz-plane over the range $y \in [-2; 2]$, $z \in [-2; 2]$ and
- polar plots of $\widetilde{\Theta}_s(\theta, \phi)$, the directivity function of the scattered pressure field normalized by a factor of $1/\left(\tilde{\mathcal{P}}_i\, a\right)$,

for a uniform impedance sphere of radius $a = 0.3\ \mathrm{m}$ were computed in MATLAB using truncated spherical harmonics expansions and plotted in Figure 4-3. Graphs are shown for three cases of surface impedance: soft surface ($\tilde{\zeta} = 0.01$), the middle row is the radially-matched surface ($\tilde{\zeta} = 1$), and the bottom row is the hard surface ($\tilde{\zeta} = 100$), at six different values of normalized frequency ka . The discrete set $ka \in \{0.5\ ,1\ ,3\ ,6\ ,10\ ,20\}$ was chosen for presenting results to match what is presented in [71]. The incident plane-wave is chosen to have a magnitude of 1 Pa across all values of ka and to arrive from the direction $(\theta_i, \varphi_i) = (\pi, \pi/2)$. Only a slice following the yz-plane is shown in the figures. The results were computed using up to $N = 438$ terms in the summations for the incident and scattered pressures to ensure that the mean-square error was always below 0.8%. This judgement was made based on the results from [83, 84].

Placing the incident plane-wave at direction $(\pi, \pi/2)$ or $(0, \pi/2)$ results in only the $m = 0$ terms of a spherical harmonic expansions contributing to the scattered field. This happens because for $\theta = \pi$ and $\theta = 0$, the associated Legendre function in the definition of $Y_{n,m}^{(\mathbb{C})}(\theta, \varphi)$ has an argument of minus one, which always leads to the value of zero when $m \neq 0$, as seen in Appendix B. The nature of this behaviour arises from the choice of coordinate system.

From analysing the right halves in Figure 4-3, it can be observed that all three cases of surface impedance show important similarities, but also some essential differences. The main conclusion to be drawn is that in the lower frequency regime, the obstacle has a minor effect on the incident plane-wave; however, significant scattering artefacts are created as the wavelength becomes smaller than the dimensions of the sphere, which manifest as a `shadow' region downstream of the point of contact between incident wave and obstacle.

In the case of the rigid sphere, for lower values of ka, the scattered field is small in amplitude relative to the magnitude of the incident wave, thus the total near-field shows minimal changes due to the obstacle. In terms of normalized far-field directivity, the behaviour exhibits a main lobe in the upstream direction and an additional, smaller lobe in the downstream direction. As ka increases, the total near-field shows the planar wavefronts being affected further and further way from the sphere, in both upstream and downstream directions. However, as seen in Figure 4-3 , the main lobe still is significantly dominant compared to the additional lobe, even if they both increase in magnitude as ka increases.

The results for the value of $ka = 3$ suggest that, at some stage, the downstream scattering artefacts start to be more significant than the upstream ones. As ka increases after this stage, the shadow created by the obstacle in the total near-field, downstream, becomes larger and larger while encompassing a beam region that becomes narrower and more elongated away from the sphere. This beaming behaviour forms in the direction of propagation of the incident wave and creates more and more side-artefacts between $\theta = \pi/2$ and $\theta = 0$. The same characteristics are observed in the case of the normalized far-field directivity, where the initial main lobe starts to decrease after

$ka = 3$, then remains around the same magnitude, and the additional lobe of the scattered pressure directivity starts to beam downstream while forming smaller side lobes.

The case where $\tilde{\zeta} = 1$ exemplifies what happens as the surface impedance becomes matched in the radial direction to $\rho_0 c_0$ of the surrounding medium. Compared to the rigid sphere, in the low ka regime, the normalized far-field directivity is close to omnidirectional and larger in magnitude for the same values of ka. As the normalized frequency increases, the omnidirectional pattern is off-centred in the downstream direction and starts forming the beaming lobe between $ka = 1$ and $ka = 3$, at a lower frequency than the rigid sphere. Furthermore, in the upstream direction, the normalized directivity tends to zero; as the wavelength of the incident field becomes smaller and smaller relative to the size of the obstacle, the curvature of the sphere acts more and more as an infinite planar wall. Thus, a significant portion of the energy is absorbed due to the impedance of the surface matching the characteristic impedance of the propagation medium. The side lobes are also formed as ka increases, however, they are fewer in number than before. All of this behaviour is echoed in the total near-field plots, where the plane-wave is mostly unaffected in the upstream direction at all values of ka , but the shadow and beaming region still appear.

When adding the case of the soft sphere to the previous comparison, all of what was noted in the previous paragraph applies to this as well, with two major exceptions. Firstly, in the low ka regime, the incident field does not remain unaffected by the obstacle as the pressure has to reach zero on its surface. Also, the magnitude of the normalized directivity has the highest magnitude of the three impedance cases. Secondly, as ka increases, the normalized directivity that was somewhat omnidirectional starts forming both upstream and downstream lobes. This resembles more the case of the rigid sphere, as opposed to that of the $\tilde{\zeta} = 1$ sphere, for which very little scattering is created in the region upstream. It is worth mentioning that the soft sphere exhibits the least amount of side lobes at large values of the normalized frequency.

The shadow and beaming regions of the three cases discussed above have very clear distinctions. The shadow region of the rigid sphere is the least prominent while the one of the soft sphere is the most prominent. The wavefronts in the beaming region are planar, even very close to the sphere, for the rigid condition. This is not the same for the other two; closer to the obstacle the wavefronts in the beam are bent and then become planar at a distance away from the surface.

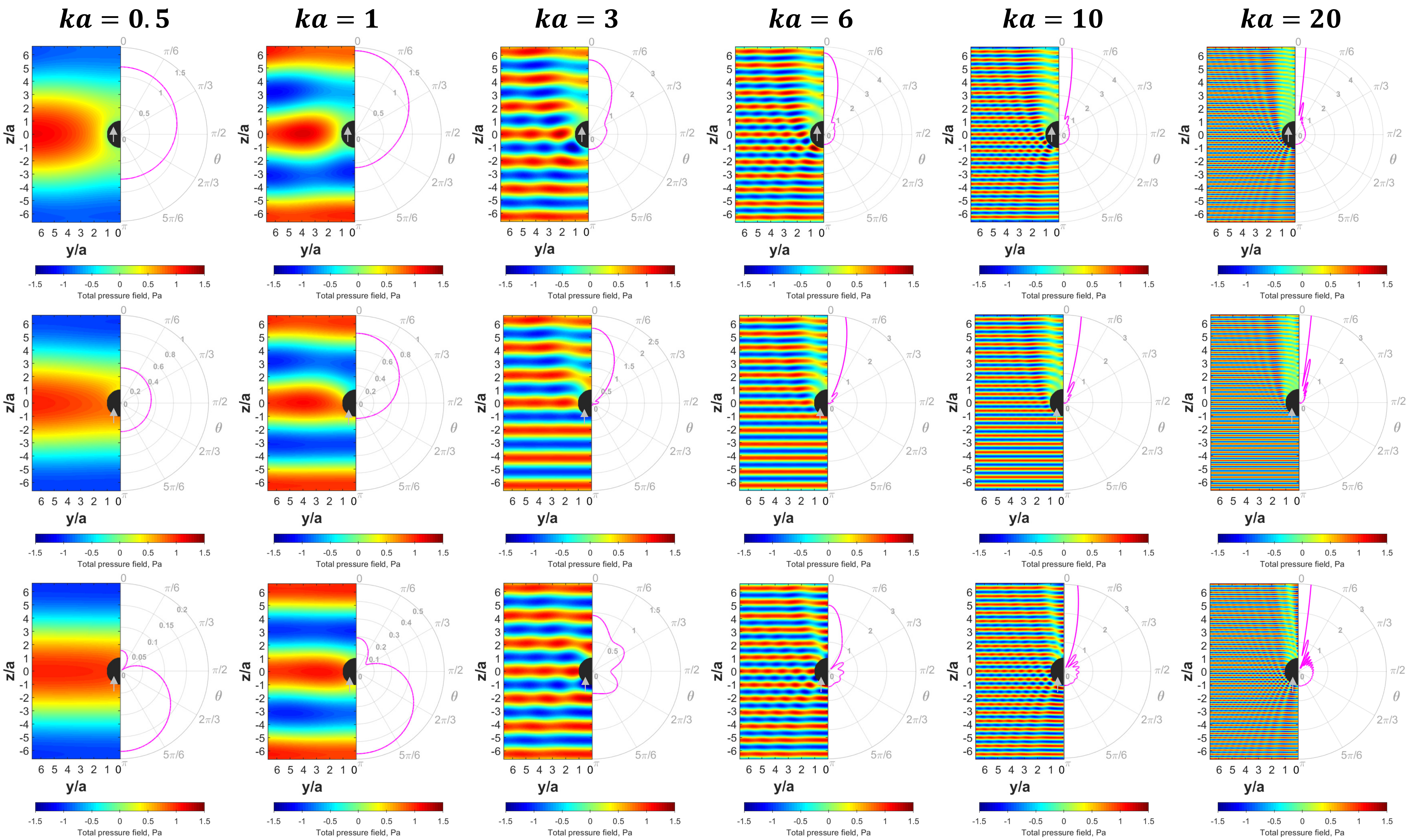

Figure 4-3: Contour plots of the total pressure field (on the left) and for normalized far-field scattered pressure (on the right) due to for scattering of a monochromatic plane-wave by a sphere with different values for the uniform, locally-reacting impedance on its surface. The plane-wave has a magnitude of 1 Pa across all values of ka and arrives from the direction $(\theta_i, \varphi_i) = (\pi, \pi/2)$, i.e. from bottom of the figure towards the top. The top row is the soft surface ($\tilde{\zeta} = 0.01$), the middle row is the radially-matched surface ($\tilde{\zeta} = 1$), and the bottom row is the hard surface ($\tilde{\zeta} = 100$).

4.2.4 Scattered sound power and its asymptotic behaviour with ka

The acoustic scattered power by the impedance sphere interacting with a plane-wave is

$$\widetilde{W}_s = \frac{1}{2\rho_0 c_0 k^2} \sum_{n=0}^{\infty} \sum_{m=-n}^{n} \left| \widetilde{D}_{n,m}^{(\mathbb{C},pw)} \right|^2, \qquad (4.15)$$

which can be simplified to

$$\widetilde{W}_s = \frac{2\pi \widetilde{P}_i^2}{\rho_0 c_0 k^2} \sum_{n=0}^{\infty} (2n+1) \left| \widetilde{\mathcal{W}}_n^{(pw)} \right|^2, \qquad (4.16)$$

when using the weightings in (4.6) and the closure relationship of the spherical harmonics. If the acoustic power associated with the incident plane-wave is defined as the product of the incident intensity and the cross-sectional area of the sphere

$$\widetilde{W}_i = \frac{\pi a^2 \widetilde{\mathcal{P}}_i^2}{2\rho_0 c_0}, \qquad (4.17)$$

then the normalized scattered power can be written as

$$\widetilde{\Pi}_s = \frac{\widetilde{W}_s}{\widetilde{W}_i} = \frac{1}{\pi (ka)^2 \widetilde{\mathcal{P}}_i^2} \sum_{n=0}^{\infty} \sum_{m=-n}^{n} \left| \widetilde{D}_{n,m}^{(\mathbb{C},pw)} \right|^2, \qquad (4.18)$$

and

$$\widetilde{\Pi}_s = \frac{4}{(ka)^2} \sum_{n=0}^{\infty} (2n+1) \left| \widetilde{\mathcal{W}}_n^{(pw)} \right|^2. \qquad (4.19)$$

The normalized scattered power is equal to the scattering cross section, as used, for example, in [88, 89], divided by πa^2. It should be noted that although the scattered power, as defined in equation (4.19), is a useful measure of the space-averaged mean square pressure that is scattered into the far field, it does not represent the actual power radiated by the sphere, which depends on the interaction between the incident and scattered fields.

Figure 4-4 shows the variation in the normalized scattered power, $\widetilde{\Pi}_s$, with normalized frequency, ka, calculated for three different values of locally-reacting surface impedance. These were computed using a finite summation in equation (4.19), up to $N = 100$, which was found to accurately represent the scattered power up to $ka = 100$, since doubling the number of terms resulted in differences of less than $0.06\ dB$ in the scattered power at any frequency [78]. When the

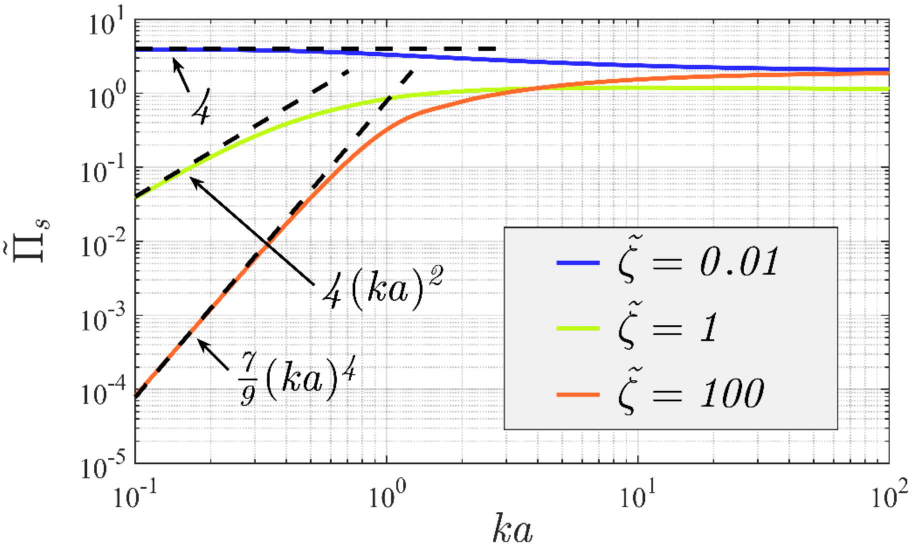

Figure 4-4: The scattered sound power divided by the power associated with the incident plane-wave, versus ka, for the soft $\tilde{\zeta} = 0.01$, radially-matched $\tilde{\zeta} = 1$, and hard $\tilde{\zeta} = 100$ spheres.

surface impedance is the same as the characteristic impedance of the fluid surrounding the sphere so that $\zeta = 1$, which is described as the 'radially-matched' case, the normalized scattered power initially increases in proportion to $(ka)^2$ and has a limiting value of unity at high frequency. This is because a sound power equal to the incident sound power is absorbed by the sphere, but the sphere casts a shadow at higher frequencies. If the normalized surface impedance of the sphere is 10^{-2}, the variation in the scattered sound power with ka cannot be distinguished from that of a sphere whose surface impedance is zero over the frequency range and on the resolution of Figure 4-4. This finite surface impedance is used here as an example of a soft sphere, however, since a monopole placed on its surface will generate a finite external pressure field, unlike when the surface impedance is zero as described below. In the case of the soft sphere, the scattered power is four times the incident sound power as defined by (4.17) for small ka [88]. The soft sphere scatters sound strongly at low frequencies since to realize the pressure-release boundary condition at the surface, the incident pressure, which is uniform over the surface of the sphere at low frequencies, can be thought of as being balanced by that due to a monopole source at the centre of the sphere of strength $4\pi a\tilde{\mathcal{P}}_i/(i\rho c)$. The power radiated by such a monopole is $\pi a^2\tilde{\mathcal{P}}_i/(\rho c)$, so that when divided by the incident sound power in (4.17), the normalized scattered power is equal to four. At high frequencies, the scattered power is twice the incident power since not only is a shadow generated by the sphere, but the incident sound field is reflected off the almost-pressure-release boundary condition at the front of the sphere.

When the normalized surface impedance is 100 times the characteristic impedance of the surrounding fluid, the results are indistinguishable from the case when the normalized surface impedance is infinite within the resolution used in Figure 4-4, and this is used here as a practical example of a hard sphere. In this case, the scattering is very small at low frequencies with the normalized scattered sound power rising as $7(ka)^4/9$, but at high frequencies the scattered sound power is again twice the incident sound power, since the sphere both generates a shadow and reflects the incident wave off the almost-zero-velocity surface. In the low frequency value $4(ka)^4/9$ corresponds to the contribution of the $n = 0$ component, and $3(ka)^4/9$ corresponds to the contribution of the $n = 1$ component, as described by Lamb [4].

Using the results from Table 4-1, the limiting behaviour of scattered sound power, $\widetilde{W}_s$, and normalized scattered sound power, $\widetilde{\Pi}_s$, when $ka \ll 1$, are calculated and presented in Table 4-3.

$ka \ll 1$	$\tilde{\zeta}$	$\tilde{\zeta} = 100$	$\tilde{\zeta} = 0.01$
$\widetilde{W}_s$	$\frac{\tilde{\mathcal{P}}_i^2}{\rho_0 c_0}\left\lvert\frac{1-\tilde{\zeta}\, ika/3}{\tilde{\zeta}-ika}\right\rvert^2 2\pi\, a^2\,(ka)^2$	$\frac{\tilde{\mathcal{P}}_i^2}{\rho_0 c_0}\,\frac{7\pi}{18}\,a^2\,(ka)^4$	$\frac{\tilde{\mathcal{P}}_i^2}{\rho_0 c_0}\,2\pi\,a^2$
$ka \ll 1$	$\tilde{\zeta} = 1$	$\tilde{\zeta} = 100$	$\tilde{\zeta} = 0.01$
$\widetilde{\Pi}_s$	$4\,(ka)^2$	$\frac{7}{9}\,(ka)^4$	4

Table 4-3 Asymptotic behaviour as ka approaches zero of scattered sound power, $\widetilde{W}_s$, and normalized scattered sound power, $\widetilde{\Pi}_s$, due to an incident monochromatic plane-wave scattering from a spherical obstacle with uniform, locally-reacting impedance on its surface.

4.3 Radiation of a monochromatic point-monopole source on the surface of the sphere

4.3.1 Coefficients in spherical harmonic expansion

The radiation of a point-monopole situated on the surface of an 'impedance sphere' can be obtained by allowing the radial position of the source, r' , to tend to the radius of the sphere, a , while maintaining its angular position (θ', φ') in relation. Therefore, $r' = a < r$ and the coefficients in the spherical harmonic expansion are

$$\begin{aligned}\widetilde{D}_{n,m}^{(\mathbb{C},pm)} &= k^2 \rho_0 c_0\, \tilde{q} \left[j_n(ka) - \frac{j_n(ka) + i\tilde{\zeta} j_n'(ka)}{h_n(ka) + i\tilde{\zeta} h_n'(ka)}\, h_n(ka) \right] \bar{Y}_{n,m}^{(\mathbb{C})}(\theta', \varphi') = \\ &= k^2 \rho_0 c_0 \left[j_n(ka) - \widetilde{\mathcal{W}}_n\, h_n(ka) \right] \bar{Y}_{n,m}^{(\mathbb{C})}(\theta', \varphi') = \frac{\rho_0 c_0}{a^2} \widetilde{\mathcal{W}}_n^{(pm)}\, \bar{Y}_{n,m}^{(\mathbb{C})}(\theta', \varphi'),\end{aligned} \qquad (4.20)$$

where $\widetilde{\mathcal{W}}_n$ is the same as in (4.6), and where the modal frequency weighting for the point-monopole is given by

$$\widetilde{\mathcal{W}}_n^{(pm)}(a, \tilde{\zeta}, ka) = (ka)^2 \left[j_n(ka) - \widetilde{\mathcal{W}}_n\, h_n(ka) \right] = \frac{\tilde{\zeta}}{h_n(ka) + i\tilde{\zeta} h_n'(ka)}\ . \qquad (4.21)$$

The final form of (4.20) is obtained by bringing the expression in the initial square brackets at a common denominator and then applying the Wronskian relation described in Appendix D.

It is important to note that, when the impedance is zero, i.e. for a soft boundary, all coefficients in the spherical harmonic expansion are zero and the point-monopole cannot radiate when placed on the surface, as demonstrated by relation (4.19). Because of this, the rest of the analysis uses a sphere with $\tilde{\zeta} = 0.01$ in place of the software, such that the behaviour can be observed as in that region of impedance values.

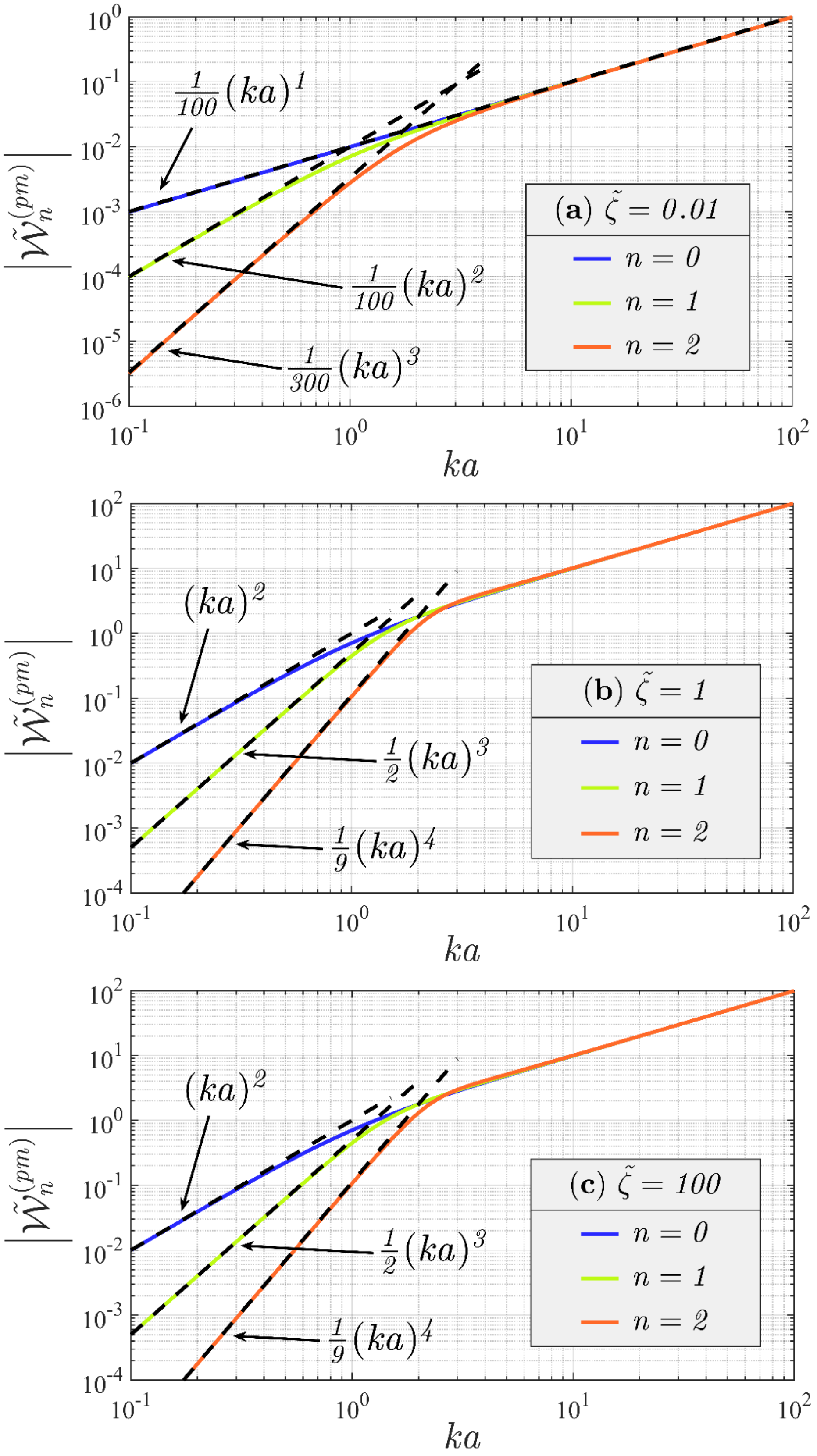

Figure 4-5 Modal frequency weightings $\widetilde{\mathcal{W}}_n^{(pm)}$ of sound field radiated by point-monopole on the surface of soft $\tilde{\zeta} = 0.01$ (a), radially-matched $\tilde{\zeta} = 1$ (b), and hard $\tilde{\zeta} = 100$ (c) spheres.

4.3.2 Asymptotic behaviour of coefficients with ka

Following the same procedure applied in [75] and the same structure as in subsection 4.2.2, the asymptotic behaviour of $\widetilde{\mathcal{W}}_n^{(pm)}$ when $ka \ll 1$ is first plotted in Figure 4-5 for the rigid and radially-matched spheres. Similar to the scenario of the plane-wave, given a fixed value of ka, the coefficients with the lowest n are the most dominant when ka is close to zero, and as ka increases to higher values, the contributions of more and more orders of $\widetilde{\mathcal{W}}_n^{(pm)}$ become significant. However, the $n = 0$ coefficient is the most dominant at low ka for both types of spheres.

$ka \ll 1$	$\widetilde{\mathcal{W}}_n^{(pm)}(\tilde{\zeta}, ka)$	$\widetilde{\mathcal{W}}_n^{(pm)}(100, ka)$
$n = 0$	$(ka)^2 \dfrac{i\tilde{\zeta}}{i\tilde{\zeta} - ka\, e^{-ika}}$	$(ka)^2$
$n = 1$	$\dfrac{(ka)^3}{2} \dfrac{i\tilde{\zeta}}{2i\tilde{\zeta} - ka}$	$\dfrac{1}{2}(ka)^3$
$n \geq 1$	$\dfrac{(ka)^{n+2}}{(2n-1)!!} \dfrac{i\tilde{\zeta}}{i\tilde{\zeta}(n+1) - ka}$	$\dfrac{(ka)^{n+2}}{(2n-1)!!}$

Table 4-4 Asymptotic behaviour modal frequency weightings $\widetilde{\mathcal{W}}_n^{(pm)}$ when $ka \ll 1$, calculated for different regimes of $\tilde{\zeta}$. Expressions are obtained for $n = 0$ and for $n \geq 1$. All expressions above omit a factor of $1 + O(k^2a^2)$.

$ka \ll 1$	$\widetilde{\mathcal{W}}_n^{(pm)}(100, ka)$	$\widetilde{\mathcal{W}}_n^{(pm)}(1, ka)$	$\widetilde{\mathcal{W}}_n^{(pm)}(0.01, ka)$
$n = 0$	$(ka)^2$	$(ka)^2$	$\dfrac{-i}{100}(ka)^1$
$n = 1$	$\dfrac{1}{2}(ka)^3$	$\dfrac{1}{2}(ka)^3$	$\dfrac{-i}{100}(ka)^2$
$n = 2$	$\dfrac{1}{9}(ka)^4$	$\dfrac{1}{9}(ka)^4$	$\dfrac{-i}{300}(ka)^3$

Table 4-5 Asymptotic behaviour of modal frequency weighting $\widetilde{\mathcal{W}}_n^{(pm)}$ when $ka \ll 1$, calculated for different regimes of $\tilde{\zeta}$. Expressions are obtained for $n = 0, 1, 2$.

The different asymptotic behaviours of the spherical Bessel and Hankel functions, lead to the analytical results contained in Table 4-4. The results for all n demonstrate that the formulation of $\widetilde{\mathcal{W}}_n^{(pm)}$ for a general uniform, locally-reacting impedance becomes that of $\widetilde{\mathcal{W}}_n^{(pm)}$ for the rigid when $|\tilde{\zeta}| \gg ka$, i.e. the magnitude of the impedance rises closer and closer towards infinity. The asymptotic behaviour derived in Table 4-4 are presented in a straightforward way in Table 4-5, for the normalized impedances of interest and first few orders. These are added in the plots from Figure 4-5 to demonstrate the limiting behaviour as the normalized frequency approaches zero.

4.3.3 Radiated field expressed in terms of spherical harmonics

The radiated field of the point-monopole on the surface of the spherical obstacle is given by

$$\tilde{p}_{pm}(\vec{r}) =$$

$$= k^2 \rho_0 c_0\, \tilde{q} \sum_{n=0}^{\infty} \sum_{m=-n}^{n} \left[j_n(ka) - \widetilde{\mathcal{W}}_n\, h_n(ka) \right] h_n(kr)\, Y_{n,m}^{(\mathbb{C})}(\theta,\varphi)\, \bar{Y}_{n,m}^{(\mathbb{C})}(\theta',\varphi') = \tag{4.22}$$

$$= k^2 \rho_0 c_0\, \tilde{q} \sum_{n=0}^{\infty} \sum_{m=-n}^{n} \left[j_n(ka) - \frac{j_n(ka) + i\tilde{\zeta} j_n'(ka)}{h_n(ka) + i\tilde{\zeta} h_n'(ka)}\, h_n(ka) \right] h_n(kr)\, Y_{n,m}^{(\mathbb{C})}(\theta,\varphi)\, \bar{Y}_{n,m}^{(\mathbb{C})}(\theta',\varphi') \ ,$$

which, using (4.21) can be re-arranged as

$$\tilde{p}_{pm}(\vec{r}) = \frac{\rho_0 c_0 \tilde{q}}{a^2} \sum_{n=0}^{\infty} \sum_{m=-n}^{n} \frac{\tilde{\zeta}}{h_n(ka) + i\tilde{\zeta} h_n'(ka)}\, h_n(kr)\, Y_{n,m}^{(\mathbb{C})}(\theta,\varphi)\, \bar{Y}_{n,m}^{(\mathbb{C})}(\theta',\varphi') \, . \tag{4.23}$$

It is important to note that expression (4.23) still has the form of the diverging wave from subsection 2.2.3, in the current coordinate system, and its corresponding coefficients are given by

$$\widetilde{D}_{n,m}^{(\mathbb{C},pm)} = \frac{\rho_0 c_0}{a^2} \frac{\tilde{\zeta}}{h_n(ka) + i\tilde{\zeta} h_n'(ka)}\, \bar{Y}_{n,m}^{(\mathbb{C})}(\theta',\varphi') \ . \tag{4.24}$$

For the rigid sphere, in (4.23) , the fraction of spherical Hankel functions of argument ka becomes $-1/h_n'(ka)$ as $\tilde{\zeta}$ tends to $+\infty$, therefore

$$\tilde{p}_{pm}(\vec{r}) = -\frac{i\rho_0 c_0 \tilde{q}}{a^2} \sum_{n=0}^{\infty} \sum_{m=-n}^{n} \frac{h_n(kr)}{h_n'(ka)}\, Y_{n,m}^{(\mathbb{C})}(\theta,\varphi)\, \bar{Y}_{n,m}^{(\mathbb{C})}(\theta',\varphi') \ , \tag{4.25}$$

In the case of a rigid sphere. In the case of the soft sphere, the fraction of spherical Hankel functions of ka from expression (4.23) is proportional to $\tilde{\zeta}$ and thus becomes zero as $\tilde{\zeta} \rightarrow 0$, leading to no radiation.

To demonstrate the essential aspects of the radiating scenario under discussion,

- contour plots of the instantaneous, radiated pressure field on the yz-plane over the range $y \in [-2; 2]$, $z \in [-2; 2]$, and
- polar plots of $\widetilde{\Theta}_s(\theta, \phi)$, the directivity function of the radiated pressure field normalized by a factor of $1/(ak^2\rho_0 c_0 \tilde{q})$,

for a uniform impedance sphere of radius $a = 0.3\,\mathrm{m}$ were computed in MATLAB using the truncated spherical harmonics expansions and plotted in Figure 4-6. Graphs are shown for three cases of surface impedance: the top row is the soft surface ($\tilde{\zeta} = 0.01$), the middle row is the radially-matched surface ($\tilde{\zeta} = 1$), and the bottom row is the hard surface ($\tilde{\zeta} = 100$), at six different values of normalized frequency ka . The discrete set $ka \in \{0.5 , 1 , 3 , 6 , 10 , 20\}$, as in subsection 4.2.3. The point-monopole is chosen to have a source strength of $1/k^2\rho_0 c_0 \tilde{q}\ \mathrm{m}^3/\mathrm{s}$ (equivalent value, not units) across all values of ka and to be placed at the direction $(\theta', \varphi') = (\pi, \pi/2)$. Only a slice of the yz-plane is shown in the figures. The results were computed using up to $N = 438$ terms in the summations for the incident and scattered pressures to ensure that the mean-square error was always below 0.8%. This judgement was made based on the results from [83, 84].

As for the case of the plane-wave, placing the angular position of the point-monopole at $(\pi, \pi/2)$ or $(0, \pi/2)$ results in only the $m = 0$ terms of a spherical harmonic expansions contributing to the scattered field. This happens because for $\theta = \pi$ and $\theta = 0$, the associated Legendre function in the definition of $Y_{n,m}^{(\mathbb{C})}(\theta, \varphi)$ has an argument of minus one, which always leads to the value of zero when $m \neq 0$, as seen in Appendix B.

From analysing Figure 4-6, it can be observed that both cases of surface impedance behave in a similar way with few differences. In terms of normalized radiated pressure, both the rigid and the radially-matched spheres are close to omnidirectional in the low ka regime. The omnidirectional characteristic begins to change somewhere between $ka = 0.5$ and $ka = 1$. As the dimenssionless wavenumber gradually increases and the wavelength becomes more and more comparable to the size of the sphere, a directivity pattern similar to a super-cardioid shape; a main downstream lobe becomes increasingly large as a secondary upstream lobe becomes diminishingly small and elongates towards the direction given by $(\theta, \varphi) = (0, \pi/2)$.

The secondary lobe decreases with higher ka more rapidly for the $\tilde{Z} = \rho_0 c_0$ sphere than for the rigid sphere. At $ka = 20$ and higher, it can be observed in Figure 4-6 that the normalized pressure directivity is almost zero in the upstream direction for the first of the two cases. This is to be expected as the surface impedance can absorb some of the source`s energy. For the rigid sphere, some tiny oscillation can also be noticed when the main lobe connects with the secondary one as the value of φ approaches π . These are very small compared to the size of the two lobes, and it is difficult to state if they occur or not when $\tilde{\zeta} = 1$ from the realized graphs.

All the behaviour described in the two paragraphs above is echoed in the near-field plots of the radiated pressure. The spherical wave is mostly unaffected by the presence of the obstacle at lower values of ka; however, as the normalized frequency increases, the sound field becomes shadowed by the sphere, first upstream, and then increasingly more in the side regions. For the radially-matched sphere, cancellation is almost achieved in the direction given by $(\theta, \varphi) = (0, \pi/2)$ at higher ka . The previously discussed tiny oscillations in the normalized pressure directivity cannot be observed in Figure 4-6 because they are so small in scale compared to all the other behaviour.

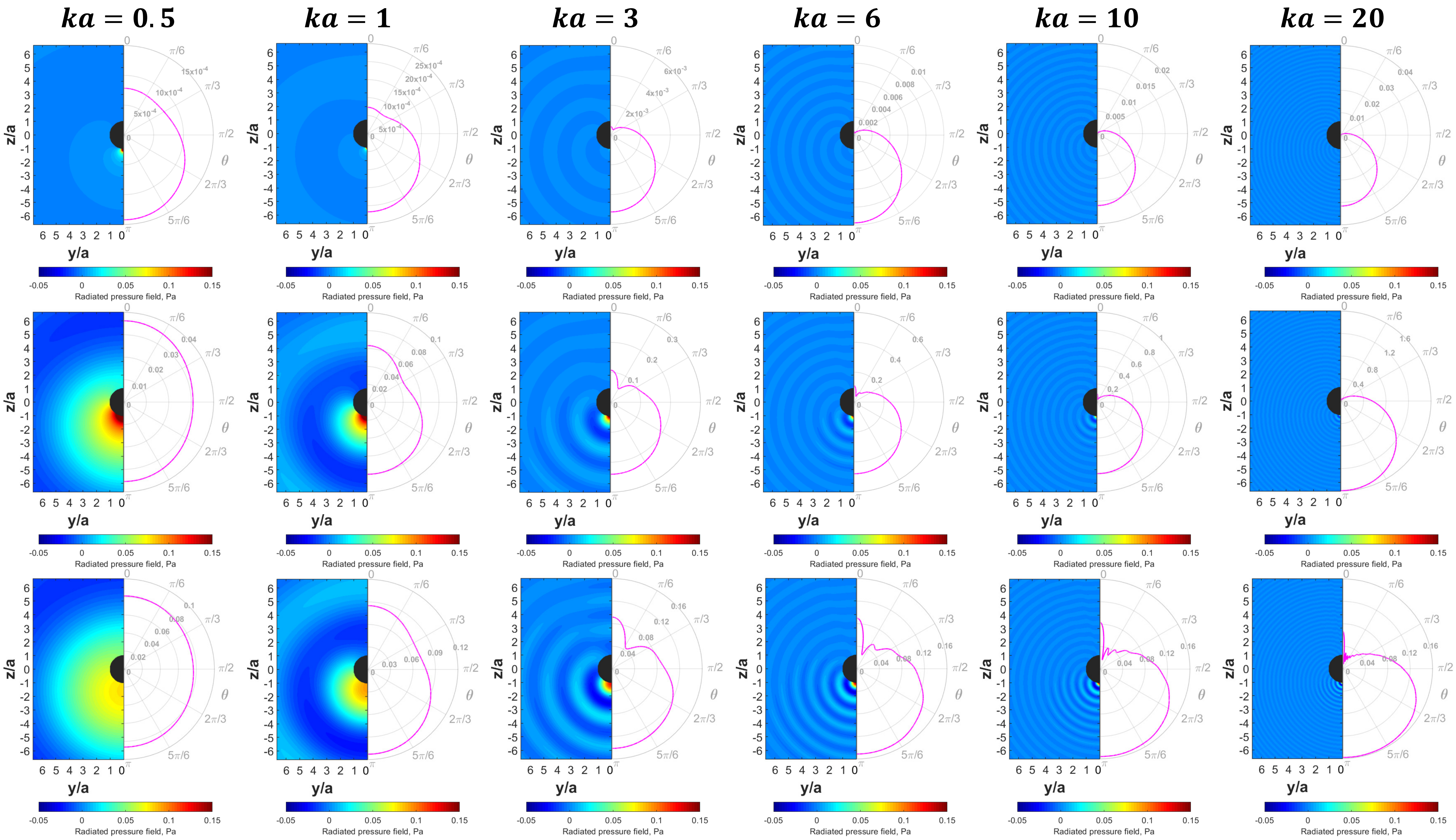

Figure 4-6: Contour plots of the radiated pressure field (on the left) and for normalized far-field radiated pressure (on the right) due to a point-monopole radiating when placed on the surface a sphere with different values for the uniform, locally-reacting impedance on its boundary. The source strength is $\tilde{q} = 0.001\ \mathrm{m}^3/\mathrm{s}$ across all values of ka and the source is placed at the direction $(\theta', \varphi') = (\pi, \pi/2)$, i.e. from bottom of the figure towards the top. The top row is the $\tilde{\zeta} = 0.01$ soft sphere, the middle row is the $\tilde{\zeta} = 1$ radially-matched sphere, and the bottom row is the $\tilde{\zeta} = 100$ hard sphere.

4.3.4 Radiated sound power and its asymptotic behaviour with ka

The acoustic scattered power by the impedance sphere interacting with a point-monopole radiating from its surface is

$$\widetilde{W}_{pm} = \frac{|\tilde{q}|^2}{2\rho_0 c_0 k^2} \sum_{n=0}^{\infty} \sum_{m=-n}^{n} \left| \widetilde{D}_{n,m}^{(\mathbb{C},pm)} \right|^2, \tag{4.26}$$

which can be simplified to

$$\widetilde{W}_{pm} = \frac{\rho_0 c_0 |\tilde{q}|^2}{8\pi a^4 k^2} \sum_{n=0}^{\infty} (2n+1) \left| \widetilde{\mathcal{W}}_n^{(pm)}\left(a, \tilde{\zeta}, ka\right) \right|^2, \tag{4.27}$$

when using the coefficients in (4.24), the weightings in (4.21), and the closure relationship of the spherical harmonics. The acoustic power of a free-field point-monopole of volumetric source strength $\tilde{q}$ is [24, 71]

$$\widetilde{W}_{ffpm} = \frac{k^2 \rho_0 c_0 |\tilde{q}|^2}{8\pi}, \tag{4.28}$$

then the normalized radiated power of the point-monopole on the spherical surface is

$$\widetilde{\Pi}_{pm} = \frac{\widetilde{W}_{pm}}{\widetilde{W}_{ffpm}} = \frac{4\pi}{(\rho_0 c_0)^2 k^4} \sum_{n=0}^{\infty} \sum_{m=-n}^{n} \left| \widetilde{D}_{n,m}^{(\mathbb{C},pm)} \right|^2, \tag{4.29}$$

and

$$\widetilde{\Pi}_{pm} = \frac{1}{(ka)^4} \sum_{n=0}^{\infty} (2n+1) \left| \widetilde{\mathcal{W}}_n^{(pm)}\left(a, \tilde{\zeta}, ka\right) \right|^2. \tag{4.30}$$

Using the modal frequency weightings (4.21) and $N = 100$ terms in the spherical harmonic series for the used frequency range, the normalized radiated sound power, $\widetilde{\Pi}_{pm}$, is plotted versus ka in Figure 4-7, for the soft sphere ($\tilde{\zeta} = 0.01$), radially-matched sphere ($\tilde{\zeta} = 1$), and hard sphere ($\tilde{\zeta} = 100$). The lines corresponding to the latter two cases both exhibit an overall ascent and, in the lower ka regime, they are very similar to each other and to the radiation of a free-field point-monopole. However, as ka increases, the rigid sphere becomes a better and better radiator of sound. This behaviour between the two types of surface impedance is similar when compared to the sound power scattered due to a plane-wave at higher ka (see Figure 4-4). The result suggests that bringing a sound source closer to the surface of the obstacle potentially makes the resulting scattered sound power invariant to changes of the locally-reacting impedance at low frequencies. In the case of the soft sphere, it radiates very poorly, as expected. Starting from low frequencies, the radiated power descends proportional to $(ka)^{-2}$, and then continues to descend not as abrupt when frequency increases. Eventually, a fixed valued is reached at high frequencies.

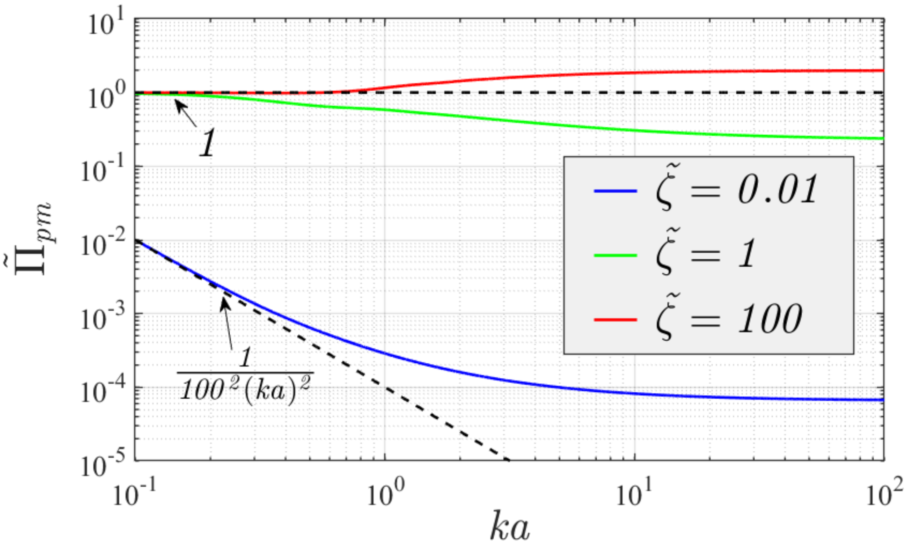

Figure 4-7: The radiated sound power of a point-monopole on the surface of an impedance sphere, divided by the power radiated by a free-field point-monopole of the same characteristics, versus ka, for the soft $\tilde{\zeta} = 0.01$, radially-matched $\tilde{\zeta} = 1$, and hard $\tilde{\zeta} = 100$ spheres.

Using the asymptotic behaviour when $ka \rightarrow 0$ described in in Table 4-4 and Table 4-5, the low frequency formulations for the radiated sound power, $\widetilde{W}_{pm}$, and normalized radiate sound power, $\widetilde{\Pi}_{pm}$, of the point-monopole placed on the surface of different impedance spheres are obtained. These are presented in Table 4-6.

It is important to highlight that the point-monopole radiating from the rigid spherical baffle resembles a free-field point-monopole in the 'Rayleigh region' (see [71] for far-field and power of a point-monopole). For the case of a radially-matched baffle, there is an extra factor in the formulation for the acoustic pressure and, hence, in that of the sound power. This factor is dependent on the surface impedance; however, it becomes equal to one as $\tilde{\zeta} \gg ka$.

$ka \ll 1$	$\tilde{\zeta}$	$\tilde{\zeta} = 100$	
$\widetilde{W}_{pm}$	$\frac{k^2\rho_0 c_0 \lvert\tilde{q}\rvert^2}{8\pi}\left\lvert\frac{i\tilde{\zeta}}{i\tilde{\zeta} - ka}\right\rvert^2$	$\frac{k^2\rho_0 c_0 \lvert\tilde{q}\rvert^2}{8\pi}$	
$ka \ll 1$	$\tilde{\zeta} = 1$	$\tilde{\zeta} = 100$	$\tilde{\zeta} = 0.01$
$\widetilde{\Pi}_{pm}$	1	1	$\frac{1}{\tilde{\zeta}^2}\frac{1}{(ka)^2}$

Table 4-6 Asymptotic behaviour as ka approaches zero of radiated sound power, $\widetilde{W}_{pm}$, and normalized radiated sound power, $\widetilde{\Pi}_{pm}$, due to a monochromatic point-monopole on the surface of a spherical obstacle with uniform, locally-reacting impedance on its surface.

4.4 Chapter summary

This chapter has presented a spherical harmonic analysis of the 3D sound scattering from a uniform impedance sphere in a fluid, and of the 3D sound radiation from an acoustic source in the vicinity of such a sphere. Physical quantities such as scattered/radiated sound pressure in the near-field, directivity of scattered/radiated sound pressure in the far-field and scattered/radiated sound power have been illustrated with computer-modelled results for idealized cases such as a plane-wave or a point-monopole and for three representative values of surface impedance. The spherical harmonic components of the quantities have been studied and used to make analytical predictions at low frequencies. In this regime, one or two spherical harmonic components dominate, and a hierarchy based on degree n is maintained given an ideal placement of an incidence or source relative to the scatterer, i.e. on the z-axis. With increasing frequency, more and more spherical harmonic components become dominant in the series at the same time. The content in this chapter is later used to exemplify the effect of tonal active control on suppressing sound scattering, when employing the idealized control strategy outlined in subsection 2.4.2 and subsection 3.3.1. The example results for control are contained in Chapter 5, where the primary is represented by the scattering of a plane-wave from the impedance sphere, and the secondary sources are represented by point-monopoles radiating on the surface or in the vicinity of the impedance sphere.

Chapter 5 Active control of Sound Scattering from Uniform Impedance Sphere in a Fluid

In this chapter, centralized control in the form of active tonal suppression is exemplified for the sound scattering from a uniform impedance sphere with computer-modelled results. These are obtained from the spherical harmonic representations discussed in Chapter 4. The analysis pursues a straightforward case where the incidence is represented by a single monochromatic plane-wave and the secondary is represented by a finite number of point-monopole sound radiators.

For the impedance sphere scatterer, the active control examples represent the ideal outcomes from solving the mathematical models presented in Chapter 2 without taking into consideration practical limitations. The practical-oriented models presented in Chapter 3 either lead to an equivalent of these models in a feedforward control arrangement or modify the impedance on the surface in a feedback arrangement. The impedance of the scatterer in question is considered to be a fixed value that does not vary with frequency or modal index; as such, the study in this chapter only considers the active control arrangement that maintains this property, i.e. with no feedback control.

The benefit of active control is affected by the number of secondary sources, the position of the secondary sources relative to the primary disturbances, and the position of the secondary sources relative to each other. The presentation in this chapter first looks at the results using either one or two secondary sources placed on the surface of the obstacle, along the direction of arrival of the plane-wave. This is done to take advantage of the axisymmetric properties of the spherical shape and simplify some of the mathematics involving spherical harmonic series expansions. Secondly, the number of secondary sources is increased to a very high number, and they are distributed evenly on the surface. And lastly, the pattern of many secondary sources is moved away from the surface of the obstacle, all at the same radial distance.

The discussion builds upon what was presented in section 4.1, in particular, it focuses on results for the rigid, soft and radially-matched spheres as the normalized frequency ka is varied. However, a sound source does not radiate when placed on a soft boundary, thus it cannot be used as a control source in this scenario. Because of this, in the following paragraphs, the active control with radiators on the surface of the scatter is instead studied when the boundary is close to soft, i.e. the $\tilde{\zeta} = 0.01$ sphere is used to approximate the case of a soft boundary. Furthermore, the $\tilde{\zeta} = 100$ sphere is used to approximate the case of a rigid boundary, for consistency.

5.1 Active control with a small number of surface radiators

For active control with a small number of control sources on the surface of the sphere, the two studied arrangements are depicted schematically in Figure 5-1. These consist of a monochromatic plane-wave of unit magnitude as the arriving incidence, which produces the scattering that represents the primary disturbance. This is placed along the z-axis, travelling from minus to plus. In the first instance, one point-monopole secondary source is placed either in the $\theta = \pi$ position or the $\theta = 0$ position. Then, two point-monopoles are placed at both $\theta = \pi$ and $\theta = 0$. In these arrangements, the spherical harmonic formulations defined in Chapter 4 for the primary and the secondary consist of only the terms that have $m = 0$, as all other terms do not contribute. Only the $m = 0$ spherical harmonic components are used when computing the active control results.

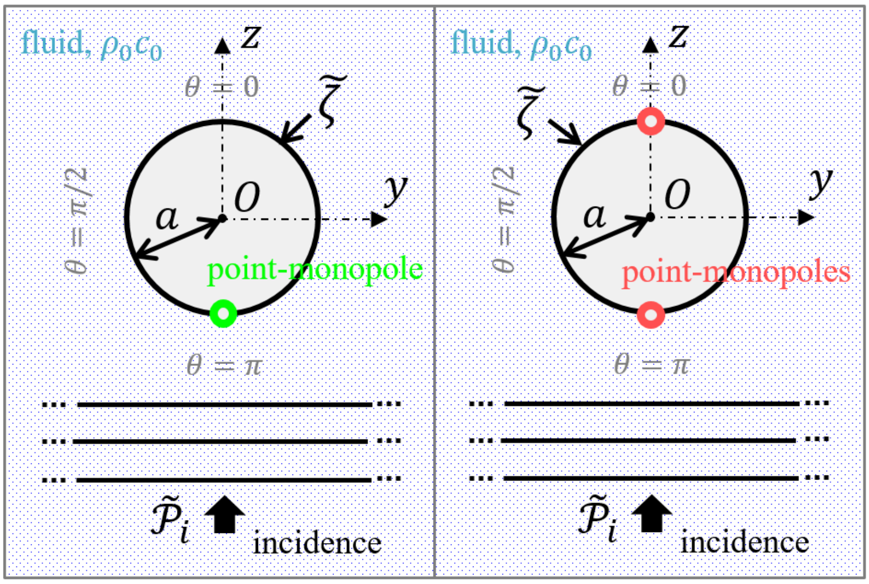

Figure 5-1: 2D view of 3D arrangements of secondary sources for the study of tonal active control of scattering due to a monochromatic plane-wave impinging on an uniform impedance sphere. The single secondary source can be placed either at $\theta = \pi$ or $\theta = 0$.

5.1.1 Effects of minimizing the scattered sound power with one or two surface radiators

Taking the modal frequency weightings $\tilde{\mathcal{W}}_n^{(pw)}$ of the coefficients corresponding to the scattering of the plane-wave, i.e. expression (4.6), and the weightings $\tilde{\mathcal{W}}_n^{(pm)}$ corresponding to the source coupling of a point-monopole radiating on the surface of the sphere, i.e. expression (4.21), the theory outlined in subsection 2.4.2 is now used to calculate the effect of minimizing scattered sound power due to a plane-wave with point-monopole secondary sources. The optimal source strength $\tilde{q}_{opt}^{(1)}$ required to achieve this with one point-monopole is computed from expression (2.53) and plotted in Figure 5-2 when normalized by a factor of $4\pi a^2 \tilde{\mathcal{P}}_i/(\rho_0 c_0)$. Furthermore, in Figure 5-3, the normalized scattered sound power versus normalized frequency ka is computed before and after power minimization with secondary sources in the arrangements described in Figure 5-1. The results from Figure 5-2 and Figure 5-3 are realized for the soft $\tilde{\zeta} = 0.01$, radially-matched $\tilde{\zeta} = 1$, and hard $\tilde{\zeta} = 100$ spheres. $N = 100$ terms were calculated in MATLAB in the spherical harmonic series of the scattered sound power and in the power after minimization.

Using the strategy described in [78], the low frequency behaviour after power minimization can be analysed based on the low frequency behaviour of the modal frequency weightings $\widetilde{\mathcal{W}}_n^{(pw)}$ and $\widetilde{\mathcal{W}}_n^{(pm)}$. As seen in Figure 4-2, at low ka, the primary (scattering due to the plane-wave) is dominated by the $n = 0$ spherical harmonic component for the soft and radially-matched spheres, and by both the $n = 0$ and $n = 1$ spherical harmonic components for the rigid sphere. Also, as shown in Figure 4-5, at low ka, the secondary (single point-monopole) is dominated by the $n = 0$ spherical harmonic component for all three cases of impedance sphere. For these circumstances, assuming that the power minimization described in subsection 2.4.2 cancels the leading order term

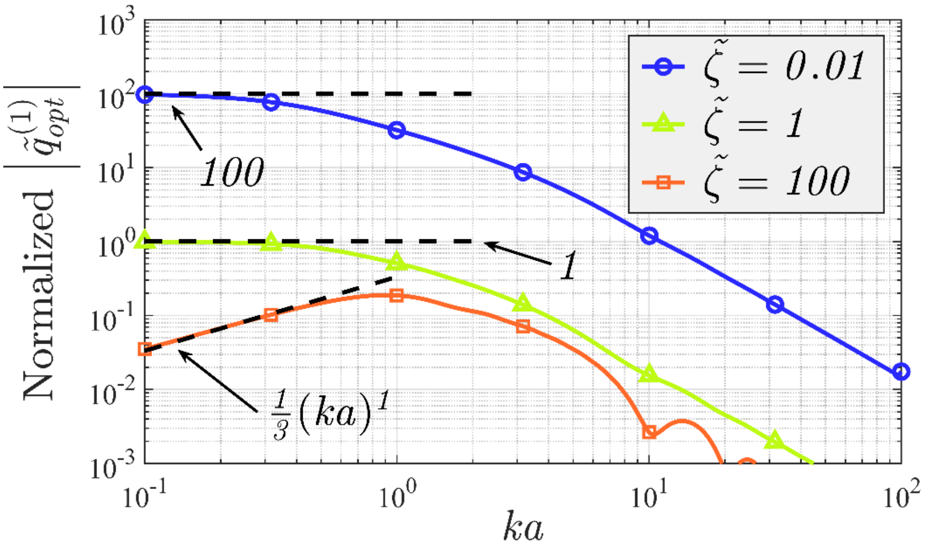

Figure 5-2 The optimal source strength $\tilde{q}_{opt}^{(1)}$, normalized by $4\pi a^2 \tilde{\mathcal{P}}_i/(\rho_0 c_0)$, for one secondary point-monopole at either $\theta = \pi$ or $\theta = \pi$ when minimizing the scattered power due to a plane-wave incidence on the soft, radially-matched, and hard spheres.

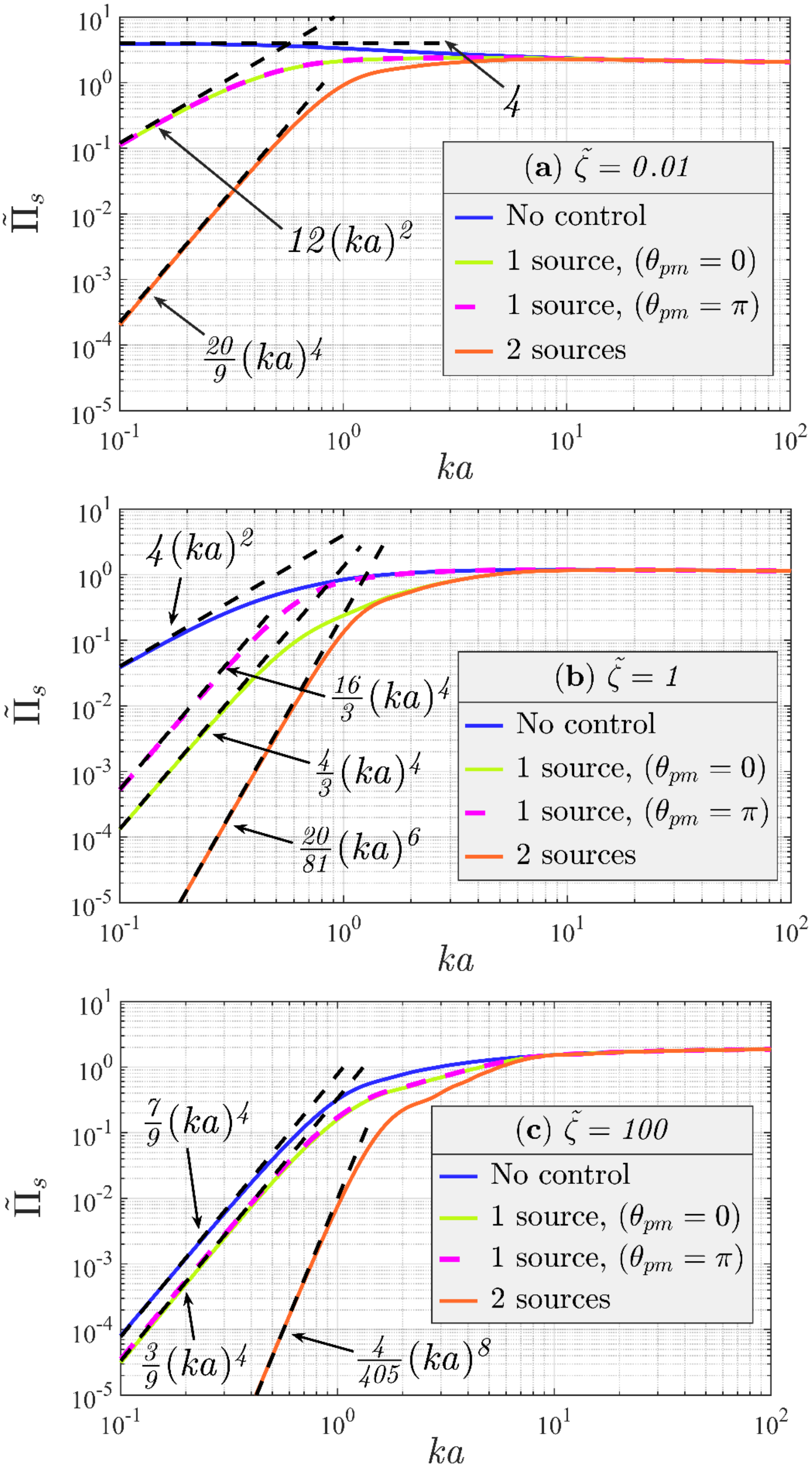

Figure 5-3 The normalized scattered sound power as a function of ka for the soft $\tilde{\zeta} = 0.01$ (a), radially-matched $\tilde{\zeta} = 1$ (b), and hard $\tilde{\zeta} = 100$ (c) spheres, with no active control and with active control using 1 or 2 secondary sources, as shown in Figure 5-1.

of the dominant $n = 0$ component in the primary, then, the optimal source strength must be

$$\tilde{q}_{opt}^{(1)} \frac{\rho_0 c_0}{4\pi \, \tilde{\mathcal{P}}_i \, a^2} = \frac{\widetilde{\mathcal{W}}_0^{(pw)}(\tilde{\zeta}, ka)}{\widetilde{\mathcal{W}}_0^{(pm)}(a, \tilde{\zeta}, ka)} \;, \qquad (5.1)$$

which leaves the residual $n = 1$ component as most dominant after control, while the hierarchy with order n of the frequency weightings in the primary is maintained for $n \geq 2$. The frequency weighting of the residual $n = 1$ component is then given by

$$\widetilde{\mathcal{W}}_1^{(c)}(\tilde{\zeta}, ka) = i\widetilde{\mathcal{W}}_1^{(pw)}(\tilde{\zeta}, ka) \mp \frac{\widetilde{\mathcal{W}}_1^{(pm)}(a, \tilde{\zeta}, ka)}{\widetilde{\mathcal{W}}_0^{(pm)}(a, \tilde{\zeta}, ka)} \, \widetilde{\mathcal{W}}_0^{(pw)}(\tilde{\zeta}, ka) \;, \qquad (5.2)$$

where the minus sign corresponds to the secondary source in the $\theta = \pi$ position, and the plus sign corresponds to the secondary source in the $\theta = 0$ position.

Using the values in Table 4-2 and Table 4-5, the normalized optimal source strengths from (5.1) are equal to $-i(ka)^3/3$, 1 and 100 for the $\tilde{\zeta} = 100$, $\tilde{\zeta} = 1$ and $\tilde{\zeta} = 0.01$ spheres, respectively. These values are the same when changing the position of the secondary source between $\theta = \pi$ and $\theta = 0$, as this does not alter the $n = 0$ component. In (5.2), the first term, which corresponds to the primary, has a lower leading power of (ka) than the second term for the rigid sphere, leading to a residual $n = 1$ component that remains mostly unaffected at low ka after power minimization, i.e. $\widetilde{\mathcal{W}}_1^{(c)}(100, ka) = -i(ka)^3/6$, regardless of point-monopole placement. For the soft sphere, the second term in (5.2), which corresponds to the optimized secondary, has a lower leading power of (ka), such that the frequency weighting of the residual $n = 1$ component is $\widetilde{\mathcal{W}}_1^{(c)}(0.01, ka) = \mp i(ka)^2$ after power minimization, where '$\mp$' corresponds to $\theta = \pi$ and $\theta = 0$, respectively. For the radially-matched sphere, both terms in (5.2) have the same leading power of (ka), such that $\widetilde{\mathcal{W}}_1^{(c)}(1, ka)$ is equal to $-2(ka)^3/3$ when the source is positioned at $\theta = \pi$, and is equal to $-(ka)^3/3$ when the source is positioned at $\theta = 0$. The calculated frequency weightings after control predict the normalized scattered sound powers after control being equal to $12(ka)^2$ for the soft sphere, $3(ka)^4/9$ for the hard sphere, $16(ka)^4/3$ for the radially-matched sphere with the source placed at $\theta = \pi$, and $4(ka)^4/3$ for the radially-matched sphere with the source placed at $\theta = 0$.

The low ka behaviours described above for the normalized optimal source strengths and for the normalized scattered sound power after control match the computed results from Figure 5-2 and Figure 5-3, thus confirming the initially assumed outcome of the power minimization. Furthermore, it can be observed from Figure 5-3 that, overall, the smallest reduction after control is obtained for the rigid sphere, and the greatest reduction is obtained for the radially-matched sphere when the source is in the $\theta = 0$ position. The lesser suppression when the source is in the $\theta = 0$ position on the radially-matched sphere may be a result of the power minimization negatively interfering with the passive scattering suppression properties of this impedance sphere in the hemisphere corresponding to the direction of incidence ($\theta = \pi$), which can be observed in Figure 4-3.

At low ka, the respectively obtained benefits after control require the highest magnitude of optimized source strength for the soft sphere, followed by the radially-matched one, and then the rigid one. The strengths of the first two spheres in the enumeration differ by a factor of 100, which makes actively controlling the case of the soft sphere with one secondary source highly unpractical.

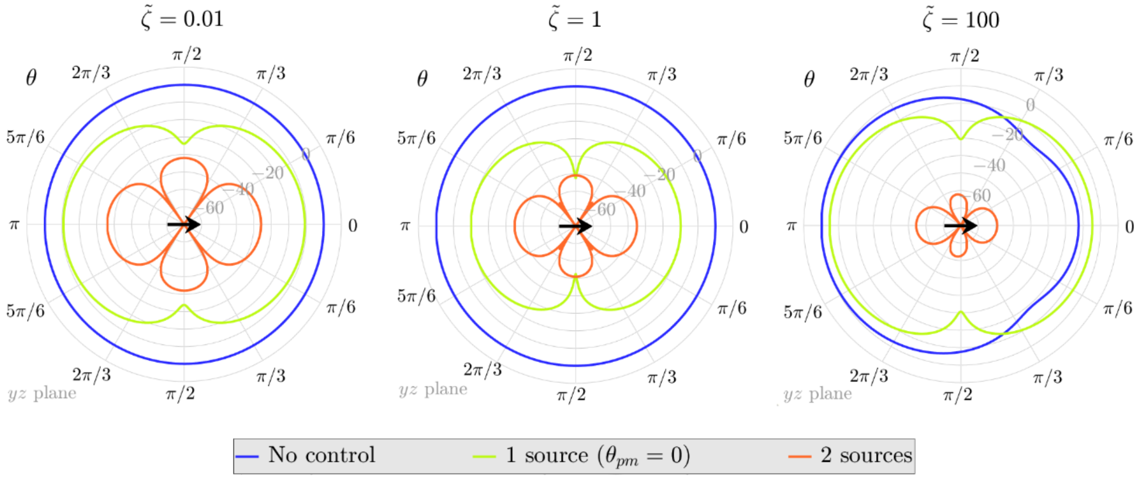

Figure 5-4 The directivity of the scattered field for the soft, radially-matched and hard spheres at a normalized frequency of $ka = 0.1$ with no control (blue solid) and after active control using one point-monopole placed at $\theta = 0$ (green dashed) or two point-monopoles (orange dotted-dashed) secondary sources. The backscattered pressure ($\theta = \pi$) before control has been taken as the 0 dB reference in each case.

The observed effects at low frequencies of the power minimization on the global measure of scattered sound power are also echoed in the behaviour of a regional quantity such as the far-field directivity of the scattered pressure, expressed as (2.28). This is exemplified in Figure 5-4 at normalized frequency of $ka = 0.1$, for the three cases of studied impedance spheres. This shows that the far-field directivity of the scattered pressures becomes a figure-of-eight shape after control for all three cases of impedance, which corresponds to the $(n, m) = (1,0)$ spherical harmonic, i.e.

the dominant component after control. At $\theta = \pm\pi/2$, the differences in the amount of attenuation between the different impedance cases result from numerical limitations, i.e. evaluating the frequency range at a discrete set of values. The backscattering ($\theta = \pi$) is more significantly reduced for the radially-matched sphere than for either the soft or hard spheres, which partially reflects the greater level of reduction in the scattered power for the radially-matched sphere with one secondary source located at $\theta = 0$.

As ka increases, more and more spherical harmonic components contribute simultaneously in the series representations of the primary and secondary, hence ‘least means squares’ optimisation based on a single control parameter has less and less of an effect while the magnitude of $\tilde{q}_{opt}^{(1)}$ becomes smaller and smaller (see Figure 5-2). This leads to relatively insignificant differences between the normalized scattered sound power before and after control (see Figure 5-3), and between primary and controlled far-field directivity of the scattered pressure, especially in the shadow regions, as can be observed in the upcoming results of Figure 5-5 and Figure 5-6 in the following subsection about regional active control.

Now, two secondary sources placed as depicted in Figure 5-1 are used and their optimal strengths are computed using expression (2.53). A similar analysis as the one for a single source can be employed to interpret the low frequency behaviour. For all three studied impedance spheres, the two most dominant spherical harmonic components at low ka are $n = 0$ and $n = 1$, so, it is assumed that the action of the two point-monopoles in minimizing the scattered power is to cancel the leading order powers of (ka) in these two components. In this case, the sum of the two optimal source strengths is the same as the result in (5.1) and is proportional to both the $n = 0$ spherical harmonic component after control, which is suppressed, and the $n = 2$ harmonic term after control, which becomes the most dominant residual component. The difference of the two optimal source strengths is proportional to the $n = 1$ spherical harmonic component after control, which is also suppressed. The frequency weighting of the $n = 2$ spherical harmonic component, after suppression of the $n = 0$ and $n = 1$ components, can then be written as

$$\widetilde{\mathcal{W}}_2^{(c)}\big(\tilde{\zeta}, ka\big) = \widetilde{\mathcal{W}}_2^{(pw)}\big(\tilde{\zeta}, ka\big) + \frac{\widetilde{\mathcal{W}}_2^{(pm)}\big(a, \tilde{\zeta}, ka\big)}{\widetilde{\mathcal{W}}_0^{(pm)}\big(a, \tilde{\zeta}, ka\big)}\, \widetilde{\mathcal{W}}_0^{(pw)}\big(\tilde{\zeta}, ka\big), \tag{5.3}$$

When using the values from Table 4-2 and Table 4-5 in (5.3), the frequency weightings of the dominant $n = 2$ component after power minimization are $\widetilde{\mathcal{W}}_2^{(c)}(100, ka) = -i(ka)^5/45$ for the hard sphere, $\widetilde{\mathcal{W}}_2^{(c)}(1, ka) = (ka)^4/9$ for the radially-matched sphere, $\widetilde{\mathcal{W}}_2^{(c)}(0.01, ka) = -i(ka)^3/3$ and for the soft sphere. For the first of the three, both terms in (5.3) have the same leading order term of (ka) and contribute to the final value. For the second, the initial term in (5.3), which corresponds to the primary, has a lower leading order power of (ka), which translates in the primary $n = 2$ component not being affected by the power minimization. For the third, the term at the end in (5.3), which corresponds to the optimized secondary, has a lower leading order power of (ka) and dominates the final value. The hierarchy based on orders is maintained for $n \geq 3$ after control. The calculated frequency weightings after control predict the normalized scattered sound powers after control being equal to $4(ka)^8/405$ for the hard sphere, $20(ka)^6/81$ for the radially-matched sphere, and $20(ka)^4/9$ for the soft sphere.

The low ka behaviours described above for the normalized scattered sound power after control match the computed results from Figure 5-3, thus confirming the initially assumed outcome of the power minimization. Furthermore, it can be observed from Figure 5-3 that, overall, significant amounts of attenuation are obtained with two secondary point-monopoles for all three cases of impedance sphere, especially for the rigid sphere, where addressing both dominant $n = 0$ and $n = 1$ spherical harmonic components drastically improves performance. The effects of the power minimization with two sources on a regional quantity such as the far-field directivity of the scattered pressure can be observed in Figure 5-4, and echo the effects on the global measure of scattered sound power. For all three cases of impedance sphere, the directivity after control significantly reduced for all angles, especially for the rigid sphere, and dominated by the directivity of the residual $n = 2$ spherical harmonic component, which is similar to that of a longitudinal quadrupole.

5.1.2 Effects of cancelling the far-field backscattered pressure with one surface radiator

In the previous subsection, the effects of minimizing a global measure such as scattered sound power have been investigated with a single secondary point-monopoles on the surface of the impedance sphere. In this subsection, the investigation is concerned with the complete cancellation of the normalized far-field scattered pressure directivity, $\widetilde{\Theta}_s$, in the backscattering direction $\theta = \pi$, which is outlined in subsection 2.4.3. The regional and global effects of this regional control method are computed in MATLAB using up to $N = 438$ terms in the spherical harmonic series for the far-field directivity, and $N = 100$ in the spherical harmonic series for the scattered sound power. This is done to accurately represent the frequency range used in the upcoming figures of results.

For a target cancellation direction around the sphere, the optimal source strength $\tilde{q}_{opt}$ is given by expression (2.59), where the coefficients of the primary belong to the scattered pressure due to the plane-wave, and the coupling coefficients of the secondary belong to the point-monopole source on the sphere. The optimal choice for this parameter can be explained with the plots in the first row of Figure 5-5, which show the normalized far-field pressure directivities of the primary and un-optimized secondary of the hard sphere as a function of angle θ around the sphere for three different frequencies. If direction $\theta = \pi$ is to be perfectly cancelled, then both olive and orange lines must be scaled up to reach the value of the blue line at all three frequencies. Depending on the frequency, some regions of angle θ on the olive and orange lines become larger in magnitude than the blue line, i.e. the primary is enhanced rather than suppressed.

Analytical predictions at low ka of the optimal source strength for backscattering ($\theta = \pi$) cancellation require a different tactic than that used for the predictions used in the previous subsection. The asymptotes of $n = 0$ and $n = 1$ components in both numerator and denominator of (2.59) must be considered. This leads to $\tilde{q}_{opt}$, normalized by a factor of $4\pi a^2 \tilde{\mathcal{P}}_i/(\rho_0 c_0)$, being equal to $5i(ka)^3/6$ for the $\tilde{\zeta} = 100$ sphere in both single source positions, to $1 - 2ika$ for the $\tilde{\zeta} = 1$ sphere when $\theta_{pm} = \pi$, to $1 + ika$ for the $\tilde{\zeta} = 1$ sphere when $\theta_{pm} = 0$, to $100(1 - 3ika)$ for the $\tilde{\zeta} = 0.01$ sphere when $\theta_{pm} = \pi$, and to $100(1 + 3ika)$ for the $\tilde{\zeta} = 0.01$ sphere when $\theta_{pm} = 0$. The magnitudes of these values are consistent with the results illustrated in the second row of Figure 5-5 and are approximately the same as those for power minimization. However, the variations of the optimal source strengths associated with the $\tilde{\zeta} = 1$ and $\tilde{\zeta} = 0.01$ spheres are equal to the sum of two powers of (ka), where the term of a larger power contributes very little to the magnitude but significantly to the phase. This translates in the $n = 0$ spherical harmonic component not being perfectly cancelled as for the power minimization. For all three impedances, given the two source positions, both $n = 0$ and $n = 1$ components contribute to the pressure directivity $\widetilde{\Theta}_s$ after backscattering cancellation. Using the values from Table 4-2 and Table 4-5,when $\tilde{\zeta} = 100$, the $n = 0$ and $n = 1$ components after control are a pure imaginary value and a real value, respectively. When $\tilde{\zeta} = 1$ or $\tilde{\zeta} = 0.01$, the term of lower power of (ka) in the optimal source strength combines with the coupling factors of the secondary such that the term due to the primary is cancelled in the $n = 0$ component and is dominant in the $n = 1$ one, after control. The aftermath is thus the $n = 0$ component being dictated by the product between the higher power of (ka) in the optimal source strength and the corresponding coupling factor of the secondary, resulting in a pure imaginary value for the $\tilde{\zeta} = 1$ sphere and a real value for the $\tilde{\zeta} = 0.01$ sphere. Furthermore, the $n = 1$ component is now dictated by the product between the lower power of (ka) in the optimal source strength and the corresponding coupling factor of the secondary, which leads to a real value for the $\tilde{\zeta} = 1$ sphere and a pure imaginary value for the $\tilde{\zeta} = 0.01$ sphere.

The behaviours described above generate normalized scattered sound power after control that varies as $4(ka)^4/3$ and $45(ka)^2$ for the $\tilde{\zeta} = 100$ and, respectively, $\tilde{\zeta} = 0.01$ spheres, regardless of source position. For the $\tilde{\zeta} = 1$ sphere, a source at $\theta_{pm} = 0$ leads to a variation of $16(ka)^4/3$, while a source at $\theta_{pm} = \pi$ leads to a variation of $64(ka)^4/3$. Thus, for all three spheres, backscattering cancellation is less beneficial at suppressing the scattered power compared to direct minimization using the same secondary source position. In the case of the $\tilde{\zeta} = 100$ sphere, the scattered power is even slightly enhanced after backscattering cancellation (see third row of Figure 5-5), while in the case of the $\tilde{\zeta} = 1$ sphere using a source in the same direction as the backscattering is, interestingly, more detrimental to suppressing the power than when using the opposite direction. The behaviours described in this paragraph are echoed in Figure 5-6 and Figure 5-7, where the magnitude of the normalized far-field pressure directivity after control is larger over the half-space opposite $\theta = \pi$ while being attenuated in a region around direction $\theta = \pi$.

At large values of ka, when $\theta_{pm} = \pi$, the half-space corresponding to the backscattering direction is favourably discriminated against by the secondary source (see first row of Figure 5-5). The backscattering cancellation in this position enhances the scattered power by factors that are constant with ka and equal to approximately 0.25 and approx. 0.08 for the $\tilde{\zeta} = 100$ and, respectively, $\tilde{\zeta} = 0.01$ spheres. The power remains unaffected for the $\tilde{\zeta} = 1$ sphere (see third row of Figure 5-5). For all three impedance spheres, these outcomes are the result of a $\tilde{q}_{opt}$ greater in magnitude with increasing ka and greater in magnitude than the one necessary for power minimization with the same secondary source position (see second row of Figure 5-5). Furthermore, the normalized far-field scattered pressure directivity exhibits a wide region of attenuation around direction $\theta = \pi$ and almost no change in the region around the opposite direction (see Figure 5-6).

When $\theta_{pm} = 0$, the shape of the orange line seen in the first row of Figure 5-5 has to be scaled up until its relatively small value at $\theta = \pi$ is matched to that of the primary. Because of this, scattered power after control is enhanced more and more as ka increases. The outcome is most detrimental for suppressing scattered power for the $\tilde{\zeta} = 0.01$ sphere, then for the $\tilde{\zeta} = 100$ one, and then for the $\tilde{\zeta} = 1$ one (see third row of Figure 5-5). At $ka = 100$, the enhancements are, respectively, by factors of approx. $4 \cdot 10^7$, approx. 21 and approx. 10. This sequence of values does not correspond to the one describing which sphere has the largest difference in magnitude of the optimized secondary directivity between directions $\theta = \pi$ and $\theta = 0$. This other order is the $\tilde{\zeta} = 0.01$ sphere having the largest difference, followed by the $\tilde{\zeta} = 1$ one and then the $\tilde{\zeta} = 100$ one. Achieving backscattering cancellation of the far-field scattered directivity when $\theta_{pm} = 0$ requires an optimal source strength than is greater in magnitude with increasing ka and much greater in magnitude than any optimized strength from the other studied control scenarios. The far-field scattered directivity after control exhibits a narrow region of attenuation around direction $\theta = \pi$ and large enhancement in many of the other directions, particularly in the half-plane corresponding to $\theta = 0$ (see Figure 5-7). In the shadow direction ($\theta = 0$), the magnitude of far-field scattered directivity after control does not change for the $\tilde{\zeta} = 100$ and $\tilde{\zeta} = 1$ spheres after control while it does significantly for the $\tilde{\zeta} = 0.01$ sphere.

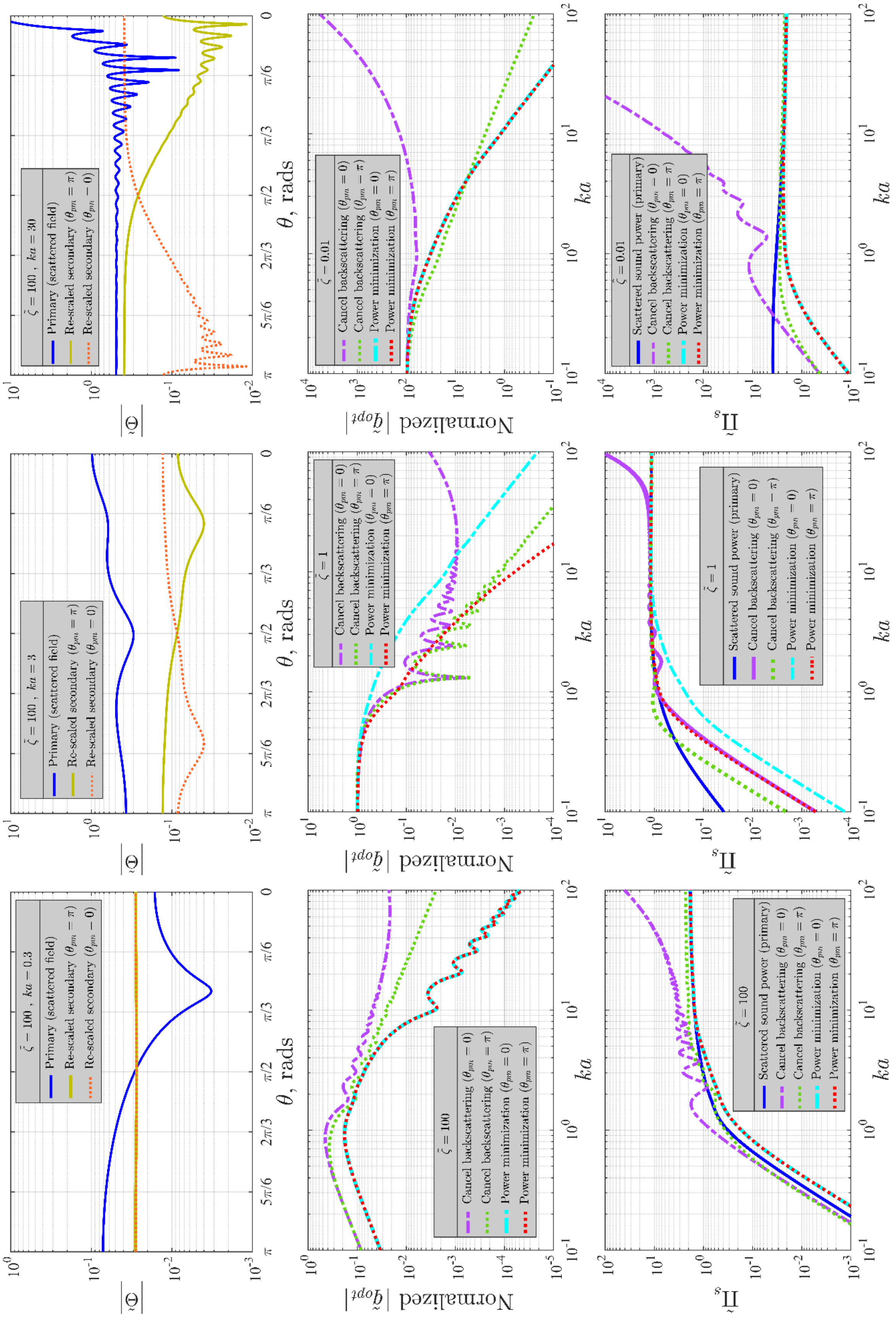

Figure 5-5 Normalized far-field directivity of primary and secondary pressures (first row), magnitude of optimal source strength vs ka (second row), normalized scattered sound power vs ka (third row), for power minimization and backscattering cancellation.

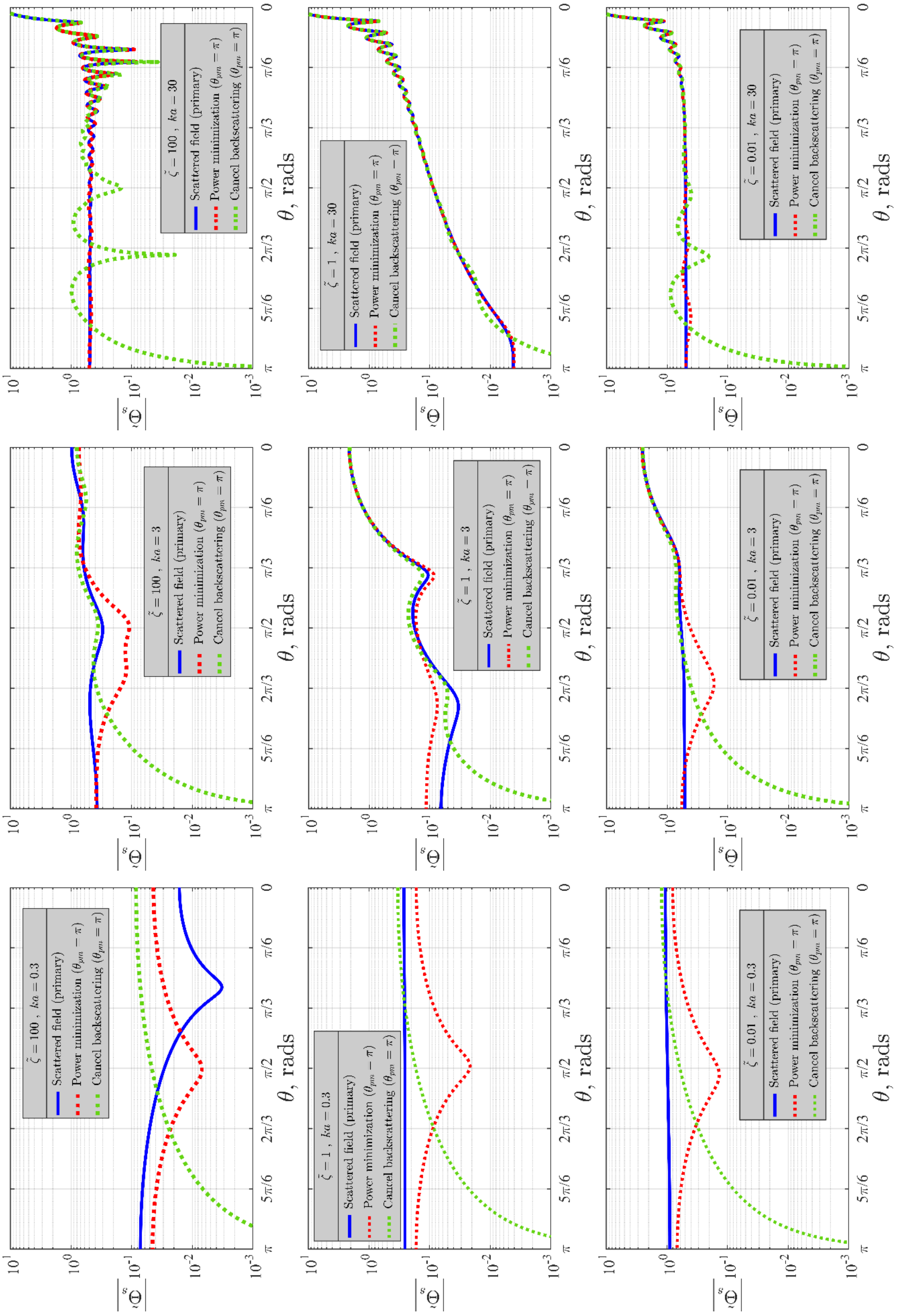

Figure 5-6 Normalized directivity of far-field pressure versus angle θ around the sphere, for primary, controlled after power minimization, and controlled after backscattering cancellation (secondary source at $\theta_{pm} = \pi$), at three different frequencies.

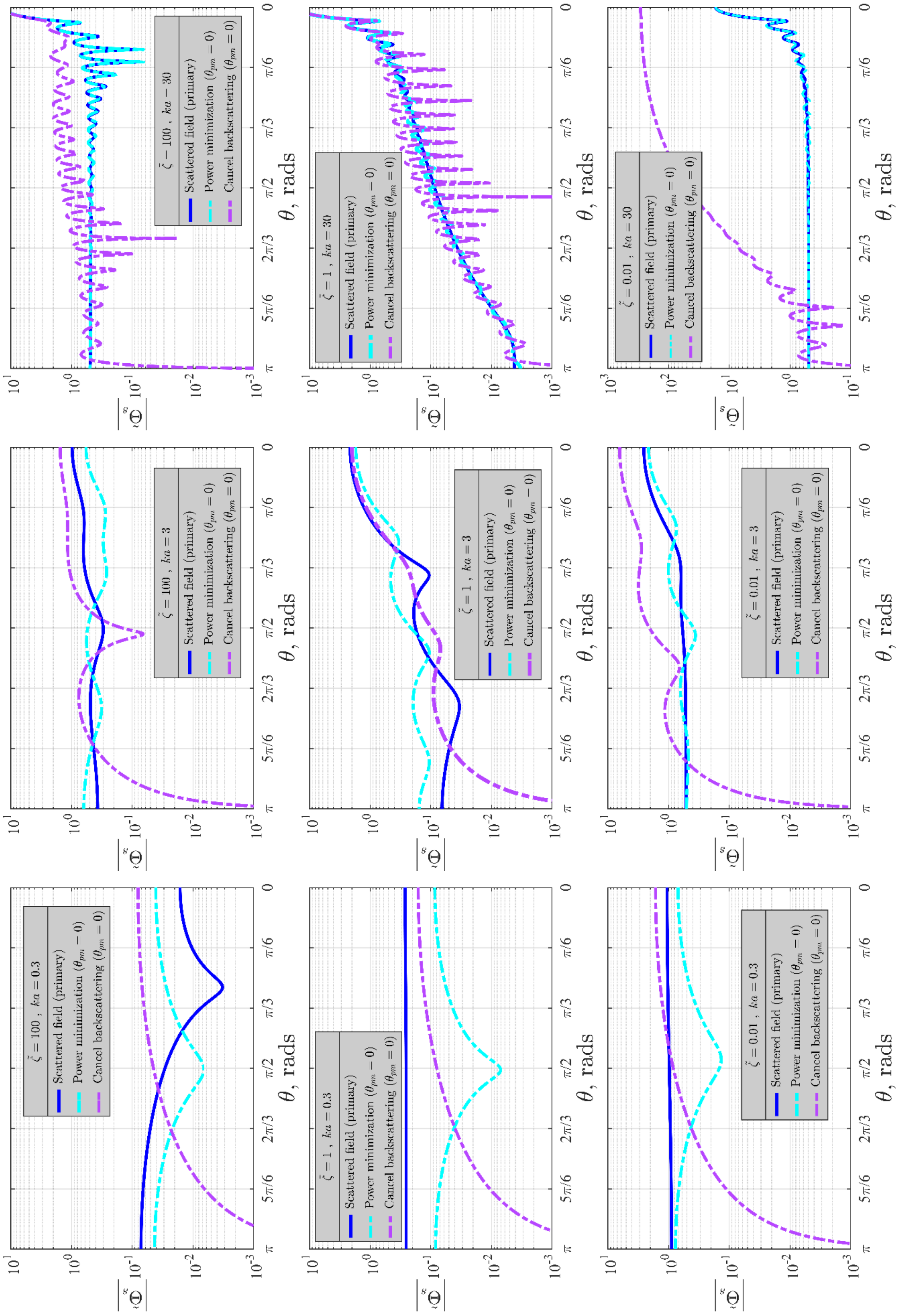

Figure 5-7 Normalized directivity of far-field pressure versus angle θ around the sphere, for primary, controlled after power minimization, and controlled after backscattering cancellation (secondary source at $\theta_{pm} = 0$), at three different frequencies.

5.1.3 Effects of cancelling the far-field pressure in the shadow with one surface radiator

This subsection now considers the same study as in the previous subsection, but for cancelling the shadow direction $\theta = 0$. The same computational strategies are used to obtain the same sets of results contained in the upcoming figures.

At small values of ka, the same procedure used to predict the behaviour due to backscattering cancellation can be employed when cancelling the normalized far-field scattered pressure directivity, $\widetilde{\Theta}_s$, shadow instead. This leads to q_{opt}, normalized by a factor of $4\pi a^2 \tilde{\mathcal{P}}_i/(\rho_0 c_0)$, being equal to $5i(ka)^3/6$ for the $\tilde{\zeta} = 100$ sphere in both source positions, to $1 + 2ika$ for the $\tilde{\zeta} = 1$ sphere when $\theta_{pm} = \pi$, to $1 - ika$ for the $\tilde{\zeta} = 1$ sphere when $\theta_{pm} = 0$, to $100(1 + 3ika)$ for the $\tilde{\zeta} = 0.01$ sphere when $\theta_{pm} = \pi$, and to $100(1 - 3ika)$ for the $\tilde{\zeta} = 0.01$ sphere when $\theta_{pm} = 0$. It can be observed that the optimal source strengths are the same as for backscattering cancellation but, for the $\tilde{\zeta} = 1$ and $\tilde{\zeta} = 0.01$ spheres, values have a sign swapped in the term of higher power of (ka) between the two source positions. The magnitudes of all predicted values of optimal strengths are consistent with the results illustrated in the second row of Figure 5-8 and are approximately the same as those for power minimization. As before, the variations of the optimal source strengths associated with the $\tilde{\zeta} = 1$ and $\tilde{\zeta} = 0.01$ spheres are equal to the sum of two powers of (ka), where the term of a larger power contributes very little to the magnitude but significantly to the phase. This translates in the $n = 0$ spherical harmonic component not being perfectly cancelled as for the power minimization. For all three impedances, both $n = 0$ and $n = 1$ components contribute to the pressure directivity, $\widetilde{\Theta}_s$, after shadow cancellation. The change of sign due to source position which is found in the optimal source strengths of the shadow cancellation does not change the characteristics previously encountered for the backscattering cancellation, which are the same for the shadow cancellation. Therefore, the $n = 0$ and $n = 1$ components after control are still: pure imaginary and, respectively, real when $\tilde{\zeta} = 100$, pure imaginary and, respectively, real when $\tilde{\zeta} = 1$, and real and, respectively, pure imaginary when $\tilde{\zeta} = 0.01$.

The behaviours described above generate a scattered sound power after control that varies as $4(ka)^4/3$ and $45(ka)^2$ for the $\tilde{\zeta} = 100$ and, respectively, $\tilde{\zeta} = 0.01$ spheres, regardless of source position. For the $\tilde{\zeta} = 1$ sphere, a source at $\theta_{pm} = 0$ leads to a variation of $16(ka)^4/3$, while a source at $\theta_{pm} = \pi$ leads to a variation of $64(ka)^4/3$. These values are exactly the same as for backscattering cancellation because the contributing $n = 0$ and $n = 1$ components are either real and purely imaginary or vice versa, so, when taking the absolute value squared of these complex numbers to obtain the power, the sign change based on source position when cancelling the shadow does not have an effect. It can be concluded that, for all three spheres, shadow cancellation is less beneficial at suppressing the scattered power compared to direct minimization using the same secondary source position. In the case of the $\tilde{\zeta} = 100$ sphere, the scattered power is even slightly enhanced after shadow cancellation (see third row of Figure 5-8). The behaviours described in this paragraph are echoed in Figure 5-9 and Figure 5-10, where the magnitude of the normalized scattered directivity after control is larger over the half-space corresponding to $\theta = \pi$ while being attenuated in a region around direction $\theta = 0$.

At large values of ka, when $\theta_{pm} = \pi$, the half-space corresponding to the shadow direction is unfavourably discriminated against by the secondary source (see first row of Figure 5-8). The shape of the olive line seen in the first row of Figure 5-8 must be scaled up until its relatively small value at $\theta = 0$ is matched to that of the primary. Because of this, scattered power after control is enhanced more and more as ka increases. The outcome is most detrimental for suppressing power in the case of the $\tilde{\zeta} = 0.01$ sphere, then for the $\tilde{\zeta} = 1$ one and then for the $\tilde{\zeta} = 100$ one (see third row of Figure 5-8). The order follows which sphere exhibits the largest difference in magnitude of the optimized secondary directivity between directions $\theta = \pi$ and $\theta = 0$. At $ka = 100$, the enhancements in power are, respectively, factors of approx. $53 \cdot 10^{10}$, approx. $1.7 \cdot 10^{10}$ and approx. $2 \cdot 10^{5}$, which are significantly larger than those for cancelling backscattering with a source in the worst of the two locations. Achieving the shadow cancellation with a source at $\theta_{pm} = \pi$ requires an optimal source strength than is greater in magnitude with increasing ka and much greater in magnitude than any optimized strength from the other studied control scenarios (see second rows of Figure 5-5 and Figure 5-8). The normalized far-field scattered pressure after control exhibits a narrow region of attenuation around direction $\theta = 0$ and large enhancement in many other directions, particularly in the half-plane corresponding to $\theta = \pi$ (see Figure 5-9).

At very large ka, when $\theta_{pm} = 0$, the half-space corresponding to the shadow direction is favourably discriminated against by the secondary source; however, the far-field scattered directivity exhibits a very narrow beam around the shadow direction (see first row of Figure 5-10). In matching the far-field directivities of the primary and secondary, the primary directivity outside the shadow but in the same half-plane as the shadow gets significantly enhanced after control, which results in the effects seen in Figure 5-10. The normalized scattered directivity exhibits a narrow region of attenuation around direction $\theta = 0$ that is barely wider than the region of attention obtained with a secondary source in the other position when cancelling the shadow. At all other angles, the normalized scattered directivity after control is enhanced, more so closer to the shadow direction than the backscattering direction. In the backscattering direction, the enhancement is greatest for the $\tilde{\zeta} = 1$ sphere, followed by the $\tilde{\zeta} = 100$ sphere and then by the $\tilde{\zeta} = 0.01$ sphere, which suffers no enhancement. Surprisingly, this sequence does not correspond to the one describing which sphere has the largest difference in magnitude of the optimized secondary directivity between directions $\theta = \pi$ and $\theta = 0$. In this new case, the order is the $\tilde{\zeta} = 0.01$ sphere having the largest difference, followed by the $\tilde{\zeta} = 1$ one and then the $\tilde{\zeta} = 100$ one. The behaviours described in this paragraph lead to the scattered sound power after control being enhanced more and more as ka increases even though the position of the secondary source matches the direction of cancellation (see third row of Figure 5-8). At $ka = 100$, the enhancements in power are, respectively, factors of approx. 2446, approx. 2294 and approx. 913 for the $\tilde{\zeta} = 0.01$, $\tilde{\zeta} = 1$ and $\tilde{\zeta} = 100$ spheres. For the last two sphere, these values are significantly larger than those for cancelling backscattering with a source in the worst of the two locations. Achieving the shadow cancellation with a source at $\theta_{pm} = 0$ requires an optimal source strength that is relatively constant in magnitude with increasing ka and much greater in magnitude than the one required for power minimization with a source in the same position, but much lesser in magnitude than the one required for shadow cancellation with a secondary source in the location $\theta_{pm} = \pi$.

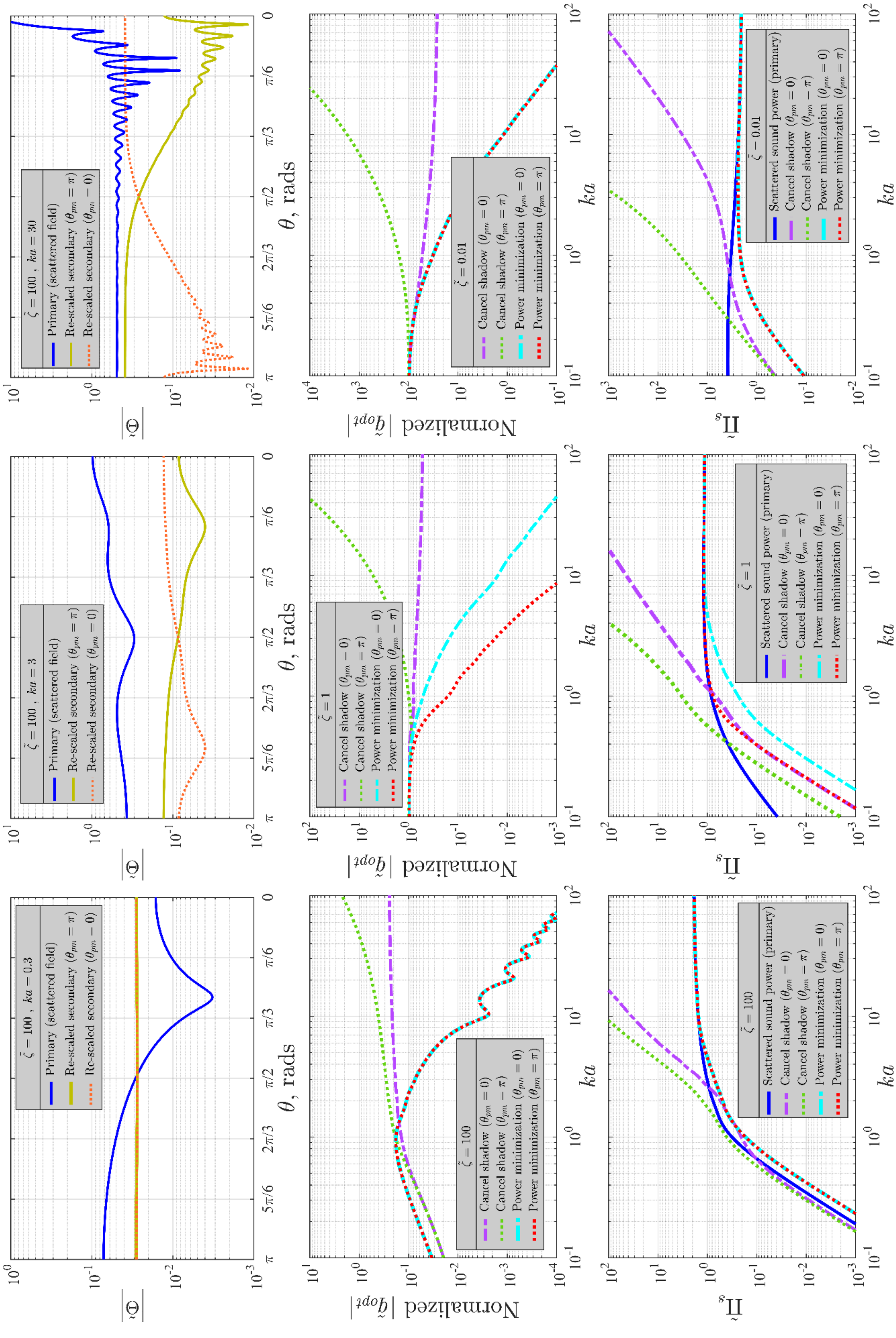

Figure 5-8 Normalized far-field directivity of primary and secondary pressures (first row), magnitude of optimal source strength versus ka (second row), normalized scattered sound power versus ka (third row), for power minimization and shadow cancellation.

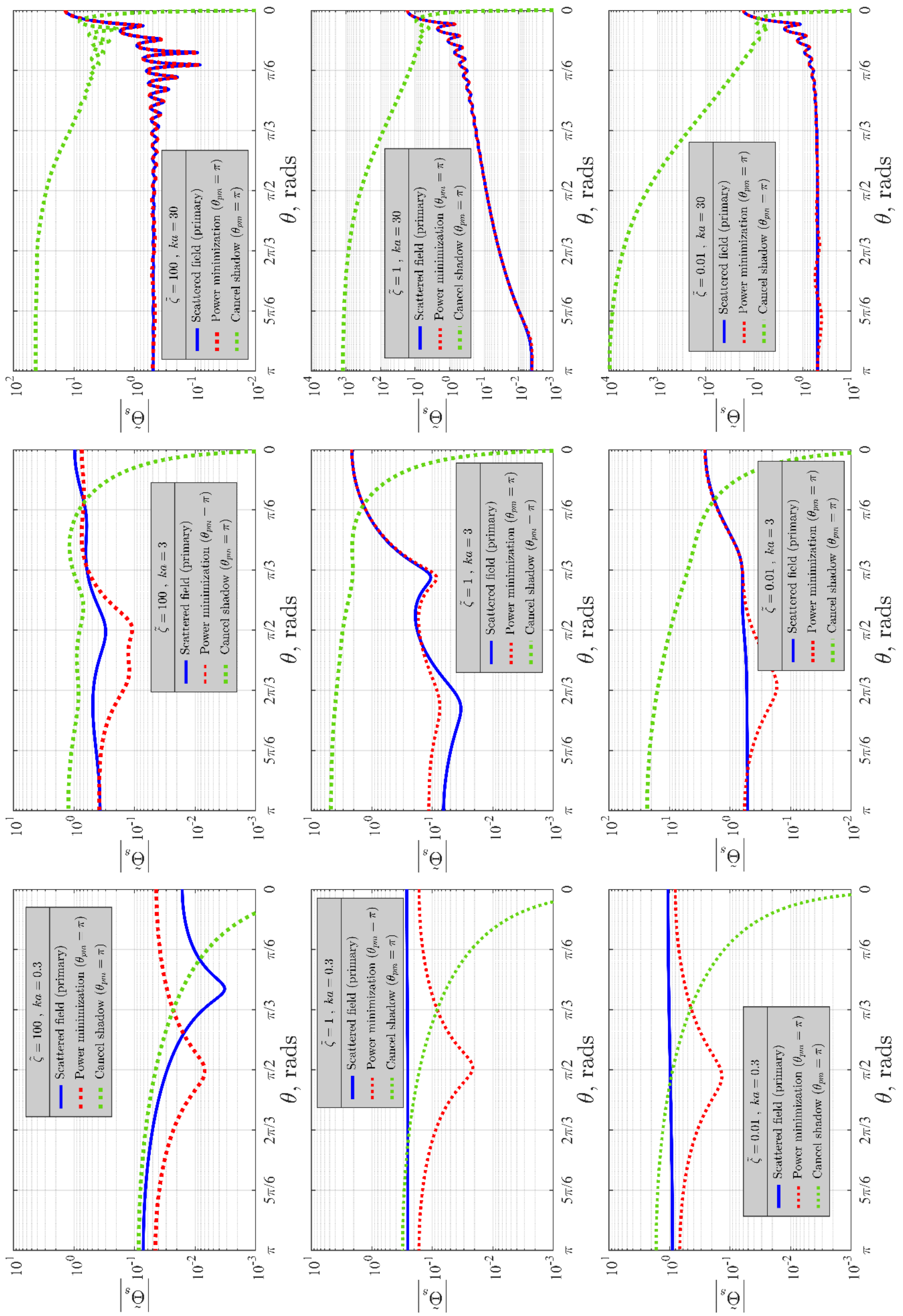

Figure 5-9 Normalized directivity of far-field pressure versus angle θ around the sphere, for primary, controlled after power minimization, and controlled after shadow cancellation (secondary source at $\theta_{pm} = \pi$), at three different frequencies.

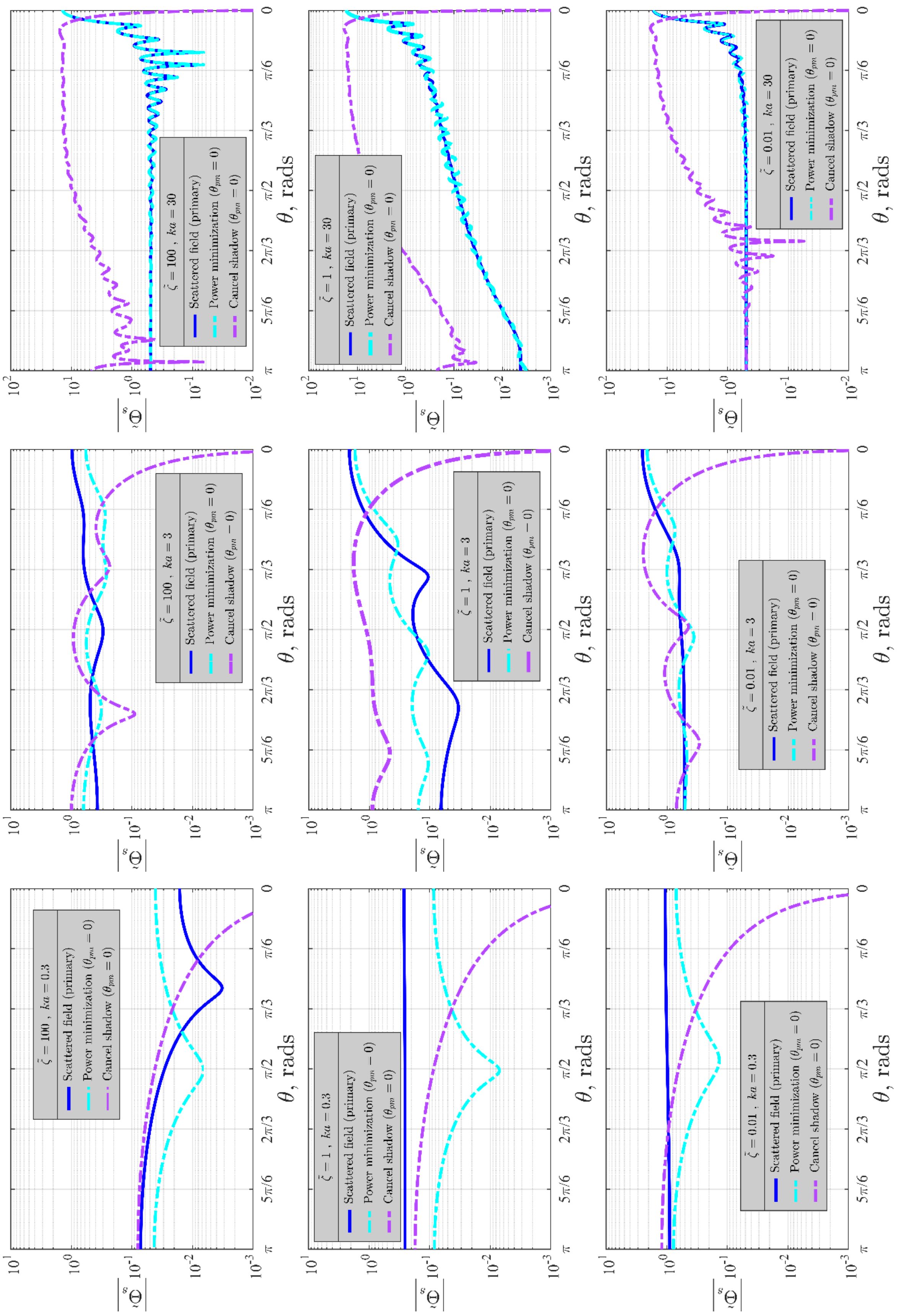

Figure 5-10 Normalized directivity of far-field pressure versus angle θ around the sphere, for primary, controlled after power minimization, and controlled after shadow cancellation (secondary source at $\theta_{pm} = 0$), at three different frequencies.

5.2 Active control with a large number of surface radiators

It is difficult to physically interpret the results if distributions of secondary sources that are not aligned along the z-axis are used, partially because the complex-valued spherical harmonics for $n = 1$ and different values of m do not correspond to dipoles aligned along the three Cartesian axes. Nevertheless, it is still interesting to use the theory described above to calculate the attenuation that can be obtained with a larger number of secondary sources. For the three types of impedance sphere previously used, Figure 5-11 shows the percentage reduction in the scattered sound power as a function of ka and the number of secondary sources, which were arranged in a sunflower pattern, depicted in Figure 5-12. This pattern divides the spherical surface into patches of equal surface area and was chosen because it leads to a uniform spread of the point-locations. In these computations, all spherical harmonic components, including ones with $m \neq 0$, were used, given the same truncation value of $N = 100$ as before. Furthermore, the matrix $\mathbf{B}^{\mathrm{H}}\mathbf{B}$ was regularized by a factor of 10^{-6} if its condition number exceeded 10^{6}, as described in equation (2.56) from subsection 2.4.2. For the rigid and radially-matched spheres, at certain higher frequencies, the scattered sound power is enhanced after control rather than suppressed, which arises due to the frequency-independent regularization strategy not being adequate at certain frequencies.

From Figure 5-11, the number of secondary sources required for a 90% attenuation, corresponding to a 10 dB reduction in scattered power, is approximately given by $(ka + 1)^2$, which is known to be the number of sources required to accurately reproduce a given sound field up to a normalized frequency of ka [61]. It can be concluded from these results that the attenuation of scattered sound power when using a large number of control sources is relatively independent of the surface impedance of the scattering sphere.

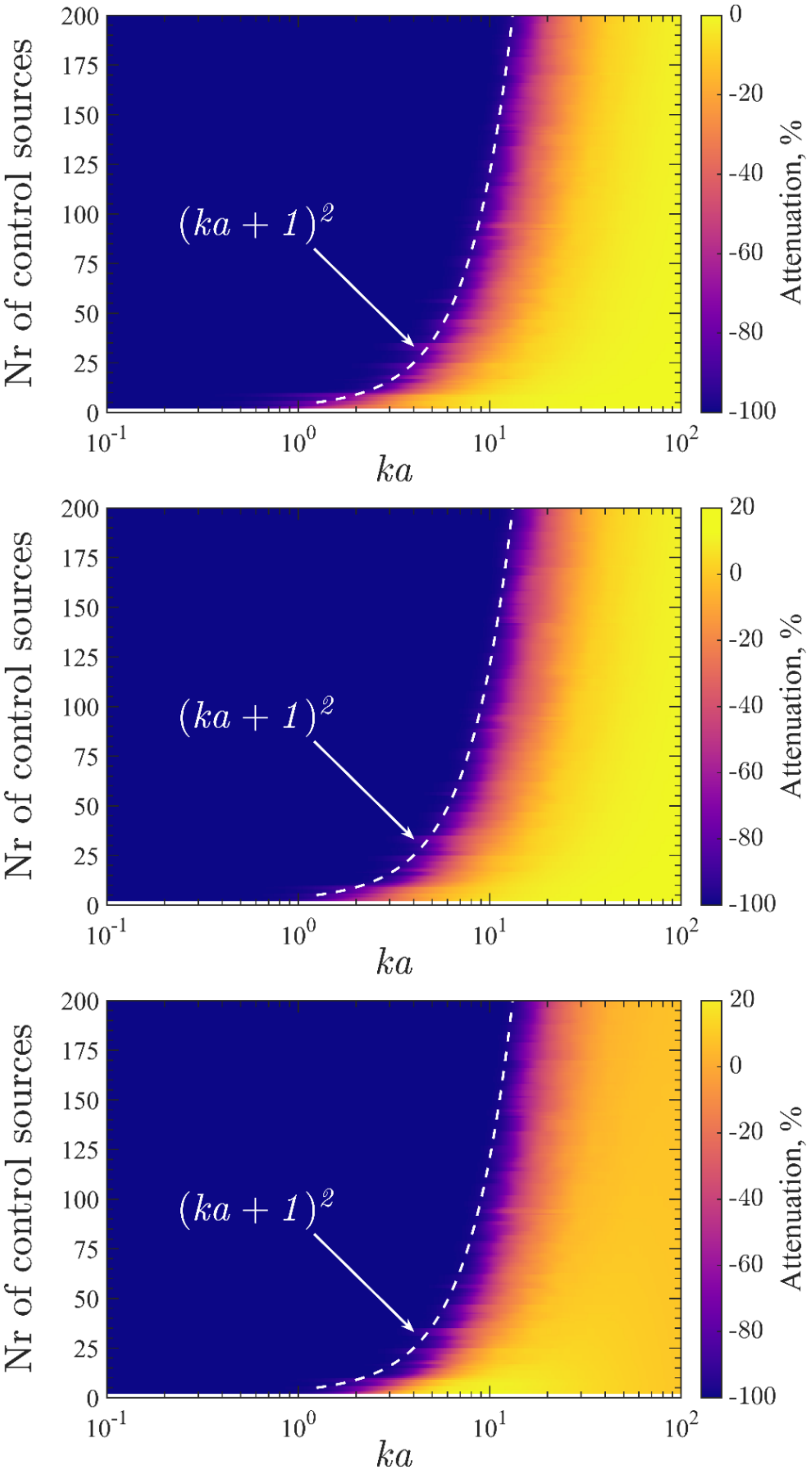

Figure 5-11 The percentage reduction in the scattered sound power for the for the soft $\tilde{\zeta} = 0.01$ (top), radially-matched $\tilde{\zeta} = 1$ (middle), and hard $\tilde{\zeta} = 100$ (bottom) spheres sphere as a function of the number of secondary source arranged in a sunflower pattern and of ka. The number of secondary sources required for a 90% attenuation, corresponding to a 10 dB reduction, is approximately given by $(ka + 1)^2$.

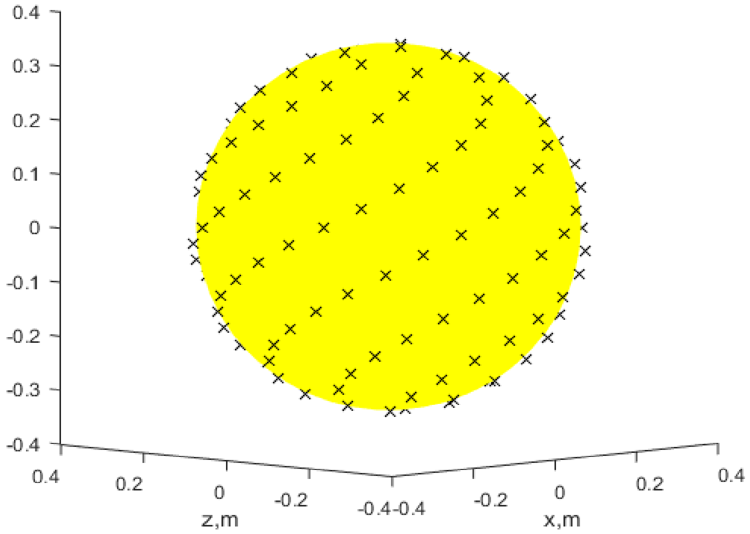

Figure 5-12 Sunflower pattern of points on the surface of a sphere, as used in [33]. Pattern spaces points such that the total surface area is split into equal patches.

5.3 Active control with a large number of radiators away from scatterer

The active control of acoustic scattering with secondary sources that are not on the surface of the sphere has been considered by a number of authors such as Vasquez et al. [30], Norris et al. [27, 28], Eggler et al. [39], and Liu et al. [29], although Cheer [33] found that for a hard sphere this was less effective than when they were positioned on the surface of the sphere. The same formulations for active control as in Chapter 2 can also be used in the case where the secondary sources are not on the surface of the sphere, except that the frequency weighting of the spherical harmonics terms of the secondary sources, $\widetilde{\mathcal{W}}_n^{(pm)}(r',\tilde{\zeta},ka)$, which dictates how the secondary couples into the primary, is given in this case by the formula

$$\widetilde{\mathcal{W}}_n^{(pm)}(r',\tilde{\zeta},ka) = (ka)^2\left[j_n(kr') - \widetilde{\mathcal{W}}_n\, h_n(kr')\right], \qquad (5.4)$$

i.e. the first expression of equation (4.9), where r' is the distance from the secondary source to the center of the sphere. Equation (5.2) reduces to equation (4.21) in the case when r' is equal to a.

The first term in Equation (5.4) can be interpreted as the direct field due to the secondary source in the absence of the scattering sphere, while the second term is due to the scattering of the sound field from the secondary source by the sphere. Figure 5-13 shows the normalized scattered sound

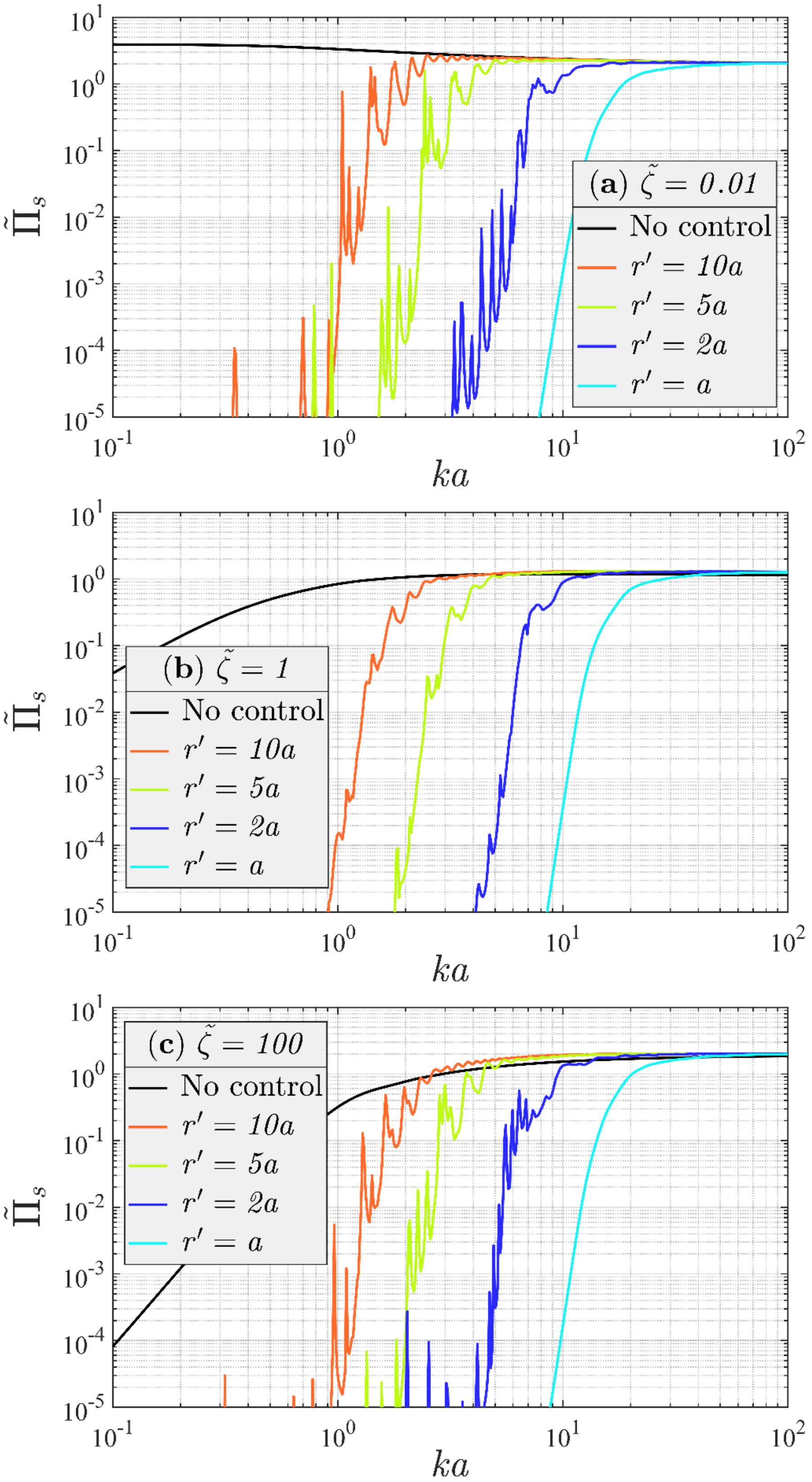

Figure 5-13 The normalized scattered power versus ka before and after control with 200 secondary sources in a sunflower pattern placed at different distances, r’, away from the the soft $\tilde{\zeta} = 0.01$ (a), radially-matched $\tilde{\zeta} = 1$ (b), and hard $\tilde{\zeta} = 100$ (c) spheres.

power after control with 200 secondary monopole sources uniformly distributed as in Figure 5-12 over a spherical surface of radius r' centered at the origin and of different impedances. This is done for increasing values of r'. In these computations, all spherical harmonic components, including the ones with $m \neq 0$, were used for the same truncation value of $N = 100$ as before. In the plot, the frequencies at which the scattered sound power is enhanced after control are not adequately addressed by the chosen frequency-independent regularization strategy, which is the same as that for the results in Figure 5-11.

Figure 5-13 illustrates that, as the secondary sources are moved away from the surface of the scattering sphere, the active control performance, at $ka = 10$ for example, is very significantly reduced. Cheer in [33] obtained the same outcome for the hard sphere through computer simulations. The results from Figure 5-13 and from [33] indicate that as the number of sources increases, the active control performance becomes less dependent on the surface impedance.

The way that the secondary source couples into the $n = 0$ spherical harmonic component at low frequencies is found to be relatively independent of its distance from the surface of the sphere, regardless of surface impedance. In contrast, the secondary source couples much more efficiently into the higher-order spherical harmonics as it is moved away from the surface of the sphere, regardless of surface impedance. This behaviour is exemplified in Figure 5-14 for the hard sphere, which shows the modal frequency weightings $\widetilde{\mathcal{W}}_n^{(pm)}(r', \tilde{\zeta}, ka)$ of the coupling coefficients belonging to the secondary point-monopole source, plotted for $n \in \{0,1,2\}$ and various radial distances r' from the center of the sphere. At low ka, these results can be understood by taking the low frequency approximation to each of the terms in equation (5.2), which for $n \geq 1$ gives

$$\lim_{ka \ll 1} \widetilde{\mathcal{W}}_n^{(pm)}(r', \tilde{\zeta}, ka) = (ka)^2 (kr')^n \, \frac{2^n n!}{(2n)!\,(n+1)} \left[1 - \frac{(2n+1)!!}{(n+1)} \left(\frac{a}{r'}\right)^{2n+1}\right]. \qquad (5.5)$$

By examining the second term in the square brackets of equation (5.5), it is clear that if $r' > a$ then this term will be small for a sufficiently large value of n, so that the first, direct field term will dominate. At low ka, and for a sufficiently large value of n, the ratio of the modal frequency weighting for a source located at $r = r'$ to the one of a source on the surface ($r' = a$), is thus

$$\lim_{ka \ll 1} \frac{\widetilde{\mathcal{W}}_n^{(pm)}(r', \tilde{\zeta}, ka)}{\widetilde{\mathcal{W}}_n^{(pm)}(a, \tilde{\zeta}, ka)} = \left(\frac{r'}{a}\right)^n . \qquad (5.6)$$

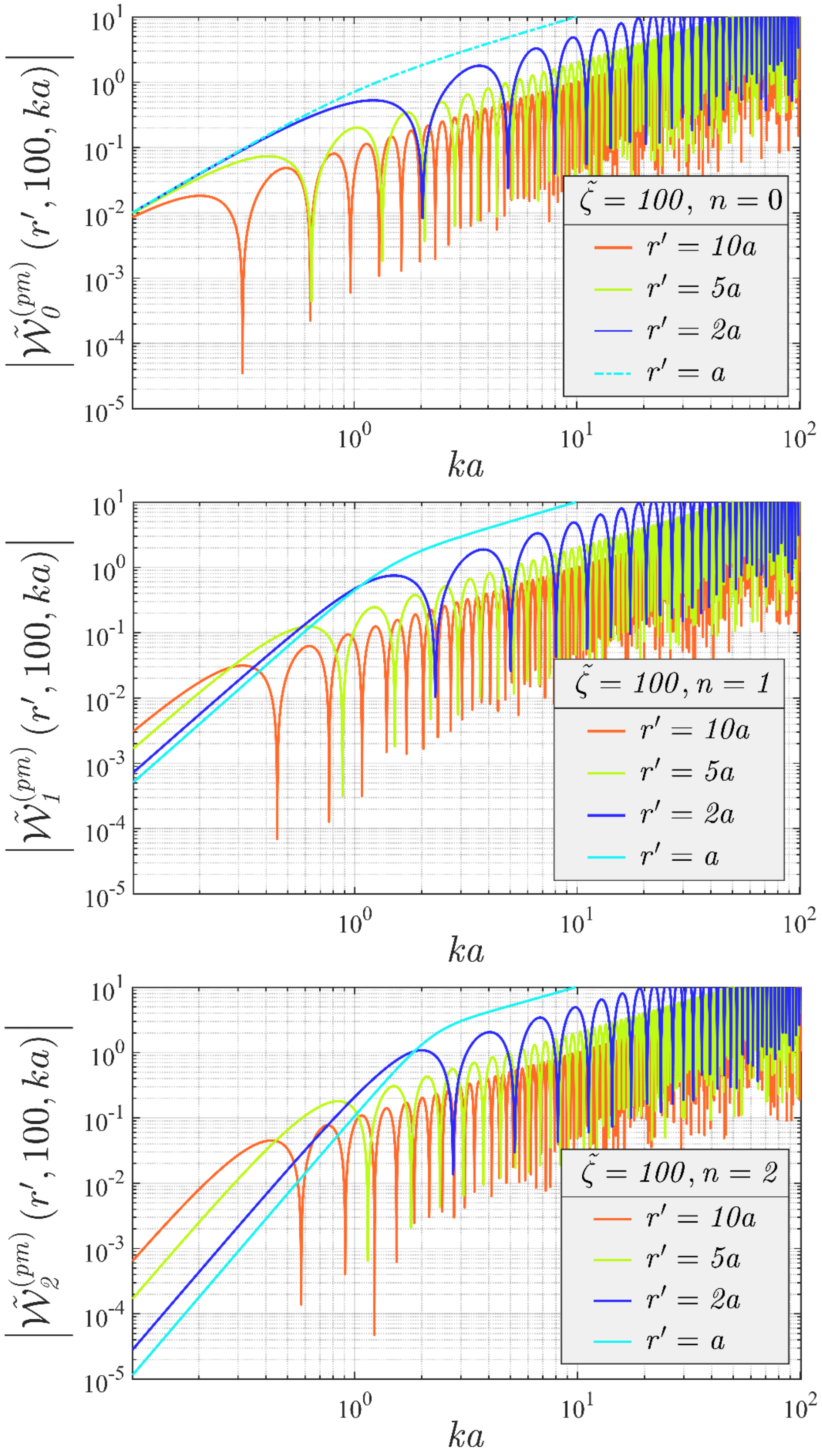

Figure 5-14 First few indices of the modal frequency weightings belonging the coupling coefficients of a secondary point-monopole source radiating when placed at different radial positions r' relative to the hard $\tilde{\zeta} = 100$ sphere.

As the secondary source is moved away from the surface of the sphere, it therefore couples more efficiently into the spherical harmonic components with a higher value of n. The scattered field to be controlled, however, remains dominated by the lower order components, as shown in Figure 4-2. So, in controlling these lower order components, the secondary sources will increasingly excite the higher order spherical harmonic components as they are moved away from the surface of the sphere, which will degrade the control performance. This is similar to the control spillover effect seen in the active control of modal systems, such as vibration in structures [50, 90] where the secondary sources can excite higher order and previously poorly excited, structural modes when they are used to attenuate the effects of lower order structural modes.

To a first approximation, however, the guideline used in the previous section for the number of sources needed for effective active control being $L = (ka+1)^2$ can be generalized for sources away from the surface so that the required number of sources is $L = (kr'+1)^2$. Control will thus be effective for larger values of ka up to a normalized frequency of

$$(ka)_{att} = \frac{a}{r'}\sqrt{L}\,. \tag{5.7}$$

where L is the number of secondary sources, which gives a reasonable prediction of the results in Figure 5-13 as further illustrated in Figure 5-15.

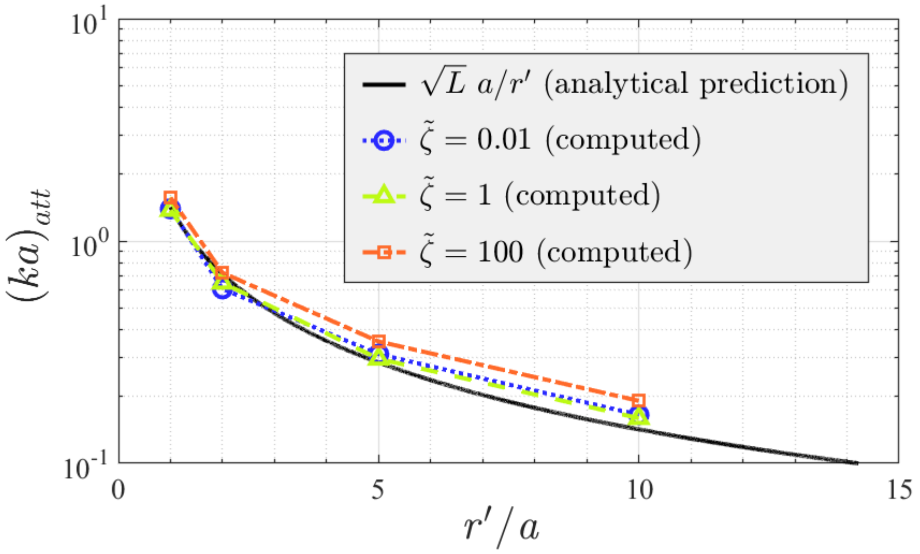

Figure 5-15 Normalized frequency $(ka)_{att}$ up to which -10dB of attenuation is achieved, versus distance away from sphere for active control with a spherical array situated at r' and constituting of 200 sources distributed as in Figure 5-12.

5.4 Chapter summary

In this chapter, the idealized control strategy described in subsection 2.4.2, which is equivalent to that from subsection 3.3.1 for the sound power minimization, was illustrated through computer-modelled results of the uniform impedance sphere in a fluid, given three representative values of surface impedance. Using the spherical harmonic representations of the primary and secondary, a number of aspects that govern the performance of the control where investigated. Firstly, one or two secondary sources in the form of monochromatic point-monopoles were used to suppress the scattering due to a monochromatic plane-wave, when placed on the scattering boundary in an ideal position relative to the incidence. It was found that tonal minimization of a global quantity such as scattered sound power produces attenuation only in the low frequency regime with a small number of secondary sources. This occurs because only the first few spherical harmonic components dominate in this regime for both the primary and the secondary. Using the asymptotic behaviour of the spherical harmonic coefficients in these two entities, the attenuation at low frequencies was analytically predicted. Comparing the prediction to the computed results lead to the conclusion that the tonal minimization with one or two secondary sources is equivalent to completely cancelling the first or, respectively, first two dominant components in the primary that the secondary also couples best into. In this context, the coupling at a given frequency is better when the magnitude of the secondary is low compared to that of the primary by a smaller amount, or when the magnitude of the secondary is big compared to that of the primary by a larger amount.

In contrast, with a single point-monopole on the surface of the spherical obstacle, a regional quantity such as the far-field radiation pattern of the scattering can be significantly suppressed in the proximity of a single chosen direction of space. However, this can generate significant enhancement of the pattern in other directions or of the scattered sound power after control, depending on the directivity patterns of the primary and secondary, as well as how these two are placed relative to each other.

Secondly, the tonal minimization for scattered sound power was investigated when using a large number of secondary point-monopoles spread uniformly on the surface of the impedance sphere. It was found that increasing the number of secondary sources extends the frequency range exhibiting attenuation after control towards higher values. However, this behaviour is governed by a power law, such that, after a certain point, using more sources creates diminishing returns for broadening the benefited frequency regime.

Lastly, results are presented for tonal minimization of scattered sound power when the arrangement of point-monopoles on a virtual sphere is moved away from the scattering surface. It was found that proximity to the scatterer resulted in better suppression, which can be explained and predicted at low frequencies using spherical harmonic components. In this regime, moving the secondary sources away leads to the $n = 0$ spherical harmonic component remaining largely unaffected and to the components with $n \geq 1$ coupling better into the primary, thus degrading the control performance. An analytical prediction was found for the frequency up to which the control is effective, given a specific number of secondary sources.

Chapter 6 Sound Scattering and Radiation: The Thin, Uniform, Empty, Elastic Spherical Shell in Fluid

This chapter explores the mathematical models for scattering from and radiation in the vicinity of a thin, uniform, empty, elastic spherical shell submerged in a fluid (see figure 6.1). The dynamic motion of the shell is first modelled in a vacuum, which is then used to model the effect on the dynamics of externally loading the shell with an idealized surrounding fluid. These chosen shell models are based on Love`s first approximations as explained in the work of Junger [65]. Furthermore, they describe the flexural and bending motion of an elastic structure, and lead to the dynamic motion of the shell not varying with position along the thickness of the shell. The hydrostatic effects due to the static fluid loading are ignored in the considered models, which helps simplify the overall investigation. However, these do have an effect on the dynamic response of the structure as presented in [91].

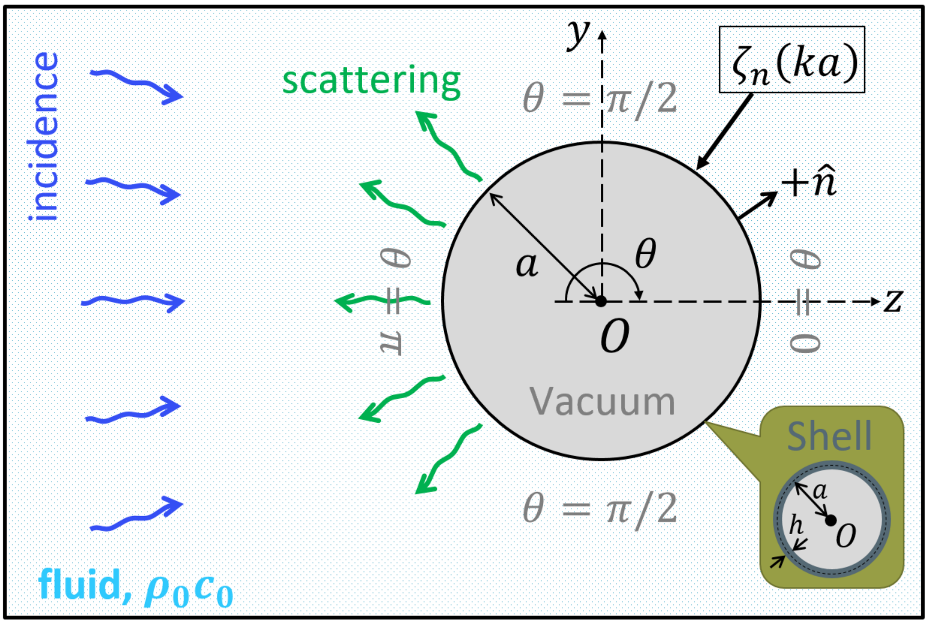

Figure 6-1 Diagram of geometry and notation for 3D sound scattering from thin, uniform, empty, elastic spherical shell in a fluid, shown as slice along yz-plane.

With the assumptions considered above, the motion of the shell can be simplified to that on its exterior surface, i.e. a line border in the shape of a sphere. From this perspective, the chosen model for the fluid-loaded and internally voided thin shell represents an exterior boundary-value problem with an impedance to acoustic wave motion on the surface of the structure that is a function of frequency and of modal index. These functions exhibit poles and zeros of the impedance, which correspond to physical behaviour not encountered for the previously studied impedance sphere, for example, structural resonances when the impedance is zero.

Classic solutions to the Helmholtz equation, such as a plane-wave, a point-monopole and a point-force acting on the surface of the shell, are exemplified for different types of material parameters of the scattering structure. The scenarios discussed here correspond with the passive case where no active control is considered and are later used in Chapter 7 as either the primary or the secondary to exemplify the effects of active controlling the sound scattering from the shell.

The asymptotic behaviour at low normalized frequency is analysed for the exemplified cases of scattering and radiation. This is the region in frequency where active control is expected to provide performance when using a practical small number of control source, as explained in classic active control of sound textbooks [24, 51].

It is important to note that the thin shell theory employed in this thesis imposes an upper limit on the frequency range of interest. For the shell to appear thin, the wavelength corresponding to the slowest wave speed travelling through its structure must be considerably larger than the thickness of the shell. This speed is that of a shear wave and is given by $c_{sw} = \sqrt{E/[2\rho_s(1+\nu)]}$, where ρ_s, E, and ν are, respectively, the density, Young`s Modulus, and Poisson`s ratio of the shell material. Material combinations between rubber, steel, ‘silver alloy’, water and air are later exemplified in this chapter and in Chapter 7, when the shell has an outer radius of $a = 0.5\ \mathrm{m}$ and a thickness of $h/a = 3\%$. Under these circumstances, the results of the used thin shell theory are respectively accurate in the following regimes of normalized frequency ka:

- for a rubber shell in water, $ka \ll 4.29$,
- for a rubber shell in air, $ka \ll 18.28$,
- for a steel shell in water, $ka \ll 447.12$,
- for a steel shell in air, $ka \ll 1903.18$,
- for a ‘silver alloy’ shell in water, $ka \ll 230.53$,

Even with this limitation, the results presented in this chapter and in Chapter 7 are typically shown for the same normalized frequency range regardless of wavenumber in the exterior fluid, i.e. ka

between 10^{-4} to 10^{2}. While this renders certain parts of the plots as an inaccurate representation of the physics, typically at the higher frequencies, it was done to illustrate how the mathematical model changes for drastically different choices of materials when shell thickness is constant. Observations are made about the features in these inaccurate regions without repeating the upper frequency limit at each instance. Furthermore, the focus of this thesis is to demonstrate how spherical harmonic components can be employed in describing 3D sound scattering behaviour and be manipulated in active control strategies. The values mentioned in this paragraph should be referred to in order to judge whether any modelled results from Chapter 6 or Chapter 7 can be used to judge practical outcomes.

6.1 Free vibration of shell in vacuum

Let there be a spherical shell centred at the origin of the coordinate system. For axisymmetric motion, the vibration of a thin spherical shell (non-torsional motion with small deflections of membrane/extensional and flexural/inextensional nature) in vacuum at a single frequency is described by the radial deflection [65]

$$\widetilde{w}_r(\theta) = \sum_{n=0}^{\infty} \tilde{\alpha}_n \, P_n \, (\cos\theta)\,, \tag{6.1}$$

and tangential deflection [65]

$$\widetilde{w}_\theta(\theta) = \sum_{n=1}^{\infty} \tilde{\beta}_n \, P_n'(\cos\theta)\,, \tag{6.2}$$

of the exterior shell surface, which can be expressed as an infinite series of Legendre polynomials $P_n \, (\cos\theta)$, where a factor of $e^{i\omega t}$ corresponding to the used time-frequency convention is omitted. $\tilde{\alpha}_n$ and $\tilde{\beta}_n$ are coefficients depending on frequency and the mechanical wave impedance of the shell, which is $\tilde{Z}_n$ for radial motion. Tangential motion is ignored as it does not couple with the inviscid fluid. $P_n'(\cos\theta)$ signifies derivation of $P_n \, (\cos\theta)$ with respect to $\cos\theta$.

The above expressions can be extended to spherical harmonic series through Legendre`s addition theorem for two angular positions, where one is fixed on an arbitrary direction (θ', φ') and the other embodies the variation with (θ, φ). This leads to (6.1) and (6.2) taking the forms

$$\tilde{w}_r = \sum_{n=0}^{\infty} \sum_{m=-n}^{n} \frac{4\pi}{2n+1} \, \tilde{\alpha}_n \; Y_{n,m}^{(\mathbb{C})}(\theta,\varphi) \, \bar{Y}_{n,m}^{(\mathbb{C})}(\theta',\varphi') \, , \tag{6.3}$$

$$\begin{aligned} \tilde{w}_\theta = \sum_{n=0}^{\infty} \tilde{\beta}_n \, 4\pi \, \frac{n}{\sin^2\theta} \sum_{m=-n}^{n} \frac{1}{2n+1} \cos\theta \; Y_{n,m}^{(\mathbb{C})}(\theta,\varphi) \, \bar{Y}_{n,m}^{(\mathbb{C})}(\theta',\varphi') \, - \\ - \frac{1}{2n-1} Y_{n-1,m}^{(\mathbb{C})}(\theta,\varphi) \, \bar{Y}_{n-1,m}^{(\mathbb{C})}(\theta',\varphi') \, , \end{aligned} \tag{6.4}$$

when using the derivative of the Legendre polynomial,

$$\frac{dP_n\,(z)}{dz} = \frac{n}{z^2-1}\Big(zP_n\,(z) - P_{n-1}(z)\Big) \, .$$

However, the extension performed above does not guarantee that the spherical harmonic functions are the all the non-axisymmetric modeshapes of the used 3D model for a thin spherical shell. This is further discussed in the [92], which speculates that, for such a thin shell model, the non-axisymmetric dynamic motion has the same modeshapes and modal impedances as the axisymmetric one. However, no proof is provided. A demonstration of the result is presented in [93], and put further into context in [94]. With all this considered, it can be concluded that in expressions (6.3) and (6.4) for the given deflections, all possible modes of the shell are accounted for in the series expansion. Furthermore, these modes are governed by the same modal impedance as for the axisymmetric case described in [65].

6.1.1 Mechanical impedance, mechanical admittance, and their asymptotic behaviour

At a single frequency, on the surface of the spherical shell in vacuum, the modal wave impedance for radial motion, which corresponds to the ratio between the modal pressure and modal velocity at each modal order n, is expressed as [65]

$$\tilde{Z}_n(\Omega) = i \frac{\rho_s c_p}{\Omega} \frac{h}{a} \frac{\mathcal{D}_1}{\Omega^2 - (1+\beta^2)(\nu + \lambda_n - 1)} \, , \tag{6.5}$$

with

$$\begin{aligned} \mathcal{D}_1 = \Omega^4 - [1 + 3\nu + \lambda_n - \beta^2(1 - \nu - \lambda_n^2 - \nu\lambda_n)]\Omega^2 + (\lambda_n - 2)(1 - \nu^2) \\ + \beta^2[\lambda_n^3 - 4\lambda_n^2 + \lambda_n(5 - \nu^2) - 2(1 - \nu^2)] \, , \end{aligned} \tag{6.6}$$

where a is the outer radius of the shell, h is the thickness of the shell, ρ_s is the density of the shell, E and v are the Young`s Modulus and Poisson`s ratio of the shell material, $\Omega = \omega a/c_p = (c_0/c_p)ka$ is a non-dimensional frequency, $c_p^2 = E/[\rho_s(1-v^2)]$ is the low frequency phase velocity of compressional waves in an elastic plate made of the shell material, $\lambda_n = n(n+1)$ is a modal parameter, and $\beta^2 = h^2/(12a^2)$ is a geometrical parameter. The quantities c_0, k and ω are the speed of sound, wave number and angular frequency in a reference medium, which will be later used as the exterior fluid surrounding the shell. Compared to a locally-reacting surface impedance of a sphere in a fluid, this mechanical impedance is a rational function of a dimensionless frequency, with poles and zeroes. It is important to highlight that using a non-dimensional frequency makes $\tilde{Z}_n$ dependent only on the material properties of the shell and not on the reference fluid.

Expression (6.5) can be re-written as

$$\tilde{Z}_n(ka) = \frac{i\rho_s c_0 h}{a} \frac{\mathcal{D}_2}{(ka)\left[(ka)^2 - \left(\frac{c_p}{c_0}\right)^2 (1+\beta^2)(v+\lambda_n-1)\right]}, \tag{6.7}$$

with

$$\begin{aligned}\mathcal{D}_2 = (ka)^4 - \left(\frac{c_p}{c_0}\right)^2 [1+3v+\lambda_n-\beta^2(1-v-\lambda_n^2-v\lambda_n)](ka)^2 \\ + \left(\frac{c_p}{c_0}\right)^4 \{(\lambda_n-2)(1-v^2) \\ + \beta^2[\lambda_n^3 - 4\lambda_n^2 + \lambda_n(5-v^2) - 2(1-v^2)]\},\end{aligned} \tag{6.8}$$

such that the corresponding modal wave admittance, i.e. the reciprocal of $\tilde{Z}_n(ka)$, is

$$\tilde{Y}_n(ka) = \frac{1}{\tilde{Z}_n} = -i\frac{1}{\rho_s c_0}\frac{a}{h}\frac{(ka)\left[(ka)^2 - \left(\frac{c_p}{c_0}\right)^2 (1+\beta^2)(v+\lambda_n-1)\right]}{\mathcal{D}_2}. \tag{6.9}$$

For small ka ($ka \ll 1$), when $n = 0$, the terms corresponding to $(ka)^2$ and $(ka)^4$ in the numerator and denominator of (6.7) become negligible, so that the wave impedance simplifies to

$$\begin{aligned}&\lim_{ka\ll 1} \tilde{Z}_0(ka) = \\ &= \frac{i\rho_s c_0 h}{a} \frac{\left(\frac{c_p}{c_0}\right)^4 \{(\lambda_0-2)(1-v^2) + \beta^2[\lambda_0^3 - 4\lambda_0^2 + \lambda_0(5-v^2) - 2(1-v^2)]\}}{-(ka)\left(\frac{c_p}{c_0}\right)^2 (1+\beta^2)(v+\lambda_0-1)} = \\ &= i\frac{h}{a}\frac{\rho_s c_p^2}{c_0}\frac{2(1-v^2)}{(v-1)(ka)} = -i\frac{h}{a}\frac{2E}{c_0(1-v)(ka)} = \frac{k'}{i\omega},\end{aligned} \tag{6.10}$$

where $k' = 2Eh/[a^2(1-v)]$. This behaviour of the impedance is controlled by the stiffness of the structure. When $n = 1$, the $(ka)^0$ term in the denominator of (6.9) is zero, such that $(ka)^2$ term is dominant instead and the asymptotic behaviour of the impedance is given by

$$\lim_{ka\ll 1} \tilde{Z}_1(ka) = \frac{i\rho_s c_0 h}{a} \frac{-\left(\frac{c_p}{c_0}\right)^2 [1+3v+\lambda_1-\beta^2(1-v-\lambda_1^2-v\lambda_1)](ka)^2}{-(ka)\left(\frac{c_p}{c_0}\right)^2 (1+\beta^2)(v+\lambda_1-1)} = \\ = \frac{i\rho_s c_0 h}{a} \frac{3(1+v)(1+\beta^2)(ka)}{(1+v)(1+\beta^2)} = 3i\rho_s c_0 \frac{h}{a}(ka) = i\omega m' \ , \tag{6.11}$$

where $m' = 3h\rho_s$. This behaviour of the impedance is controlled by the mass of the structure. For $n \geq 2$, the situation is similar to that for $n = 0$, such that

$$\lim_{ka\ll 1} \tilde{Z}_n(ka) = \\ = \frac{i\rho_s c h}{a} \frac{\left(\frac{c_p}{c_0}\right)^4 \{(\lambda_n-2)(1-v^2)+\beta^2[\lambda_n^3-4\lambda_n^2+\lambda_n(5-v^2)-2(1-v^2)]\}}{-(ka)\left(\frac{c_p}{c_0}\right)^2 (1+\beta^2)(v+\lambda_n-1)} = \\ = -i\frac{h}{a}\frac{\rho_s c_p^2}{c_0}\frac{(\lambda_n-2)(1-v^2)+\beta^2[\lambda_n^3-4\lambda_n^2+\lambda_n(5-v^2)-2(1-v^2)]}{(ka)(1+\beta^2)(v+\lambda_n-1)} \ . \tag{6.12}$$

As for $n = 0$, the impedance at low ka is controlled by the stiffness of the structure for $n \geq 2$.

For large values of ka ($ka \to \infty$), the terms corresponding to $(ka)^2$ and $(ka)^4$ in the numerator and denominator of (6.7) are dominant, so that the wave impedance is

$$\lim_{ka\to\infty} \tilde{Z}_n(ka) = i\frac{h}{a} c_0 \rho_s (ka) \, , \tag{6.13}$$

i.e. it is controlled by the mass of the structure due to the power law of the frequency.

Consequently, for the modal wave admittance, the asymptotic behaviour at low ka is

$$\lim_{ka\ll 1} \tilde{Y}_n(ka) = \\ = i\frac{c_0 a}{\rho_s c_p^2 h}\frac{(ka)(1+\beta^2)(v+\lambda_n-1)}{(\lambda_n-2)(1-v^2)+\beta^2[\lambda_n^3-4\lambda_n^2+\lambda_n(5-v^2)-2(1-v^2)]} \ , \qquad n \geq 2 \ , \tag{6.14}$$

$$\lim_{ka\ll 1} \tilde{Y}_0(ka) = i\frac{a}{h}\frac{c_0(1-v)(ka)}{2E} = \frac{i\omega}{k'} , \tag{6.15}$$

$$\lim_{ka\ll 1} \tilde{Y}_1(ka) = -i\frac{a}{h}\frac{1}{3c_0\rho_s(ka)} = \frac{1}{i\omega m'} \ , \tag{6.16}$$

and at large values of ka is

$$\lim_{ka\to\infty} \tilde{Y}_n(ka) = -i\frac{a}{h}\frac{1}{c_0\rho_s(ka)} \ . \tag{6.17}$$

6.1.2 Natural frequencies and modeshapes for shell in vacuum

It can be seen in formulation (6.9) that the modal admittance at each order $n \neq 1$ has three real zeroes, one of which always occurs at normalized frequency of $0\ \mathrm{Hz}$ and the other two governed by the physical properties of the shell material. For $n = 1$, there is no third zero at a frequency of $0\ \mathrm{Hz}$. For a given order n, the zeroes occur at the two angular frequencies

$$g_n = \pm\frac{c_p}{c_0}[(1+\beta^2)(v+\lambda_n-1)]^{1/2} \ , \tag{6.18}$$

and represent the values in the frequency regime at which the motion of the mode n is the least. For $n = 0$, the quantity underneath the square root in (6.18) is negative, assuming material properties are not negative and Poisson`s ratio is a maximum of 0.5, and, thus, the two values g_n are complex, resulting in no troughs in the admittance versus frequency behaviour. For $n > 0$, the quantity underneath the square root in (6.18) is always positive, such that one value of g_n is always positive and the other is always negative, resulting in one trough for the admittance as a function of frequency.

Also, the admittance in (6.9) has four poles, two real and two pure-imaginary, all governed by the properties of the shell material. The real poles that are positive represents the natural frequencies of vibration for the shell, where the motion of the mode n is the highest in magnitude, i.e. where peaks appear in $Y_n(ka)$. These natural frequencies are categorized in two sets [65], a 'Upper Branch' given by

$$\begin{aligned} 2\mathcal{C}a_n^2 = {} & [1+3v+\lambda_n-\beta^2(1-v-\lambda_n^2-v\lambda_n)] \\ & + \{[1+3v+\lambda_n-\beta^2(1-v-\lambda_n^2-v\lambda_n)]^2-4(\lambda_n-2)(1-v^2) \\ & - 4\beta^2[\lambda_n^3-4\lambda_n^2+\lambda_n(5-v^2)-2(1-v^2)]\}^{1/2} \ , \end{aligned} \tag{6.19}$$

and a 'Lower branch' given by

$$\begin{aligned} 2\mathcal{C}b_n^2 = {} & [1+3\nu+\lambda_n-\beta^2(1-\nu-\lambda_n^2-\nu\lambda_n)] \\ & -\{[1+3\nu+\lambda_n-\beta^2(1-\nu-\lambda_n^2-\nu\lambda_n)]^2-4(\lambda_n-2)(1-\nu^2) \\ & -4\beta^2[\lambda_n^3-4\lambda_n^2+\lambda_n(5-\nu^2)-2(1-\nu^2)]\}^{1/2}\ , \end{aligned} \qquad (6.20)$$

where $\mathcal{C}=(1-\nu^2)\rho_s a^2/E$ and a_n , b_n are the angular natural frequencies when real and positive. These natural frequencies can be written in terms of normalized frequency ka as either $ka=a_n\, a/c_0$ and $ka=b_n\, a/c_0$. The resonances in the 'Lower branch' are typically lower in frequency then those in the 'Upper branch' [65].

For the order $n=0$, the 'Lower branch' exhibits a spurious mode where both radial and tangential displacement are zero. Additionally, for the order $n=1$, the natural frequency in the 'Lower branch' occurs at a frequency of $0\ \mathrm{Hz}$, which translates into a rigid body mode where the whole structure moves in unison by the same amount; this is the reason why, the modal admittance in (6.9) has only one peak in the frequency regime and is controlled by the mass of the structure at low frequency. The natural frequencies in the two branches are exemplified in Table 6-2 and Table 6-1 for natural rubber and steel, respectively, when the shell has a radius of $a=0.5\ \mathrm{m}$ and a thickness $h/a=3\%$. The 'Upper branch' is significantly affected by varying h/a while the 'Lower branch' is not, as discussed in [65] and as seen in Figure 6-2 for the steel shell, where the natural frequencies are expressed as normalized frequencies following $ka=a_n\, a/c_0$ and $ka=b_n\, a/c_0$.

n	a_n (rad/s)	b_n (rad/s)
0	207.39	-
1	254.01	0
2	341.47	72.81
3	447.5	88.27
4	560.23	95.71
5	675.79	101.22
6	792.75	107.06
7	910.51	114.36
8	1028.77	123.84
9	1147.37	135.89
10	1266.2	150.74

Table 6-2 Natural frequencies for rubber spherical shell in vacuum.

n	a_n (rad/s)	b_n (rad/s)
0	16444.29	-
1	20140.81	0
2	27885.55	7359.49
3	37354.69	8720.24
4	47309.64	9326.01
5	57433	9760.42
6	67630.59	10217.21
7	77866.94	10792.88
8	88126.02	11547.14
9	98399.59	12517.95
10	108682.97	13726.63

Table 6-1 Natural frequencies for steel spherical shell in vacuum.

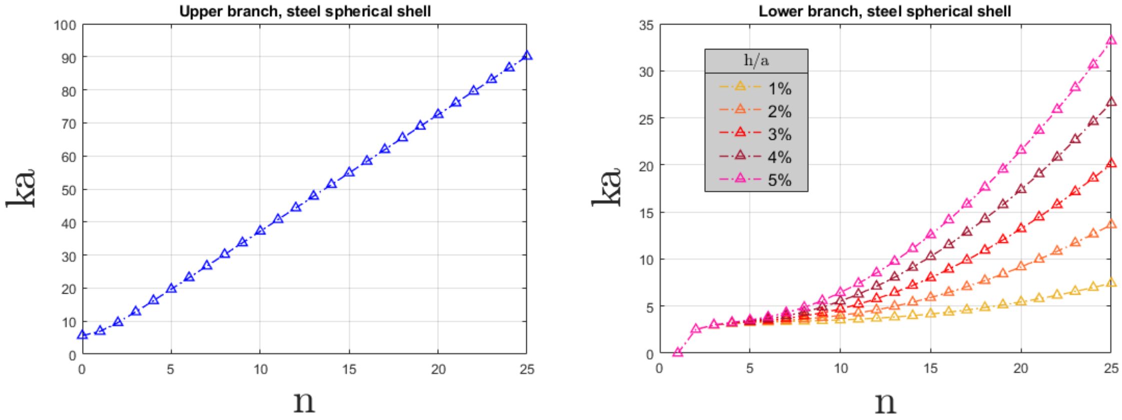

Figure 6-2 Normalized natural frequencies of steel shell in vacuum versus modal order n.

6.1.3 In-vacuo modal wave admittance versus frequency

From formulation (6.9), it can be concluded that the ratio of the thickness of the shell to its outer radius is an important parameter that governs the modal admittance. However, the analysis presented in this thesis is streamlined by exemplified only shells of a specific thickness value, i.e. $h/a = 3\%$. This allows the study to focus on other aspects such as the effects on the scattering at different frequencies when changing different material properties.

The magnitude of the in-vacuo wave admittance $\tilde{Y}_n$ normalized by the characteristic impedance of water or air as potential exterior surrounding fluids is plotted against the normalized frequency ka in the top rows of Figure 6-3 and Figure 6-4 for the shells of $h/a = 3\%$ thickness made out of natural rubber and steel, respectively. Results are shown for the first few modal orders n. The wavenumber is defined relative to an exterior fluid that is not yet considered. Changing between air and water for a shell made of a given material leads to shifting all lines by the same amount on the frequency axis, but also to re-scaling of all lines by the same amount on the magnitude axis as the normalization changes. In principle, the magnitudes of the peaks correspond to no motion and go up to infinity, while the magnitude of the troughs correspond to resonant motion and go down to infinity. However, these peaks and troughs appear as finite in the results because they have been simulated numerically over a discrete range of frequencies and, respectively, due to the use of a logarithmic scale. Thus, any changes to the peaks and troughs when using different material combinations cannot be attributed to any specific physical reason.

For $n = 0$, the normalized in-vacuo wave admittance has only one peak corresponding to the positive, real root a_n of the denominator in (6.9) and no troughs; it rises proportional to ka at low values of ka (stiffness controlled) and it descends proportional to $1/(ka)$ at large values of ka (mass controlled). For $n = 1$, the admittance has only one peak corresponding to the positive, real root a_n of the denominator in (6.9), and one trough corresponding to the real, positive root of the numerator in (6.9); it descends proportional to ka at low values of ka as well as at large values of ka. For the orders n higher than 1, the admittance has two peaks corresponding to the positive, real roots a_n and b_n of the denominator in (6.9), and one trough corresponding to the real, positive root of the numerator in (6.9); it rises proportional to ka at low values of ka (stiffness controlled) and it descends proportional to $1/(ka)$ at large values of ka (mass controlled).

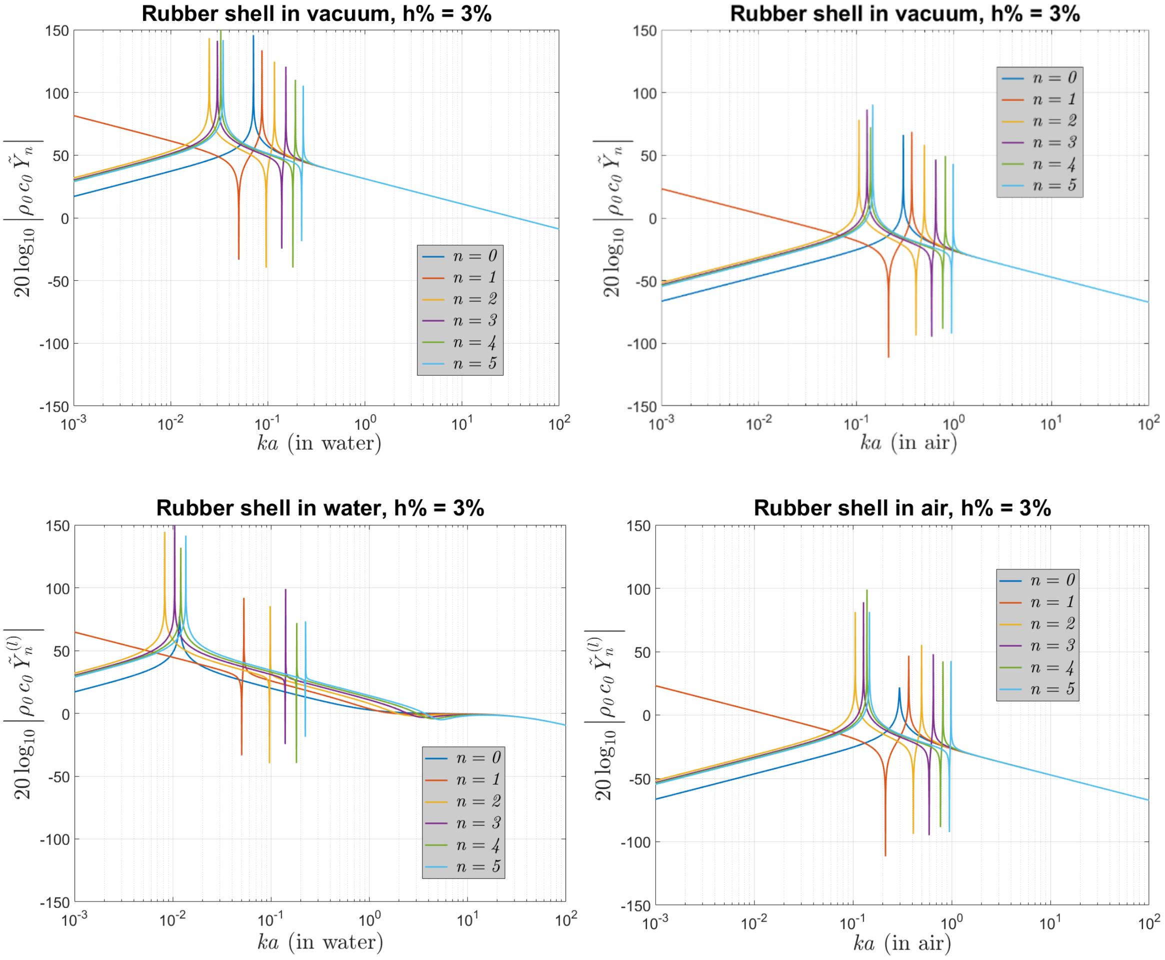

Figure 6-3 Normalized modal wave admittance versus normalized frequency at the first few modal orders n for thin spherical shell made of rubber, in vacuum (first row) and loaded externally (second row) by either water (first column) or air (second column).

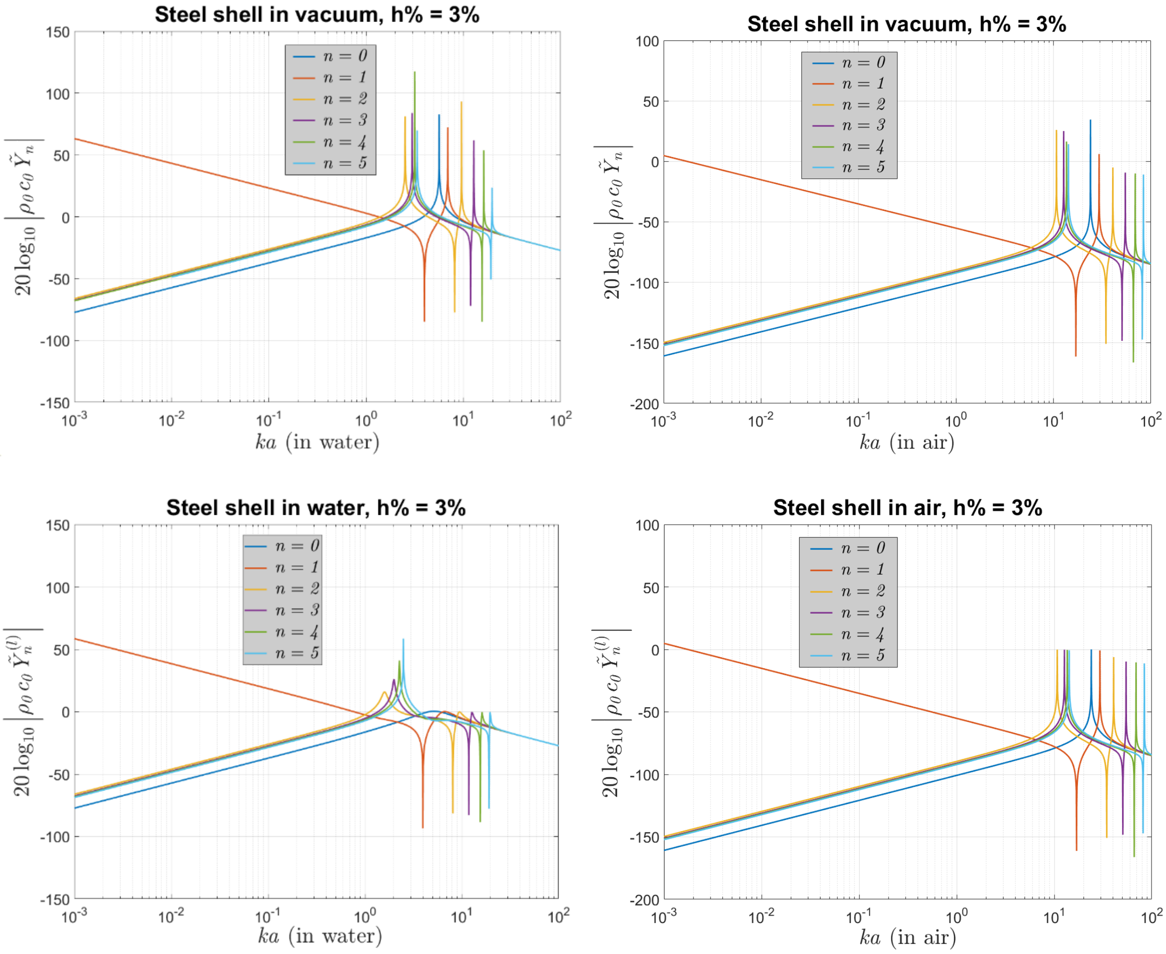

Figure 6-4 Normalized modal wave admittance versus normalized frequency at the first few modal orders n for thin spherical shell made of steel, in vacuum (first row) and loaded externally (second row) by either water (first column) or air (second column).

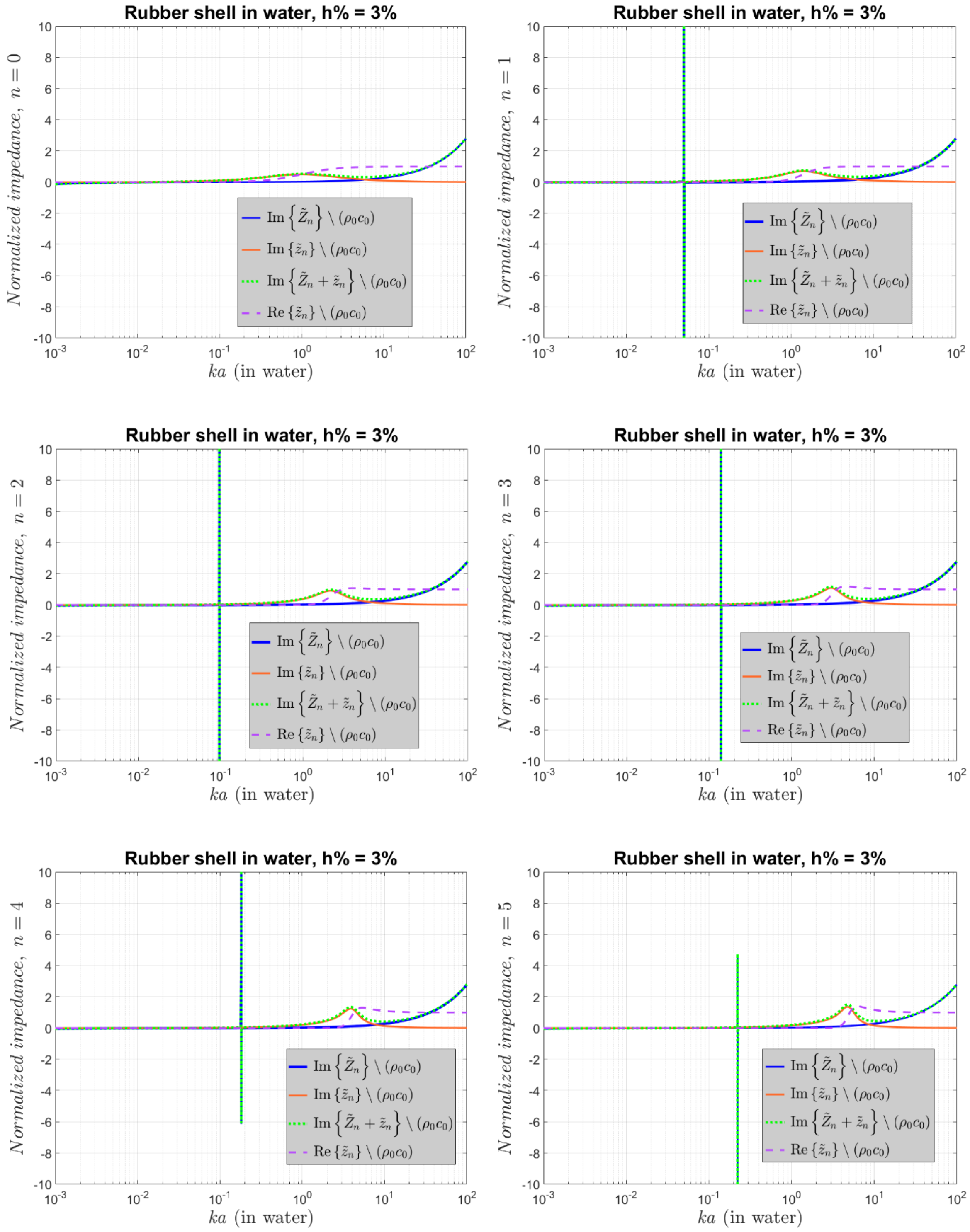

Rubber shell in water, h% = 3%

Rubber shell in water, h% = 3%

Rubber shell in water, h% = 3%

Rubber shell in water, h% = 3%

Rubber shell in water, h% = 3%

Rubber shell in water, h% = 3%

Figure 6-5 Real and imaginary parts of modal impedance for the in-vacuo and fluid loaded rubber shell in water, as function of normalized frequency ka, shown for the very first few modal indices n.

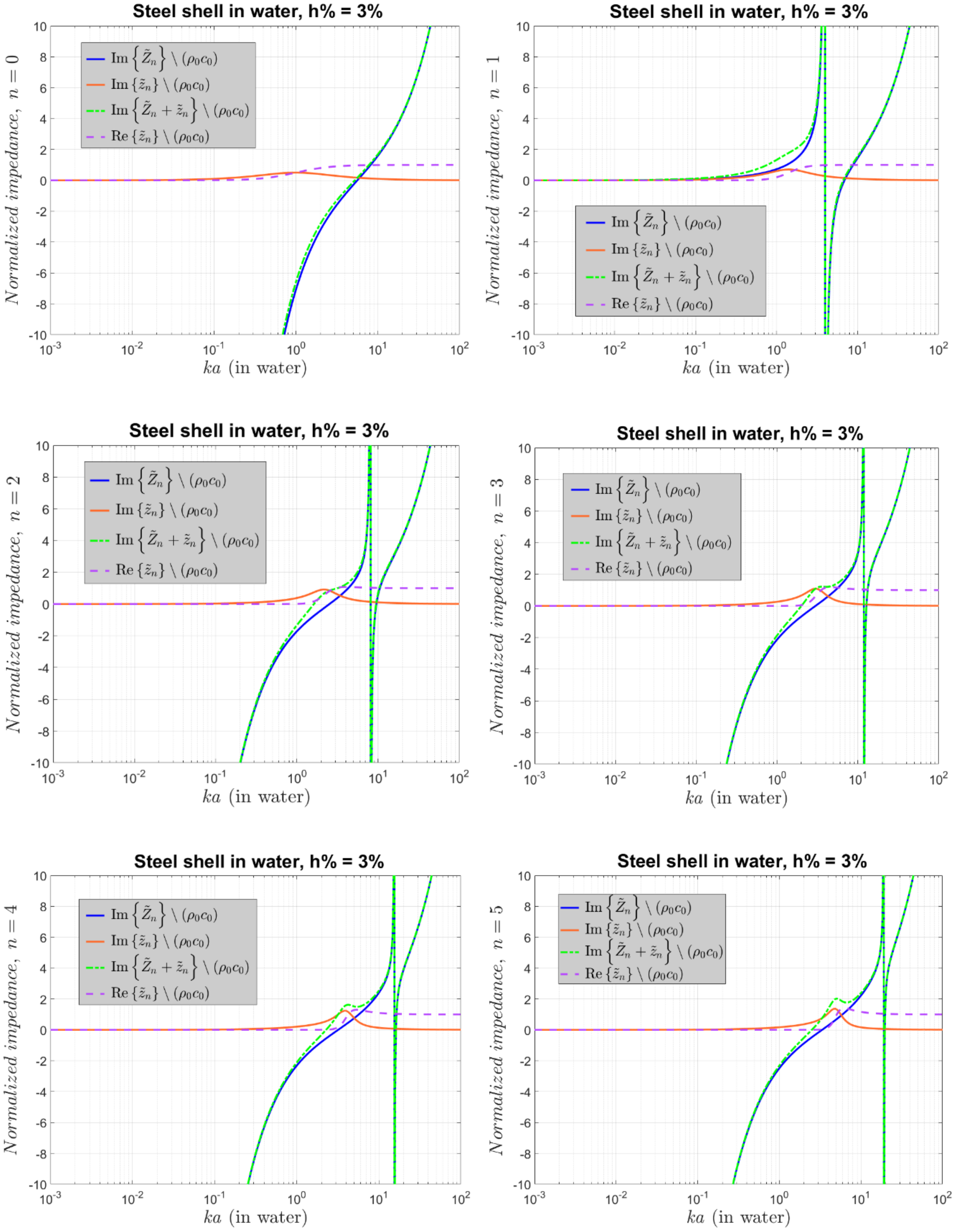

Figure 6-6 Real and imaginary parts of modal impedance for the in-vacuo and fluid loaded steel shell in water, as function of normalized frequency ka, shown for the very first few modal indices n.

6.2 Vibration of elastic shell loaded externally by fluid

In the used spherical shell model, the modal wave impedance of the structure at each modal order n when externally loaded by a fluid is a modified version of the modal wave impedance in vacuum, such that the new loaded impedance characterizing the separation boundary is [65]

$$\tilde{Z}_n^{(l)}(ka) = \tilde{Z}_n(ka) + \tilde{z}_n(ka) = \tilde{Z}_n(ka) - i\rho_0 c_0 \frac{h_n\,(ka)}{h_n'(ka)} \quad , \tag{6.21}$$

where $\tilde{z}_n(ka)$ is the modal impedance of the free-field fluid towards an outgoing wave as in equation (2.26), i.e. the radiation loading, and is added to the modal wave impedance of the spherical shell in vacuum, $\tilde{Z}_n(ka)$. The radiation loading has both a real part (resistive) and an imaginary part (reactive) while the latter is purely imaginary (reactive), therefore, the real part of $\tilde{Z}_n^{(l)}(ka)$ is the real part of the second term, $\tilde{z}_n(ka)$, in (6.21). This translates in the structure being damped solely due to the loading of the fluid in this model.

The behaviours of $\tilde{Z}_n^{(l)}(ka)$, $\tilde{Z}_n(ka)$ and $\tilde{z}_n(ka)$ with frequency are exemplified in Figure 6-5 and Figure 6-6 for the rubber spherical shell in water and, respectively, the steel spherical shell in water. It can be seen in the figures that the imaginary part of $\tilde{z}_n(ka)$ for all modal orders has no zeroes or poles and is significantly small in magnitude at low ka and at large ka, while having a narrow mid-frequency regime of large magnitude whose position depends on n. The real part of $\tilde{z}_n(ka)$ for all modal orders is small in magnitude at low ka, rises to a slightly higher value around the same region where the imaginary part of $\tilde{z}_n(ka)$ does, and then decreases with higher frequency. In contrast, $\tilde{Z}_n(ka)$ is significantly large in magnitude in almost all frequency regions for the steel shell in water but is significantly large only at high frequencies and resonant frequencies for the rubber shell in water. Given a modal order n, the effect of the fluid loading on the overall impedance is to add a dissipative real part, and dominate the purely imaginary $\tilde{Z}_n(ka)$ in the regions where the imaginary part $\tilde{z}_n(ka)$ shows a slight increase in magnitude. The natural frequencies of the shell in vacuum are thus lowered by the mass loading of the exterior surrounding fluid.

The corresponding loaded admittance $\tilde{Y}_n^{(l)}$ normalized by the characteristic impedance of exterior fluid is plotted against the normalized frequency ka for the first few modal orders n in the graphs on the lower row of Figure 6-3 and Figure 6-4. This is done for the rubber and, respectively, steel shells, submerged in either water or air. In Figure 6-3, when comparing the natural rubber shell in vacuum versus in water, it can be observed that the fluid loading in this case, at low values of ka, does not change the structure of the modal in-vacuo admittances and only the line corresponding to $n = 1$ is scaled down. Also, at large values of ka, the water loading creates complicated behaviour of relatively significant magnitude for all orders n. When it comes to the in-vacuo resonances, it seems that all the natural frequencies for the low modal orders are shifted down in frequency, while for higher orders, only the resonances in the 'Lower Branch' are shifted down; the ones in the 'Upper branch' do not shift in frequency significantly. The troughs in the modal admittances seem to not shift in frequency due to the fluid loading. The magnitudes of the peaks and troughs are affected by the water loading [65]. However, this is difficult to observe since the initial magnitudes at the in-vacuo resonances are meant to be zero on the logarithmic scale and those at the in-vacuo antiresonances are meant to be infinity, while the plots have been simulated numerically over a discrete range of frequencies. With that said, the peak of the admittance for $n = 0$ in particular appears to be significantly reduced by the loading in the results.

When comparing the natural rubber shell in vacuum versus in air, it can be observed in Figure 6-3 that the fluid loading seems to have no effects on the modal admittances with the exception of the magnitude change of the peaks in all modal orders when the shell is loaded by the air. But, as described before, the changed amount seen in the plots may not be the exact amount of effect produced by the loading due to numerical limitations in computation of the results. The air loading seems to not significantly shift the frequencies at which the resonances and the troughs in the admittances occur, it seems to not change the magnitude in the troughs, and it does not change the behaviour or scaling at low values of ka.

When analysing Figure 6-4 for the steel shell in water, it can be observed that the effects of the loading are similar to the observed effects of the air loading on the rubber shell, with the addition that the troughs in the in-vacuo admittances of the steel shell in water are increased in magnitude very slightly. However, the peaks in the in-vacuo admittances of the steel shell in water are reduced significantly in magnitude for both branches when compared to the air loading on the rubber shell. In the case of the steel spherical shell in air, the overall magnitude of the in-vacuo modal admittances, including those at resonances and anti-resonances, would be hardly affected even in the absence of numerical limitations as the air loading is relatively very light on the steel structure.

6.3 Scattering of plane-wave from an elastic shell

Generalising the discussion around equation (2.43), a monochromatic plane-wave of magnitude $\tilde{\mathcal{P}}_i$ arriving from the incidence direction (θ_i, φ_i) creates a pressure scattered from the shell equal to

$$\tilde{p}_s(\vec{r}) = \sum_{n=0}^{\infty} \sum_{m=-n}^{n} \widetilde{D}^{\mathbb{C}}_{n,m} \, h_n(kr) \, Y^{(\mathbb{C})}_{n,m}(\theta, \varphi), \ , \tag{6.22}$$

where the coefficients are

$$\widetilde{D}^{\mathbb{C}}_{n,m} = -\tilde{\mathcal{P}}_i \, 4\pi \, i^n \, \widetilde{\mathcal{W}}_n \, \bar{Y}^{(\mathbb{C})}_{n,m}(\theta_i, \varphi_i) \ , \tag{6.23}$$

and the modal frequency weightings are

$$\widetilde{\mathcal{W}}_n(\tilde{\zeta}_n, ka) = \frac{j_n(ka) + i \, \tilde{\zeta}_n(ka) \, j_n{}'(ka)}{h_n(ka) + i \, \tilde{\zeta}_n(ka) \, h_n'(ka)} \ . \tag{6.24}$$

where $\tilde{\zeta}_n(ka)$ are the modal impedances of the shell in-vacuo, normalized by the characteristic impedance of the surrounding fluid, $(\rho_0 c_0)$, and are functions of the modal order n, as well as the normalized frequency ka. These $\tilde{\zeta}_n(ka)$ now replace the normalized impedance $\tilde{\zeta}$ of the locally-reacting sphere, which was independent of n and ka.

In [65], the axisymmetric form of expression (6.22) is described, which has the Legendre polynomials as the basis functions and is obtained from (6.22) via Legendre`s addition theorem.

The normalized scattered power can then again be written as

$$\widetilde{\Pi}_s = \frac{\widetilde{W}_s}{\widetilde{W}_i} = \frac{1}{\pi (ka)^2 \tilde{\mathcal{P}}_i^2} \sum_{n=0}^{\infty} \sum_{m=-n}^{n} \left| \widetilde{D}^{\mathbb{C}}_{n,m} \right|^2, \tag{6.25}$$

or

$$\widetilde{\Pi}_s = \frac{4}{(ka)^2} \sum_{n=0}^{\infty} (2n+1) \left| \widetilde{\mathcal{W}}_n(\tilde{\zeta}_n, ka) \right|^2, \tag{6.26}$$

where $\widetilde{W}_i$ is the same as in equation (4.17).

6.3.1 Low frequency asymptotes for modal frequency weightings of scattering

Using the asymptotic behaviour at low ka of the mechanical modal impedance from formulas (6.10), (6.11) and (6.12) together with the asymptotic behaviour at low ka of the scattering coefficients for a locally-reacting impedance sphere [78], and combining these together in (6.24) leads to the following asymptotes of the modal frequency weightings of the plane-wave scattering from the thin shell, $\widetilde{\mathcal{W}}_n^{(pw)} = \widetilde{\mathcal{W}}_n(\tilde{\zeta}_n, ka)$,

$$\lim_{ka \ll 1} \widetilde{\mathcal{W}}_0^{(pw)} = -i \frac{(ka)^3}{3} \left(1 - \frac{3\rho c_0^2 (1-\nu)}{2E} \frac{a}{h} \right) , \tag{6.27}$$

$$\lim_{ka \ll 1} \widetilde{\mathcal{W}}_1^{(pw)} = i \frac{(ka)^3}{3} \frac{3 \frac{h}{a} \frac{\rho_s}{\rho} - 1}{1 + 6 \frac{h}{a} \frac{\rho_s}{\rho}} , \tag{6.28}$$

$$\lim_{ka \ll 1} \widetilde{\mathcal{W}}_n^{(pw)} = i \left[\frac{2^n n!}{(2n)!} \right]^2 \frac{(ka)^{2n+1}}{(2n+1)} \frac{n}{(n+1)} , \qquad n \geq 2 . \tag{6.29}$$

When comparing the above relations with the asymptotic behaviour of the modal scattering amplitudes of a rigid sphere, the $n = 0$ and $n = 1$ components have additional factors governed by the stiffness and mass of the shell, respectively, but the higher modal weightings behave in the same way as those of a rigid sphere at low ka.

As commented in [78], at low ka, the ideal locally-reacting impedance that passively cancels the leading order power of (ka) in the $n = 0$ scattering component is $\tilde{\tilde{\zeta}} = 3/(ika)$, and the one that passively cancels the leading order power of (ka) in the $n = 1$ scattering component is $\tilde{\tilde{\zeta}} = (ika)$, which cannot be satisfied at the same time for a locally-reacting impedance sphere. In the case of the dynamic spherical shell, however, formulation (6.27) shows that the condition for completely cancelling the $n = 0$ scattering component at low values of ka is

$$\frac{E}{\rho c_0^2 (1-\nu)} \frac{h}{a} = \frac{3}{2} . \tag{6.30}$$

Also, equation (6.28) shows that the condition for completely cancelling the $n = 1$ scattering component at low values of ka is

$$\frac{h}{a} \frac{\rho_s}{\rho} = \frac{1}{3} . \tag{6.31}$$

Equating relations (6.30) and (6.31) leads the condition

$$c_0^2 \frac{(1-\nu)\rho_s}{E} = \frac{2}{9} \ , \tag{6.32}$$

which can be satisfied in practice. This means that choosing appropriate material properties for the spherical shell to satisfy (6.30), (6.31) and (6.32) at the same time, allows the simultaneous passive cancellation of the $n = 0$ and $n = 1$ scattering components.

Searching through a database of existing materials, the closest one in material properties that can satisfy (6.30) – (6.32) while maintaining the thin spherical shell condition ($h/a < 5\%$) is a silver shell loaded externally by water. Thus, a silver alloy or silver-based composite that exhibits all the exact number values satisfying (6.30) – (6.32) could potentially be possible to manufacture.

	ρ_s (kg/m^3)	E_s (GPa)	ν	h/a (%)
Natural Rubber	930	0.0025	0.5	3%
Steel	7700	190	0.27	3%
Silver Alloy	11111.111	74.606	0.3	3%

Table 6-3 Physical properties of materials used in current study of thin spherical shells.

$ka \ll 1$	Rigid	Water - rubber	Air - rubber	Water - steel	Air - steel	Water – 'Silver Alloy'
$\widetilde{\mathcal{W}}_0^{(pw)}$	$-0.3333i(ka)^3$	$7105i(ka)^3$	$0.1412i(ka)^3$	$-0.1968i(ka)^3$	$-0.3333i(ka)^3$	~ 0
$\widetilde{\mathcal{W}}_1^{(pw)}$	$0.1667i(ka)^3$	$-0.2616i(ka)^3$	$0.163i(ka)^3$	$-0.049i(ka)^3$	$0.1662i(ka)^3$	~ 0
$\widetilde{\mathcal{W}}_2^{(pw)}$	$2i(ka)^5/135$	$2i(ka)^5/135$	$2i(ka)^5/135$	$2i(ka)^5/135$	$2i(ka)^5/135$	$2i(ka)^5/135$
$\widetilde{\Pi}_s$	$0.7778(ka)^4$	$201924101(ka)^4$	$0.3988(ka)^4$	$0.1771(ka)^4$	$0.776(ka)^4$	$0.0044(ka)^8$

Table 6-4 Asymptotic behaviour for first few indices of frequency weighting $\widetilde{\mathcal{W}}_n^{(pw)}$ of scattering coefficients and normalized scattered sound power $\widetilde{\Pi}_s$ due to plane-wave scattering from different elastic spherical shells surrounded by certain fluids.

The asymptotic behaviour of the modal scattering amplitudes and of the scattered power at low values of ka is showcased through five examples of spherical shell materials and external fluids. These are natural rubber, steel and 'silver alloy' for the shell, and water and air for the external fluid. The 'silver alloy' is fictional, close to the properties of actual silver; these properties are $E = 74.606\ \mathrm{GPa}$, $\nu = 0.3$, $\rho_s = 11111.11\ \mathrm{kg/m^3}$, $h/a = 0.03$, as compiled in Table 6-3.

The asymptotes of the modal scattering coefficients and the scattered power calculated from (6.30) – (6.32), and (6.26) are tabulated in Table 6-4 for the five scenarios. The resulting values paint a picture that different material properties for the spherical shell or the external fluid can produce very different effects on the scattering at low frequency. For the rubber – water case, the $n = 0$ component is dominant over the $n = 1$ which results in a very large amount of scattering of the plane-wave. For the rubber – air case, the $n = 1$ component is approximately the same as that of a rigid sphere but the $n = 0$ component is very slightly less dominant than the $n = 1$ one while following the same power law. The steel – water and steel – air cases behave similar to a rigid sphere where both the $n = 0$ and $n = 1$ components are dominant at low ka; however, the latter scenario is almost exactly the same as a rigid sphere, while for the first one, the magnitudes of both $n = 0$ and $n = 1$ components are lower than they would be for a rigid sphere, leading to less scattered power. All of these previously described behaviours are reflected in the asymptotes of the scattered power. In the case of the 'silver alloy' shell, cancelling the leading order power of (ka) for $n = 0$ and $n = 1$ components leaves the $n = 2$ component dominant in the hierarchy of components at low ka, which in turn also dominates the scattered power. In this fictional scenario, the scattered power would be more than two times lower than that for a rigid sphere after power minimization with two ideally placed point-monopole secondary source as in Figure 5-1, on the right, for which the scattered power after control behaves as $0.0099(ka)^8$ at low values of ka (see Figure 5-3c).

6.3.2 The scattering coefficients and their modal frequency weightings

In Figure 6-7 and Figure 6-8, the loaded modal wave admittance plots from the previous section are presented alongside plots of the magnitude of the modal frequency weightings $\widetilde{\mathcal{W}}_n^{(pw)}$ belonging to the scattering coefficients. This is done for the natural rubber shell and, respectively, the steel shell, each submerged either in air or in water.

For the natural rubber shell, when submerged both in water or in air, the 'Lower branch' and 'Upper branch' natural frequencies can be clearly identified in the behaviour of the modal frequency weightings, where they exhibit peaks in magnitude in the region below $ka = 1$. At low values of ka, the water loading exhibits a dominant $n = 0$ component of the scattering except for one frequency point where a natural resonance from the 'Upper branch' of the $n = 1$ component is dominant. On the other hand, the air loading has both $n = 0$ an $n = 1$ scattering components dominant at the same power law of (ka) and almost equal in magnitude (the latter is slightly higher), except for a small region where the natural frequencies corresponding to $n = 0$ and $n = 1$ of the 'Upper branch' are close to each other in frequency.

For the steel shell in water, the 'Lower branch' natural frequencies can be clearly identified in the behaviour of the modal amplitudes where they exhibit peaks in magnitude in the region below $ka = 1$. However, even the lowest natural resonance of the 'Upper branch' occurs at frequency in the regime where many modal scattering coefficients are dominant at the same time; thus, the 'Upper branch' cannot be easily identified in this plot. At low values of ka, the water loading makes the steel sphere exhibit behaviour similar to a rigid sphere, where the $n = 0$ and $n = 1$ scattering components are both dominant and vary as $(ka)^3/3$ and $(ka)^3/6$, respectively. However, the laws in this case are approx. $(ka)^3/5$ and $(ka)^3/22$. In the mid-frequency regime, just above $ka = 1$, the modal scattering component of orders $n > 1$ becomes dominant due to peaks corresponding to the natural frequencies of the 'Lower branch'.

For the steel shell in air, it is difficult to identify the natural frequencies of vibration in the behaviour of the modal amplitudes, given the scale on the plot. Furthermore, the 'Lower branch' and 'Upper branch' occur at relatively higher frequencies and are thus present in the regime where many modal scattering components are dominant at the same time. The modal scattering components of the spherical shell behave as those of a rigid sphere for most of the other frequency regime. This can be observed, in particular, at low values of ka, where the $n = 0$ and $n = 1$ modal scattering components are both dominant and vary as approximately $(ka)^3/3$ and $(ka)^3/6$.

Ignoring the peaks and troughs due to resonances and antiresonances, it can be observed in all figures that a hierarchy is generally maintained in the modal amplitudes at low frequency, where a higher order n translates into a less dominant behaviour, except for some cases where the $n = 0$ and $n = 1$ modal amplitudes are close in magnitude to each other. Also, as the frequency becomes larger, increasingly more orders n become simultaneously dominant at a given frequency. These two characteristics are shared by a locally-reacting impedance sphere in a fluid.

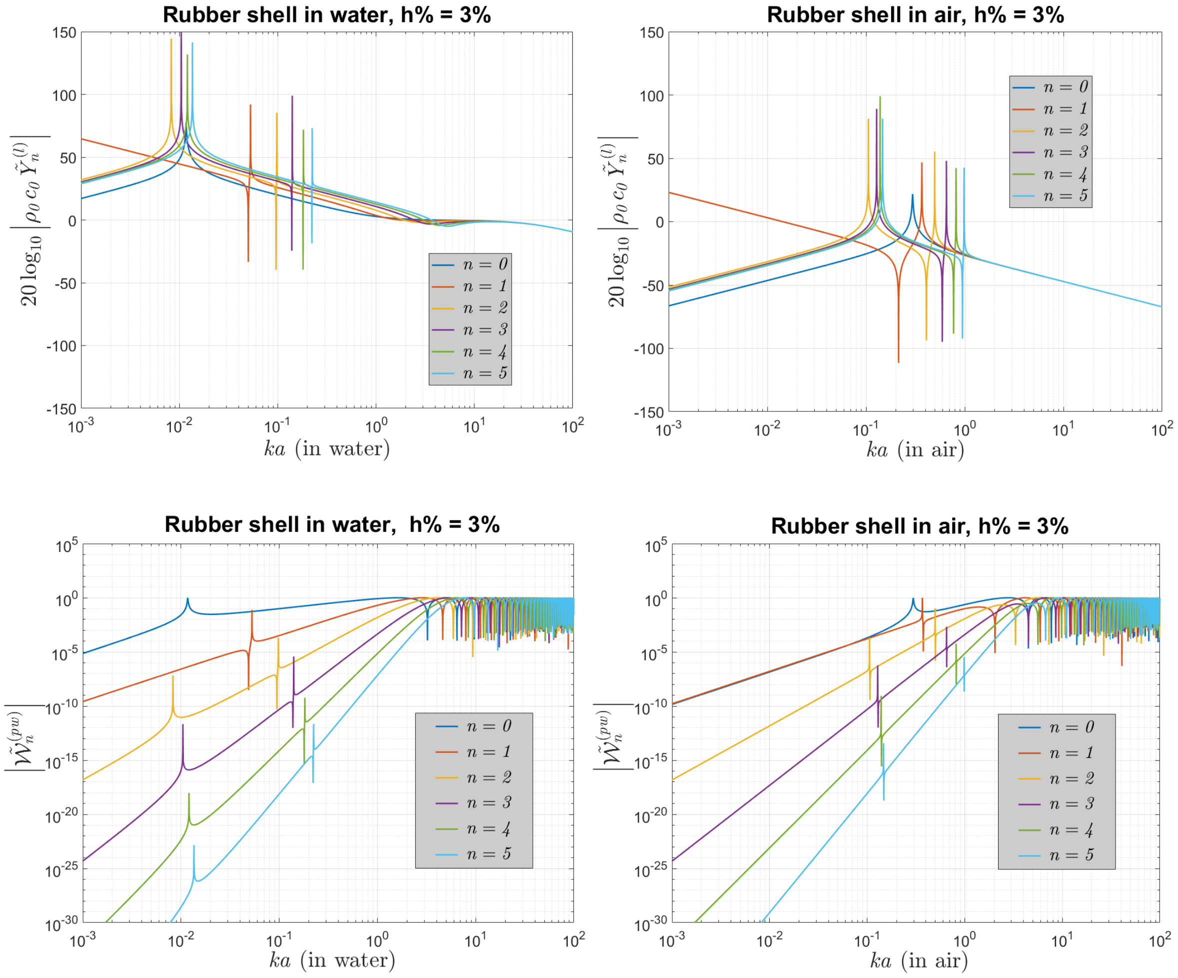

Figure 6-7 Normalized modal wave admittance versus normalized frequency ka (first row) and modal frequency weightings of scattering coefficients due to plane-wave incidence (second row), for the first few modal orders n, given a thin spherical shell made of natural rubber loaded externally by either water (first column) or air (second column).

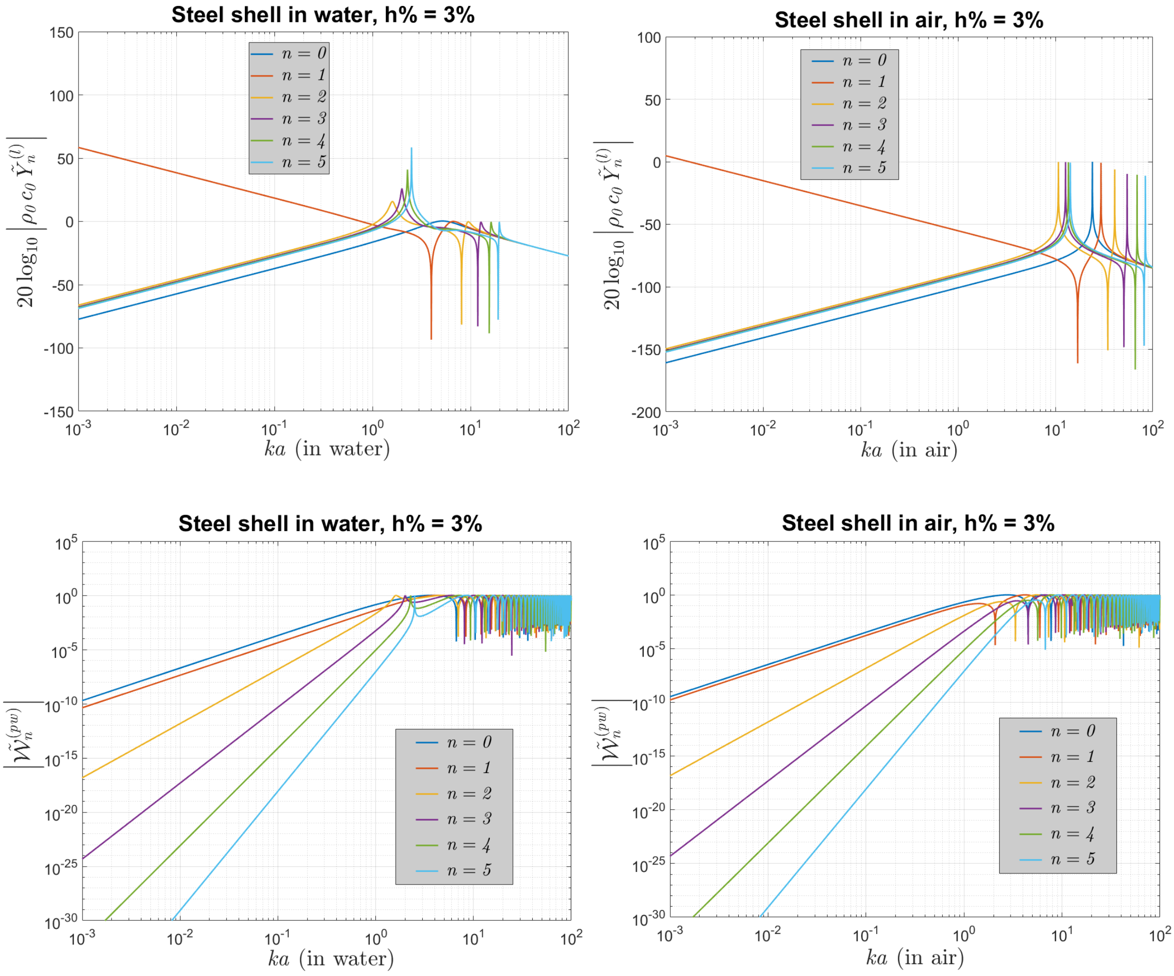

Figure 6-8 Normalized modal wave admittance versus normalized frequency ka (first row) and modal frequency weightings of scattering coefficients due to plane-wave incidence (second row), for the first few modal orders n, given a thin spherical shell made of steel loaded externally by either water (first column) or air (second column).

6.3.3 The scattered sound power

In Figure 6-9 and Figure 6-10, the plots of the modal frequency weightings of the scattering coefficients from the previous subsection are again presented alongside plots of the normalized scattered sound power $\widetilde{\Pi}_s$ for the natural rubber shell and, respectively, the steel shell. Each shell is submerged either in air or in water. The scattered power was computed in MATLAB using $N = 100$ terms in the spherical harmonic series for the given frequency range, as in previous chapters. The scale on the plots for rubber shells is different from that on the plots for the steel shells in order to accommodate a clear presentation of the results in each case.

For the natural rubber shell, when submerged in water, comparing the frequency weightings and scattered power in the used frequency range leads to the conclusion that the first peak in the scatter power occurs due to the 'Upper branch' resonant peak of the $n = 0$ scattering component, which is significantly more dominant that all other contributions. The following and only other peak is generated by the 'Upper branch' resonance of the $n = 1$ scattering component. All other resonant frequencies of the 'Lower branch' and 'Upper branch' seem to ultimately not generate peaks in the scattered power. After these two peaks in the scattered power, which occur at very low values of ka, the rubber shell in water behaves like a soft spherical scatterer.

In the case of the rubber shell submerged in air, four peaks can be identified in the scattered power. The first one corresponds roughly to the 'Lower branch' resonance of the $n = 2$ component and is relatively small. The other three correspond roughly to the first three resonant frequencies of the 'Upper branch'; the first peak is dominated by the $n = 0$ scattering components, the second peak is dominated by both the $n = 0$ and $n = 1$ scattering component, and the third peak is dominated by all three $n = 0$, $n = 1$ and $n = 2$ scattering components. After these three peaks, subsequent resonances do not cause further peaks at higher frequencies and the spherical shell behaves in a similar way to rigid spherical scatterer.

For the steel shell, when submerged in water, comparing the set of two corresponding plots leads to the conclusion that the clearly identified set of peaks that are close to each other occur due to a combination of many components. This combination is formed by rigid-like contributions of the $n = 0$ and $n = 1$ scattering components, together with the peaks corresponding to higher orders n of the 'Lower branch'. The first distinguishable peak occurs at the 'Lower branch' resonant frequency of $n = 2$. At low values of ka, the scattered power of the spherical shell is proportional to the same power law as a rigid sphere, but scaled down (i.e. less scattering). At large values of ka, the behaviour of the spherical shell is almost the same as a rigid spherical scatterer, with the exceptions of some relatively small in magnitude artefacts, generated by the contributions of the resonant peaks in the 'Upper branch'.

In the case of the steel shell submerged in air, the scattered power of the spherical shell is almost the same as that of a rigid spherical scatterer except for some very small peaks at higher frequencies. It is difficult to distinguish which peak occurs first from the scale on the plot. Furthermore, the peaks are present in the regime of ka where many spherical harmonic components contribute significantly to the scattered power at the same time, which makes it further difficult to establish individual component contributions to the peaks in the power from the two types of used plots.

The admittance plots of the fluid-loaded shells shown in the previous subsection thus illustrate the natural frequencies and dynamic behaviour of the structure, while the plots of modal frequency weightings of the scattering coefficients illustrate how the different modes couple into the external fluid. A combination these results the allows then allows the interpretation of the plots depicting scattered sound power as a function of frequency in the various cases of shells. These cases vary from being almost entirely soft above $ka = 0.1$ for the rubber shell in water, to almost entirely hard for most of the frequency range in the case of the steel shell in air.

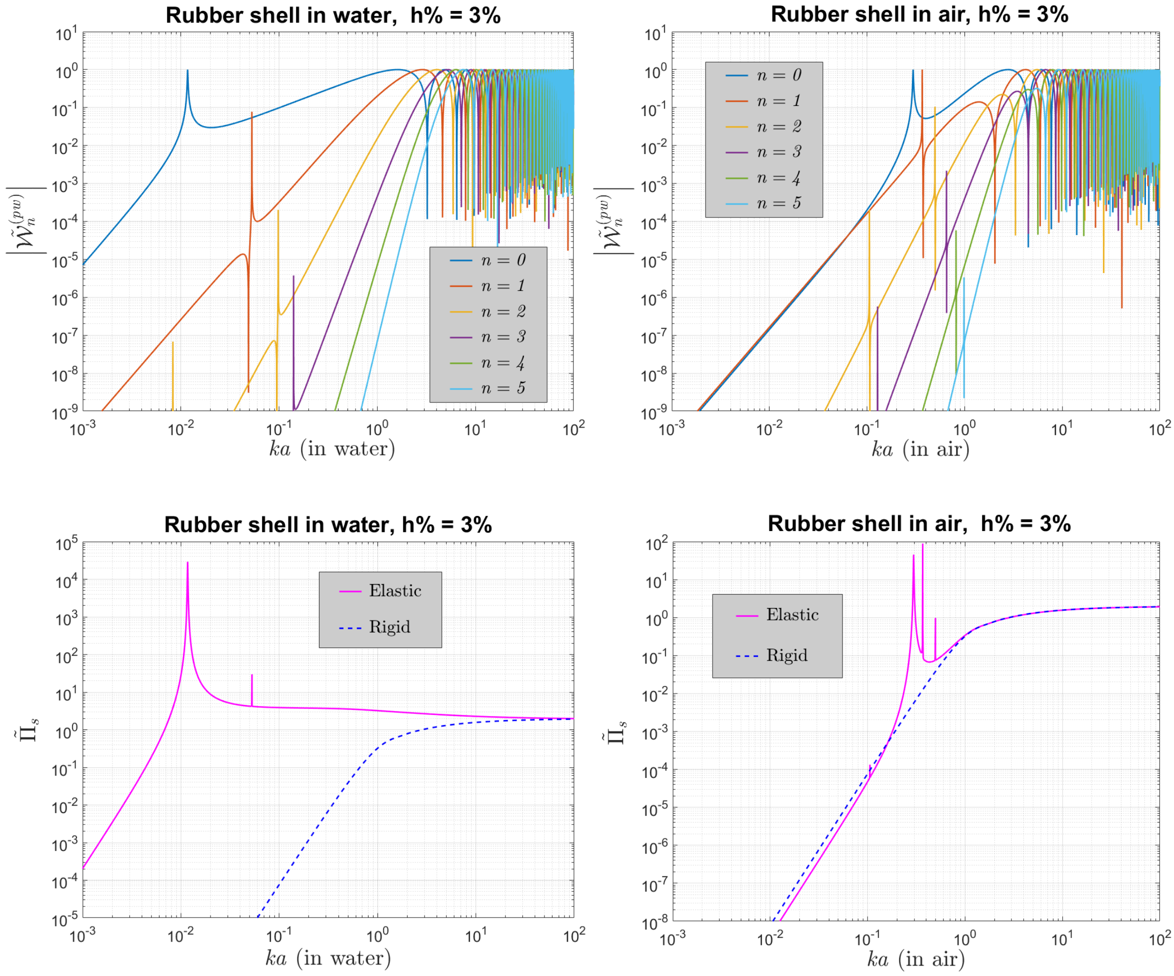

Figure 6-9 Modal frequency weightings of scattering coefficients due to plane-wave incidence for the first few values of orders n (first row), and normalized scattered sound power due plane-wave incidence, given a thin spherical shell made of natural rubber loaded externally by either water (first column) or air (second column).

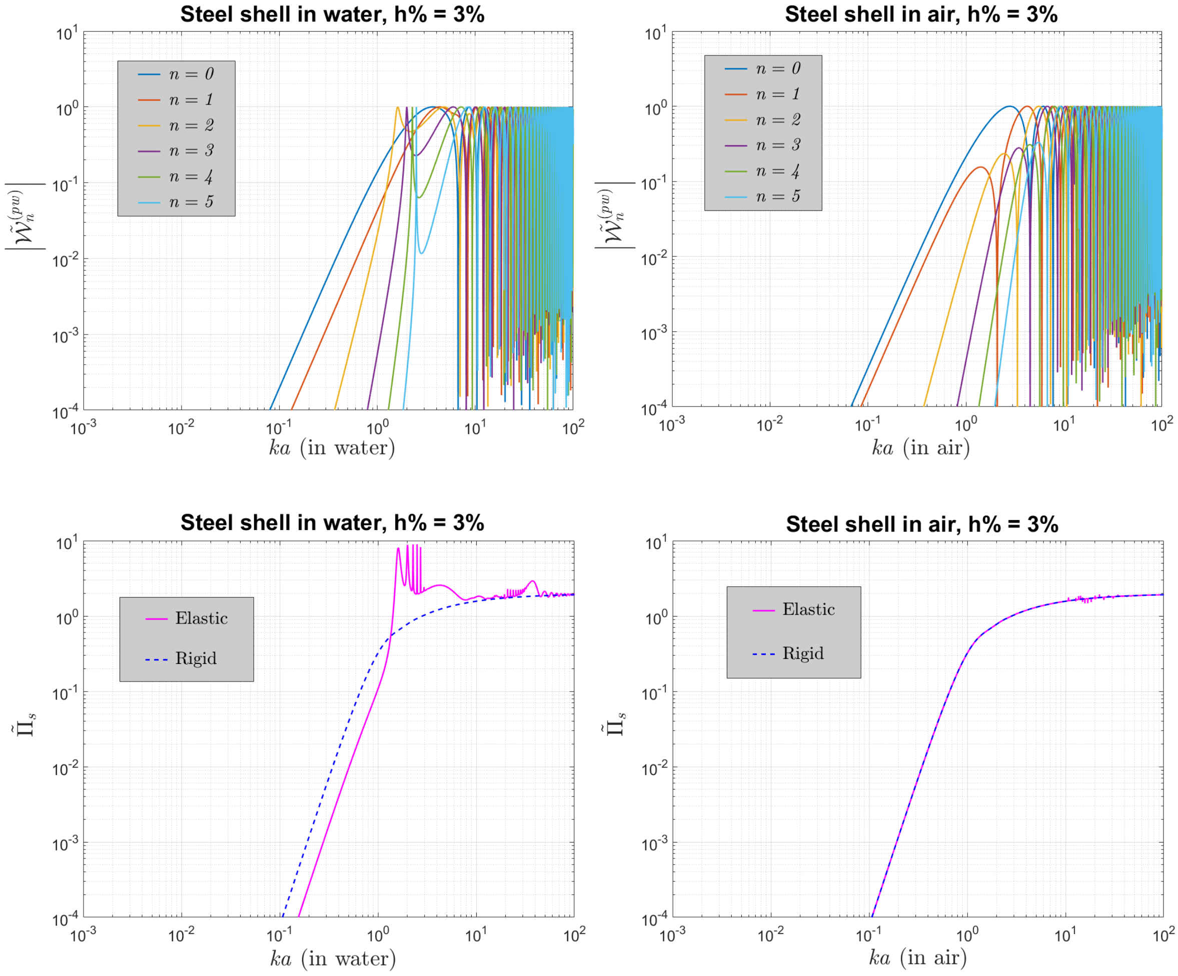

Figure 6-10 Modal frequency weightings of scattering coefficients due to plane-wave incidence for the first few values of orders n (first row), and normalized scattered sound power due plane-wave incidence, given a thin spherical shell made of steel loaded externally by either water (first column) or air (second column).

The 'silver alloy' spherical shell described by equations (6.30) – (6.32) is exemplified in Figure 6-11 when it comes to normalized scattered sound power versus ka. This is done for water as the surrounding medium and the behaviours of a soft sphere and rigid sphere, as well as those of the thin spherical shell made of rubber and of the thin spherical shell made of steel, are included for comparison. From the plot, at low values of $ka < 1$, it is observed that the passive optimization of the shell to cancel the $n = 0$ and $n = 1$ components in the plane-wave scattering has a significant effect. The normalized scattered power from the 'silver alloy' shell is a couple of orders of magnitude lower than those corresponding to the rigid sphere and steel shell. However, the passive optimization leads to the first few peaks in the scattered power of the 'silver alloy' shell being significantly strong. Also, these are higher than the first few peaks of the steel shell case and higher than the power of a soft sphere, but not as strong as the two peaks in the case of the rubber shell. In terms of normalized frequency, the first few peaks of the 'silver alloy' are situated between those of the rubber shell and those of the steel shell, i.e. around and slightly above $ka = 1$, transitioning past the low frequency regime.

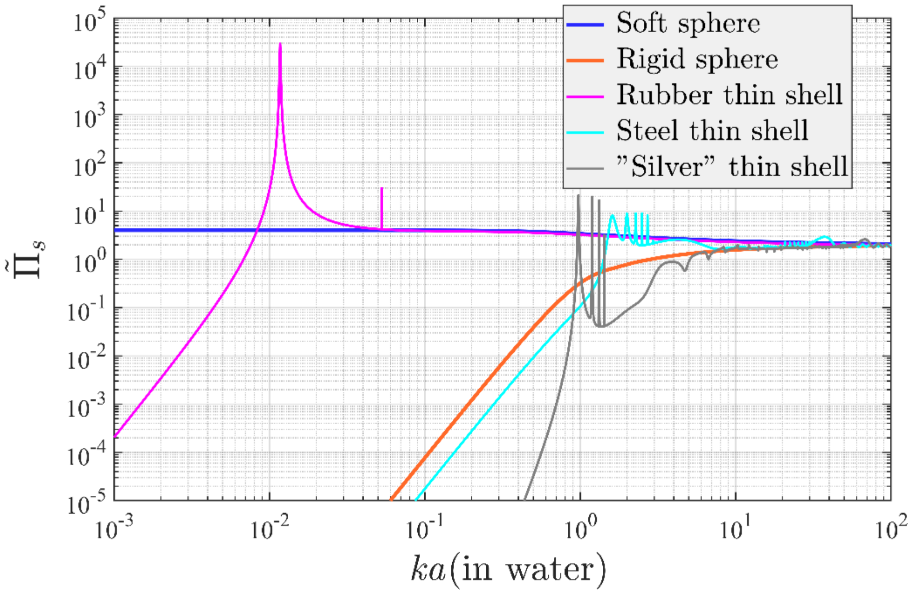

Figure 6-11 The normalized scattered sound power versus ka, when in water, for the soft $\tilde{\zeta} = 0.01$ sphere, the hard $\tilde{\zeta} = 100$ sphere, the thin spherical shell made of rubber, the thin spherical shell made of steel, and the thin spherical shell made of the 'silver alloy'.

6.4 Radiation due to a point-monopole on the surface of the shell

In order to compute and analyse the effect of active sound control using acoustic secondary sources on the surface of the shell, which is covered in Chapter 7, the sound radiation due to such sources must first be calculated. Similar to the progression from section 4.1 to section 4.3, a point-monopole with acoustic strength $\tilde{q}$ is first allowed to radiate in the exterior fluid at a position (r', θ', φ'), some distance away from the scatterer. This distance is brought down to $r' = a$, such that the new situation represents a source radiating from a baffle which is the spherical structure, thus acoustic pressure is created in the exterior fluid and on the surface of the shell, excluding the singularity at (a, θ', φ'). As in section 4.3, this acoustic pressure takes the form,

$$\tilde{p}_{pm}(\vec{r}) = \tilde{q} \sum_{n=0}^{\infty} \sum_{m=-n}^{n} \widetilde{D}_{n,m}^{(\mathbb{C},pm)}\, h_n(kr)\, Y_{n,m}^{(\mathbb{C})}(\theta, \varphi) \ , \qquad (6.33)$$

where the radiation coefficients are

$$\widetilde{D}_{n,m}^{(\mathbb{C},pm)} = \frac{\rho_0 c_0}{a^2}\, \widetilde{\mathcal{W}}_n^{(pm)}(a, \tilde{\zeta}_n, ka)\, \bar{Y}_{n,m}^{(\mathbb{C})}(\theta', \varphi'), \qquad (6.34)$$

and the modal frequency weightings are

$$\widetilde{\mathcal{W}}_n^{(pm)}(a, \tilde{\zeta}_n, ka) = \frac{\tilde{\zeta}_n}{h_n(ka) + i\tilde{\zeta}_n h_n'(ka)} \ . \qquad (6.35)$$

$ka \ll 1$	Rigid	Water - rubber	Air - rubber	Water - steel	Air - steel
$\widetilde{\mathcal{W}}_0^{(pm)}$	$(ka)^2$	$(ka)^2$	$(ka)^2$	$(ka)^2$	$(ka)^2$
$\widetilde{\mathcal{W}}_1^{(pm)}$	$0.5\ (ka)^3$	$0.0717(ka)^3$	$0.4964(ka)^3$	$0.2904(ka)^3$	$0.4996(ka)^3$
$\widetilde{\mathcal{W}}_2^{(pm)}$	$\frac{1}{9}(ka)^4$	$\frac{1}{9}(ka)^4$	$\frac{1}{9}(ka)^4$	$\frac{1}{9}(ka)^4$	$\frac{1}{9}(ka)^4$

Table 6-5 Asymptotic behaviour for first few indices of frequency weighting $\widetilde{\mathcal{W}}_n^{(pm)}(a, \tilde{\zeta}_n, ka)$ of the coupling coefficients belonging to an acoustic point-monopole radiating from on the surface of different elastic spherical shells surrounded by certain fluids.

6.4.1 Low frequency asymptotes for modal frequency weightings of radiation

Using the asymptotic behaviour at low ka of the mechanical modal impedance from formulas (6.10), (6.11) and (6.12) together with the asymptotic behaviour at low ka of the modal frequency weightings from Table 4-2, and combining everything in (6.35) leads to the asymptotes of the modal frequency weightings $\widetilde{\mathcal{W}}_n^{(pm)}$ of the coupling coefficients belonging to an acoustic point-monopole radiating from on the surface of different elastic spherical shells surrounded by certain fluids. These asymptotes are compiled in Table 6-5. It is important to note that, interestingly, the point-monopole on the surface of the shell at low frequencies has the $n = 0$ and $n \geq 2$ components behaving as those for radiation from a rigid sphere. As a result, the behaviour of the $n = 1$

component solely distinguishes the radiation from the elastic shell from that corresponding to the rigid sphere case. And even so, the low ka behaviour of the $n = 1$ component in the case of air – rubber and air – steel are approximately the same to that of the rigid sphere.

6.4.2 The radiation coefficients and their modal frequency weightings

Figure 6-12 sows the magnitude of the modal frequency weightings $\widetilde{\mathcal{W}}_n^{(pm)}$ for the point-monopole radiation coefficients, in the case of the natural rubber shell and, respectively, the steel shell. Each shell is submerged either in air or in water. In the figure, it can be observed that at low ka, up to the corresponding first resonance, there is a hierarchy of modal orders n, where a lowest order is more dominant. All cases of material combinations are dominated in this frequency region solely by the $n = 0$ omnidirectional component, and exhibit $\widetilde{\mathcal{W}}_n^{(pm)}$ increasing with frequency in the same way for all modal orders at large ka.

For the rubber shell cases, the ‘Upper branch’ and ‘Lower branch’ of resonances can be clearly distinguished in Figure 6-12 for both water and air, where the first peak belongs to the ‘Lower branch’ and is dominated by the combined effect of the non-resonant behaviour of the $n = 0$ component and the ‘Lower branch’ resonance of the $n = 2$ component, which is lower in magnitude. The next three subsequent peaks are dominated, respectively, by solely the ‘Upper branch’ resonance of the $n = 0$ component, solely the ‘Upper branch’ resonance of the $n = 1$, and solely the ‘Upper branch’ resonance of the $n = 2$.

For the steel shell in air, the results in Figure 6-12 are similar to the behaviour exhibited for the rigid sphere shown in Figure 4-5c, and the ‘Upper branch’ and ‘Lower branch’ of resonances cannot be distinguished. For the steel shell in water, the distinguishable peaks belong to the ‘Lower branch’, where the first resonance that occurs is dominated by the non-resonant behaviour of the $n = 0$ component and the ‘Lower branch’ resonance of the $n = 2$ component. The subsequent two peaks are dominated by the ‘Lower branch’ resonances of the $n = 3$ and, respectively, $n = 4$ components, with some contribution of the non-resonant behaviour of $n = 0$ and $n = 1$ components. The ‘Upper branch’ is not distinguishable in Figure 6-12 for this case.

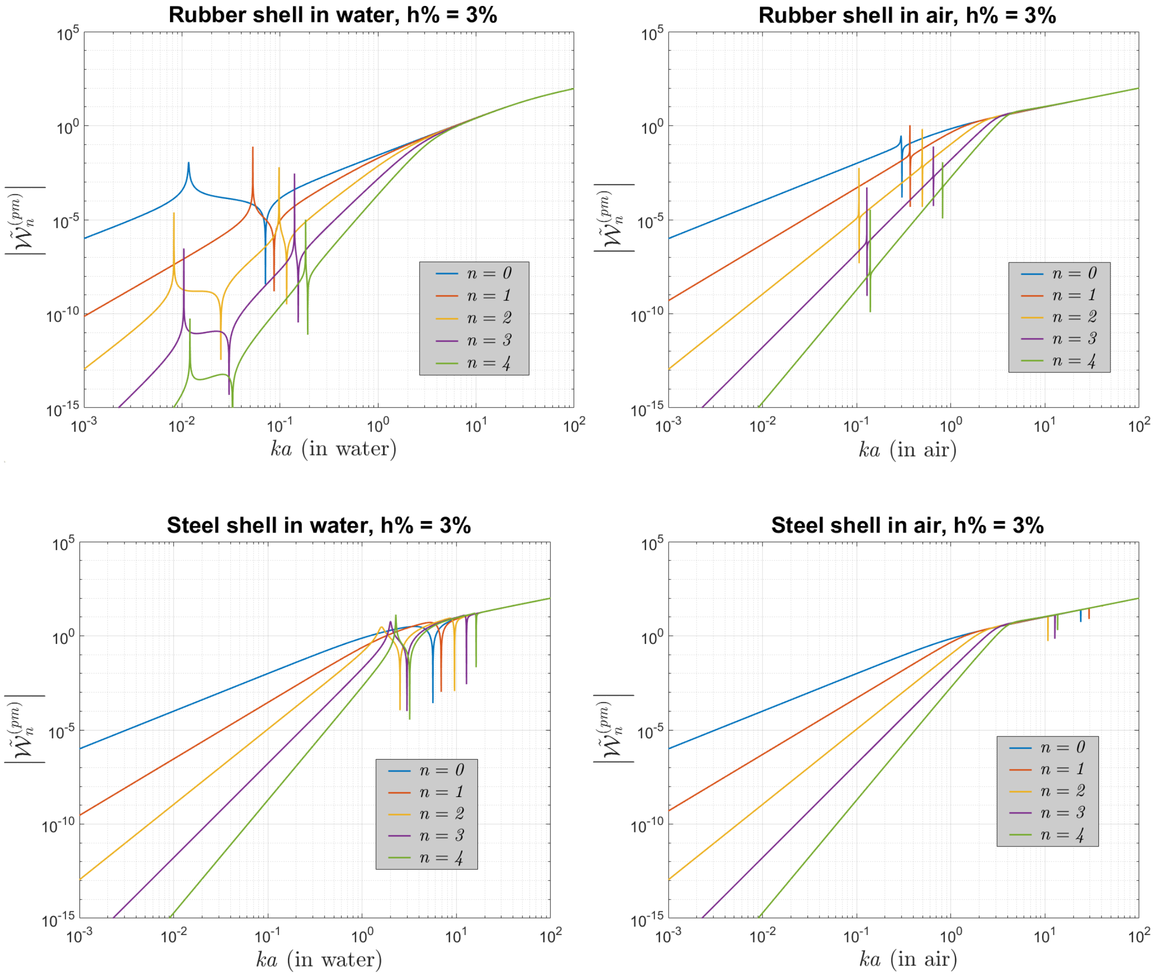

Figure 6-12 Modal frequency weightings of point-monopole radiation coefficients for the first few values of n, when on the surface of a thin spherical shell made of rubber (first row) or steel (second row), loaded externally by either water (first column) or air (second column).

6.5 Radiation due to a point-force acting on the surface of the shell

An alternative form of secondary actuator for the thin spherical shell is a force acting on its surface, pointed in the direction of the outward normal. In order to compute and analyse the effect of active sound control using point-forces exciting on the surface of the shell into radiation, which is covered in Chapter 7, the sound radiation due to such forces must first be calculated.

A point-force of magnitude $\tilde{F}$ acting on the surface of the shell at position (θ', φ'), in the direction of the outward normal, generates a pressure field in the exterior fluid equal to [65]

$$\tilde{p}_{pf}(\vec{r}) = \tilde{F} \sum_{n=0}^{\infty} \sum_{m=-n}^{n} \widetilde{D}_{n,m}^{(\mathbb{C},pf)} \, h_n(kr) \, Y_{n,m}^{(\mathbb{C})}(\theta,\varphi) \ , \tag{6.36}$$

where the radiation coefficients are

$$\begin{aligned} \widetilde{D}_{n,m}^{(\mathbb{C},pf)} &= -i\rho_0 c_0 \frac{1}{a^2} \frac{1}{h_n'(ka)} \frac{1}{\tilde{Z}_n + \tilde{z}_n} \bar{Y}_{n,m}^{(\mathbb{C})}(\theta',\varphi') = \\ &= \frac{1}{a^2} \frac{1}{h_n(ka) + i\,\tilde{\zeta}_n\, h_n'(ka)} \bar{Y}_{n,m}^{(\mathbb{C})}(\theta',\varphi') \ , \end{aligned} \tag{6.37}$$

and the modal frequency weightings are

$$\widetilde{\mathcal{W}}_n^{(pf)}\big(a,\tilde{\zeta}_n,ka\big) = \frac{1}{h_n(ka) + i\,\tilde{\zeta}_n\, h_n'(ka)} = \widetilde{D}_{n,m}^{(\mathbb{C},pf)} / \left[\frac{1}{a^2} \bar{Y}_{n,m}^{(\mathbb{C})}(\theta',\varphi')\right]. \tag{6.38}$$

$ka \ll 1$	Water - rubber	Air - rubber	Water - steel	Air - steel
$\widetilde{\mathcal{W}}_0^{(pf)}$	$21276.6i\frac{(ka)^3}{3}$	$1.4236i\frac{(ka)^3}{3}$	$0.4095i\frac{(ka)^3}{3}$	$2.73 \times 10^{-5} i(ka)^3/3$
$\widetilde{\mathcal{W}}_1^{(pf)}$	$-0.8566\, i(ka)^2$	$-71.8 \times 10^{-4} i(ka)^2$	$-0.4191 i(ka)^2$	$-8.72 \times 10^{-4} i(ka)^2$
$\widetilde{\mathcal{W}}_2^{(pf)}$	$4273.5\, i(ka)^5$	$0.28923\, i(ka)^5$	$0.05464\, i(ka)^5$	$3.65 \times 10^{-6}\, i(ka)^5$

Table 6-6 Asymptotic behaviour for first few indices of frequency weighting $\widetilde{\mathcal{W}}_n^{(pf)}(a,\tilde{\zeta}_n,ka)$ of the coupling coefficients belonging to point-force exciting the surface of different elastic spherical shells surrounded by certain fluids into acoustic radiation.

6.5.1 Low frequency asymptotes for modal frequency weightings of radiation

Using the asymptotic behaviour at low ka of the mechanical modal impedance from formulas (6.10), (6.11) and (6.12) together with the asymptotic behaviour at low ka of the spherical Hankel functions, and combining everything in (6.38) leads to the asymptotes of modal frequency weightings $\widetilde{\mathcal{W}}_n^{(pf)}$ of the coupling coefficients belonging to a point-force exciting the surface of different elastic spherical shells surrounded by certain fluids into acoustic radiation. These asymptotes are compiled in Table 6-6. It is important to highlight that the point-force on the surface of the shell at low frequency has the $n = 1$ component as the dominating one. This is followed by the $n = 0$ and then $n = 3$, $n = 4$ and so on. Between the used material combinations, the largest $n = 1$ component in magnitude is exhibited by the rubber shell in water, followed by the steel shell in water, the steel shell in air, and the rubber shell in air. The largest $n = 0$ component in magnitude is manifested by the rubber shell in water, followed by the rubber shell in air, the steel shell in water, and the steel shell in air, but all have a leading order power of (ka) that is higher than that of the corresponding $n = 1$ components, while also being lower than that of the corresponding $n = 2$ components.

6.5.2 The radiation coefficients and their modal frequency weightings

Figure 6-13 shows the magnitude of the modal frequency weightings $\widetilde{\mathcal{W}}_n^{(pf)}$ for the point-force excited radiation coefficients, in the case of the natural rubber shell and, respectively, the steel shell. Each shell is submerged either in air or in water. In the figure, it can be observed that at low ka, there is a hierarchy of modal orders n, where the $n = 2$ component dominates, followed by the $n = 0$ component and then the $n = 3$, the $n = 4$ and so on. The largest magnitude differences between $n = 1$ and $n = 0$ components in this ka regime are observed for the steel shells, in particular, the steel shell in air. For the rubber shell in either fluid, as frequency increases while still at low ka, and up to the first corresponding resonance, the $n = 0$ component eventually becomes dominant over the $n = 1$ component, such that the hierarchy becomes ‘a lower order has a larger magnitude’ for a narrow range of frequencies. This does not occur for the steel shells.

In Figure 6-13, for all combinations of materials, both the ‘Lower branch’ and ‘Upper branch’ resonances are distinguishable. The first peak is exhibited by the ‘Lower branch’ resonance of the $n = 2$ component, which is dominant, with the exception of the rubber shell in water, for which the $n = 2$ ‘Lower branch’ resonance is very close to and smaller in magnitude than the $n = 0$ ‘Upper branch’ resonance. After the first peak, the rubber shell in water manifests a peak dominated by the ‘Upper branch’ of the $n = 1$ component, and the rubber shell in air manifests a peak dominated by the ‘Upper branch’ of the $n = 0$ component. After the first peak, the steel shell in water exhibits a peak dominated by the ‘Lower branch’ of the $n = 3$ component, and the steel shell in air exhibits peaks corresponding to the ‘Lower branch’ resonances for $n = 3$, $n = 4$ and so on, which are very close to the $n = 2$ one; this proximity is followed by peaks corresponding to the dominant resonances in the ‘Upper branch’ belonging to $n = 0$, $n = 1$, $n = 2$ and so on.

By comparing Figure 6-12 and Figure 6-13, it becomes clear that the point-force surface actuator excites the n=1 component of radiation more strongly than the acoustic point-monopole on the surface. Also, the point-force couples more efficiently into the higher frequency resonances of the loaded structure, as can be seen by comparing the magnitudes of the peaks between Figure 6-12 and Figure 6-13 for corresponding types of shell. In particular, the point-force couples very well into the higher-order resonances of the steel shell in air.

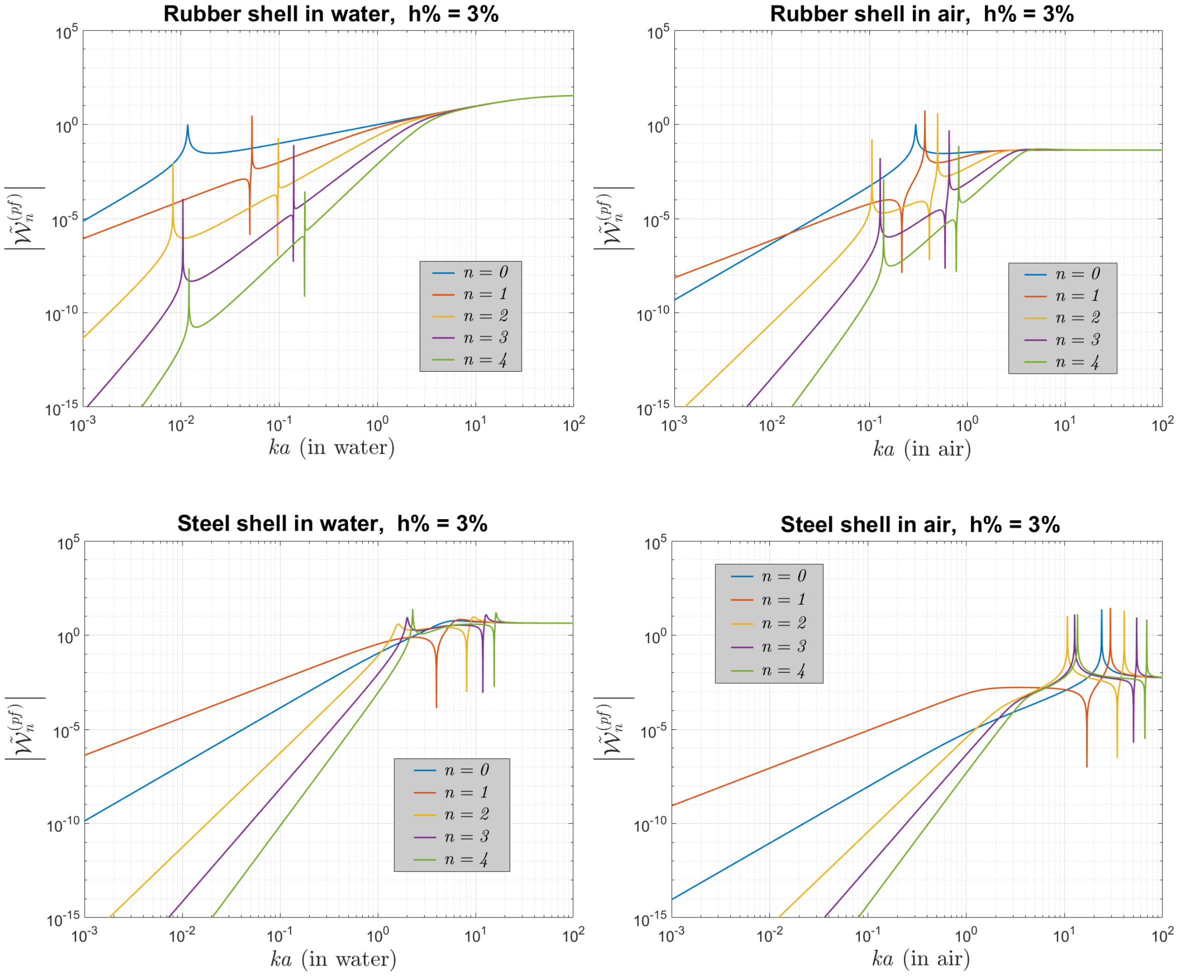

Figure 6-13 Modal frequency weightings of point-force excited radiation coefficients for the first few values of orders n, when on the surface of a thin spherical shell made of rubber (first row) or steel (second row), loaded externally by either water (first column) or air (second column).

6.6 Chapter summary

This chapter has presented a spherical harmonic analysis of the 3D sound radiation generated by a thin, uniform, empty spherical shell, when surrounded by a fluid and excited via one of two different mechanisms. The shell is set into harmonic motion via direct excitation of its outer surface or via the motion of the fluid. The situation was modelled using thin shell theory based on Love`s first approximations, as in [65], which leads to the sound scattering from the structure and the sound radiation generated by the structure being characterized only by the dynamic motion of its outer surface. This motion is governed by a modal impedance that depends on frequency and on the material properties of the shell, as well as the fluid. However, such a model accurately describes the physics of the situation only up to a certain frequency, which is also dictated by the fluid – structure combination of materials.

The formulations in [65] that describe the 3D sound scattering and 3D radiation involving the thin spherical shell only consider axisymmetric motion, first when in vacuum and, then, when loaded by the fluid through the exploitation of linearity and reciprocity. This leads to a simplified series expansions based on Legendre polynomials; however, these expansions were extended to spherical harmonic in order to also account for motion that is not axisymmetric. A property of the used shell model is that the modal surface impedance at the separation boundary remains the same for axisymmetric and non-axisymmetric motion.

In this chapter, the modal impedances of the shell when in vacuum and when loaded by the fluid were first studied. These exhibit zeroes and resonant poles at different frequencies, which contrasts the impedance sphere from the previous chapters. Secondly, physical quantities such as scattered/radiated sound pressure in the fluid and scattered/radiated sound power were investigated using spherical harmonic representations. The relation between these quantities and the surface impedance was monitored when changing the fluid – structure material combination between four representative cases. This was done with computer-modelled results for an incoming monochromatic plane-wave impinging on the shell, for exciting the exterior fluid and shell via a monochromatic point-monopole on the separation boundary, and for exciting the shell in motion with a monochromatic point-force on its outer surface. The previous entities were respectively placed ideally relative to the scatterer, i.e. on the z-axis. It was found that the zeros and resonant poles of the surface impedance can produce noticeable peaks and troughs in the frequency domains of the quantities describing scattering or radiation. Furthermore, the choice of involved materials can place these peaks and troughs at higher or lower frequencies relative to the size of the scatterer. Similar to Chapter 4, it was established that the low frequency regime before the first resonant peak is dominated by the first few components, which form a hierarchy based on index n, while many components dominate in the high frequency regime at the same time. However, in the first regime, the point-monopole is dominated by the omnidirectional $n = 0$ component (breathing mode) while the point-force is dominated by the figure-of-eight $n = 1$ component (translational mode). The asymptotic behaviour of the spherical harmonic coefficients was again used to make analytical predictions at low frequencies.

The content in this chapter is later used to exemplify the effect of tonal active control on suppressing sound scattering, when employing either:

- the feedforward control strategy outlined in subsection 3.3.1, which is equivalent to the idealized control described in subsection 2.4.2, or
- the velocity feedback control strategy outlined in subsection 3.3.2.

The example results for control are contained in Chapter 7, where the primary is represented by the scattering of a plane-wave from the impedance sphere and the secondary is represented either by point-monopoles radiating on the surface of the spherical shell, or by point-forces exciting the surface of the shell into harmonic motion.

Chapter 7 Active Control of Sound Scattering from Thin, Uniform, Empty, elastic Spherical Shell in a Fluid

In this chapter, centralized control in the form of active tonal suppression is exemplified with computer-modelled results for the sound scattering from a thin, uniform, empty, elastic spherical shell. These are obtained from the spherical harmonic representations discussed in Chapter 4. The analysis pursues a straightforward case where the incidence is represented by a single monochromatic plane-wave and the secondary is represented by a small number of either point-monopole sound radiators on the exterior surface of the shell or point-forces exciting the exterior surface of the shell into acoustic radiation.

The chapter initially covers examples that represent the ideal outcomes from solving the mathematical models presented in Chapter 2 without taking into consideration practical limitations. This is equivalent to investigating a feedforward active control arrangement, where all physical quantities are known at all times. Once again, the modal frequency weighting of the scattering coefficients and of the coupling coefficients belonging to the acoustic source or point-force excited radiations are used in the formulations from subsection 2.4.2 to calculate the optimum performance when minimizing scattered sound power. Results are computed for the combinations of surrounding fluids and shell materials highlighted in Chapter 6, where either one secondary entity is placed in the backscattering position $\theta = \pi$, or two secondary entities are placed in the $\theta = \pi$ and $\theta = 0$ positions. An analysis of the asymptotic behaviour after control at low values of normalized frequency ka is performed, where calculations are done in the same way as in Chapter 5 for the uniform impedance sphere scatterer.

The results of practical-oriented velocity feedback control discussed in Chapter 3 is then exemplified and discussed when using a co-located point-force control actuator and point velocity sensor in the backscattering position, for the steel shell in water.

7.1 Ideal active control with small number of surface radiators

For ideal active control with a small number of point-monopole control sources on the exterior surface of the shell, the two studied arrangements are depicted schematically in Figure 7-1. These consist of a monochromatic plane-wave of unit magnitude as the arriving incidence, which produces a scattered pressure that represents the primary. This is placed along the z-axis, travelling from minus to plus. In the first instance, one point-monopole secondary source is placed in the $\theta = \pi$ position. Then, two point-monopoles are placed at $\theta = \pi$ and $\theta = 0$ respectively. In these arrangements, the spherical harmonic formulations defined in Chapter 6 for the primary, i.e. expression (6.22), and the secondary, i.e. expression (6.33), consist of only the terms that have $m = 0$, as all other terms do not contribute. Only the $m = 0$ spherical harmonic components are used when computing the active control results.

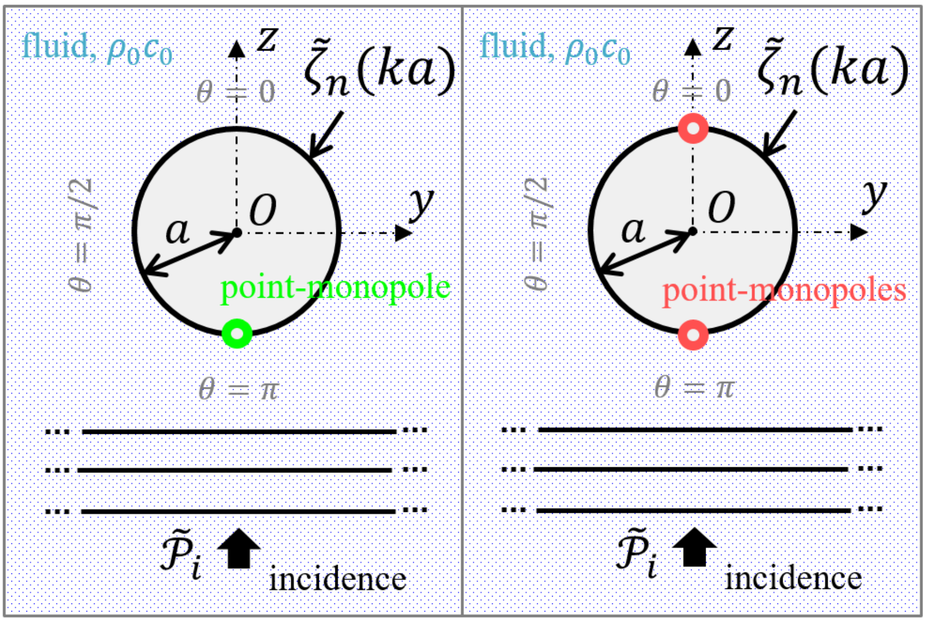

Figure 7-1 2D view of 3D arrangements of secondary point-monopoles for the study of tonal active control of scattering in the case of an incoming monochromatic plane-wave impinging on the thin spherical shell.

7.1.1 Active control with one surface radiator

In Figure 7-2, Figure 7-3, Figure 7-4 and Figure 7-5, the ideal active control results with one point-monopole in the backscattering direction ($\theta = \pi$) are presented for the rubber shell in water, the rubber shell in air, the steel shell in water and, respectively the steel shell in air. The scale on the plots for rubber shells is different from that on the plots for the steel shells in order to accommodate a clear presentation of the results in each case. $N = 100$ terms were calculated in MATLAB for the spherical harmonic series of the scattered power and for the tonal power minimization over the shown frequency range.

Similar to Chapter 5 and [78], an analysis can be performed at low ka to predict the behaviours of the involved modal frequency weightings of the spherical harmonic coefficients. As seen in Figure 7-2 to Figure 7-5, the primary is dominated by the $n = 0$ and $n = 1$ components with the exception of the rubber shell in water, which is dominated only by the $n = 0$ component. The secondary for all four combinations is dominated by the $n = 0$ component. For these circumstances, assuming that the power minimization described in subsection 2.4.2 completely cancels the leading order power of (ka) for the $n = 0$ component in the primary at low frequencies, the normalized optimal source strength is

$$\tilde{q}_{opt}\frac{\rho_0 c_0}{4\pi\,\tilde{\mathcal{P}}_i\,a^2} = \frac{\widetilde{\mathcal{W}}_0^{(pw)}\left(\tilde{\zeta}_0, ka\right)}{\widetilde{\mathcal{W}}_0^{(pm)}\left(a, \tilde{\zeta}_0, ka\right)}, \tag{7.1}$$

which leaves the dominant residual after control as

$$\widetilde{\mathcal{W}}_1^{(c)}\left(\tilde{\zeta}_1, ka\right) = i\widetilde{\mathcal{W}}_1^{(pw)}\left(\tilde{\zeta}_1, ka\right) + \frac{\widetilde{\mathcal{W}}_1^{(pm)}\left(a, \tilde{\zeta}_1, ka\right)}{\widetilde{\mathcal{W}}_0^{(pm)}\left(a, \tilde{\zeta}_0, ka\right)}\,\widetilde{\mathcal{W}}_0^{(pw)}\left(\tilde{\zeta}_0, ka\right), \tag{7.2}$$

Using the values in Table 6-4 and Table 6-5, the optimized source strengths from (7.1) are $0.3333i(ka)$ for the steel shell in air, $0.1968i(ka)$ for the steel shell in water, $0.1412i(ka)$ for the rubber shell in air, and $7091.8666i(ka)$ for the rubber shell in water. In (7.2), the first term dominates the outcome after control for all material combinations, which yields $\widetilde{\mathcal{W}}_1^{(c)}$ after control equal to $0.1662i(ka)^3$ for the steel shell in air, $-0.0429i(ka)^3$ for the steel shell in water, $0.1631i(ka)^3$ for the rubber shell in air, and $-0.2616i(ka)^3$ for the rubber shell in water. These residuals represent the $n = 1$ component in the primary unaltered by the power minimization and correspond to normalized scattered sound powers after control equal to $0.3316(ka)^4$ for the steel shell in air, $0.0221(ka)^4$ for the steel shell in water, $0.3191(ka)^4$ for the rubber shell in air, and $0.8214(ka)^4$ for the rubber shell in water. The hierarchy based on orders is maintained for $n \geq 2$

after control. The values of the optimal source strengths, the modal frequency weightings after control, and the normalized scattered sound power after control all match the simulated results at low values of ka from Figure 7-2 to Figure 7-5, thus confirming the assumption that the power minimization suppressed the $n = 0$ spherical harmonic component in the primary at low ka as described above.

The rubber shell in air exhibits both $n = 0$ and $n = 1$ components dominant at low frequencies with the same power law of ka and approximately the same magnitude. Even so, due to the nature of the secondary, the power minimization is able to suppress the $n = 0$ component of the primary, in which the secondary couples best, without altering the $n = 1$ component. In this context, the coupling at a given frequency is better when the magnitude of the secondary is low compared to that of the primary by a smaller amount, or when the magnitude of the secondary is big compared to that of the primary by a larger amount.

At large values of ka, the active control does not produce any suppression due to multiple spherical harmonic components being dominant simultaneously while only one control parameter can be optimized. In terms of resonances after control, the rubber shell in water, for which the peaks in scattered sound power before control occur at relatively low ka, exhibits a significant change in the positions and magnitudes of peaks and troughs after control. Even so, in this case, the magnitude of all peaks after control is lower than the magnitude of the primary, as seen in Figure 7-2. The rubber shell in air and the steel shell in water, for which the peaks in scattered sound power before control occur at mid-frequencies in the studied range, exhibit some attenuation of the peaks in the primary after control, as seen in Figure 7-3 and Figure 7-4. For the steel shell in air, the peaks in the scattered power before control are present in the region of relatively high frequencies and do not get significantly affected by the control as seen in Figure 7-5.

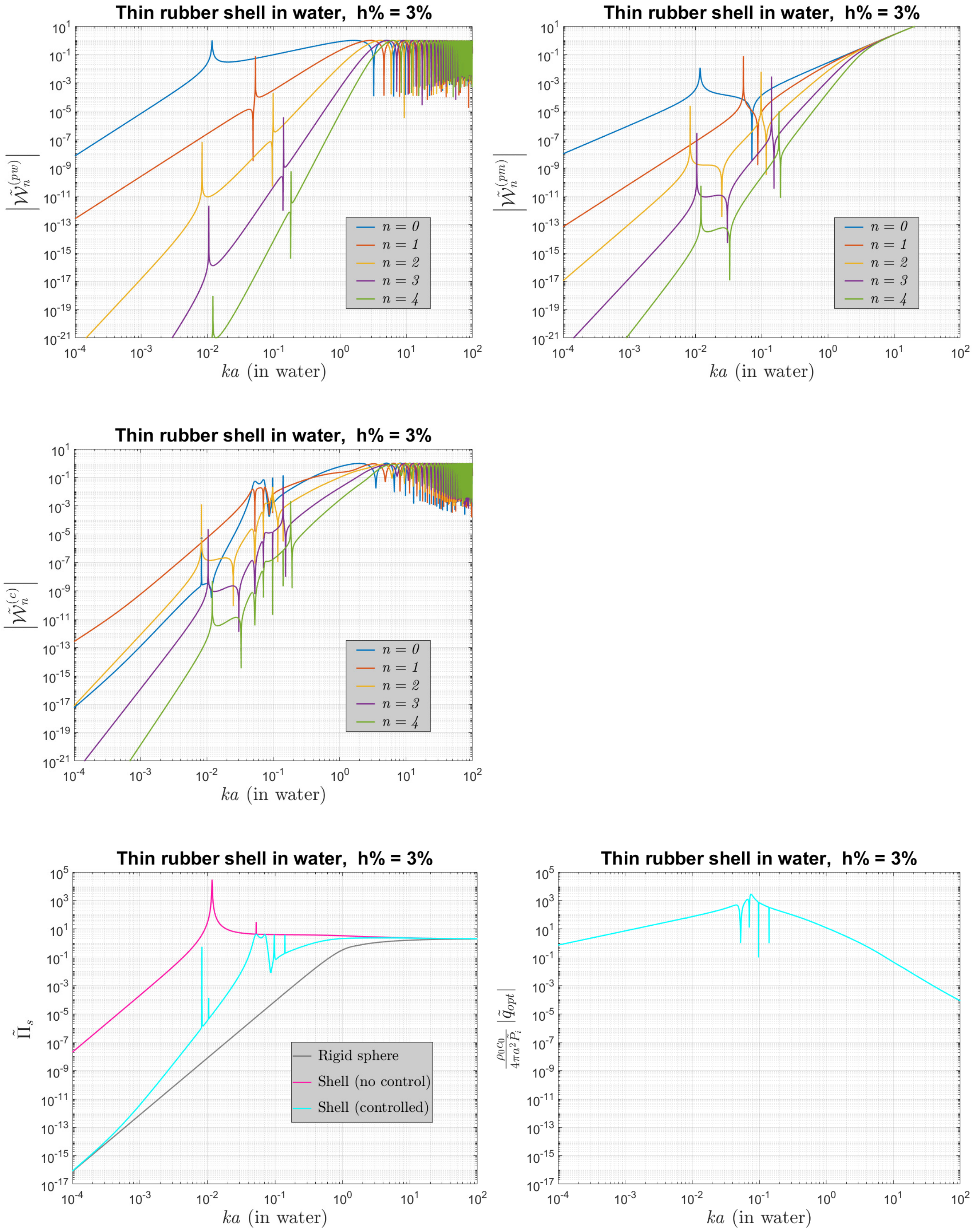

Figure 7-2 Variation of different quantities with ka when controlling the plane-wave scattering from rubber shell in water with one surface point-monopole in the $\theta = \pi$ position: magnitude of modal frequency weightings for primary $\widetilde{\mathcal{W}}_n^{(pw)}$, for secondary $\widetilde{\mathcal{W}}_n^{(pm)}$, for after control $\widetilde{\mathcal{W}}_n^{(c)}$, normalized scattered sound power $\widetilde{\Pi}_s$ after control, magnitude of optimal secondary source strength $\tilde{q}_{opt}$ (in this order, left to right, top to bottom).

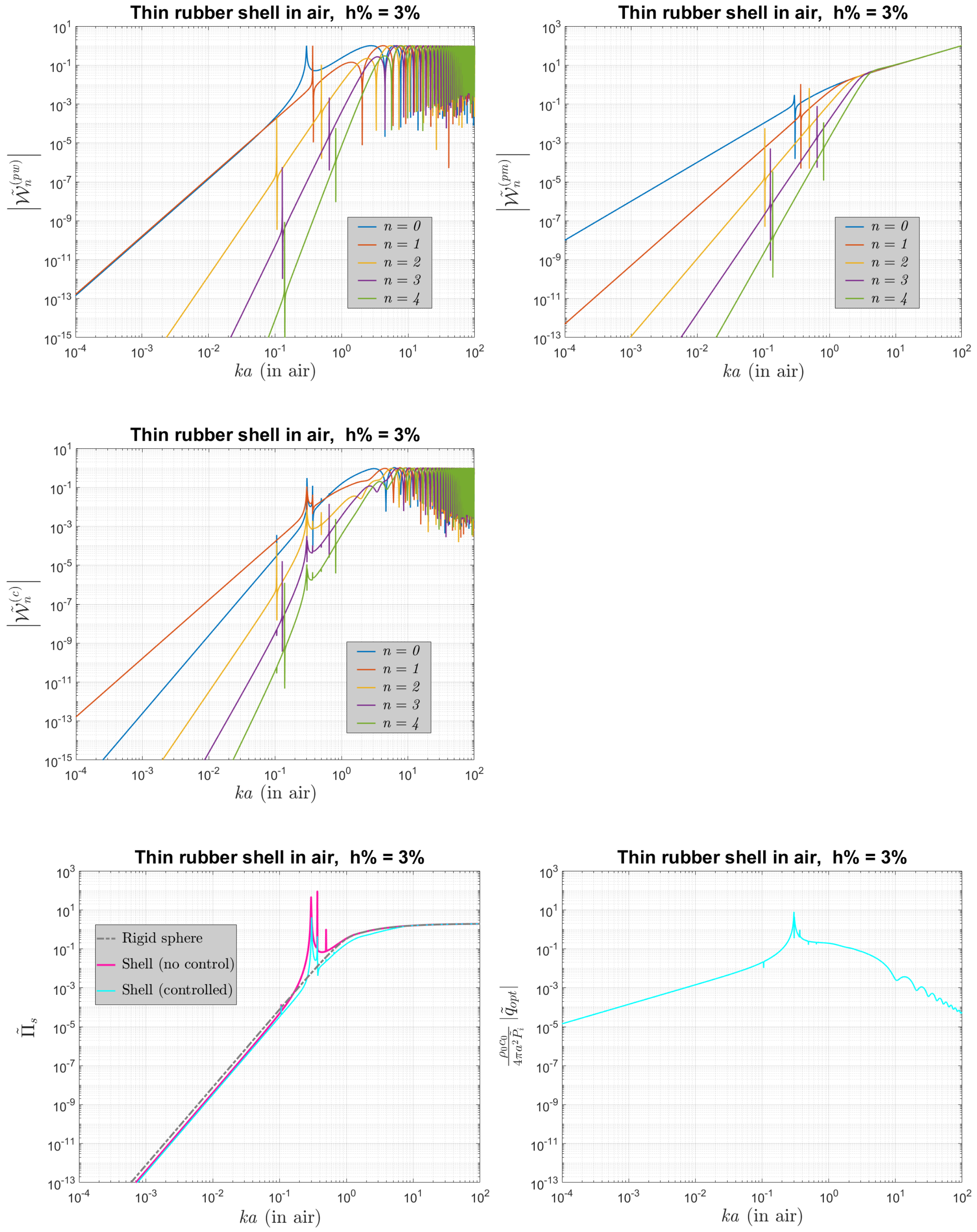

Figure 7-3 Variation of different quantities with ka when controlling the plane-wave scattering from rubber shell in air with one surface point-monopole in the $\theta = \pi$ position: magnitude of modal frequency weightings for primary $\widetilde{\mathcal{W}}_n^{(pw)}$, for secondary $\widetilde{\mathcal{W}}_n^{(pm)}$, for after control $\widetilde{\mathcal{W}}_n^{(c)}$, normalized scattered sound power $\widetilde{\Pi}_s$ after control, magnitude of optimal secondary source strength $\tilde{q}_{opt}$ (in this order, left to right, top to bottom).

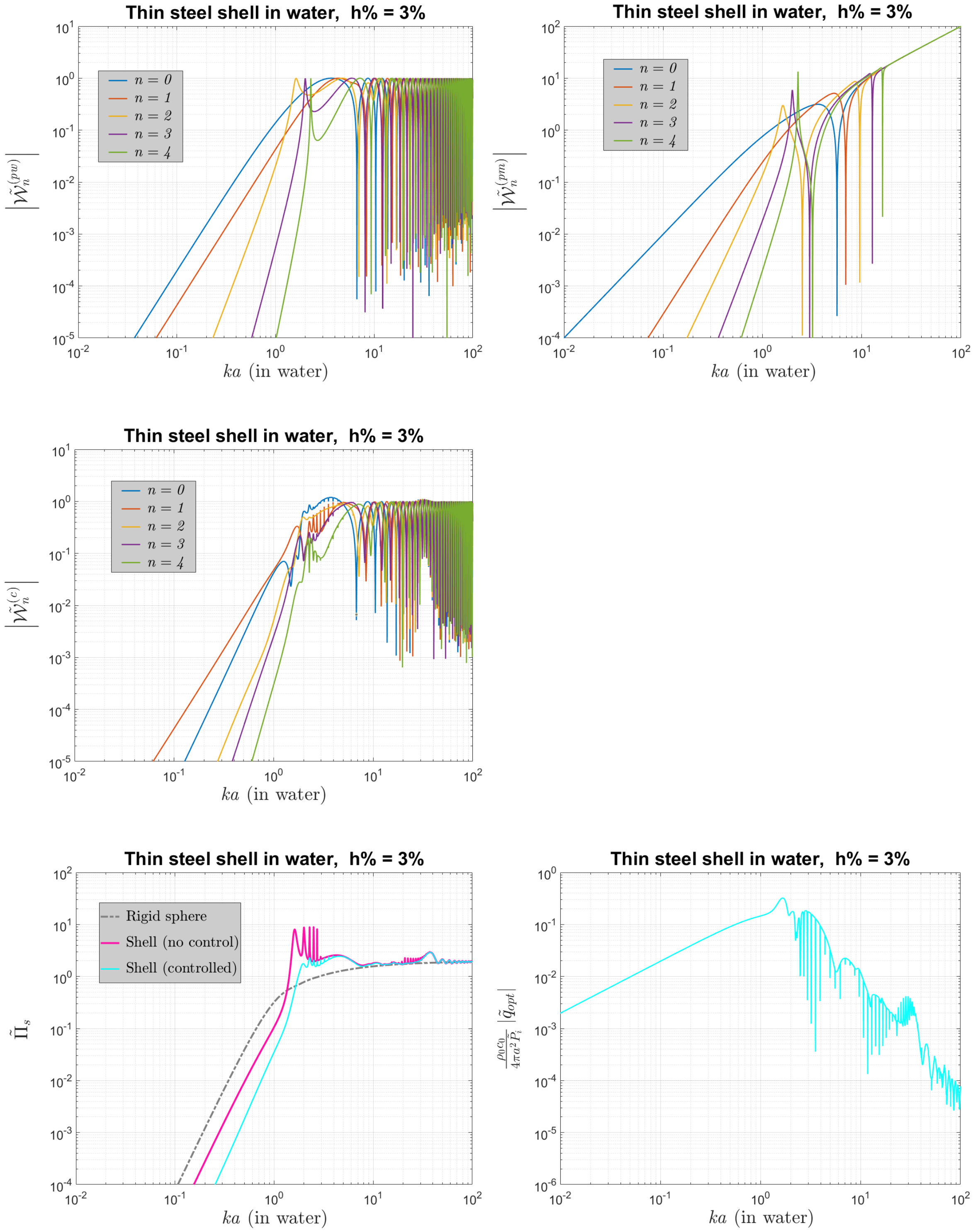

Figure 7-4 Variation of different quantities with ka when controlling the plane-wave scattering from steel shell in water with one surface point-monopole in the $\theta = \pi$ position: magnitude of modal frequency weightings for primary $\widetilde{\mathcal{W}}_n^{(pw)}$, for secondary $\widetilde{\mathcal{W}}_n^{(pm)}$, for after control $\widetilde{\mathcal{W}}_n^{(c)}$, normalized scattered sound power $\widetilde{\Pi}_s$ after control, magnitude of optimal secondary source strength $\tilde{q}_{opt}$ (in this order, left to right, top to bottom).

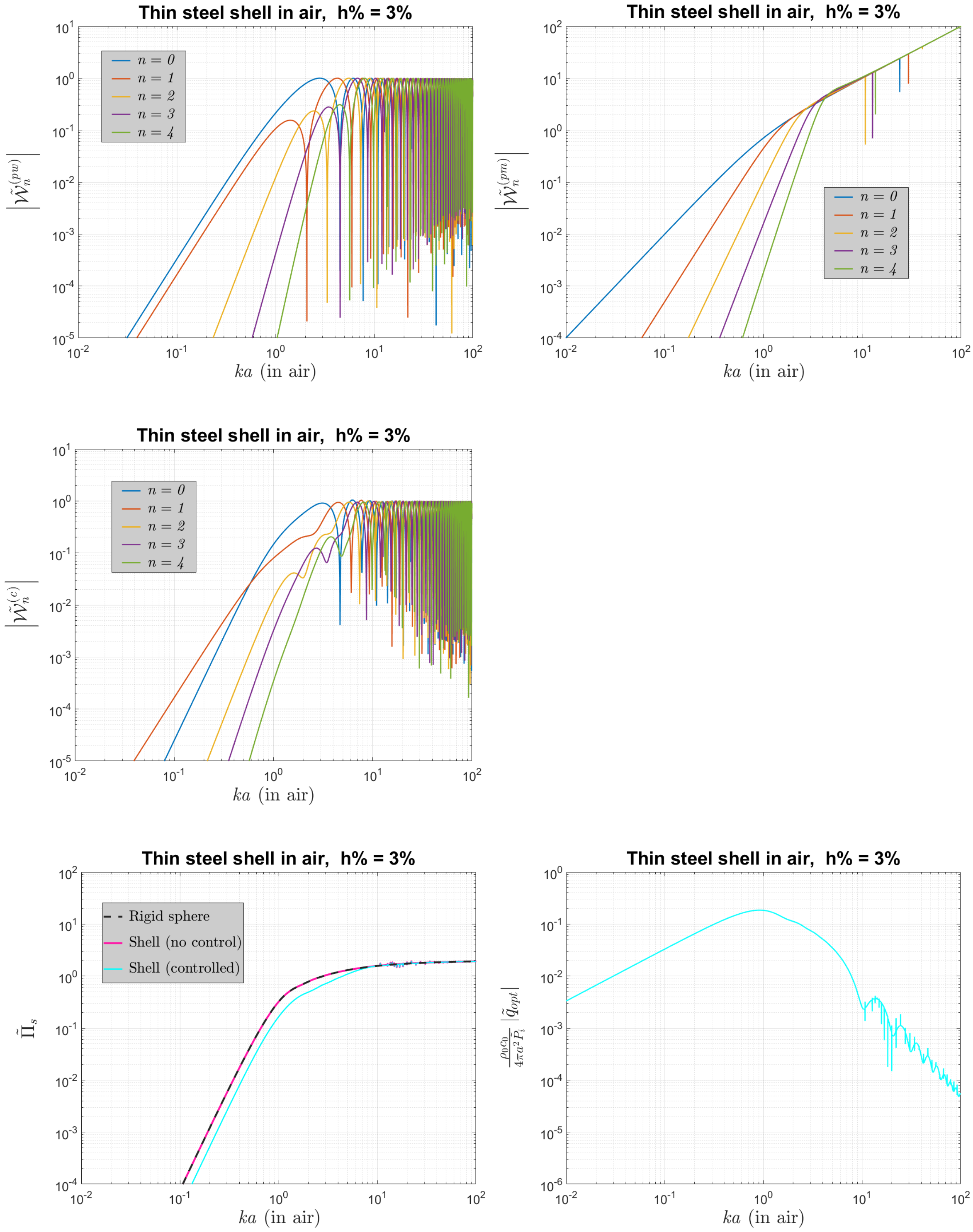

Figure 7-5 Variation of different quantities with ka when controlling the plane-wave scattering from steel shell in air with one surface point-monopole in the $\theta = \pi$ position: magnitude of modal frequency weightings for primary $\widetilde{\mathcal{W}}_n^{(pw)}$, for secondary $\widetilde{\mathcal{W}}_n^{(pm)}$, for after control $\widetilde{\mathcal{W}}_n^{(c)}$, normalized scattered sound power $\widetilde{\Pi}_s$ after control, magnitude of optimal secondary source strength $\tilde{q}_{opt}$ (in this order, left to right, top to bottom).

7.1.2 Active control with two surface radiators

In Figure 7-6, Figure 7-7, Figure 7-8 and Figure 7-9, the ideal active control results with two point-monopoles in the backscattering ($\theta = \pi$) and shadow directions ($\theta = 0$) are presented for the rubber shell in water, the rubber shell in air, the steel shell in water and, respectively the steel shell in air. The scale on the plots for rubber shells is different from that on the plots for the steel shells in order to accommodate a clear presentation of the results in each case $N = 100$ terms were calculated in MATLAB for the spherical harmonic series of the scattered power and for the tonal power minimization over the shown frequency range.

Similar to Chapter 5 and [78], an analysis can be performed at low ka to predict the behaviours of the involved modal frequency weightings of the spherical harmonic coefficients. As seen in Figure 7-6 to Figure 7-9, the primary is dominated by the $n = 0$ and $n = 1$ components with the exception of rubber shell in water, which is dominated only by the $n = 0$ component. The secondary for all four combinations is dominated by the $n = 0$ component. For these circumstances, assuming that the power minimization described in subsection 2.4.2 completely cancels the leading order powers of (ka) for $n = 0$ and $n = 1$ components in the primary at low frequencies, the sum of the normalized optimal source strengths is

$$\left(\tilde{q}_{opt,1} + \tilde{q}_{opt,2}\right)\frac{\rho_0 c_0}{4\pi\,\tilde{\mathcal{P}}_i\,a^2} = \frac{\tilde{\mathcal{W}}_0^{(pw)}\left(\tilde{\bar{\zeta}}_0, ka\right)}{\tilde{\mathcal{W}}_0^{(pm)}\left(a, \tilde{\bar{\zeta}}_0, ka\right)}, \tag{7.3}$$

which leaves the dominant residual after control as

$$\tilde{\mathcal{W}}_2^{(c)}\left(\tilde{\bar{\zeta}}_2, ka\right) = \tilde{\mathcal{W}}_2^{(pw)}\left(\tilde{\bar{\zeta}}_2, ka\right) + \frac{\tilde{\mathcal{W}}_2^{(pm)}\left(a, \tilde{\bar{\zeta}}_2, ka\right)}{\tilde{\mathcal{W}}_0^{(pm)}\left(a, \tilde{\bar{\zeta}}_0, ka\right)}\,\tilde{\mathcal{W}}_0^{(pw)}\left(\tilde{\bar{\zeta}}_0, ka\right), \tag{7.4}$$

Using the values in Table 6-4 and Table 6-5, the optimized sums of source strengths from (7.3) are $0.3333i(ka)$ for the steel shell in air, $0.1968i(ka)$ for the steel shell in water, $0.1412i(ka)$ for the rubber shell in air, and $7091.8666i(ka)$ for the rubber shell in water. In (7.4), both terms contribute to the outcome after control for all material combinations, which yields $\tilde{\mathcal{W}}_2^{(c)}$ after control equal to $0.0518i(ka)^5$ for the steel shell in air, $0.0367i(ka)^5$ for the steel shell in water, $0.0305i(ka)^5$ for the rubber shell in air, and $788i(ka)^5$ for the rubber shell in water. These residuals correspond to normalized scattered sound powers after control equal to $9.68(ka)^8$ for the steel shell in air, $9.9405 \cdot 10^{-4}(ka)^8$ for the steel shell in water, $0.0186(ka)^8$ for the rubber shell in air, and $1241880(ka)^8$ for the rubber shell in water. The hierarchy based on orders is maintained for $n \geq 3$ after control. The values of the optimal source strengths, the modal frequency weightings after control, and the normalized scattered sound power after control all match the simulated results at low values of ka from Figure 7-6 to Figure 7-9, thus confirming the assumption that the power minimization suppressed the $n = 0$ and $n = 1$ spherical harmonic components in the primary at low ka as described above.

At large values of ka, the active control does not produce any suppression due to multiple spherical harmonic components being dominant simultaneously while only two control parameters can be optimized. In terms of resonances after control, the rubber shell in water for which the peaks in the scattered sound power before control occur at relatively low ka, exhibits a significant change in the positions and magnitudes of peaks and troughs after control. In this case, some peaks are higher in magnitude than the primary, as seen in Figure 7-6, which suggest a potential numerical issue in the power minimization for this scenario. The rubber shell in air and the steel shell in water, for which the peaks in scattered sound power before control occur at mid-frequencies in the studied range, exhibit some attenuation of the peaks in the primary after control, but complicates the positions of the peaks and the troughs of the resonances with frequency, as seen in Figure 7-7 and Figure 7-8. For the steel shell in air, the peaks in the scattered power before control are present in the region of relatively high frequencies and do not get significantly affected by the control as seen in Figure 7-9.

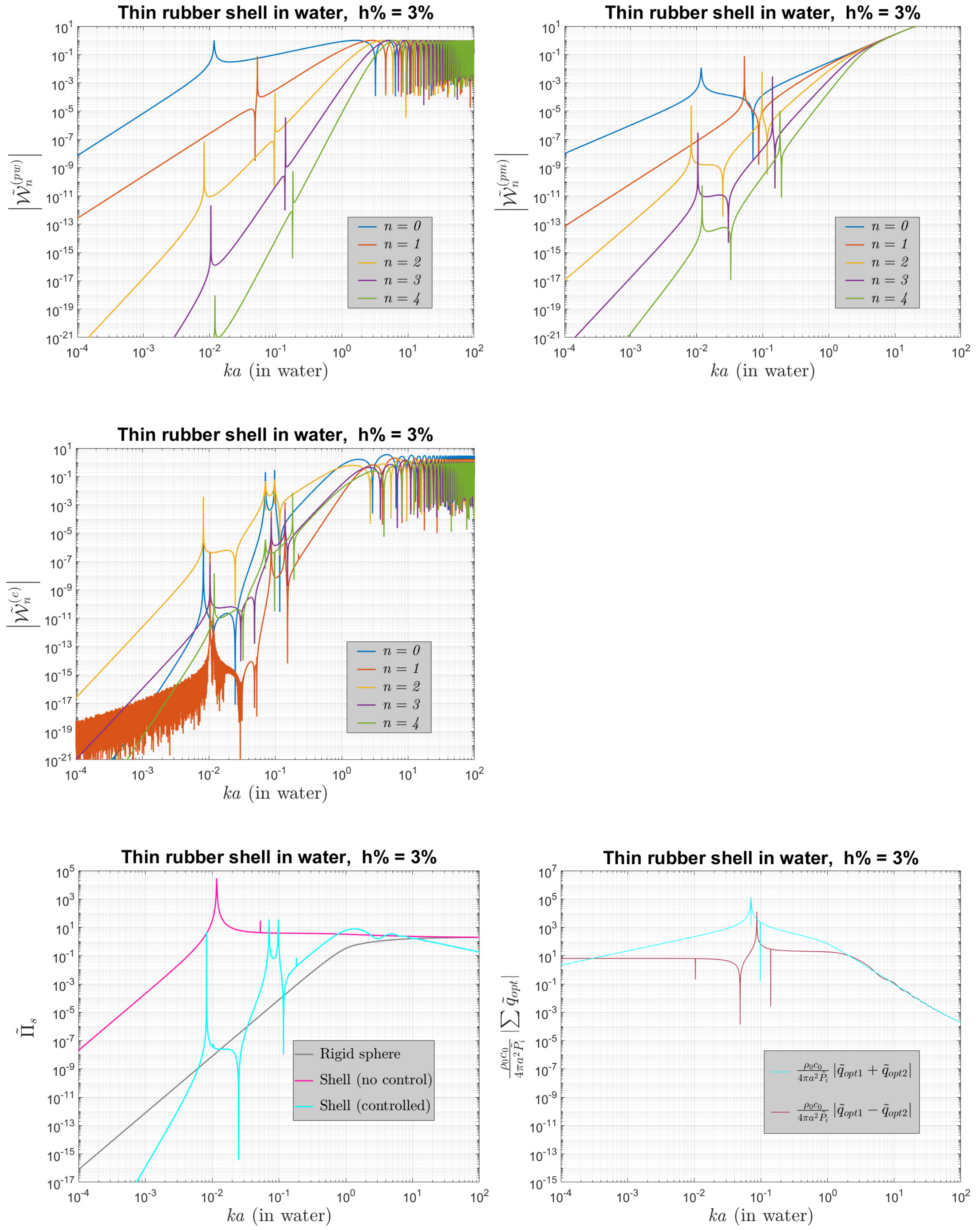

Thin rubber shell in water, h% = 3%

Thin rubber shell in water, h% = 3%

Thin rubber shell in water, h% = 3%

Thin rubber shell in water, h% = 3%

Thin rubber shell in water, h% = 3%

Figure 7-6 Variation of different quantities with ka when controlling the plane-wave scattering from rubber shell in water with two surface point-monopoles at $\theta = \pi$ and $\theta = 0$: magnitude of modal frequency weightings for primary $\widetilde{\mathcal{W}}_n^{(pw)}$, for secondary $\widetilde{\mathcal{W}}_n^{(pm)}$, for after control $\widetilde{\mathcal{W}}_n^{(c)}$, normalized scattered sound power $\widetilde{\Pi}_s$ after control, magnitude of optimal secondary source strengths $\tilde{q}_{opt}$ (in this order, left to right, top to bottom).

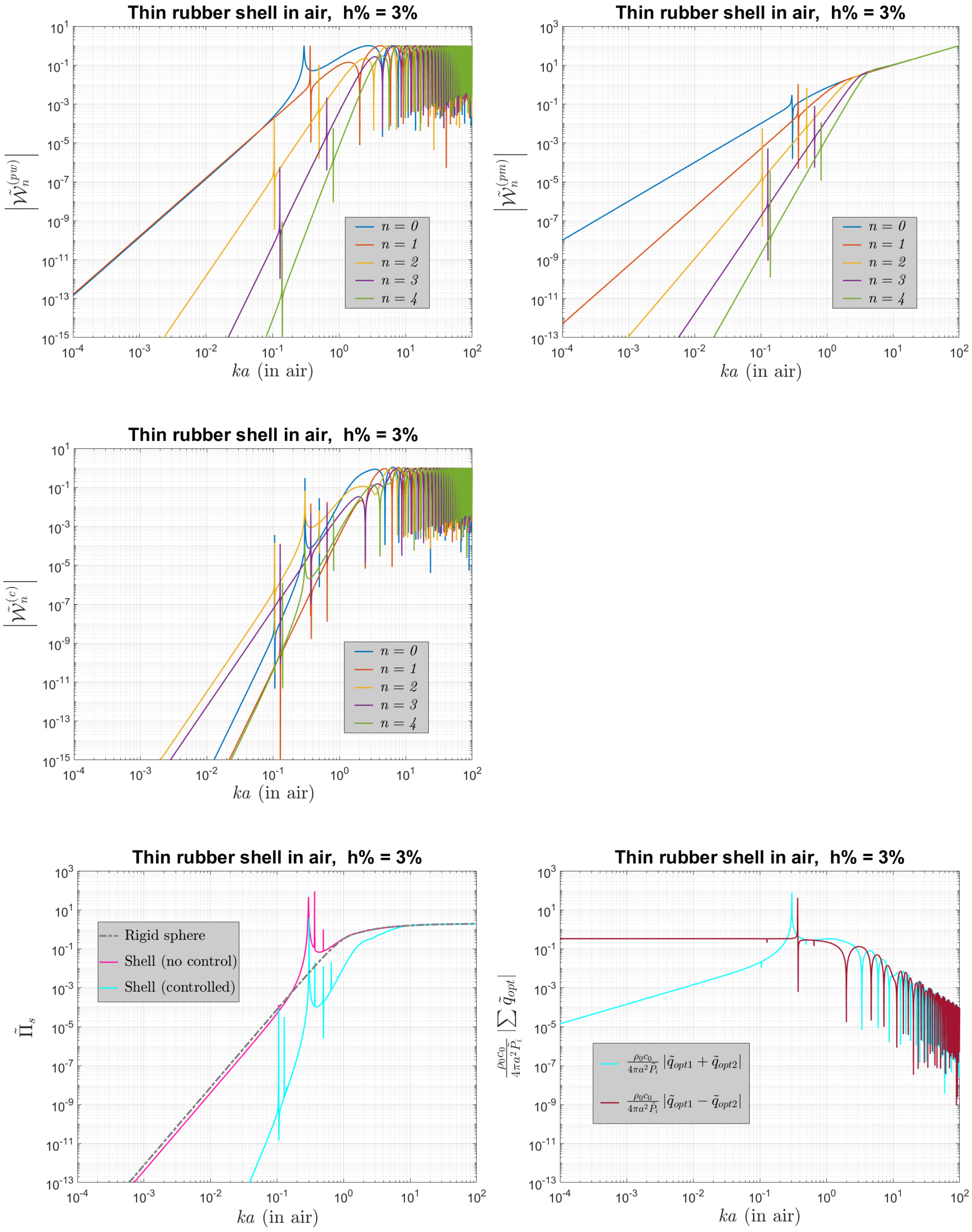

Figure 7-7 Variation of different quantities with ka when controlling the plane-wave scattering from rubber shell in air with two surface point-monopoles at $\theta = \pi$ and $\theta = 0$: magnitude of modal frequency weightings for primary $\widetilde{\mathcal{W}}_n^{(pw)}$, for secondary $\widetilde{\mathcal{W}}_n^{(pm)}$, for after control $\widetilde{\mathcal{W}}_n^{(c)}$, normalized scattered sound power $\widetilde{\Pi}_s$ after control, magnitude of optimal secondary source strengths $\tilde{q}_{opt}$ (in this order, left to right, top to bottom).

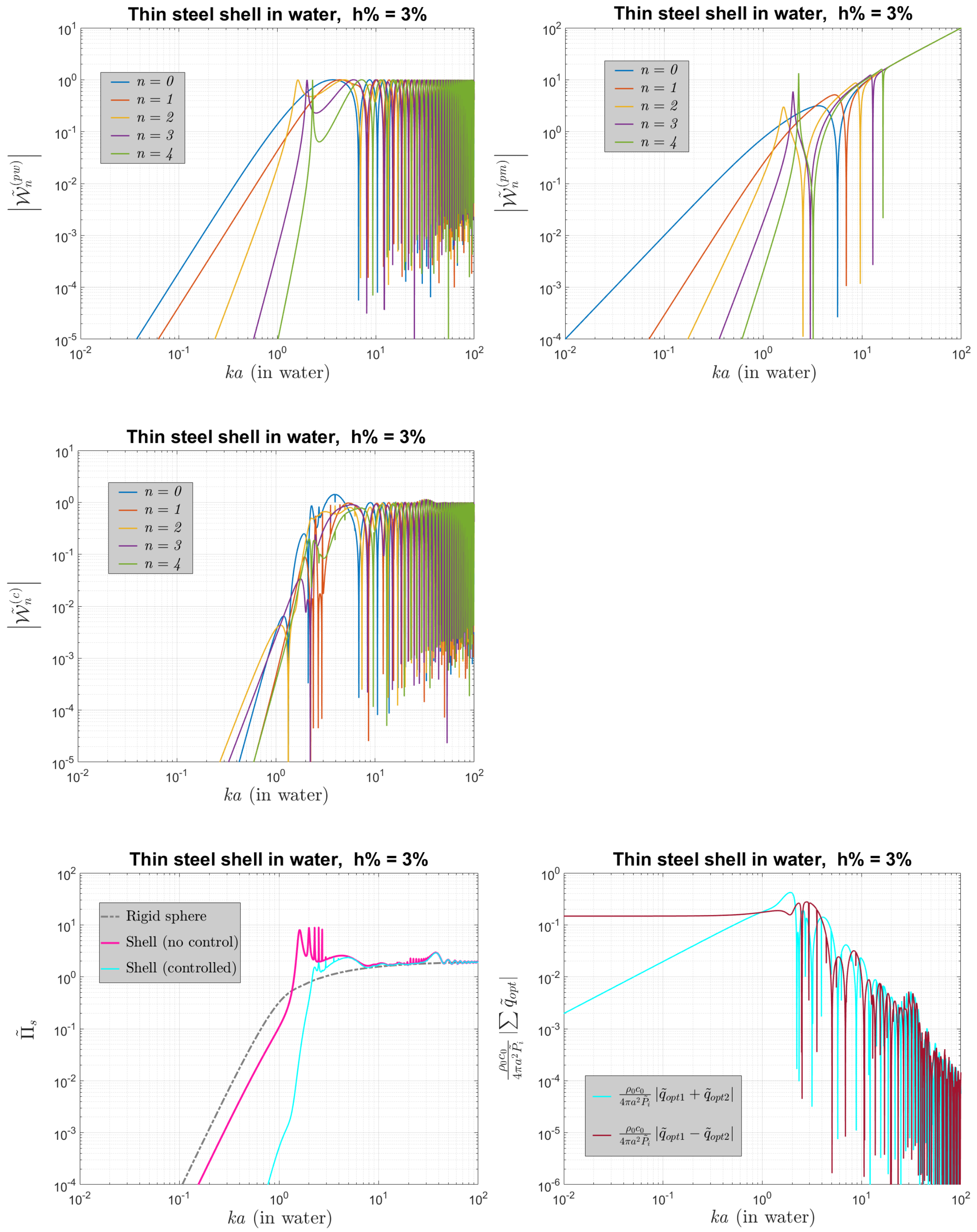

Figure 7-8 Variation of different quantities with ka when controlling the plane-wave scattering from steel shell in water with two surface point-monopoles at $\theta = \pi$ and $\theta = 0$: magnitude of modal frequency weightings for primary $\widetilde{\mathcal{W}}_n^{(pw)}$, for secondary $\widetilde{\mathcal{W}}_n^{(pm)}$, for after control $\widetilde{\mathcal{W}}_n^{(c)}$, normalized scattered sound power $\widetilde{\Pi}_s$ after control, magnitude of optimal secondary source strengths $\tilde{q}_{opt}$ (in this order, left to right, top to bottom).

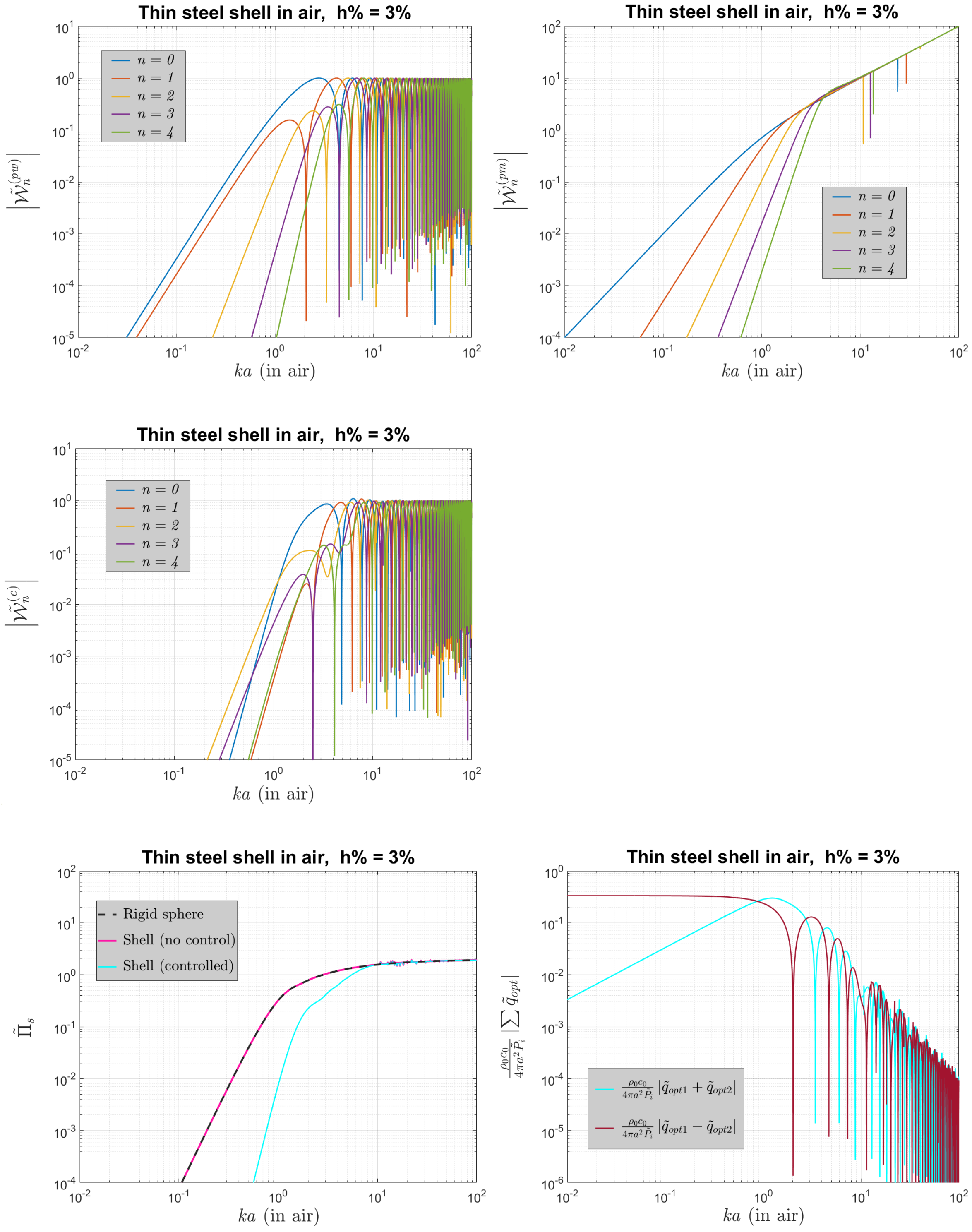

Figure 7-9 Variation of different quantities with ka when controlling the plane-wave scattering from steel shell in air with two surface point-monopoles at $\theta = \pi$ and $\theta = 0$: magnitude of modal frequency weightings for primary $\widetilde{\mathcal{W}}_n^{(pw)}$, for secondary $\widetilde{\mathcal{W}}_n^{(pm)}$, for after control $\widetilde{\mathcal{W}}_n^{(c)}$, normalized scattered sound power $\widetilde{\Pi}_s$ after control, magnitude of optimal secondary source strengths $\tilde{q}_{opt}$ (in this order, left to right, top to bottom).

7.2 Ideal active control with a small number of forces on the surface

For ideal active control with a small number of point-forces exciting the exterior surface of the shell, the two studied arrangements are depicted schematically in Figure 7-10. These consist of a monochromatic plane-wave of unit magnitude as the arriving incidence, which produces a scattered pressure that represents the primary. This is placed along the z-axis, travelling from minus to plus. In the first instance, one secondary point-force in the direction of the outward normal is placed in the $\theta = \pi$ position. Then, secondary two point-forces in the directions of the outward normal are placed at $\theta = \pi$ and $\theta = 0$ respectively. In these arrangements, the spherical harmonic formulations defined in Chapter 6 for the primary, expression (6.22), and the secondary, i.e. expression (6.36), consist of only the terms that have $m = 0$, as all other terms do not contribute. Only the $m = 0$ spherical harmonic components are used when computing the active control results.

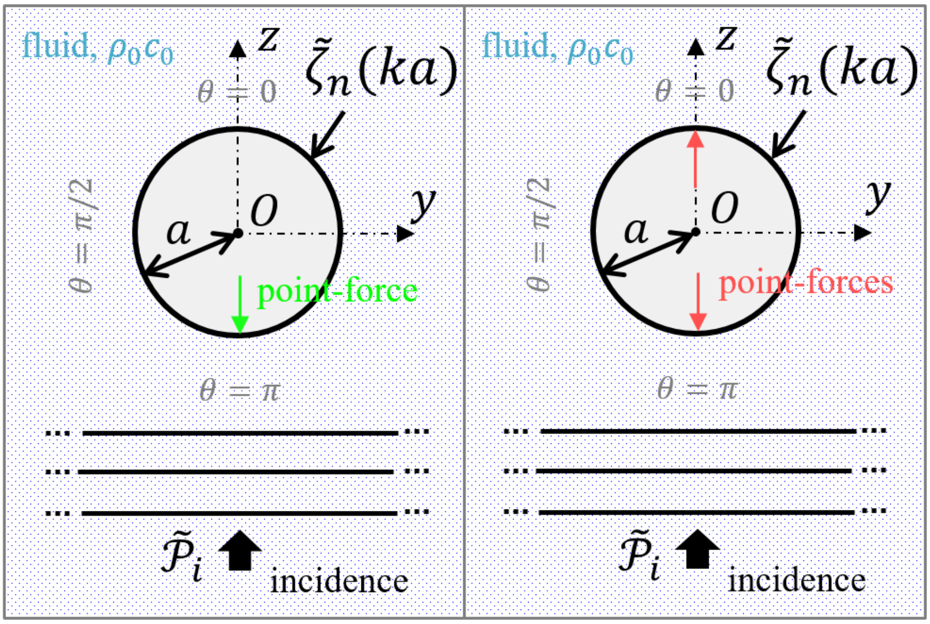

Figure 7-10 2D view of 3D arrangements of secondary point-forces for the study of tonal active control of scattering in the case of an incoming monochromatic plane-wave impinging on the thin spherical shell.

7.2.1 Active control with one force excitation on the surface

In Figure 7-11, Figure 7-12, Figure 7.13 and Figure 7.14, the ideal active control results with one point-force in the backscattering direction ($\theta = \pi$) are presented for the rubber shell in water, the rubber shell in air, the steel shell in water and, respectively the steel shell in air. The scale on the plots for rubber shells is different from that on the plots for the steel shells in order to accommodate a clear presentation of the results in each case. $N = 100$ terms were calculated in MATLAB for the spherical harmonic series of the scattered power and for the tonal power minimization over the shown frequency range.

Similar to Chapter 5 and [78], an analysis can be performed at low ka to predict the behaviours of the involved modal frequency weightings of the spherical harmonic coefficients. As seen in Figure 7-11 to Figure 7-14, the primary is dominated by the $n = 0$ and $n = 1$ components with the exception of rubber shell in water, which is dominated only by the $n = 0$ component. The secondary for all four combinations is dominated by the $n = 1$ component. For these circumstances, assuming that the power minimization described in subsection 2.4.2 completely cancels the leading order power of (ka) for the $n = 1$ component in the primary at low frequencies, the normalized optimal force magnitude is

$$\tilde{F}_{opt}\frac{1}{4\pi\,\tilde{\mathcal{P}}_i\,a^2} = -i\,\frac{\widetilde{\mathcal{W}}_1^{(pw)}(\tilde{\zeta}_1, ka)}{\widetilde{\mathcal{W}}_1^{(pf)}(a, \tilde{\zeta}_1, ka)}, \tag{7.5}$$

which leaves the dominant residual after control as

$$\widetilde{\mathcal{W}}_0^{(c)}(\tilde{\zeta}_0, ka) = \widetilde{\mathcal{W}}_0^{(pw)}(\tilde{\zeta}_0, ka) + i\,\frac{\widetilde{\mathcal{W}}_0^{(pf)}(a, \tilde{\zeta}_0, ka)}{\widetilde{\mathcal{W}}_1^{(pf)}(a, \tilde{\zeta}_1, ka)}\,\widetilde{\mathcal{W}}_1^{(pw)}(\tilde{\zeta}_1, ka)\,, \tag{7.6}$$

Using the values in Table 6-4 and Table 6-6, the optimized force magnitudes from (7.5) are $190.6346i(ka)$ for the steel shell in air, $-0.1023i(ka)$ for the steel shell in water, $22.7112i(ka)$ for the rubber shell in air, and $-0.3054i(ka)$ for the rubber shell in water. In (7.6), the first term dominates the outcome after control for all material combinations, which yields $\widetilde{\mathcal{W}}_0^{(c)}$ after control equal to $-0.3333i(ka)^3$ for the steel shell in air, $-0.1968i(ka)^3$ for the steel shell in water, $0.1412i(ka)^3$ for the rubber shell in air, and $7091.8666i(ka)^3$ for the rubber shell in water. These residuals represent the $n = 0$ component in the primary unaltered by the power minimization and correspond to normalized scattered sound powers after control equal to $0.776(ka)^4$ for the steel shell in air, $0.1771(ka)^4$ for the steel shell in water, $0.3988(ka)^4$ for the rubber shell in air, and $20.12 \cdot 10^7(ka)^4$ for the rubber shell in water. The hierarchy based on orders is maintained for $n \geq$

2 after control. The values of the optimal source strengths, the modal frequency weightings after control, and the normalized scattered sound power after control all match the simulated results at low values of ka from Figure 7-12 to Figure 7-14, thus confirming the assumption that the power minimization suppressed the $n = 1$ spherical harmonic component in the primary at low ka as described above. However, these do not match for the rubber shell in water, and there is no clear reason as to why, but may potential be numerical error from the model at these low frequencies.

At large values of ka, the active control does not produce any suppression due to multiple spherical harmonic components being dominant simultaneously while only one control parameter can be optimized. In terms of resonances after control, the rubber shell in water for which the peaks in the scattered sound power before control occur at relatively low ka, exhibits a significant change in the positions and magnitudes of peaks and troughs after control. In this case, some peaks are higher in magnitude than the primary, as seen in Figure 7-12, which suggest a potential numerical issue in the power minimization for this scenario. The rubber shell in air and the steel shell in water, for which the peaks in scattered sound power before control occur at mid-frequencies in the studied range, exhibit some attenuation of the peaks in the primary after control, as seen in Figure 7-12 and Figure 7-13. For the steel shell in air, the peaks in the scattered power before control are present in the region of relatively high frequencies and do not get significantly affected by the control as seen in Figure 7-14.

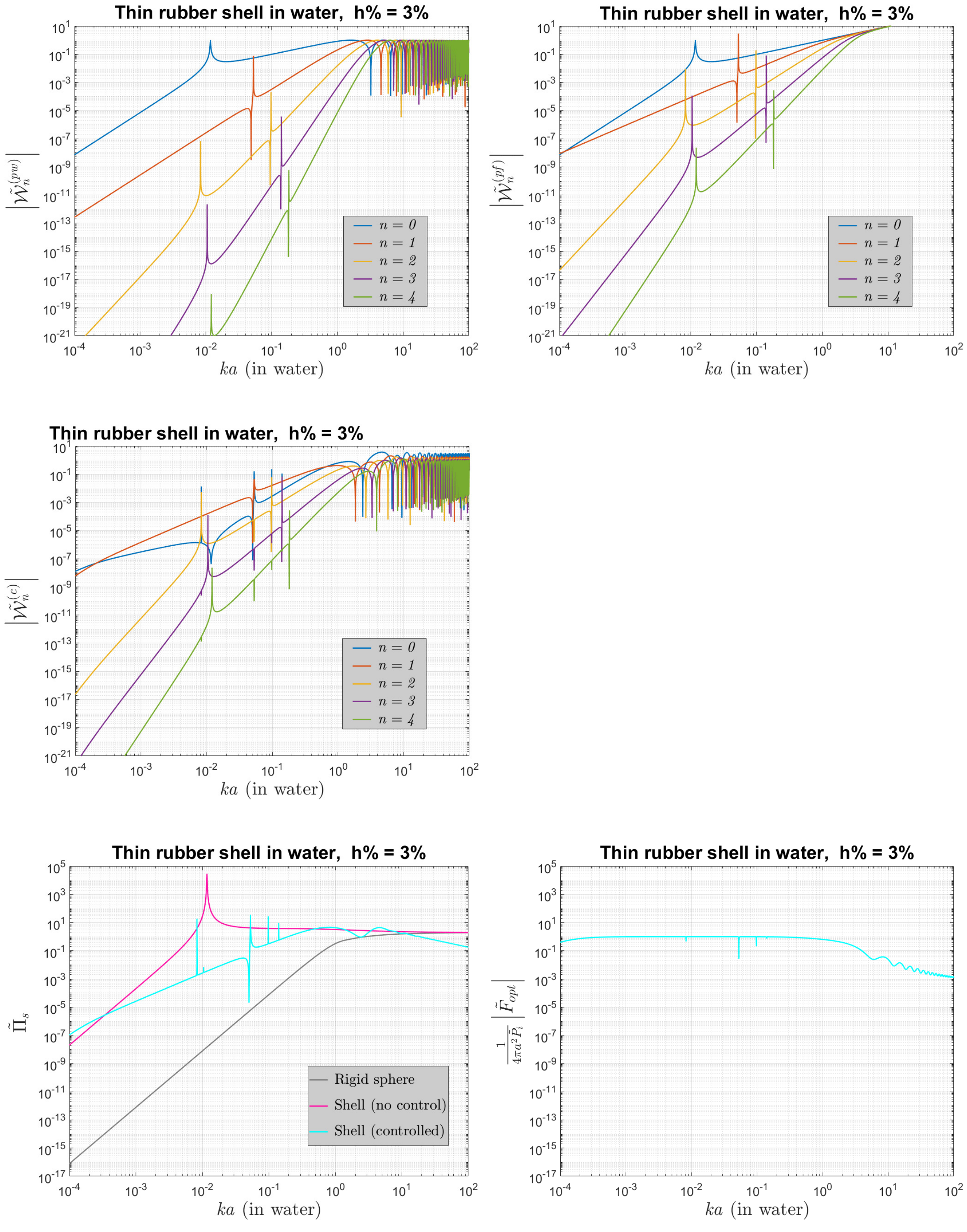

Figure 7-11 Variation of different quantities with ka when controlling the plane-wave scattering from rubber shell in water with one surface point-force at the $\theta = \pi$ position: magnitude of modal frequency weightings for primary $\widetilde{\mathcal{W}}_n^{(pw)}$, for secondary $\widetilde{\mathcal{W}}_n^{(pf)}$, for after control $\widetilde{\mathcal{W}}_n^{(c)}$, normalized scattered sound power $\widetilde{\Pi}_s$ after control, magnitude of optimal secondary forcing $\tilde{F}_{opt}$ (in this order, left to right, top to bottom).

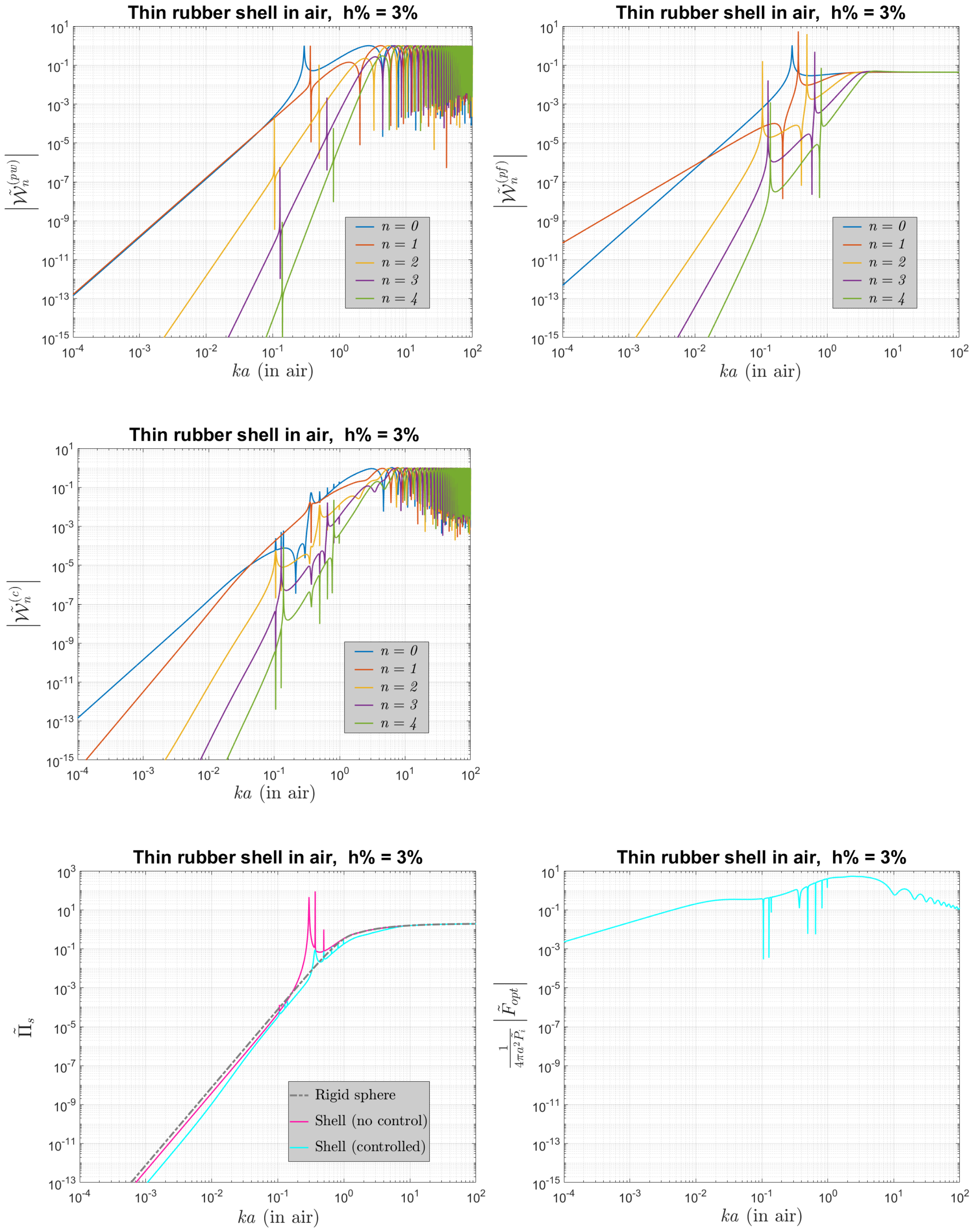

Figure 7-12 Variation of different quantities with ka when controlling the plane-wave scattering from rubber shell in air with one surface point-force at the $\theta = \pi$ position: magnitude of modal frequency weightings for primary $\widetilde{\mathcal{W}}_n^{(pw)}$, for secondary $\widetilde{\mathcal{W}}_n^{(pf)}$, for after control $\widetilde{\mathcal{W}}_n^{(c)}$, normalized scattered sound power $\widetilde{\Pi}_s$ after control, magnitude of optimal secondary forcing $\tilde{F}_{opt}$ (in this order, left to right, top to bottom).

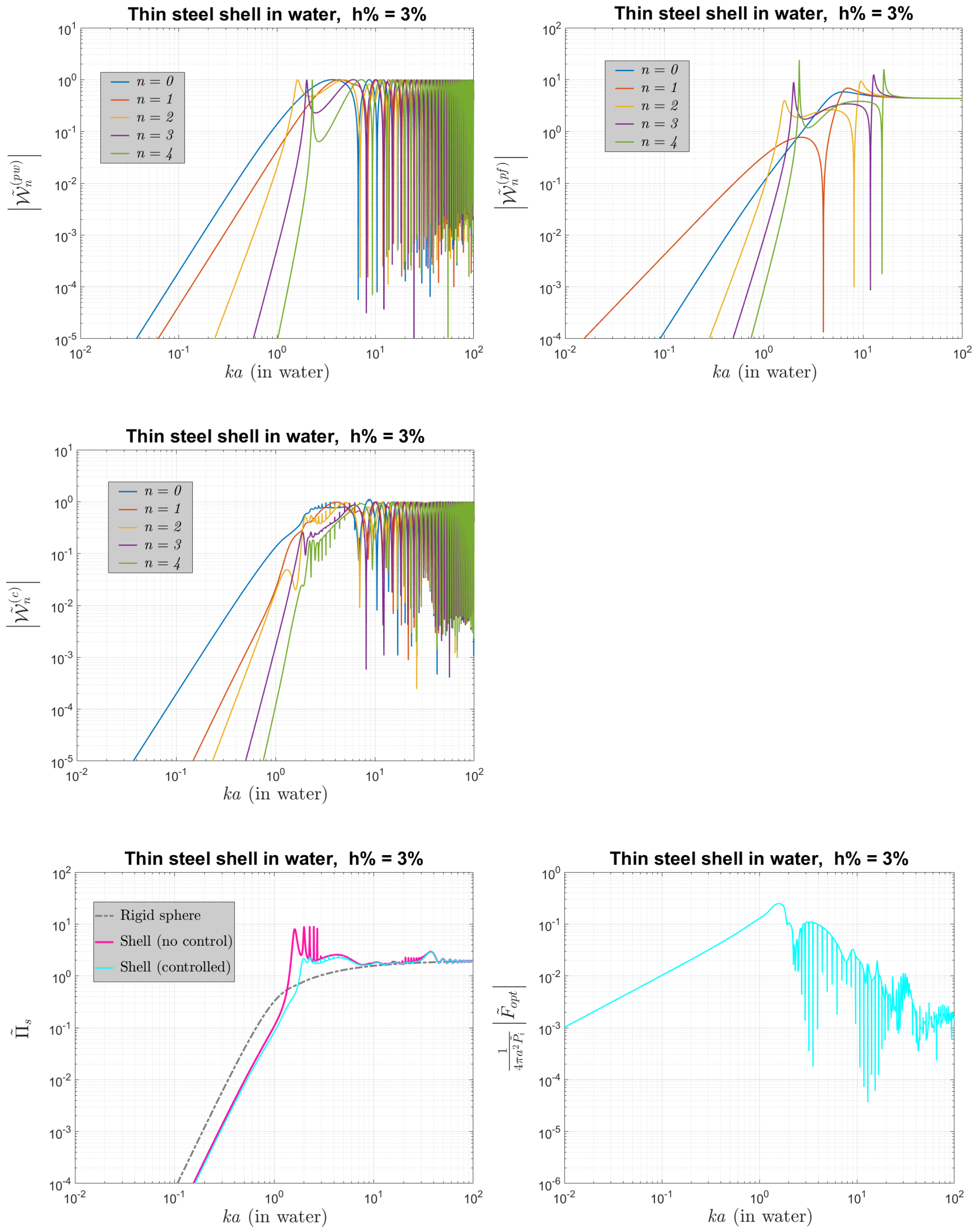

Figure 7-13 Variation of different quantities with ka when controlling the plane-wave scattering from steel shell in water with one surface point-force at the $\theta = \pi$ position: magnitude of modal frequency weightings for primary $\widetilde{\mathcal{W}}_n^{(pw)}$, for secondary $\widetilde{\mathcal{W}}_n^{(pf)}$, for after control $\widetilde{\mathcal{W}}_n^{(c)}$, normalized scattered sound power $\widetilde{\Pi}_s$ after control, magnitude of optimal secondary forcing $\tilde{F}_{opt}$ (in this order, left to right, top to bottom).

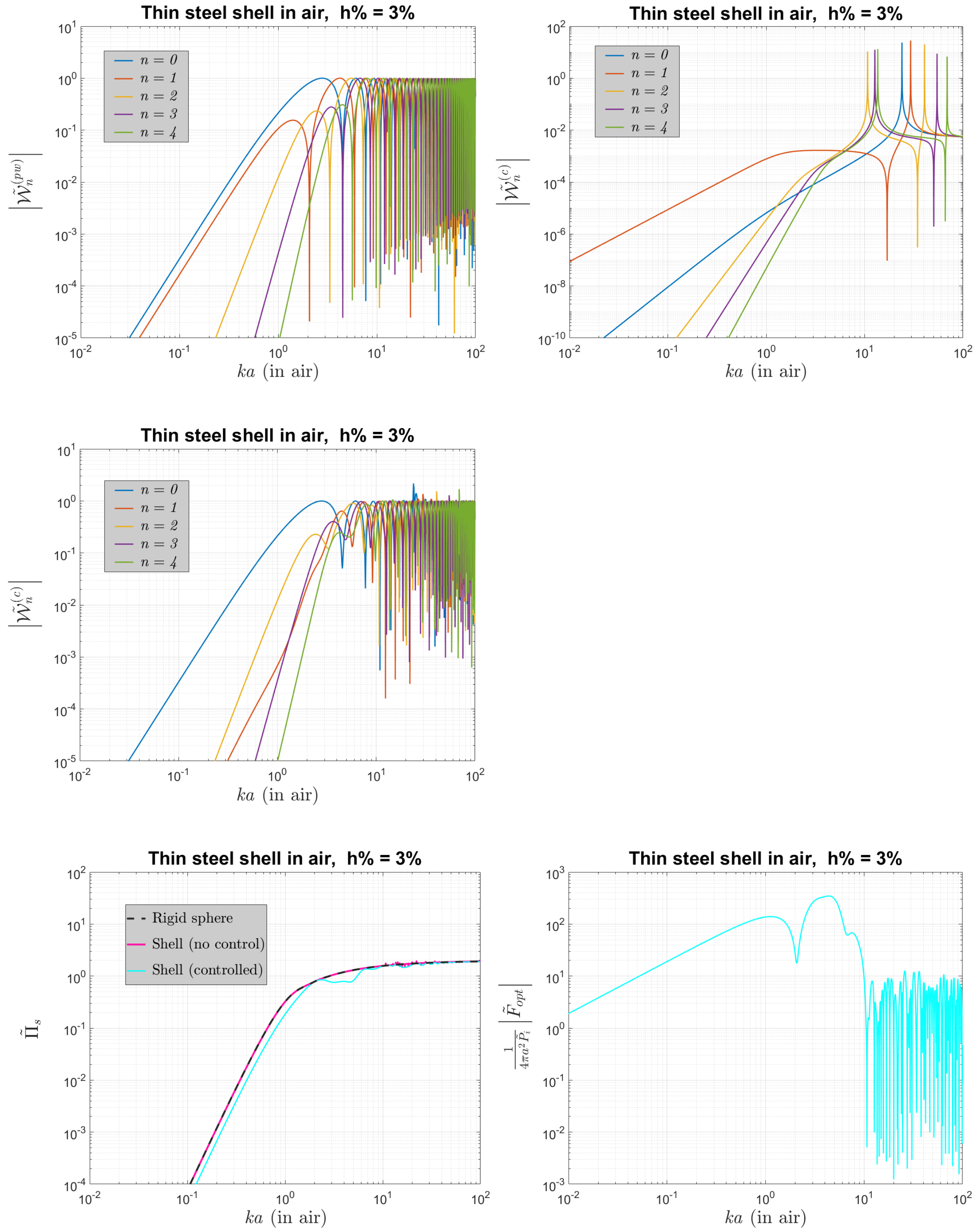

Figure 7-14 Variation of different quantities with ka when controlling the plane-wave scattering from steel shell in air with one surface point-force at the $\theta = \pi$ position: magnitude of modal frequency weightings for primary $\widetilde{\mathcal{W}}_n^{(pw)}$, for secondary $\widetilde{\mathcal{W}}_n^{(pf)}$, for after control $\widetilde{\mathcal{W}}_n^{(c)}$, normalized scattered sound power $\widetilde{\Pi}_s$ after control, magnitude of optimal secondary forcing $\tilde{F}_{opt}$ (in this order, left to right, top to bottom).

7.2.2 Active control with two force excitations on the surface

In Figure 7-15, Figure 7-16, Figure 7-17 and Figure 7-18, the ideal active control results with two point-forces in the backscattering ($\theta = \pi$) and shadow directions ($\theta = 0$) are presented for the rubber shell in water, the rubber shell in air, the steel shell in water and, respectively the steel shell in air. The scale on the plots for rubber shells is different from that on the plots for the steel shells in order to accommodate a clear presentation of the results in each case. $N = 100$ terms were calculated in MATLAB for the spherical harmonic series of the scattered power and for the tonal power minimization over the shown frequency range.

Similar to Chapter 5 and [78], an analysis can be performed at low ka to predict the behaviours of the involved modal frequency weightings of the spherical harmonic coefficients. As seen in Figure 7-15 to Figure 7-18, the primary is dominated by the $n = 0$ and $n = 1$ components with the exception of rubber shell in water, which is dominated only by the $n = 0$ component. The secondary for all four combinations is dominated by the $n = 1$ component. For these circumstances, assuming that the power minimization described in subsection 2.4.2 completely cancels the leading order powers of (ka) for $n = 0$ and $n = 1$ components in the primary at low frequencies, the sum of the normalized optimal source strengths is

$$\left(\tilde{F}_{opt,1} + \tilde{F}_{opt,2}\right)\frac{1}{4\pi\,\tilde{\mathcal{P}}_i\,a^2} = \frac{\widetilde{\mathcal{W}}_0^{(pw)}\left(\tilde{\zeta}_0, ka\right)}{\widetilde{\mathcal{W}}_0^{(pf)}\left(a, \tilde{\zeta}_0, ka\right)}, \qquad (7.7)$$

which leaves the dominant residual after control as

$$\widetilde{\mathcal{W}}_2^{(c)}\left(a, \tilde{\zeta}_2, ka\right) = \widetilde{\mathcal{W}}_2^{(pw)}\left(\tilde{\zeta}_2, ka\right) + \frac{\widetilde{\mathcal{W}}_2^{(pf)}\left(a, \tilde{\zeta}_2, ka\right)}{\widetilde{\mathcal{W}}_0^{(pf)}\left(a, \tilde{\zeta}_0, ka\right)}\,\widetilde{\mathcal{W}}_0^{(pw)}\left(\tilde{\zeta}_0, ka\right), \qquad (7.8)$$

Using the values in Table 6-4 and Table 6-6, the optimized sums of force magnitudes from (7.7) are -36626.3736 for the steel shell in air, -1.442 for the steel shell in water, 0.2976 for the rubber shell in air, and 0.9999 for the rubber shell in water. In (7.8), both terms contribute to the outcome after control for all material combinations, which yields $\widetilde{\mathcal{W}}_2^{(c)}$ after control equal to $-0.11887i(ka)^5$ for the steel shell in air, $-0.06397i(ka)^5$ for the steel shell in water, $0.1008i(ka)^5$ for the rubber shell in air, and $4273.3011i(ka)^5$ for the rubber shell in water. These residuals correspond to normalized scattered sound powers after control equal to $0.2823(ka)^8$ for the steel shell in air, $0.0817(ka)^8$ for the steel shell in water, $0.2032(ka)^8$ for the rubber shell in air, and $3.6522 \cdot 10^8(ka)^8$ for the rubber shell in water. The hierarchy based on orders is maintained for $n \geq 3$ after control. The values of the optimal source strengths, the modal frequency weightings after control, and the normalized scattered sound power after control all match the simulated results at low values of ka from Figure 7-16 to Figure 7-18, thus confirming the assumption that the power minimization suppressed the $n = 0$ and $n = 1$ spherical harmonic components in the primary at low ka as described above. However, these do not match for the rubber shell in water, and there is no clear reason as to why, but may potential be numerical error in the results at these low frequencies.

At large values of ka, the active control does not produce any suppression due to multiple spherical harmonic components being dominant simultaneously while only two control parameters can be optimized. In terms of resonances after control, the rubber shell in water for which the peaks in the scattered sound power before control occur at relatively low ka, exhibits a significant change in the positions and magnitudes of peaks and troughs after control. In this case, some peaks are higher in magnitude than the primary, as seen in Figure 7-15, which suggest a potential numerical issue in the power minimization for this scenario. The rubber shell in air and the steel shell in water, for which the peaks in scattered sound power before control occur at mid-frequencies in the studied range, exhibit some attenuation of the peaks in the primary after control, but complicates the positions of the peaks and the troughs of the resonances with frequency, as seen in Figure 7-16 and Figure 7-17. For the steel shell in air, the peaks in the scattered power before control are present in the region of relatively high frequencies and do not get significantly affected by the control as seen in Figure 7-18.

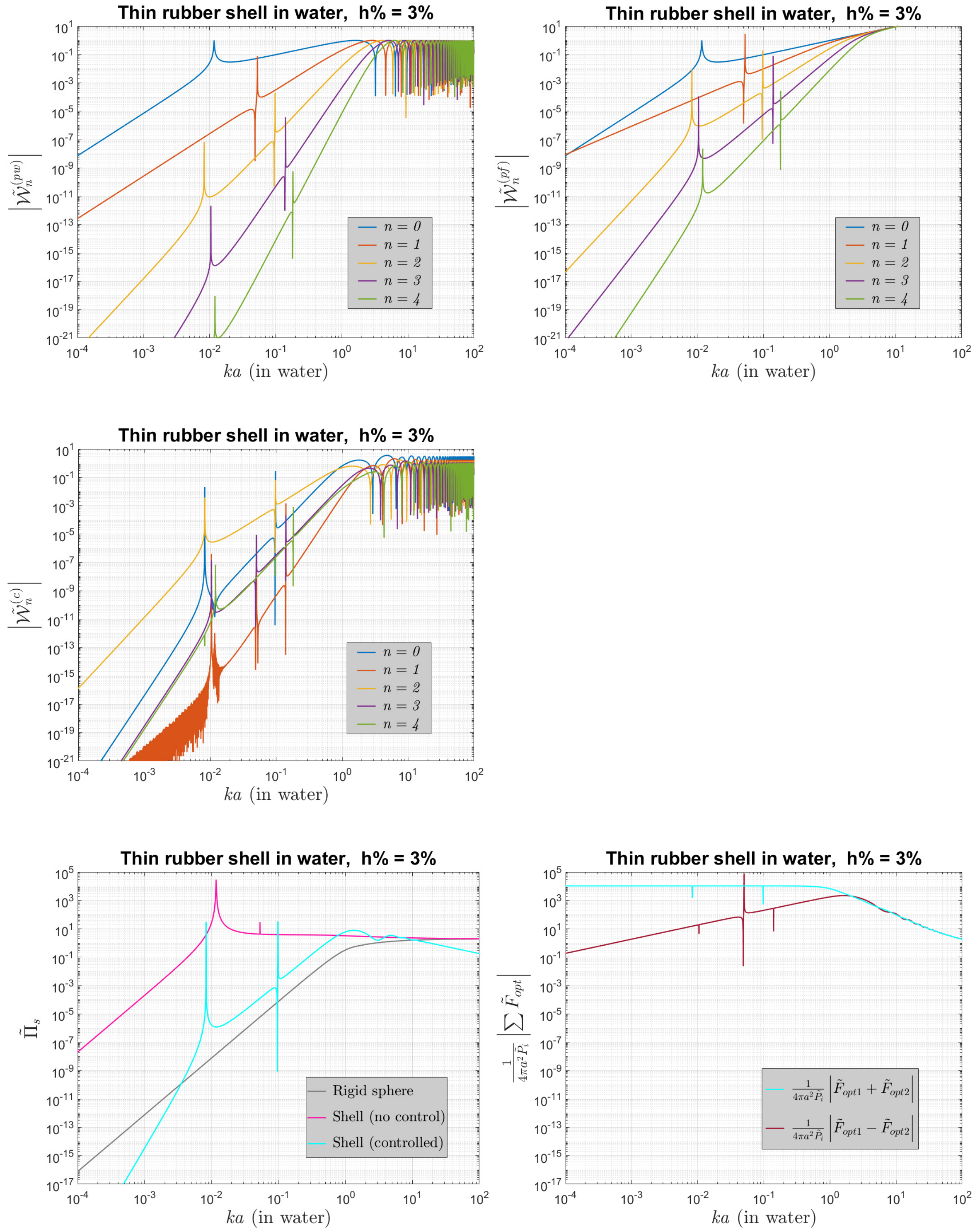

Thin rubber shell in water, h% = 3%

Thin rubber shell in water, h% = 3%

Thin rubber shell in water, h% = 3%

Thin rubber shell in water, h% = 3%

Thin rubber shell in water, h% = 3%

Figure 7-15 Variation of different quantities with ka when controlling the plane-wave scattering from rubber shell in water with two surface point-forces at $\theta = \pi$ and $\theta = 0$: magnitude of modal frequency weightings for primary $\widetilde{\mathcal{W}}_n^{(pw)}$, for secondary $\widetilde{\mathcal{W}}_n^{(pf)}$, for after control $\widetilde{\mathcal{W}}_n^{(c)}$, normalized scattered sound power $\widetilde{\Pi}_s$ after control, magnitude of optimal secondary forcing $\tilde{F}_{opt}$ (in this order, left to right, top to bottom).

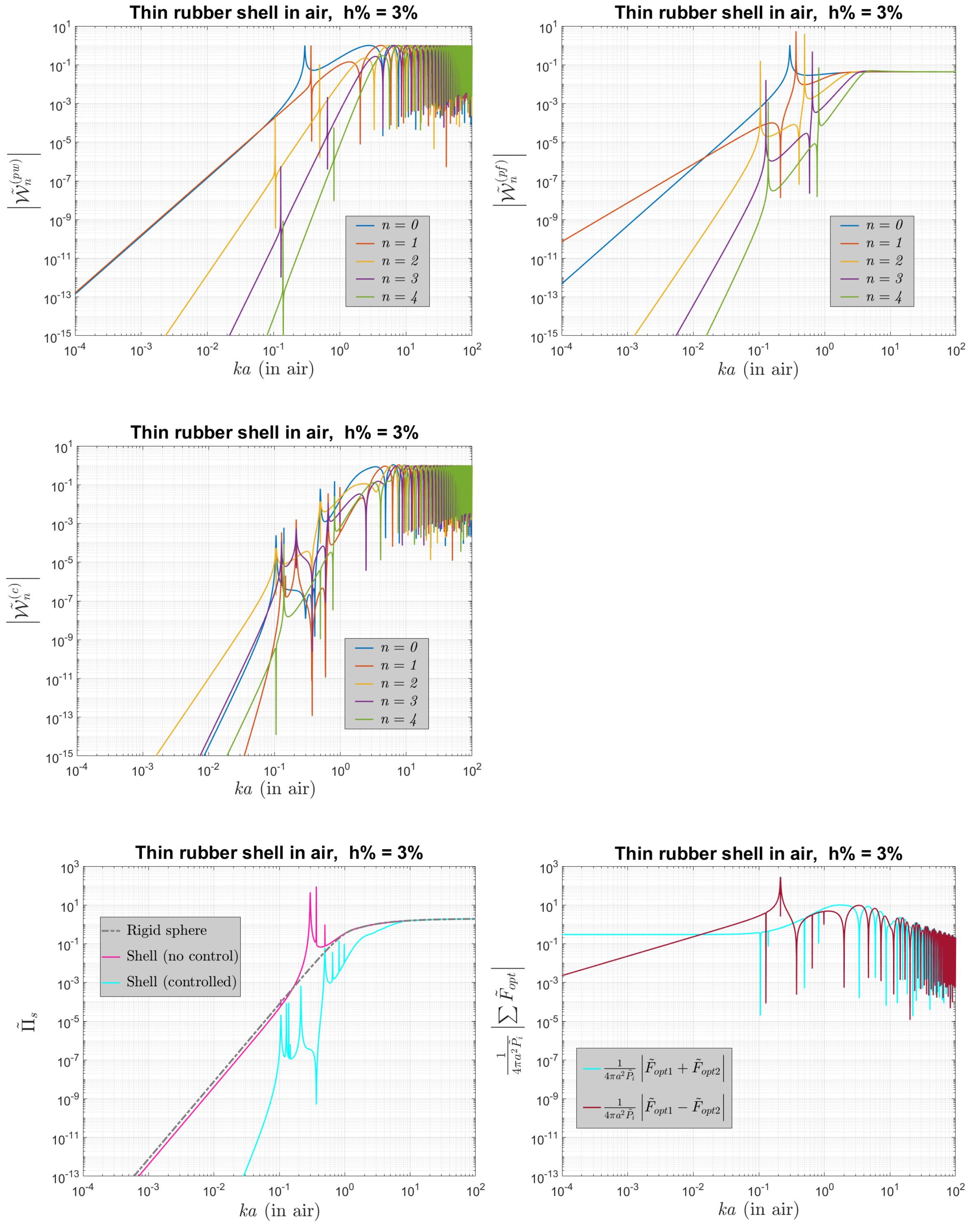

Figure 7-16 Variation of different quantities with ka when controlling the plane-wave scattering from rubber shell in air with two surface point-forces at $\theta = \pi$ and $\theta = 0$: magnitude of modal frequency weightings for primary $\widetilde{\mathcal{W}}_n^{(pw)}$, for secondary $\widetilde{\mathcal{W}}_n^{(pf)}$, for after control $\widetilde{\mathcal{W}}_n^{(c)}$, normalized scattered sound power $\widetilde{\Pi}_s$ after control, magnitude of optimal secondary forcing $\widetilde{F}_{opt}$ (in this order, left to right, top to bottom).

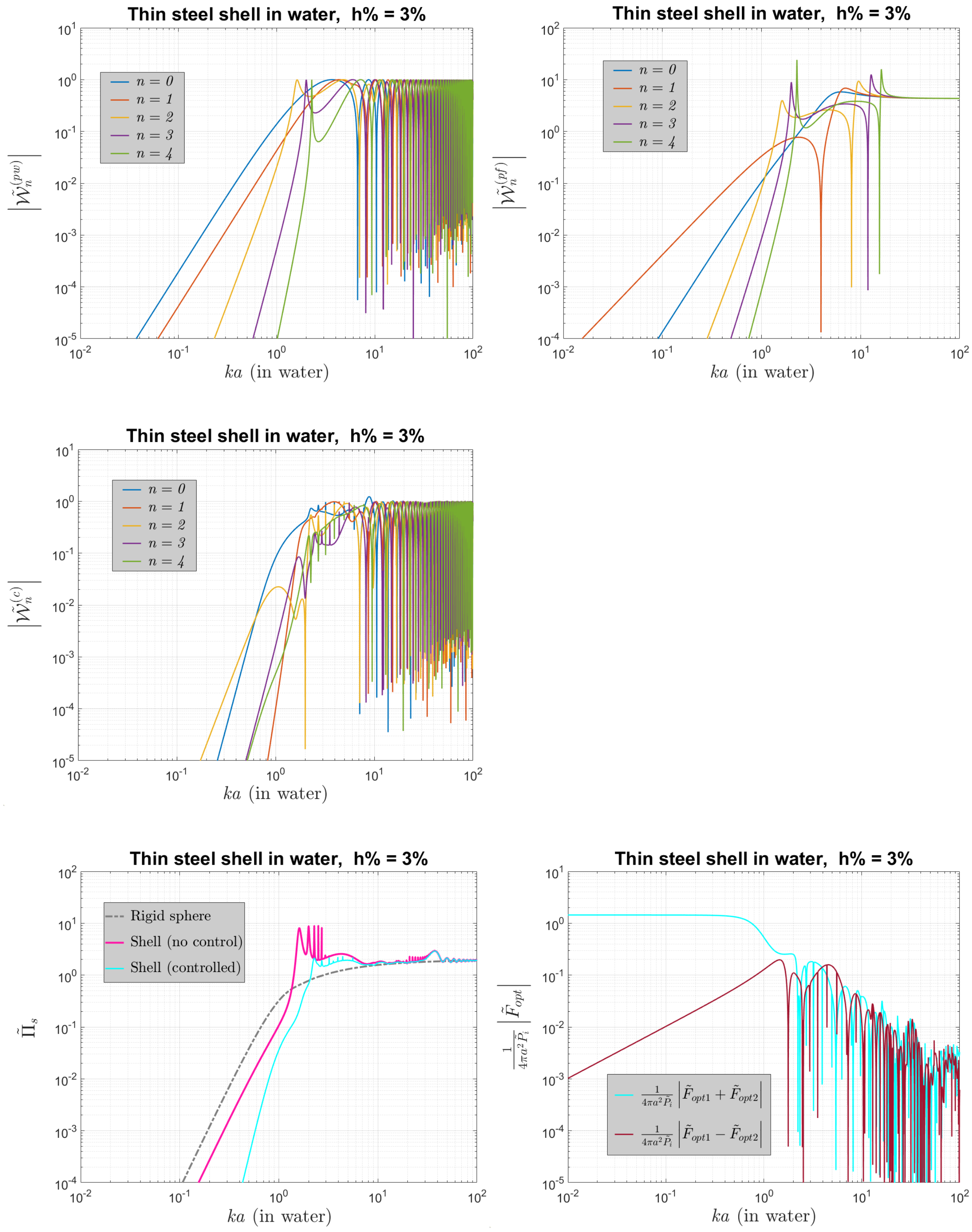

Figure 7-17 Variation of different quantities with ka when controlling the plane-wave scattering from steel shell in water with two surface point-forces at $\theta = \pi$ and $\theta = 0$: magnitude of modal frequency weightings for primary $\widetilde{\mathcal{W}}_n^{(pw)}$, for secondary $\widetilde{\mathcal{W}}_n^{(pf)}$, for after control $\widetilde{\mathcal{W}}_n^{(c)}$, normalized scattered sound power $\widetilde{\Pi}_s$ after control, magnitude of optimal secondary forcing $\tilde{F}_{opt}$ (in this order, left to right, top to bottom).

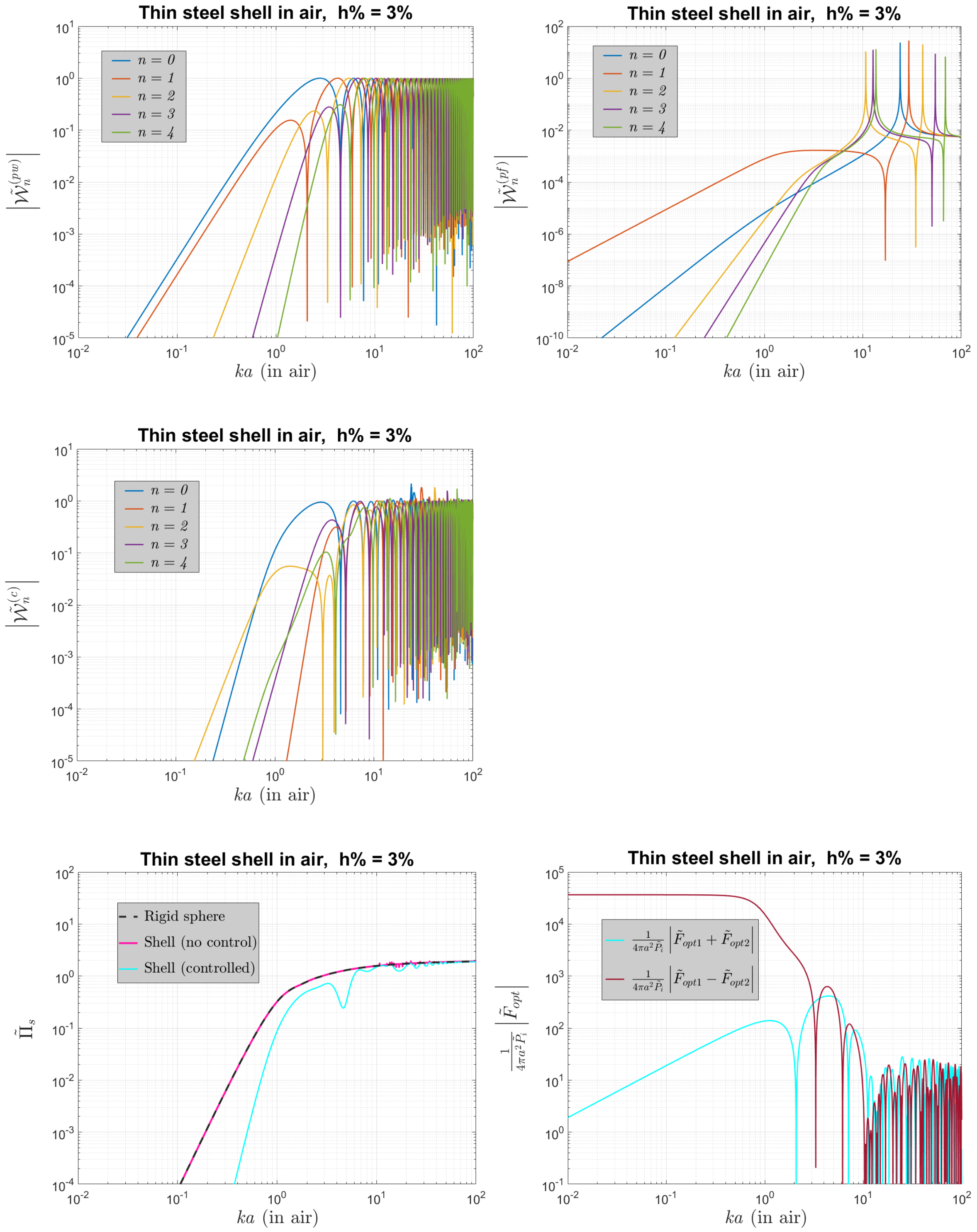

Figure 7-18 Variation of different quantities with ka when controlling the plane-wave scattering from steel shell in air with two surface point-forces at $\theta = \pi$ and $\theta = 0$: magnitude of modal frequency weightings for primary $\widetilde{\mathcal{W}}_n^{(pw)}$, for secondary $\widetilde{\mathcal{W}}_n^{(pf)}$, for after control $\widetilde{\mathcal{W}}_n^{(c)}$, normalized scattered sound power $\widetilde{\Pi}_s$ after control, magnitude of optimal secondary forcing $\tilde{F}_{opt}$ (in this order, left to right, top to bottom).

7.3 Summary of ideal active control with point monopoles and forces

The results presented in section 7.1 and section 7.2 for normalized scattered sound power versus ka after power minimization with different numbers and types of secondary sources, are further compared with each other in Figure 7-19 in the case of each considered material combination. It can be observed in these summary plots that, out of the four tactics, the greatest suppression at low frequencies is generally achieved with two point-monopoles, followed by with two point-forces, with one point-monopole, and then with one point-force. Overall, using two sources outperforms a single source, in particular, for the rubber shell in air and the steel shell in either air or water. This is expected for these cases because

- the primary is dominated at low ka by both $n = 0$ and $n = 1$ components,
- when increasing the number of sources, the secondary for point-monopoles suppresses the more dominant $n = 0$ component first, in which it couples the best, and
- when increasing the number of sources, the secondary for point-forces suppresses the less dominant $n = 1$ component first, in which it couples the best.

In terms of resonances, it is difficult to interpret the differences between using point-monopoles and point-forces in the plots of normalized scattered sound power after control or spherical harmonic components after control. However, from Figure 7-19, it can be observed that for the rubber shell in air and the steel shell in water, which exhibit peaks in scattered power at mid-frequencies in the studied range, the control with either two point-monopoles or two point-forces produces meaningful attenuation of these resonances.

The better performance of the acoustic point-monopoles is probably explained by the way in which they more efficiently couple into the spherical harmonic components of the extended scattering produced by the plane-wave. In contrast, the point-forces couple more effectively into the structural modes of the shell, some of which radiate more efficiently than others. As a result, the control performance achieved over the extended scattering produced by the plane-wave is less direct.

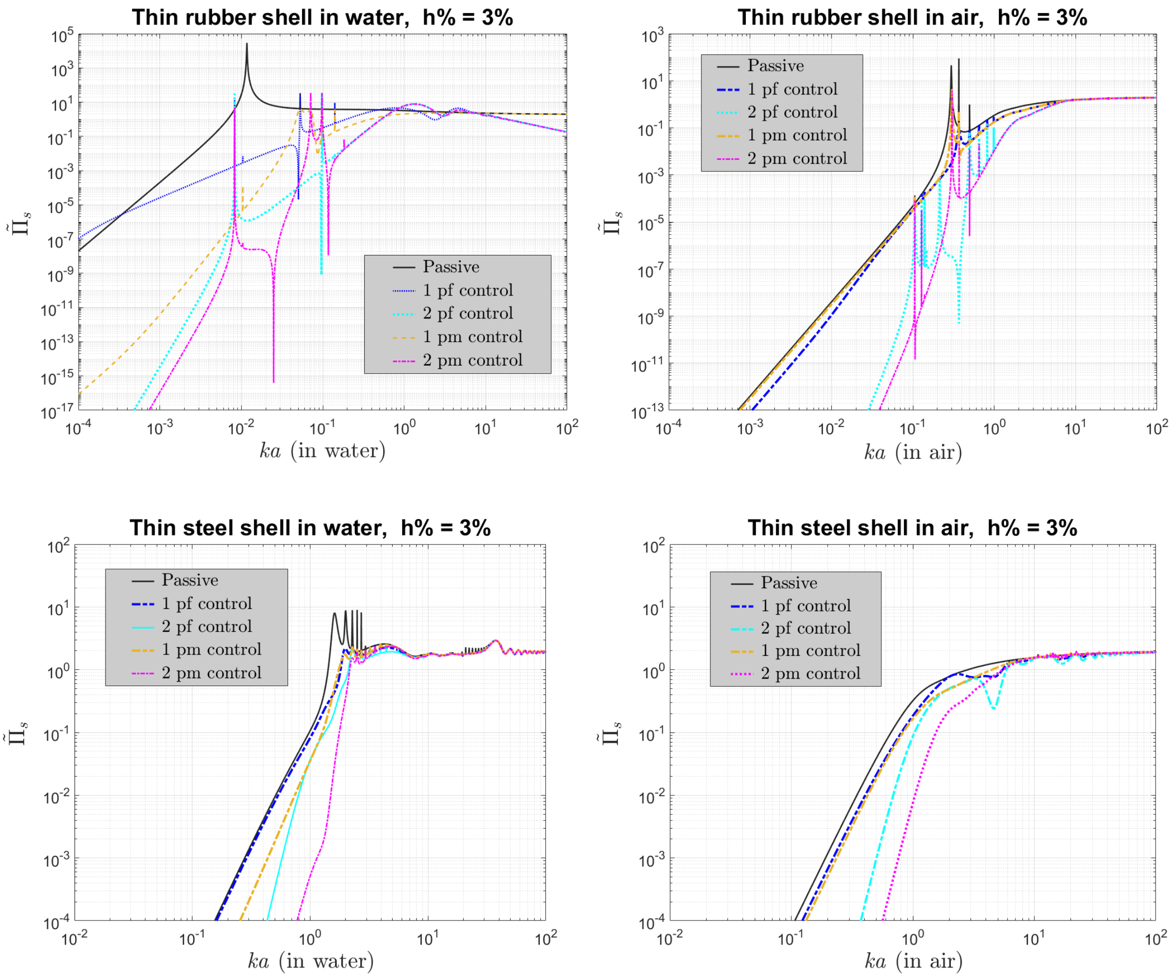

Figure 7-19 Comparison of normalized scattered sound power before and after control versus ka, for idealized tonal power minimization with either one point-monopole, two point-monopoles, one point-force, or two point-forces on the surface of the shell made out of either rubber or steel and surrounded by either water or air.

7.4 Active velocity feedback control

For the analysis of active feedback control, it is convenient to formulate the problem in terms of the modal acoustic pressures and velocities introduced in section 3.3, rather than the scattering and radiation coupling coefficients previously used for idealized active control. In the case of a thin, uniform, empty spherical shell, the three modal impedance matrices described in section 3.3 are diagonal and of size $(N+1)^2 \times (N+1)^2$, where N is the truncation value of the spherical harmonic representations. All $2n+1$ elements on the diagonals of these matrices that are associated with a given index n share the same modal value for each of the three impedances, such that

$$\tilde{Z}_I(n,m) = i\rho_0 c_0 \frac{j_n(ka)}{j_n'(ka)}\ , \tag{7.9}$$

$$\tilde{Z}_R(n,m) = -i\rho_0 c_0 \frac{h_n(ka)}{h_n'(ka)}\ , \tag{7.10}$$

$$\tilde{Z}_B(n,m) = i\frac{\rho_S c_p}{\Omega}\frac{h}{a}\frac{(\Omega^2-\Omega_{n1}^2)(\Omega^2-\Omega_{n2}^2)}{\Omega^2-(1+\beta^2)(\nu+\lambda_n-1)}\ , \tag{7.11}$$

for all $m \in \mathbb{Z}$, $|m| \leq n$, where n is fixed. Expression (7.11) is equivalent to (6.5), and the values of Ω_{n1} and Ω_{n2} are the in-vacuo natural frequencies of vibration of the shell which are given by the roots of equation (6.6).

Because of the above, a modal component of the scattered pressure on the surface of the shell, as in (3.4), and a modal component of the incident pressure on the surface of the shell, as in (3.4), form the ratio

$$\frac{\breve{p}_s(n,m)}{\breve{p}_i(n,m)} = \frac{\tilde{Y}_I(n)-\tilde{Y}_B(n)}{\tilde{Y}_R(n)+\tilde{Y}_B(n)} = -\frac{h_n(ka)}{j_n(ka)}\,\frac{j_n(ka)+i\,\tilde{\zeta}_B(n)\,j_n'(ka)}{h_n(ka)+i\,\tilde{\zeta}_B(n)\,h_n'(ka)}, \tag{7.12}$$

for a given index n, at all $m \in \mathbb{Z}$, $|m| \leq n$. Using (7.12), the normalised scattered sound power of a spherical shell due to an incident plane-wave can be calculated as [78]

$$\tilde{\Pi}_s = \frac{4}{(ka)^2}\sum_{n=0}^{N}(2n+1)\left|\frac{j_n(ka)+i\,\tilde{\zeta}_B(n)\,j_n'(ka)}{h_n(ka)+i\,\tilde{\zeta}_B(n)\,h_n'(ka)}\right|^2 . \tag{7.13}$$

The shell now is assumed to be controlled with L internal active point-forces, each of which has a magnitude $\tilde{f}_l$ acting at (θ_l, φ_l) that generates a modal pressure, as in equation (3.4) of [65]

$$\breve{p}_l(n,m) = -\left[\frac{\tilde{Z}_B(n)}{\tilde{Z}_B(n) + \tilde{Z}_R(n)}\right]\frac{\tilde{f}_l}{a^2}\ \bar{Y}_{n,m}^{(\mathbb{C})}(\theta_l, \varphi_l)\,. \tag{7.14}$$

The scattered modal pressure after control with L secondary point-forces is thus

$$\breve{p}_{sc}(n,m) = \tilde{p}_s(n,m) - \left[\frac{\tilde{Z}_B(n)}{\tilde{Z}_B(n) + \tilde{Z}_R(n)}\right]\sum_{l=1}^{L}\frac{\tilde{f}_l}{a^2}\ \bar{Y}_{n,m}^{(\mathbb{C})}(\theta_l, \varphi_l)\,, \tag{7.15}$$

which can be written in vector form as

$$\breve{\mathbf{p}}_{sc} = \breve{\mathbf{p}}_s - \breve{\mathbf{B}}\cdot\breve{\mathbf{p}}_c\,, \tag{7.16}$$

where $\breve{\mathbf{p}}_c = \left[\tilde{f}_1,\ \tilde{f}_2,\ \tilde{f}_3 \dots\ \tilde{f}_L\right]^{\mathrm{T}}$ is the vector of L control forces, which contains discrete rather than modal pressures, and $\breve{\mathbf{B}}$ is equal to $\frac{1}{a^2}\breve{\mathbf{Z}}_B\left[\breve{\mathbf{Z}}_{\boldsymbol{B}} + \breve{\mathbf{Z}}_{\boldsymbol{R}}\right]^{-1}$ times the $(N+1)^2$ by L matrix $\mathbf{S}$, where the l-th column of $\mathbf{S}$ has elements of the form $\bar{Y}_{n,m}^{(\mathbb{C})}(\theta_l, \varphi_l)$. Assuming $\left[\breve{\mathbf{Z}}_{\boldsymbol{B}} + \breve{\mathbf{Z}}_{\boldsymbol{R}}\right]$ is non-singular, the descriptions described in the paragraphs above can be used in the feedback control theory outlined in subsection 3.3.2 to calculate the scattered sound power after feedback control.

The active velocity feedback arrangement described in section 3.3 and depicted in Figure 3-3 is exemplified through computer-modelled results for the case of a single co-located control force actuator and point velocity sensor on the outer surface of a steel spherical shell surrounded by water, in the backscattering position ($\theta = \pi$). These results are presented in Figure 7-20 and were computed using only the $m = 0$ spherical harmonic components in the matrix operations as they are the only contributing ones given the ideal placement of sensor and actuator relative to the incidence and the scatterer. The matrices $\mathbf{G}_c$, $\mathbf{G}_c^{(cl)}$, and $\mathbf{H}$, which represent the open-loop response between control force actuators and velocity sensors from equation (3.18), the closed-loop response $\mathbf{G}_c^{(cl)} = (\mathbf{I} + \mathbf{G}_c\mathbf{H})^{-1}\cdot\mathbf{G}_c$, and, respectively, the feedback gain matrix, have only one element each because only one sensor and one actuator are used. As such, they are denoted as G_c, $G_c^{(cl)}$, and H on the graphs.

In Figure 7-20, the first few modal components of the open-loop response, G_c, and of the closed-loop response, $G_c^{(cl)} = G_c/(1 + G_c\cdot H)$, are plotted against normalized frequency ka for three values of constant feedback gain $H \in \{\rho_0 c_0/10,\ \rho_0 c_0,\ 10\rho_0 c_0\}$. $N = 100$ terms were calculated in MATLAB for the spherical harmonic series of the scattered power and for the tonal power minimization over the shown frequency range. The variation with frequency of the overall open-loop and closed-loop responses are compared between different feedback gains, as well as the effect on normalized scattered sound power after control.

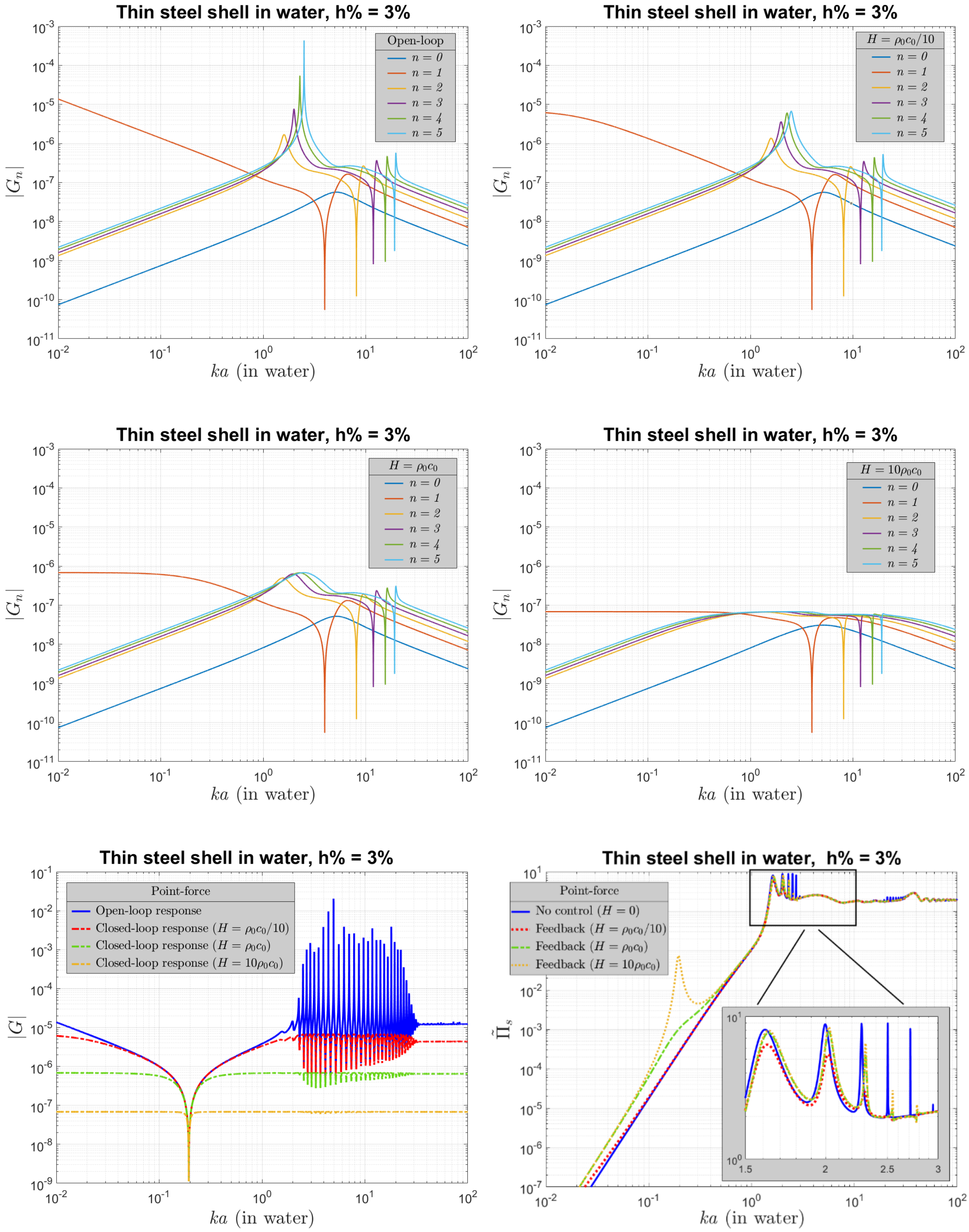

Figure 7-20 Variation of different quantities with ka for velocity feedback control of plane-wave scattering from steel shell in water, with one co-located control force actuator and point velocity sensor at $\theta = \pi$: modal magnitudes of open-loop response G_c and of closed-loop response $G_c^{(cl)}$ with feedback gains $H \in \{\rho_0 c_0/10,\ \rho_0 c_0,\ 10\rho_0 c_0\}$, overall magnitudes of open-loop and closed-loop response, and comparison of normalized scattered sound power $\widetilde{\Pi}_s$ after control (in this order, left to right, top to bottom).

In the results of the open-loop modal components, the 'Lower branch' and 'Upper branch' of in-vacuo resonances of the shell can be easily distinguished in the peaks. For the closed-loop response, as the feedback gain is increased, the peaks corresponding to the 'Lower branch' resonances get attenuated, in particular, the higher order ones, without any shift in frequency. The peaks corresponding to the 'Upper branch' resonances also start to get attenuated for a high enough feedback gain without any shift in frequency. Furthermore, it is important to highlight that increasing the feedback gain significantly lowers the magnitude of the $n = 1$ component in the closed-loop response at the lowest values of ka, while the other modal orders remain unaffected.

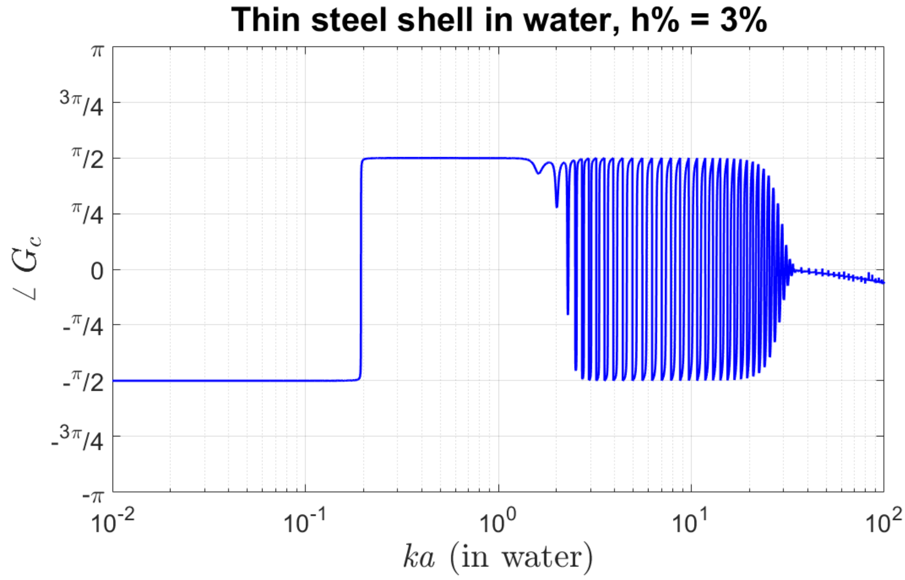

Figure 7-21 Phase of the open-loop response G_c versus normalized frequency ka for a thin steel shell of thickness $h/a = 3\%$, submerged in water, and with one co-located control force actuator and point velocity sensor at position $\theta = \pi$ on its surface.

In the overall response, the open-loop G_c and closed-loop $G_c^{(cl)}$ at low values of ka are dominated by the $n = 1$ component, less and less so with increasing feedback gain. At a point in frequency, the low frequency behaviour of the orders $n \geq 2$ becomes comparable with that of $n = 1$ and a trough is formed in the overall responses at about $ka = 0.2$. This trough is not shifted in frequency by increasing the feedback gain and is not caused by an instability in the system. The latter is proven by observing the phase of the open-loop response G_c versus ka, which is plotted in Figure 7-21. This phase does not reach anywhere close to $-\pi$ for the shown frequency range and it cannot be shifted as the feedback gain is a real-valued constant. Therefore, the value of $G_c \cdot H$ cannot reach close to -1, and the closed-loop response $G_c^{(cl)} = G_c/(1 + G_c \cdot H)$ is guaranteed to be stable. Across the shown range of frequency, except for the trough at $ka = 0.2$, it can be observed in Figure 7-20 that increasing the feedback gain reduces the overall magnitude of the closed-loop response, indicating that the feedback control is pinning the shell at the actuation position.

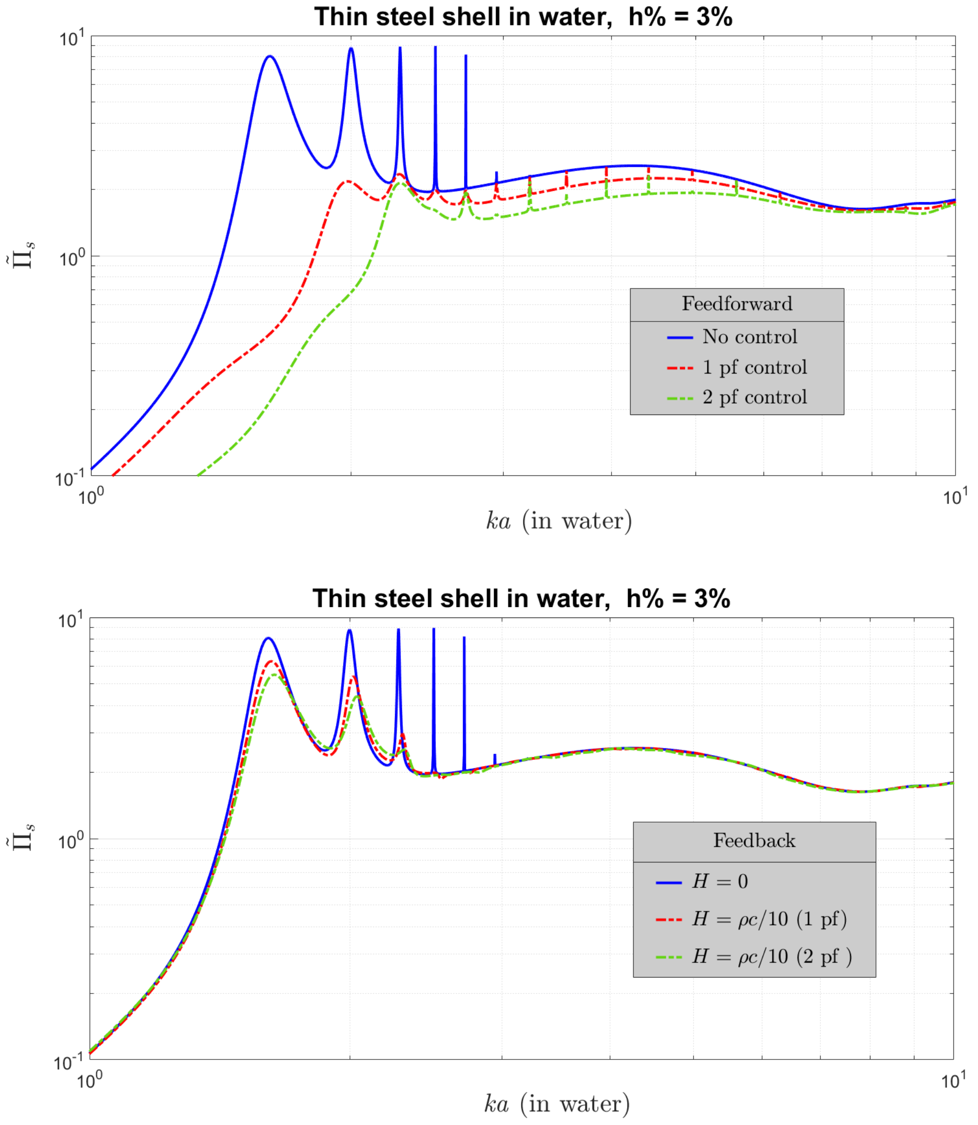

Figure 7-22 Normalized scattered sound power $\tilde{\Pi}_s$ versus normalized frequency ka for plane-wave scattering from the thin steel shell in water ($h/a = 3\%$), when using one or two point-forces on its surface for feedforward active control equivalent to the result from Figure 7-13 (top), or for velocity feedback control shown in Figure 7-20 (bottom). The ka range is zoomed-in around the first few resonances.

The decrease in magnitude of the closed-loop response at low ka due to increasing the feedback gain translates into enhancement of the normalized scattered power after control, which is severe at the frequency corresponding to the previously described trough in the response. Some attenuation of the first few resonant peaks is achieved, which is the greatest for the lowest used feedback gain. At large values of ka, insignificant alterations of the scattered sound power are produced after control, regardless of the exemplified feedback gains.

In Figure 7-22 the active velocity feedback control is compared with the ideal active control equivalent of a feedforward control for the steel shell in water, in the region of its first few resonant frequencies. This is done for one co-located control force actuator and point velocity sensor in the backscattering position ($\theta = \pi$), and two co-located control force actuator and point velocity sensor in the backscattering ($\theta = \pi$) and shadow positions ($\theta = 0$). It can be observed from the figure that the ideal feedforward control achieves significant attenuation of all the first few resonant peaks, in particular, of the very first one. The active velocity feedback control attenuates the higher order modes more than the very first one. This can be explained from the overall open-loop response G_c in Figure 7-20 (blue line), which exhibits a lower magnitude at the frequency of the first resonant peak compared to the magnitude at the subsequent ones. For both feedforward and feedback methods, using two point-forces achieves somewhat more attenuation of all resonant peaks when compared to their counterparts with one point-force.

7.5 Chapter summary

In this chapter, many results have been presented for tonal active control of the scattered power due to a plane-wave, using either secondary acoustic point-monopoles or point-force actuator on the surface of a thin, uniform, empty, elastic spherical shell. Rubber or steel were used as materials of the shell, which was surrounded either by water or air. Some conclusions have been drawn about the relative performance of different actuators in different circumstances, but the wealth of results has prevented the preparation of an exhaustive presentation. Nevertheless, some conclusions are clear. Under idealized feedforward control conditions and ideal placement of secondary entities relative to the incidence and scatterer, it was reinforced that, at low frequencies before the first resonant peak, the power minimization with one or two control entities yields outcomes equivalent to cancelling the first one or, respectively, first two most dominant components of the primary (scattering) that the secondary also couples best into. This was achieved by comparing analytical predications based on asymptotic behaviour of spherical harmonic coefficients to the computed results. In both cases of secondary entities, these first two components respecting the described characteristics are the omnidirectional $n = 0$ one (breathing mode) and the figure-of-eight $n = 1$ one (translational mode). However, the radiation due to a point-monopole couples better into the $n = 0$ component of the plane-wave scattering, while the radiation due to point-force radiation couples better into the $n = 1$ component of the plane-wave scattering. This led to a greater control performance at low frequencies after tonal power minimization with point-monopoles, when compared to using point-forces. At higher frequencies, the control strategy yielded no benefit again, due to many spherical harmonic components dominating at the same time. However, the magnitudes of the resonant peaks in the scattered sound power could be attenuated depending on where they were situated on the frequency range. Ultimately, a feedforward arrangement as described in this paragraph assumes perfect knowledge of the incidence, scattering and secondary at all times; however, this is difficult to implement in practice.

One active control arrangement that can be readily implemented is velocity feedback control, as discussed in Chapter 3, which would require the use of structural actuators. The very limited investigation of feedback control presented in this chapter demonstrated that some attenuation of the scattered power was possible with one secondary point-force actuator on the surface of a thin spherical shell made of steel and submerged in water. This secondary was ideally placed relative to the incidence and the scatterer, while also being co-located with a sensor on the surface measuring velocity normal to the boundary. For the given circumstances, computer-modelled results showed that the suppression after feedback control is achieved specifically for the first few resonant peaks in the scattered power due to an incident plane-wave, with an appropriate choice of constant feedback gain. Out of these attenuated peaks, the ones of higher modal index were supressed more due to the point-force coupling better into the dynamics of structure at that specific frequency range, as demonstrated by the open-loop response of the arrangement. When the feedback gain was too large, the structure become effectively pinned at the actuation point, and very little motion was in turn generated at the sensor after control. Further modelling and experimental work is required to validate the possible capabilities of practical force actuators on the surface of a sound radiating structure, as described in [95, 96].

Chapter 8 Final Statements

8.1 Conclusions of current work

In this thesis, the active control of 3D sound scattering has been studied from a theoretically focused perspective, which took advantage of spherical harmonic series expansions. This was used to obtain computer-modelled results of the involved physical quantities, as well as to formulate an active control procedure based on the modal components represented by the spherical harmonics. The spherical harmonics form the set of radiation modes for certain spherical structures.

Overall, the methodology of the thesis set out to explore fundamental 3D models and ideal sets of circumstances, such that physical insight of the complicated 3D physical behaviour can be observed and understood. As such, a single stationary spherical scatterer in an idealized, stationary fluid was considered and modelled as an exterior impedance boundary-value problem, ignoring any internal behaviour of the obstacle. The impedance boundary value was allowed to either be constant, corresponding to an impedance sphere model, or to be a function of frequency and modal index, corresponding to a thin spherical shell model. The analysis focused on a simple incidence, in the form of a single monochromatic travelling plane-wave. A classic method of active suppression was chosen, i.e. ‘least-mean squares’ minimization of the radiated sound power at a single frequency, and rudimentary models of secondary control entities were used, such as point-monopoles and point-forces. Furthermore, when using a small number of secondary entities, their positions relative to the incidence were chosen specifically to simplify the mathematics of the spherical harmonic formulations, and thus allow a straightforward interpretation and discussion of the results. The asymptotic behaviour at low frequencies, before and after control, were studied for the primary, secondary and their superposition after optimization, where active control with a small number of control entities is expected to produce performance [24].

Overall, it was found that at low frequencies, the power minimization approach with one control source is similar to completely cancelling the first most dominant spherical harmonic component of the scattered sound in which the secondary also couples the best. For a point-monopole secondary with the impedance sphere and the spherical shell, this component was the omnidirectional $n = 0$ component, while for a point-force with the spherical shell, this component was the figure-of-eight shaped $n = 1$ component. The residual after control was typically the next scattering component in the sequence of which is most dominant and coupled best into by the secondary. This residual could be either enhanced or suppressed after control.

With more control parameters to optimize, increasingly more of the dominant components in the primary could be completely cancelled, depending on the order of which is most dominant and, also, best coupled into by the secondary. At high frequencies, a small number of secondary sources did not produce any control performance, because a large number of spherical harmonic components are dominant simultaneously in the scattering, and only a small number of control parameters are available to individually optimize the behaviour of these components.

Other aspects of actively controls 3D scattering were also briefly explored. The control with a large number of secondary sources was studied for the impedance sphere, where the majority of positions were not ideal; however, the geometrical pattern was uniform. Increasing the number of sources was found to produce diminishing returns after a certain frequency threshold. Also, a simple rule of thumb was derived for the number of secondary sources required to control the scattered sound up to a given frequency. The effect on control performance of moving the uniform pattern some distance away from the scatter was also explored for the impedance sphere and was found to be detrimental for suppressing sound power, regardless of the surface impedance. This generalizes the previous result for the rigid sphere from [33].

Also, regional active control was explored for the impedance sphere in the form of cancelling one far-field direction around the scatterer. It was found that, under certain circumstances, this type of control can severely enhance the scattered sound power (global measure) as well as the regional behaviour of the far-field scattered pressure. The amount of suppression or enhancement after the control is governed by the impedance of the scattering surface. The most severe enhancement typically occurs at high frequencies, or if there are severe mismatches in the regional behaviour of the far-field directivity between the primary and the secondary.

Lastly, the research considered theoretical models that could potentially address some of the practical limitations of realizing the idealized active control systems previously investigated in the thesis. These limitations included:

- the inability to directly measure the scattering without it being contaminated by the incidence, and
- the constraints of measuring spherical harmonic components in real-time with sensors around the scatterer.

Bobrovnitskii`s approach to modelling scattering and its control was used for this purpose and was translated into a modal method based on spherical harmonics components rather than the original method based on a grid of spatial elements on the scattering surface. Active velocity feedback control was explored for the spherical shell in a fluid for a small number of point-force actuators co-located with point velocity sensors on the scattering surface. It was found that the behaviour of the open-loop response between forces and velocity sensors dictates the outcomes of the control when it comes to altering the scattered sound power. Furthermore, compared to the idealized active control approaches, the control performance of the feedback is severely limited or inadequate in certain frequency regions, such as low frequencies. The most significant benefit from the feedback is the attenuation of the first few resonances of the externally loaded structure by adding damping to its modal impedances. This is an expected outcome, as previously shown by the results of works such as [87].

Time constraints did not allow for any practical validation of the theoretical models studied throughout this thesis. However, two basic experiments were proposed, one for testing the idealized active control approaches (feedforward), and the other for testing the velocity feedback strategy. These experiments were designed to ignore some of the real-time constraints and allow for offline measurements, such that the focus would be on manipulating the scattering components of the spherical harmonic representation in practice.

8.2 Avenues of future work

8.2.1 Improvement of feedback approach

The nature of the open-loop response described in subsection 3.3.2 can be changed to produce different attenuation effects on the first few resonances of an externally loaded structure. For example, using distributed force actuators and distributed velocity sensors on the surface of the structure can potentially generate significantly better results. Furthermore, the feedback gain does not have to be constant, the feedback does not have to be based solely on velocity data, and the controller does not have to be restricted on a single independent feedback loop. All these aspects can be further explored for control of 3D sound scattering from structures, both theoretically with models and in practice through experiments.

8.2.2 Non-ideal placement of incidence and secondary relative to the scatterer

The formulations throughout this thesis have been written in terms of full spherical harmonic series, even though the investigation specifically illustrated positions on the z-axis for the incidence and the secondary source, which lead to only the $m = 0$ spherical harmonic components being non-zero. All formulations in this thesis can be used when the incidence and the secondary entities are not ideally located for the mathematics of the spherical harmonics. However, in these scenarios it is not straightforward to gain physical insight, for example, when it comes to the low frequency asymptotic analysis before and after control. Furthermore, a full set of spherical harmonics translates in a more components for which active control can generate spill-over or unwanted effects, as well as in additional computational cost to model. However, the power minimization method based on spherical harmonic components that was used in this work can be potentially reformulated to force different outcomes on different sets of spherical harmonics, similar to a multi-band filtering of frequencies but for the spherical harmonic orders. All things considered, the cases of non-ideal placements are a better representation of practical scenarios, and they can still be computed in a relatively straightforward way.

8.2.3 More complicated generators of sound as incidence and secondary

The theoretical models for active control that are described in this thesis focus on using a small number of idealized secondary sources that generate simple radiation patterns in order to obtain suppression in the low frequency region. This suppression was demonstrated theoretically for a simple case of incidence, i.e. a monochromatic plane-wave. Also, the used models assume that physical quantities such as sound pressure or surface velocity on the scatterer are at a single point, i.e. a mathematical abstraction. All these aspects are not a good representation of the practical circumstances.

Firstly, for certain practical situations, the incidence that generates the scattering may not be known or may not be measurable. Furthermore, this incidence may be composed from the superposition of many different types of waves, e.g. multiple polychromatic plane-waves, multiple polychromatic point-monopoles. The general frameworks from Chapter 2 and Chapter 3 can be applied to and account for any type of deterministic incidence, as long as assumptions such as linearity and reciprocity are maintained. A different type of analysis is required when considering randomly generated incident sound. When the incident sound is not a monochromatic plane-wave, the nature of the spherical harmonic components in the scattering may change. Because of this, aspects such as the low frequency hierarchy of spherical harmonic orders or the way in which the secondary couples into the components of the scattering may become difficult to interpret and predict analytically, even at low frequencies.

Secondly, additional devices such as sensors and radiating sources must be introduced in a situation to realize the active control system. These devices typically have their own dimensions, which may be comparable to the wavelength of interest and, thus, can themselves produce significant scattering the sound. As a result, the use of practical devices can pose additional challenges to be overcome.

Thirdly, real sensors and sources typically do not have simple directivity patterns such as omnidirectional or a figure-of-eight, depending on the frequency. As frequency increases, these patterns tend to become more complicated in 3D space and can be described as the contributions of several multipole components. Such complicated variations in space can be advantageous for regional active control when they are designed to be very directional. However, discriminating in favour of very narrow regions in space may not allow for proper spatial coverage when performing global control, even when using many devices. Furthermore, it is difficult to realize practical sensors and sources with complicated patterns of many multipole contributions. However, considerable technological progress has been made in the area for multipole sensors, such as the ‘eigenmike’ [97-99]. With passing time, such technology will continue to improve; thus, an investigation of using high-order multipole sensors and secondary source for actively controlling 3D scattering from structures still represents a valuable modelling and experimental exercise.

8.2.4 Moving scatterer and/or medium around it

In practice, scattering objects and the medium surrounding them may not be stationary, and their material properties may change with time. As a result, active controllers for these scenarios need the ability to account for Doppler shifts, need to perform in real-time, and need to be robust, in other words, a very challenging problem. In current times, the 3D sound scattering from non-stationary entities has been explored only in a few works, such as [42, 53, 54], but is an extremely important aspect of a practical scattering problem.

8.2.5 Layers of different materials surrounding scatterer

Surrounding a scatterer with additional material layers to help cloak it is being significantly explored in current times, as seen in metamaterial approaches [15, 16, 100-102] and approaches using layers of traditional materials [23, 103, 104]. In terms of mathematical modelling, multi-layer scenarios can be described by extending the transmission boundary-value problem described in Chapter 2 to multiple mediums. This can potentially be used to create a unified, generalized mathematical approach that encompasses both the case of continuously varying material parameters with position in the medium, as seen in metamaterial designs, and the case of material parameters that do not vary significantly with space.

8.2.6 Other active control constraints

As described in [76], multiple constraints can be imposed on a given scenario through active control. For example, the control of a global measure such as sound power can be combined with the control of a regional measure such as sound pressure in order to find a potential balance between global suppression and regional attenuation or to limit the enhancement of pressure in certain regions of space. This can be explored theoretically or in practice for 3D sound scattering from a structure, in particular, for situations where significant regional effects are generated. An example of this is represented by the shadow and backscattering regions formed around the scatterer when the involved relative frequency is high.

8.2.7 Complicated cloaking/detection environment

Ultimately, in practice, a given environment has changing circumstances and is composed of multiple sound scatterers that are not stationary. Typically, a detector that is also not stationary would be searching for scatterers using acoustic emitters, acoustic receivers, and different strategies for detection. Such a scenario is both very difficult to test experimentally, as well as very difficult to model, simulate and interpret in terms of physical insight. That is why it is important to construct rigorous mathematical procedures and research methodologies that gradually explore the effect of cloaking starting from the most fundamental circumstances, and then following with progressively more complicated features of physical behaviour.

In complicated environments as described above, the spherical harmonic decomposition as used throughout this thesis may not be the ideal approach of exploiting the spherical harmonic functions [77]. These functions are defined relative to a reference point, and the origin of the coordinate system was used as the reference in Chapter 2. This leads to the omnidirectional $n = 0$ spherical harmonic component being equivalent to the sound pressure being equal on the whole surface of virtual sphere surrounding the origin. However, the spherical harmonic decomposition can be performed about a point that is not the origin, similar to how a Taylor expansion can be performed around different values [77]. In this new scenario, the omnidirectional component obtained when decomposing at a point that is not the origin consists of contributions from multiple of the original spherical harmonic components corresponding to the decomposition at the origin. These contributions can be established mathematically [77].

In situations where multiple scattering objects or vibrating structures are present in the same environment, it may be useful to either

- decompose at a single convenient point in space, such that there is a consistency of how all entities are described in terms of spherical harmonics, or
- decompose at multiple points in space centred at each entity, such that the dynamic motion of each body relative to itself can be studied.

A structure that radiates the same in all directions, such as the sound scattering from a human head at low frequencies, does not appear as a single omnidirectional component when expressed in terms of spherical harmonics defined about a point that is not placed at the centre of the structure. However, depending on the application, it may be more important to know that the structure has an omnidirectional radiation pattern rather than its spherical harmonic description about an arbitrary origin. For example, when investigating how the acoustic scattering from a person`s head and torso affects their sound localization cues, it would be the most beneficial to use spherical harmonic components centred between the two ears. But for reproducing 3D audio in a room, it may be necessary to have the origin of the coordinate system at a specific location that is not that of the listener.

Appendices

Appendix A 3D orthogonal coordinate systems

A point P in 3D space is defined by convention as $P(x; y; z)$ in the Cartesian coordinate system, $P(\rho; \varphi, z)$ in the cylindrical coordinate system, and $P(r; \theta, \varphi)$ in the spherical coordinate system. x, y and z represent the coordinates corresponding to the *x*-axis, *y*-axis and *z*-axis, respectively. r represents the radial distance from the origin of the reference system to the point P. θ is called inclination (or polar angle or co-elevation) and it is formed between the positive direction of the *z*-axis and the position vector $\overrightarrow{OP}$. φ is called azimuth (or azimuthal angle) and it is measured from the positive direction of the *x*-axis to the projection of the position vector $\overrightarrow{OP}$ on the *xy*-plane. ρ represents the radial distance from the *z*-axis to the point P. A visual representation of these conventions can be seen in Figure A1, where the direction of the trigonometric circle is highlighted for previously defined angles.

In the cases of the cylindrical coordinates $(r; \varphi, z)$ and the spherical coordinates $(\rho; \theta, \varphi)$, any coordinate triplet denotes a single point in three-dimensional space. However, any point in space can have an infinite number of representations through these two types of triplets unless the ranges of values of the coordinates are restricted. The convention used throughout this work is:

$$r \geq 0\,, \qquad 0 \leq \theta \leq \pi\,, \qquad 0 \leq \varphi < 2\pi\,,$$

which ensures a unique triplet of cylindrical/spherical coordinates is associated with each point.

Conversions from one of the three coordinate systems to another can be achieved using the expressions presented Table A1. It is worthwhile to highlight the special cases:

- when $\theta = 0$ or $\theta = \pi$, P is on the *z*-axis, $x = y = 0$, $r = |z|$, $\rho = 0$, and φ can take any value. For practical reasons, the convention $\varphi = 0$ when $x = y = 0$ is enforced;
- when $\varphi = 0$ and $x^2 + y^2 \neq 0$, P is on the *xz*-plane, $y = 0$ and $0 \leq \theta \leq \pi$;
- $y = 0$ also when $\varphi = \pi$;
- when $x = 0$ and $x^2 + y^2 \neq 0$, P is on the *yz*-plane, $\varphi = \pi/2$, and $0 \leq \theta \leq \pi$;
- when $z = 0$ and $x^2 + y^2 \neq 0$, P is on the *xy*-plane, $\theta = \pi/2$, and $0 \leq \theta \leq \pi$;
- when $r = 0$, then $x = y = z = 0$, and $\varphi = 0$, $\theta = 0$ is chosen as the convention for this case.

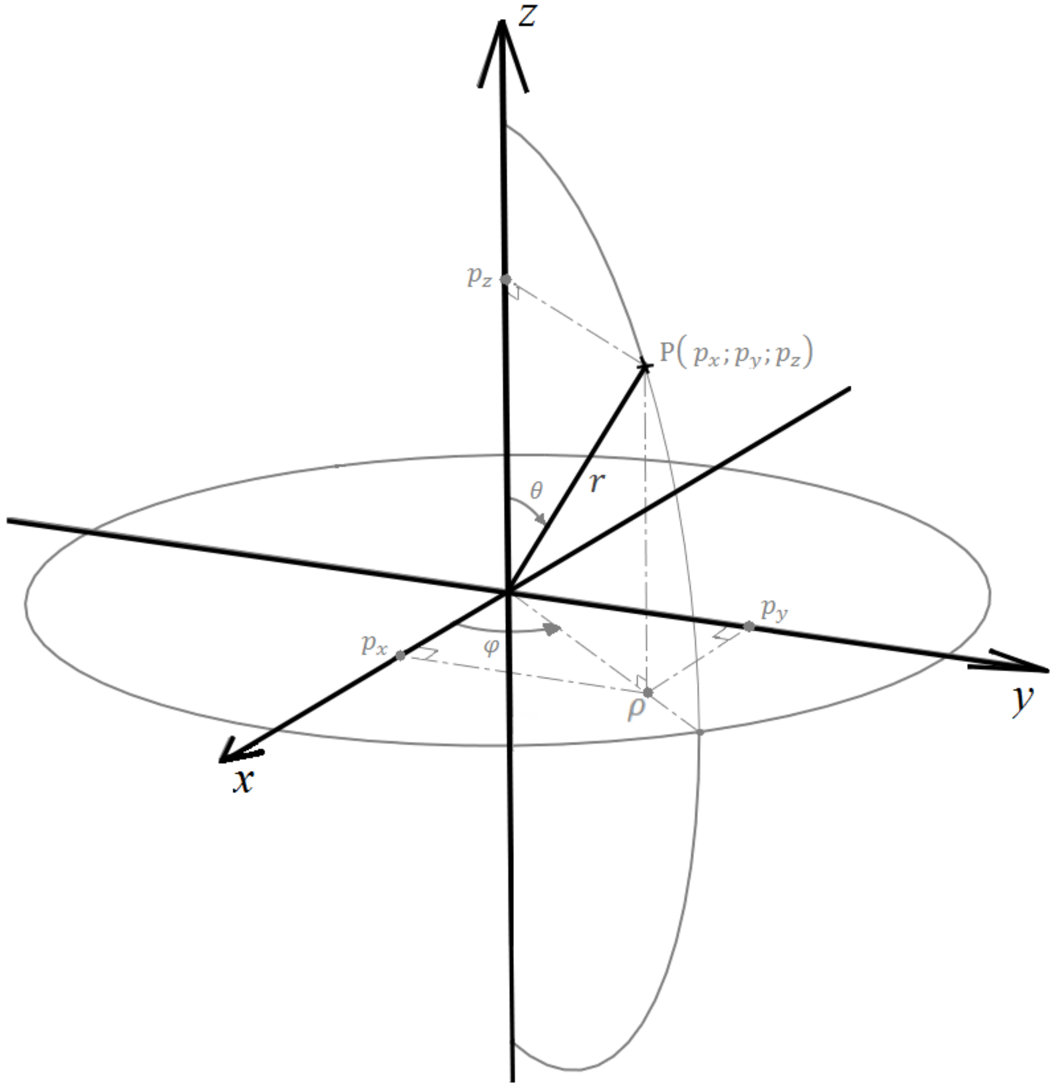

Figure A1: The convention for 3D Cartesian coordinates $(p_x; p_y; p_z)$, cylindrical coordinates $(\rho; \varphi, z)$, and spherical coordinates $(r; \theta, \varphi)$, of a point P in space. The convention for the direction of the trigonometric circle in the cases of inclination θ and azimuth φ are also shown.

$\nabla^2 f$ **in Cartesian coordinates**	**Cartesian to cylindrical**	**Cartesian to spherical**
$\nabla^2 f = \frac{\partial^2}{\partial x^2} + \frac{\partial^2}{\partial y^2} + \frac{\partial^2}{\partial z^2}$	$\rho = \sqrt{x^2 + y^2}$ $\varphi = \begin{cases} \tan^{-1}\left(\frac{y}{x}\right), & x > 0 \\ \tan^{-1}\left(\frac{y}{x}\right) + \pi, & x < 0,\ y \geq 0 \\ \tan^{-1}\left(\frac{y}{x}\right) - \pi, & x < 0,\ y \leq 0 \\ \frac{\pi}{2}, & x = 0,\ y \geq 0 \\ -\frac{\pi}{2}, & x = 0,\ y \geq 0 \\ 0, & x = y = 0 \end{cases}$ $z = z$	$r = \sqrt{x^2 + y^2 + z^2}$ $\theta = \cos^{-1}\left(\frac{z}{r}\right),\ r \neq 0$ $\varphi = \begin{cases} \tan^{-1}\left(\frac{y}{x}\right), & x > 0 \\ \tan^{-1}\left(\frac{y}{x}\right) + \pi, & x < 0,\ y \geq 0 \\ \tan^{-1}\left(\frac{y}{x}\right) - \pi, & x < 0,\ y \leq 0 \\ \frac{\pi}{2}, & x = 0,\ y \geq 0 \\ -\frac{\pi}{2}, & x = 0,\ y \geq 0 \\ 0, & x = y = 0 \end{cases}$
$\nabla^2 f$ **in cylindrical coordinates**	**Cylindrical to Cartesian**	**Cylindrical to spherical**
$\nabla^2 f = \frac{\partial^2 f}{\partial \rho^2} + \frac{1}{\rho}\frac{\partial f}{\partial \rho} + \frac{1}{\rho^2}\frac{\partial^2 f}{\partial \varphi^2} + \frac{\partial^2 f}{\partial z^2}$	$x = \rho \cos\varphi$ $y = \rho \sin\varphi$ $z = z$	$r = \sqrt{\rho^2 + z^2}$ $\theta = \begin{cases} \tan^{-1}\left(\frac{\rho}{z}\right), & z > 0 \\ \tan^{-1}\left(\frac{\rho}{z}\right) + \pi, & z < 0 \\ \frac{\pi}{2}, & z = 0 \end{cases}$ $\varphi = \varphi$
$\nabla^2 f$ **in spherical coordinates**	**Spherical to Cartesian**	**Spherical to cylindrical**
$\nabla^2 f = \frac{1}{r^2}\frac{\partial}{\partial r}\left(r^2 \frac{\partial f}{\partial r}\right) + \frac{1}{r^2 \sin\theta}\frac{\partial}{\partial \theta}\left(\sin\theta \frac{\partial f}{\partial \theta}\right) + \frac{1}{r^2 \sin^2\theta}\frac{\partial^2 f}{\partial \varphi^2}$	$x = r \sin\theta \cos\varphi$ $y = r \sin\theta \sin\varphi$ $z = r \cos\theta$	$\rho = r \sin\theta$ $\varphi = \varphi$ $z = r \cos\theta$

Table A1: Conversions between Cartesian coordinates $(x; y; z)$, cylindrical coordinates $(\rho; \varphi, z)$ and spherical coordinates $(r; \theta, \varphi)$ of a point P.

Appendix B The complex-valued spherical harmonics

Definition

$Y_{n,m}^{(\mathbb{C})}(\theta,\varphi)$ is the complex spherical harmonic of degree n and order m , where $n \geq 0$ and $|m| \leq n$ are integers. This two-variable function describes the angular dependency of the pressure field for the wave and Helmholtz equations in spherical coordinates, and is defined as [71]

$$Y_{n,m}^{(\mathbb{C})}(\theta,\varphi) = \sqrt{\frac{2n+1}{4\pi}\frac{(n-m)!}{(n+m)!}}\,P_n^m(\cos\theta)e^{im\varphi} \,, \tag{B1}$$

where $P_n^m(x)$ is the associated Legendre functions of degree n and order m (for details see [71]).

It is important to note that there are two different conventions used to define the functions $Y_{n,m}^{(\mathbb{C})}(\theta,\varphi)$, one that includes the Condon-Shortley phase and one that does not. The Condon-Shortley phase is a $(-1)^m$ factor that is included either in the expression for $Y_{n,m}^{(\mathbb{C})}(\theta,\varphi)$ or in the formulation for the associated Legendre functions $P_n^m(x)$, but not in both. The presence of this one $(-1)^m$ factor introduces an alteration of sign in the complex spherical harmonics of positive m and is especially useful in the field of quantum mechanics, as described in [72]. The convention used in this work includes the Condon-Shortley phase in the definition of $P_n^m(x)$, as is used in [71], while in [72] the $(-1)^m$ factor is contained in the definition of $Y_{n,m}^{(\mathbb{C})}(\theta,\varphi)$.

The associated Legendre function $P_n^m(x)$ is defined over the domain $x \in [-1;1]$ as [71]

$$P_n^m(x) = (-1)^m(1-x^2)^{m/2}\left(\frac{d}{dx}\right)^m \{P_n(x)\}\,, \tag{B2}$$

where $P_n(x)$ is a Legendre polynomial of degree n , which can be expressed in terms of [71]

$$P_n(x) = \frac{1}{2^n\,n!}\left(\frac{d}{dx}\right)^n \{(x^2-1)^n\} = \sum_{s=0}^{[n/2]} \frac{(-1)^s(2n-2s)!}{s!\,(n-s)!\,(n-s)!}\,\frac{x^{n-2s}}{2^n}\,. \tag{B3}$$

For $n \geq 0$, the spherical harmonics and associated Legendre functions of negative orders $-m$ are given by [71]

$$Y_{n,-m}^{(\mathbb{C})}(\theta,\varphi)(\theta,\varphi) = (-1)^m\,\bar{Y}_{n,m}^{(\mathbb{C})}(\theta,\varphi) \;, \tag{B4}$$

and, respectively, [71]

$$P_n^{-m}(x) = (-1)^m \frac{(n-m)!}{(n+m)!} P_n^m(x) \ . \tag{B5}$$

Orthogonality

The spherical harmonics form an orthonormal basis as shown by the relation [71]

$$\int_0^{\pi} \sin\theta \, d\theta \int_0^{2\pi} d\varphi \, \left\{ Y_{n,m}^{(\mathbb{C})}(\theta,\varphi) \cdot \bar{Y}_{n',m'}^{(\mathbb{C})}(\theta,\varphi) \right\} = \delta_{nn'} \, \delta_{mm'} \ , \tag{B6}$$

where (m,n) and (m',n') are two different sets of $(order, degree)$, and also δ is the Kronecker Delta function. This important result translates into any analytic, square-integrable ($\boldsymbol{L}^2$ space) function $f(\theta,\varphi)$ defined on the sphere can be written as the series expansion [71]

$$\tilde{f}(\theta,\varphi) = \sum_{n=0}^{\infty} \sum_{m=-n}^{n} \tilde{\mathcal{F}}_{n,m}^{(\mathbb{C})} \, Y_{n,m}^{(\mathbb{C})}(\theta,\varphi) \ , \tag{B7}$$

where $\tilde{\mathcal{F}}_{n,m}^{(\mathbb{C})}$ are complex constants defined as

$$\tilde{\mathcal{F}}_{n,m}^{\mathbb{C}} = \int_0^{\pi} \sin\theta \, d\theta \int_0^{2\pi} d\varphi \, \left\{ f(\theta,\varphi) \cdot \bar{Y}_{n,m}^{(\mathbb{C})}(\theta,\varphi) \right\} . \tag{B8}$$

For a given value of $m \in \mathbb{Z}$, associated Legendre functions have the orthogonality property [71]

$$\int_{-1}^{1} P_n^m(x) \, P_{n'}^m(x) \, dx = \frac{2}{2n+1} \frac{(n+m)!}{(n-m)!} \, \delta_{nn'} \ . \tag{B9}$$

Closure relations

The orthonormality of the spherical harmonics leads to the two relations [71]

$$\begin{aligned} \sum_{n=0}^{\infty} \sum_{m=-n}^{n} Y_{n,m}^{(\mathbb{C})}(\theta,\varphi) \cdot \bar{Y}_{n,m}^{(\mathbb{C})}(\theta',\varphi') &= \frac{1}{\sin\theta} \delta(\varphi-\varphi') \, \delta(\theta-\theta') \\ &= \delta(\varphi-\varphi') \, \delta(\cos\theta-\cos\theta') \end{aligned} \tag{B10}$$

and [71]

$$\sum_{m=-n}^{n} \left| Y_{n,m}^{(\mathbb{C})}(\theta, \varphi) \right|^2 = \frac{2n+1}{4\pi}, \tag{B11}$$

where (θ, φ) and (θ', φ') are two different sets of angular coordinates and where $\delta(x)$ is the Dirac delta function.

Legendre`s addition theorem

Let there be two different sets of angular positions in three-dimensional space, (θ, φ) and (θ', φ'), where the angle formed between their two position vectors is [72]

$$\cos\gamma = \cos\theta \cos\theta' + \sin\theta \sin\theta' \cos(\varphi - \varphi') \,. \tag{B12}$$

Then, the following relation is valid [72]

$$\sum_{m=-n}^{n} Y_{n,m}^{(\mathbb{C})}(\theta, \varphi) \cdot \bar{Y}_n^m(\theta', \varphi') = \frac{2n+1}{4\pi} \, P_n(\cos\gamma) \,. \tag{B13}$$

Appendix C The real-valued spherical harmonics

Relation to complex-valued spherical harmonics

The functions $Y_{n,m}^{(\mathbb{C})}(\theta,\varphi)$ presented in the previous appendix are complex-valued, where all (n,m) pairs with a $m \neq 0$ have both non-zero real and imaginary parts. However, it may be desirable in some practical or theoretical situations to re-write the spherical harmonics expansion in terms of real-valued basis functions. For example, when it comes to recording and reproducing the spherical harmonic content of a sound field, i.e. the Ambisonics technique, Polleti describes in [105] that microphones/loudspeakers can only capture/create real signals while the content to work with is complex-valued. Furthermore, the directivity pattern of a point-monopole is the same shape as $Y_{0,0}^{(\mathbb{C})}(\theta,\varphi)$ which is always real. When it comes to point-dipoles, their figure-of-eight directivity patterns are given by $\mathrm{Re}\left\{Y_{1,1}^{(\mathbb{C})}(\theta,\varphi)\right\}$, $\mathrm{Im}\left\{Y_{1,1}^{(\mathbb{C})}(\theta,\varphi)\right\}$ and $Y_{1,0}^{(\mathbb{C})}(\theta,\varphi)$, which is real, where the orientation of each is a different axis of the Cartesian coordinate system.

The complex-valued spherical harmonic used in this work is defined as

$$Y_{n,m}^{(\mathbb{C})}(\theta,\varphi) = \sqrt{\frac{2n+1}{4\pi}\frac{(n-m)!}{(n+m)!}}\, P_n^m(\cos\theta)\, e^{im\varphi} = \\ = \sqrt{\frac{2n+1}{4\pi}\frac{(n-m)!}{(n+m)!}}\, P_n^m(\cos\theta)[\cos(m\varphi) + i\sin(m\varphi)]\,, \tag{C1}$$

where the Condon-Shortley phase is included in the formulation of the associated Legendre function P_n^m. The functions P_n^m are real-valued, thus it can be observed from the above relation that the real and imaginary parts of $Y_{n,m}^{(\mathbb{C})}(\theta,\varphi)$ come from the complex exponential corresponding to the variation with angle φ. The most common way to express the real spherical harmonics is to define them as these real and imaginary components of $Y_{n,m}^{(\mathbb{C})}(\theta,\varphi)$. The paper [105] offers detailed explanations of how this can be done and of how it affects the formulations for the spherical harmonic expansions a sound field. However, it uses a description for $Y_{n,m}^{(\mathbb{C})}(\theta,\varphi)$ that does not include the Condon-Shortley phase, which makes some of the results not applicable to the definition used in this work.

In the following paragraphs, the relevant results and derivations from paper [105] are repeated briefly for the case where the Condon-Shortley phase is considered. The covered topics follow the structure: definitions for the real spherical harmonics, mapping the real spherical harmonics to the complex ones, re-writing the spherical harmonics expansions of the interior and exterior problems, and mapping the field coefficients of the real spherical harmonics to those of the complex spherical harmonics. Lastly, an extra step is done in addition to what is presented in [105]; it is shown that the change from real to complex spherical harmonics in the expansion of the exterior solution does not alter, in essence, the expression for the radiated sound power.

In expression (C1), the real and imaginary parts of $Y_{n,m}^{(\mathbb{C})}(\theta,\varphi)$ are written as two separated functions and normalized to obtain two types of real-valued spherical harmonics,

$$E_{n,m}(\theta,\varphi) = \sqrt{\varepsilon_m}\,\mathrm{Re}\left\{Y_{n,m}^{(\mathbb{C})}(\theta,\varphi)\right\}$$

$$= \sqrt{\varepsilon_m}\sqrt{\frac{(2n+1)}{4\pi}\frac{(n-m)!}{(n+m)!}}\;P_n^m(\cos\theta)\cos(m\varphi) \tag{C2}$$

$$= \frac{\sqrt{\varepsilon_m}}{2}\left[Y_{n,m}^{(\mathbb{C})}(\theta,\varphi) + \bar{Y}_{n,m}^{(\mathbb{C})}(\theta,\varphi)\right] = \frac{\sqrt{\varepsilon_m}}{2}\left[Y_{n,m}^{(\mathbb{C})}(\theta,\varphi) + (-1)^m\,Y_{n,-m}^{(\mathbb{C})}(\theta,\varphi)\right],$$

also denoted as the even function or the ‘cosine version’, and

$$O_{n,m}(\theta,\varphi) = \sqrt{\varepsilon_m}\,\mathrm{Im}\left\{Y_{n,m}^{(\mathbb{C})}(\theta,\varphi)\right\}$$

$$= \sqrt{\varepsilon_m}\sqrt{\frac{(2n+1)}{4\pi}\frac{(n-m)!}{(n+m)!}}\;P_n^m(\cos\theta)\sin(m\varphi) \tag{C3}$$

$$= \frac{\sqrt{\varepsilon_m}}{2i}\left[Y_{n,m}^{(\mathbb{C})}(\theta,\varphi) - \bar{Y}_{n,m}^{(\mathbb{C})}(\theta,\varphi)\right] = \frac{\sqrt{\varepsilon_m}}{2i}\left[Y_{n,m}^{(\mathbb{C})}(\theta,\varphi) - (-1)^m\,Y_{n,-m}^{(\mathbb{C})}(\theta,\varphi)\right],$$

also denoted as the odd function or the ‘sine version’, for all $n \in \mathbb{Z}_+$ and $m \in \mathbb{Z}$, $-n \leq m \leq n$. The normalization factor is $\varepsilon_m = 2$ for $|m| \geq 1$ and $\varepsilon_0 = 1$. This is necessary in order to maintain the orthonormality property of the complex-valued spherical harmonics, rather than just orthogonality. These formulations differ from those in [105] through the fact that negative values of m introduce an extra factor of $(-1)^m$ in $E_{n,m}(\theta,\varphi)$ and $O_{n,m}(\theta,\varphi)$ compared to the positive values of m.

The ε_m factor required to maintain the orthonormality of the real-valued spherical harmonics is different for the $m = 0$ ones because

$$E_{n,0}(\theta,\varphi) = O_{n,0}(\theta,\varphi) = Y_{n,0}(\theta,\varphi) = \sqrt{\frac{2n+1}{4\pi}}\;P_n\;(\cos\theta)\ , \tag{C4}$$

where P_n is a Legendre Polynomial. Due to $Y_{n,0}^{(\mathbb{C})}(\theta,\varphi)$ always being real-valued, Euler`s formula cannot be applied as it was to express the real-valued spherical harmonics of $m \neq 0$.

The sets of the 'sine' and 'cosine' versions $E_{n,m}(\theta,\varphi)$ and $O_{n,m}(\theta,\varphi)$ can be arranged to define the real-valued spherical harmonic functions, $Y_{n,m}^{(\mathbb{R})}(\theta,\varphi)$. However, before this, some of their properties must be rigorously established and related back to those of the complex-valued spherical harmonics. This is covered in the following sections of this appendix.

Orthogonality

There are three types of orthogonality relationships that can be established: with two 'cosine' versions, with two 'sine' versions, and with a 'cosine' version alongside a 'sine' version. These are given by

$$\int_0^{\pi} \sin\theta \, d\theta \int_0^{2\pi} d\varphi \left\{ E_{n,m}(\theta,\varphi) \cdot E_{n',m'}(\theta,\varphi) \right\} = \delta_{nn'} \, \delta_{mm'} \, , \tag{C5}$$

$$\begin{aligned} &\int_0^{\pi} sin\,\theta \, d\theta \int_0^{2\pi} d\varphi \left\{ O_{n,m}(\theta,\varphi) \cdot O_{n',m'}(\theta,\varphi) \right\} \\ &\qquad = \begin{cases} \delta_{nn'}\delta_{mm'} & , n^2 + {n'}^2 + m^2 + {m'}^2 \neq 0 \\ 0 & , \ n = n' = m = m' = 0 \end{cases} , \end{aligned} \tag{C6}$$

$$\int_0^{\pi} sin\,\theta \, d\theta \int_0^{2\pi} d\varphi \left\{ E_{n,m}(\theta,\varphi) \cdot O_{n',m'}(\theta,\varphi) \right\} = 0 \, , \tag{C7}$$

where (m,n) and (m',n') are two different sets of $(order, degree)$, and also $\delta(x)$ is the Kronecker delta function. These results can be proven by using how $E_{n,m}(\theta,\varphi)$ and $O_{n,m}(\theta,\varphi)$ are related to $Y_{n,m}^{(\mathbb{C})}(\theta,\varphi)$ and, then, exploiting the orthogonality properties of the functions that comprise $Y_{n,m}^{(\mathbb{C})}(\theta,\varphi)$.

Starting with the proof for expression (C5), it can be written that

$$\int_0^{\pi} \sin\theta \, d\theta \int_0^{2\pi} d\varphi \left\{ E_{n,m}(\theta,\varphi) \cdot E_{n',m'}(\theta,\varphi) \right\} =$$

$$= \int_0^{\pi} \sin\theta \, d\theta \int_0^{2\pi} d\varphi \left\{ \sqrt{\varepsilon_m} \sqrt{\frac{(2n+1)}{4\pi}\frac{(n-m)!}{(n+m)!}} \, P_n^m(\cos\theta) \; \cos(m'\varphi) \right.$$

$$\left. \cdot \sqrt{\varepsilon_{m'}} \sqrt{\frac{(2n'+1)}{4\pi}\frac{(n'-m')!}{(n'+m')!}} \, P_{n'}^{m'}(\cos\theta) \; \cos(m'\varphi) \right\} =$$

$$= \sqrt{\varepsilon_m}\,\sqrt{\varepsilon_{m'}} \sqrt{\frac{(2n+1)}{4\pi}\frac{(n-m)!}{(n+m)!}} \sqrt{\frac{(2n'+1)}{4\pi}\frac{(n'-m')!}{(n'+m')!}} \int_0^{\pi} \sin\theta \; P_n^m(\cos\theta)\, P_{n'}^{m'}(\cos\theta)\, d\theta$$

$$\cdot \int_0^{2\pi} \cos(m\varphi) \; \cos(m'\varphi)\, d\varphi \,,$$

where the constants that depend only on n and/or m can be taken out of the double integral, all functions depending on θ can be separated from all the functions dependent on φ , and the double integral can be split in a product of two individual integrals.

The value of the integral depending only on φ is a well-known result that is a direct consequence of the orthogonality of the cosine function,

$$\int_0^{2\pi} \cos(m\varphi) \; \cos(m'\varphi)\, d\varphi = \begin{cases} \pi\delta_{mm'} \,, & m^2 + {m'}^2 \neq 0 \\ 2\pi \quad , & m = m' \end{cases} . \tag{C8}$$

The integral depending only on θ is more complicated to calculated. The following change of variable is used, such that

$$u = \cos\theta \; => \arccos u = \theta \; => \; \frac{d(\arccos u)}{du} du = d\theta \;\; => \; -\frac{1}{\sqrt{1-u^2}} du = \theta \; d\theta \;\; ,$$

which also leads to $\sin\theta = \sqrt{1-\cos^2\theta} = \sqrt{1-u^2}$. Substituting these into the integral yields

$$\int_0^{\pi} \sin\theta \; P_n^m(\cos\theta)\, P_{n'}^{m'}(\cos\theta)\, d\theta = \int_{\cos 0}^{\cos\pi} \sqrt{1-u^2}\, \sin\theta \; P_n^m(u)\, P_{n'}^{m'}(u) \; -\frac{1}{\sqrt{1-u^2}} du =$$

$$= \int_1^{-1} - P_n^m(u)\, P_{n'}^{m'}(u)\, du = \int_{-1}^{1} P_n^m(u)\, P_{n'}^{m'}(u)\, du \;\; . \tag{C9}$$

From (C8), it can be observed that unless $m = m'$ and they are both non-zero, the integral depending on φ is always zero, making the whole expression zero. Because of this, it can be considered that $m = m'$ and they are both non-zero for expressing (C9) , which leads to the orthogonality property of the associated Legendre functions,

$$\int_0^{\pi} \sin\theta \;\, P_n^m(\cos\theta)\, P_{n'}^{m'}(\cos\theta)\, d\theta = \int_{-1}^{1} P_n^m(u)\, P_{n'}^m(u)\, du = \frac{2}{2n+1}\,\frac{(n+m)!}{(n-m)!}\,\delta_{nn'} \;. \tag{C10}$$

Putting together the relations from (C8) and (C10) back into (C5), it is obtained that

$$\int_0^{\pi} \sin\theta\, d\theta \int_0^{2\pi} d\varphi \left\{E_{n,m}(\theta,\varphi)\cdot E_{n',m'}(\theta,\varphi)\right\} =$$

$$= \begin{cases} \sqrt{\varepsilon_m \varepsilon_{m'}}\;\dfrac{1}{2}\sqrt{\dfrac{(2n'+1)}{(2n+1)}\dfrac{(n'-m')!}{(n-m)!}\dfrac{(n+m)!}{(n'+m')!}}\;\delta_{nn'}\delta_{mm'} \;, & n^2+{n'}^2+m^2+{m'}^2 \neq 0 \\[2ex] \sqrt{\varepsilon_m \varepsilon_{m'}}\sqrt{\dfrac{(2n'+1)}{(2n+1)}\dfrac{(n'-m')!}{(n-m)!}\dfrac{(n+m)!}{(n'+m')!}} \;, & n = n' = m = m' = 0 \end{cases}$$

$$= \begin{cases} \delta_{nn'}\delta_{mm'} \;, & n^2+{n'}^2+m^2+{m'}^2 \neq 0 \\ 1 \;, & n = n' = m = m' = 0 \end{cases} = \delta_{nn'}\delta_{mm'} \;. \tag{C11}$$

For expression (C6), by using the same strategy it can be written that

$$\int_0^{\pi} \sin\theta\, d\theta \int_0^{2\pi} d\varphi \left\{O_{n,m}(\theta,\varphi)\cdot O_{n',m'}(\theta,\varphi)\right\} =$$

$$= \int_0^{\pi} \sin\theta\, d\theta \int_0^{2\pi} d\varphi \left\{\sqrt{\varepsilon_m}\sqrt{\frac{(2n+1)}{4\pi}\frac{(n-m)!}{(n+m)!}}\;P_n^m(\cos\theta)\;\sin(m'\varphi)\right.$$

$$\left.\cdot\sqrt{\varepsilon_{m'}}\sqrt{\frac{(2n'+1)}{4\pi}\frac{(n'-m')!}{(n'+m')!}}\;P_{n'}^{m'}(\cos\theta)\;\sin(m'\varphi)\right\} =$$

$$= \sqrt{\varepsilon_m}\,\sqrt{\varepsilon_{m'}}\sqrt{\frac{(2n+1)}{4\pi}\frac{(n-m)!}{(n+m)!}}\sqrt{\frac{(2n'+1)}{4\pi}\frac{(n'-m')!}{(n'+m')!}}\int_0^{\pi}\sin\theta\;P_n^m(\cos\theta)\,P_{n'}^{m'}(\cos\theta)\,d\theta$$

$$\cdot\int_0^{2\pi}\sin(m\varphi)\;\sin(m'\varphi)\,d\varphi \;.$$

At this point, the integral depending only on θ has been calculated previously. The value of the integral depending only on φ is another well-known result,

$$\int_0^{2\pi} \sin(m\varphi)\ \sin(m'\varphi)\, d\varphi = \begin{cases} \pi\delta_{mm'}\ , & m^2 + {m'}^2 \neq 0 \\ 0 \quad , & m = m' \end{cases}\ , \tag{C12}$$

which is a direct consequence of the orthogonality of the sine function.

Again, bringing the components (C8), (C12) and (C6) together concludes the proof

$$\int_0^{\pi} \sin\theta\, d\theta \int_0^{2\pi} d\varphi\, \left\{O_{n,m}(\theta,\varphi)\cdot O_{n',m'}(\theta,\varphi)\right\} =$$

$$= \begin{cases} \sqrt{\varepsilon_m\varepsilon_{m'}}\ \dfrac{1}{2}\sqrt{\dfrac{(2n'+1)}{(2n+1)}\dfrac{(n'-m')!}{(n-m)!}\dfrac{(n+m)!}{(n'+m')!}}\ \delta_{nn'}\delta_{mm'}\ , & n^2 + {n'}^2 + m^2 + {m'}^2 \neq 0 \\ \sqrt{\varepsilon_m\varepsilon_{m'}}\sqrt{\dfrac{(2n'+1)}{(2n+1)}\dfrac{(n'-m')!}{(n-m)!}\dfrac{(n+m)!}{(n'+m')!}}\ 0 \qquad\qquad , & n = n' = m = m' = 0 \end{cases}$$

$$= \begin{cases} \delta_{nn'}\delta_{mm'}\ , & n^2 + {n'}^2 + m^2 + {m'}^2 \neq 0 \\ 0 \quad , & n = n' = m = m' = 0 \end{cases} = \delta_{nn'}\delta_{mm'}\ . \tag{C13}$$

Lastly, applying the same strategy a third time for (C7),

$$\int_0^{\pi} \sin\theta\, d\theta \int_0^{2\pi} d\varphi\, \left\{E_{n,m}(\theta,\varphi)\cdot O_{n',m'}(\theta,\varphi)\right\} =$$

$$= \int_0^{\pi} \sin\theta\, d\theta \int_0^{2\pi} d\varphi\, \left\{\sqrt{\varepsilon_m}\sqrt{\frac{(2n+1)}{4\pi}\frac{(n-m)!}{(n+m)!}}\ P_n^m(\cos\theta)\ \cos(m'\varphi)\right.$$

$$\left.\cdot\sqrt{\varepsilon_{m'}}\sqrt{\frac{(2n'+1)}{4\pi}\frac{(n'-m')!}{(n'+m')!}}\ P_{n'}^{m'}(\cos\theta)\ \sin(m'\varphi)\right\} =$$

$$= \sqrt{\varepsilon_m}\sqrt{\varepsilon_{m'}}\sqrt{\frac{(2n+1)}{4\pi}\frac{(n-m)!}{(n+m)!}}\sqrt{\frac{(2n'+1)}{4\pi}\frac{(n'-m')!}{(n'+m')!}}\int_0^{\pi} \sin\theta\ P_n^m(\cos\theta)\, P_{n'}^{m'}(\cos\theta)\, d\theta$$

$$\cdot\int_0^{2\pi} \cos(m\varphi)\ \sin(m'\varphi)\, d\varphi\ .$$

Using a change of integration interval on the integral depending only on φ, it is obtained that

$$\int_0^{2\pi} \cos(m\varphi)\ \sin(m'\varphi)\, d\varphi = \int_{0-\pi}^{2\pi-\pi} \cos(m\varphi - \pi\varphi)\ \sin(m'\varphi - \pi\varphi)\, d\varphi =$$

$$= \int_{-\pi}^{\pi} \cos(m\varphi - \pi\varphi)\ \sin(m'\varphi - \pi\varphi)\, d\varphi\ .$$

Cosine is an even function while sine is an odd function, which results in their product being an odd function; the integral of an odd function over a symmetric interval is equal to zero,

$$\int_{0}^{2\pi} \cos(m\varphi)\ \sin(m'\varphi)\, d\varphi = 0\ .$$

As a consequence,

$$\int_{0}^{\pi} \sin\theta\, d\theta \int_{0}^{2\pi} d\varphi\ \left\{E_n^m(\theta,\varphi)\cdot O_{n'}^{m'}(\theta,\varphi)\right\} = 0$$

for all value pairs (m,n) and (m',n') , where $n \in \mathbb{Z}_+$ and $m \in \mathbb{Z}$, $-n \leq m \leq n$, $n' \in \mathbb{Z}_+$ and $m' \in \mathbb{Z}$, $-n' \leq m' \leq n'$.

Interior and exterior solutions of the Helmholtz equations

In the case of the expansions into spherical harmonics series of the interior and exterior solutions, the pressure field, it is first written that

$$\tilde{p}(\vec{r}) = \sum_{n=0}^{\infty}\sum_{m=-n}^{n} \tilde{C}_{n,m}^{(\mathbb{C})}\, \tilde{f}(kr)\, Y_{n,m}^{(\mathbb{C})}(\theta,\varphi)$$
$$= \sum_{n=0}^{\infty}\sum_{m=-n}^{n} \tilde{C}_{n,m}^{(\mathbb{C})}\, \tilde{f}(kr) \frac{1}{\sqrt{\varepsilon_m}}\left[E_{n,m}(\theta,\varphi) + i\, O_{n,n}(\theta,\varphi)\right] . \tag{C14}$$

where the function f can either be $j_n(kr)$ or $h_n\ (kr)$. The second summation over the parameter m is now split in two, corresponding to negative and positive values of m, respectively. The terms when $m = 0$ are divided by two and each half is introduced into each of the previously obtained two new summations. The normalization factor ε_m can be used such that division by two only occurs for the $m = 0$ terms, thus the above formulation equals

$$\sum_{m=0}^{n} \tilde{C}_{n,m}^{(\mathbb{C})}\, f(kr) \frac{\varepsilon_m}{2\sqrt{\varepsilon_m}}\ \left[E_{n,m}(\theta,\varphi) + i\, O_{n,n}(\theta,\varphi)\right] +$$

$$+\sum_{m=0}^{n} \tilde{\mathcal{C}}_{n,-m}^{(\mathbb{C})} f(kr) \frac{\varepsilon_m}{2\sqrt{\varepsilon_m}} \left[E_{n,-m}(\theta,\varphi) + i\, O_{n,-m}(\theta,\varphi)\right] =$$

$$= \sum_{m=0}^{n} \tilde{\mathcal{C}}_{n,m}^{(\mathbb{C})} f(kr) \frac{\varepsilon_m}{2\sqrt{\varepsilon_m}} \left[E_{n,m}(\theta,\varphi) + i\, (-1)^m\, O_{n,m}(\theta,\varphi)\right] +$$

$$+\sum_{m=0}^{n} \tilde{\mathcal{C}}_{n,-m}^{(\mathbb{C})} f(kr) \frac{\varepsilon_m}{2\sqrt{\varepsilon_m}} \left[E_{n,m}(\theta,\varphi) - i\, (-1)^m\, O_{n,m}(\theta,\varphi)\right] =$$

$$= \sum_{m=0}^{n} \sqrt{\varepsilon_m}\, \frac{\tilde{\mathcal{C}}_{n,m}^{(\mathbb{C})} + (-1)^m\, \tilde{\mathcal{C}}_{n,-m}^{(\mathbb{C})}}{2}\, f(kr)\, E_{n,m}(\theta,\varphi) +$$

$$+i \sum_{m=0}^{n} \sqrt{\varepsilon_m}\, \frac{\tilde{\mathcal{C}}_{n,m}^{(\mathbb{C})} - (-1)^m\, \tilde{\mathcal{C}}_{n,-m}^{(\mathbb{C})}}{2}\, f(kr)\, O_{n,m}(\theta,\varphi) =$$

$$= \sum_{m=0}^{n} \tilde{\mathcal{A}}_{n,m}^{(\mathbb{R})} f(kr)\, E_{n,m}(\theta,\varphi) + \sum_{m=0}^{n} \tilde{\mathfrak{B}}_{n,m}^{(\mathbb{R})} f(kr)\, O_{n,m}(\theta,\varphi)\,. \tag{C15}$$

In (C15), it can be observed that the original expansion using complex-valued basis functions is now written as the sum of two separate expansions that have real-valued basis functions. However, these new sets of coefficients, $\tilde{\mathcal{A}}_{n,m}^{(\mathbb{R})}$ and $\tilde{\mathfrak{B}}_{n,m}^{(\mathbb{R})}$, can still be complex-valued. The previous phase information from the functions $Y_{n,m}^{(\mathbb{C})}(\theta,\varphi)$ has migrated into the coefficients sets as a result of the change. For a given value of n, there are $n+1$ coefficients of type $\tilde{\mathcal{A}}_{n,m}^{(\mathbb{R})}$ and there are $n+1$ coefficients of type $\tilde{\mathfrak{B}}_{n,m}^{(\mathbb{R})}$. Truncating the infinite series (C15) to $n=N$ results in having $(N+1)^2+N$ terms in the overall summation.

The new two sets of field coefficients are

$$\tilde{\mathcal{A}}_{n,m}^{(\mathbb{R})} = \sqrt{\varepsilon_m}\, \frac{\tilde{\mathcal{C}}_{n,m}^{(\mathbb{C})} + (-1)^m\, \tilde{\mathcal{C}}_{n,-m}^{(\mathbb{C})}}{2}\,, \qquad m \geq 0\,, \tag{C16}$$

associated with the ‘cosine version’ of the real spherical harmonic and

$$\tilde{\mathfrak{B}}_{n,m}^{(\mathbb{R})} = i\,\sqrt{\varepsilon_m}\, \frac{\tilde{\mathcal{C}}_{n,m}^{(\mathbb{C})} - (-1)^m\, \tilde{\mathcal{C}}_{n,-m}^{(\mathbb{C})}}{2}\,, \qquad m \geq 0\,, \tag{C17}$$

associated with the ‘sine version’ of the real spherical harmonic, where the superscript ℝ denotes the fact that they correspond to real-valued basis functions. Both these sets of coefficients can still be complex-valued.

For a fixed n, when $m = 0$, the relations $\tilde{\mathcal{A}}^{(\mathbb{R})}_{n,0} = \tilde{\mathcal{C}}^{(\mathbb{C})}_{n,0}$ and $\tilde{\mathfrak{B}}^{(\mathbb{R})}_{n,0} = 0$ hold. Based on this, the $\tilde{\mathcal{A}}^{(\mathbb{R})}_{n,0}$ coefficient and the $\tilde{\mathfrak{B}}^{(\mathbb{R})}_{n,0}$ coefficient can be combined to form a new overall coefficient. In this way, for a given n, there are n coefficients of type $\tilde{\mathcal{A}}^{(\mathbb{R})}_{n,m}$, each one strictly associated with a 'cosine version' of the real spherical harmonic, there are n coefficients of the type $\tilde{\mathfrak{B}}^{(\mathbb{R})}_{n,m}$, each one strictly associated with a 'sine version' of the real spherical harmonic, and one coefficient for $m = 0$ that is equal to the coefficient associated with the complex-valued spherical harmonic. Overall, all these equate to a total of $2n + 1$ coefficients, i.e. the same number as for the formulations based on complex-valued spherical harmonics.

Expressions (C16) and (C17) can be used to determine the extra relations

$$\tilde{\mathcal{C}}^{(\mathbb{C})}_{n,m} = \frac{1}{\sqrt{\varepsilon_m}}\left[\tilde{\mathcal{A}}^{(\mathbb{R})}_{n,m} - i\,\tilde{\mathfrak{B}}^{(\mathbb{R})}_{n,m}\right], \qquad m \geq 0\,, \tag{C18}$$

and

$$\tilde{\mathcal{C}}^{(\mathbb{C})}_{n,-m} = \frac{(-1)^m}{\sqrt{\varepsilon_m}}\left[\tilde{\mathcal{A}}^{(\mathbb{R})}_{n,m} + i\,\tilde{\mathfrak{B}}^{(\mathbb{R})}_{n,m}\right], \qquad m \geq 0\,. \tag{C19}$$

The formulation for the radiated sound power, can be re-written as

$$\tilde{\Pi} = \frac{1}{2\rho_0 c_0 k^2}\sum_{n=0}^{\infty}\sum_{m=-n}^{n}\left|\tilde{\mathcal{C}}^{(\mathbb{C})}_{n,m}\right|^2 = \frac{1}{2\rho_0 c_0 k^2}\sum_{n=0}^{\infty}\sum_{m=-n}^{n}\left|\frac{1}{\sqrt{\varepsilon_m}}\left[\tilde{\mathcal{A}}^{(\mathbb{R})}_{n,m} - i\tilde{\mathfrak{B}}^{(\mathbb{R})}_{n,m}\right]\right|^2 =$$

$$= \frac{1}{2\rho_0 c_0 k^2}\sum_{n=0}^{\infty}\sum_{m=0}^{n}\frac{1}{\varepsilon_m}\left(\tilde{\mathcal{A}}^{(\mathbb{R})}_{n,m} - i\tilde{\mathfrak{B}}^{(\mathbb{R})}_{n,m}\right)\left(\overline{\tilde{\mathcal{A}}^{(\mathbb{R})}_{n,m} - i\tilde{\mathfrak{B}}^{(\mathbb{R})}_{n,m}}\right) +$$

$$+ \frac{1}{2\rho_0 c_0 k^2}\sum_{n=0}^{\infty}\sum_{m=1}^{n}\frac{1}{2}\left(\tilde{\mathcal{A}}^{(\mathbb{R})}_{n,m} + i\tilde{\mathfrak{B}}^{(\mathbb{R})}_{n,m}\right)\left(\overline{\tilde{\mathcal{A}}^{(\mathbb{R})}_{n,m} + i\tilde{\mathfrak{B}}^{(\mathbb{R})}_{n,m}}\right) =$$

$$= \frac{1}{2\rho_0 c_0 k^2}\sum_{n=0}^{\infty}\sum_{m=1}^{n}\frac{1}{2}\left(\left|\tilde{\mathcal{A}}^{(\mathbb{R})}_{n,m}\right|^2 + \left|\tilde{\mathfrak{B}}^{(\mathbb{R})}_{n,m}\right|^2 - i\tilde{\mathfrak{B}}^{(\mathbb{R})}_{n,m}\overline{\tilde{\mathcal{A}}^{(\mathbb{R})}_{n,m}} + i\tilde{\mathcal{A}}^{(\mathbb{R})}_{n,m}\overline{\tilde{\mathfrak{B}}^{(\mathbb{R})}_{n,m}}\right) + \frac{1}{2\rho_0 c_0 k^2}\sum_{n=0}^{\infty}\left|\tilde{\mathcal{C}}^{(\mathbb{C})}_{n,0}\right|^2$$

$$+ \frac{1}{2\rho_0 c_0 k^2}\sum_{n=0}^{\infty}\sum_{m=1}^{n}\frac{1}{2}\left(\left|\tilde{\mathcal{A}}^{(\mathbb{R})}_{n,m}\right|^2 + \left|\tilde{\mathfrak{B}}^{(\mathbb{R})}_{n,m}\right|^2 + i\tilde{\mathfrak{B}}^{(\mathbb{R})}_{n,m}\overline{\tilde{\mathcal{A}}^{(\mathbb{R})}_{n,m}} - i\tilde{\mathcal{A}}^{(\mathbb{R})}_{n,m}\overline{\tilde{\mathfrak{B}}^{(\mathbb{R})}_{n,m}}\right) =$$

$$= \frac{1}{2\rho_0 c_0 k^2}\sum_{n=0}^{\infty}\sum_{m=1}^{n}\left(\left|\tilde{\mathcal{A}}^{(\mathbb{R})}_{n,m}\right|^2 + \left|\tilde{\mathfrak{B}}^{(\mathbb{R})}_{n,m}\right|^2\right) + \frac{1}{2\rho_0 c_0 k^2}\sum_{n=0}^{\infty}\left|\tilde{\mathcal{C}}^{(\mathbb{C})}_{n,0}\right|^2\,. \tag{C20}$$

$$= \frac{1}{2\rho_0 c_0 k^2} \sum_{n=0}^{\infty} \left(\left| \tilde{\mathcal{C}}_{n,0}^{(\mathbb{C})} \right|^2 + \sum_{m=1}^{n} \left| \tilde{\mathcal{A}}_{n,m}^{(\mathbb{R})} \right|^2 + \left| \widetilde{\mathfrak{B}}_{n,m}^{(\mathbb{R})} \right|^2 \right). \qquad \text{(C21)}$$

It can be observed in (C21) that coefficients associated with the negative values of m and the coefficients associated with the positive values of m are no longer present; instead, the summation is now comprised of terms associated with $\tilde{\mathcal{A}}_{n,m}^{(\mathbb{R})}$, $\widetilde{\mathfrak{B}}_{n,m}^{(\mathbb{R})}$ and $\widetilde{D}_{n,0}^{(\mathbb{C})}$. In other words, using the set of coefficients from (C21) in the expression of the radiated sound power is equivalent to using the set of coefficients $\tilde{\mathcal{C}}_{n,m}^{(\mathbb{C})}$. There is still the same overall number of coefficients involved in the formulation as before, when given a truncation value $n = N$ for the infinite series. Furthermore, $\tilde{\mathcal{A}}_{n,m}^{(\mathbb{R})}$, $\widetilde{\mathfrak{B}}_{n,m}^{(\mathbb{R})}$ and $\widetilde{D}_{n,0}^{(\mathbb{C})}$ are effectively decoupled from each other such that they have individual, independent contributions to the total radiated sound power. However, these individual contributions are not the same as the previous ones, except for the terms with $m = 0$. For given set (n, m) where $n \neq 0$ and $\neq 0$, the contributions to the power of components (n, m) and $(n, -m)$ are redistributed to the term corresponding to $\tilde{\mathcal{A}}_{n,m}^{(\mathbb{R})}$ and the one corresponding to $\widetilde{\mathfrak{B}}_{n,m}^{(\mathbb{R})}$.

Definition of the real-valued spherical harmonics

From the previous sections in this appendix, it has been demonstrated that the complex-valued and real-valued spherical harmonics share key properties when it comes to orthonormality and expressing converging and diverging waves as series of spherical harmonic components. It is convenient to have a single notation for the whole set of real-spherical harmonics rather than using $\tilde{\mathcal{A}}_{n,m}^{(\mathbb{R})}$ and $\widetilde{\mathfrak{B}}_{n,m}^{(\mathbb{R})}$ simultaneously.

The most common arrangement used for the values of the complex-valued spherical harmonic coefficients $\tilde{\mathcal{C}}_{n,m}^{(\mathbb{C})}$ is

$$\left[\tilde{\mathcal{C}}_{0,0}^{(\mathbb{C})} \; \tilde{\mathcal{C}}_{-1,m}^{(\mathbb{C})} \; \tilde{\mathcal{C}}_{0,m}^{(\mathbb{C})} \; \tilde{\mathcal{C}}_{1,m}^{(\mathbb{C})} \; \tilde{\mathcal{C}}_{2,-2}^{(\mathbb{C})} \; \tilde{\mathcal{C}}_{2,-1}^{(\mathbb{C})} \; \tilde{\mathcal{C}}_{2,0}^{(\mathbb{C})} \; \tilde{\mathcal{C}}_{2,1}^{(\mathbb{C})} \; \tilde{\mathcal{C}}_{2,2}^{(\mathbb{C})} \; \dots \; \tilde{\mathcal{C}}_{-N,N}^{(\mathbb{C})} \; \dots \; \tilde{\mathcal{C}}_{0,0}^{(\mathbb{C})} \; \dots \; \tilde{\mathcal{C}}_{N,N}^{(\mathbb{C})} \; \dots \right] \qquad \text{(C22)}$$

and it can be mapped one-to-one to the arrangement

$$\left[\tilde{\mathcal{C}}_{0,0}^{(\mathbb{C})} \; \widetilde{\mathfrak{B}}_{1,m}^{(\mathbb{C})} \; \tilde{\mathcal{C}}_{0,m}^{(\mathbb{C})} \; \tilde{\mathcal{A}}_{1,m}^{(\mathbb{C})} \; \widetilde{\mathfrak{B}}_{2,2}^{(\mathbb{C})} \; \widetilde{\mathfrak{B}}_{2,1}^{(\mathbb{C})} \; \tilde{\mathcal{C}}_{2,0}^{(\mathbb{C})} \; \tilde{\mathcal{A}}_{2,1}^{(\mathbb{C})} \; \tilde{\mathcal{A}}_{2,2}^{(\mathbb{C})} \; \dots \; \widetilde{\mathfrak{B}}_{-N,N}^{(\mathbb{C})} \; \dots \; \tilde{\mathcal{C}}_{0,0}^{(\mathbb{C})} \; \dots \; \tilde{\mathcal{A}}_{N,N}^{(\mathbb{C})} \; \dots \right] \qquad \text{(C23)}$$

of coefficients corresponding the real-valued spherical harmonics. The $m = 0$ coefficients are left in the same positions, the $\widetilde{\mathfrak{B}}_{n,m}^{(\mathbb{R})}$ coefficients are placed in the positions of the negative values of m, and the $\tilde{\mathcal{A}}_{n,m}^{(\mathbb{R})}$ coefficients are placed in the positions of the positive values of m. The negative values of m denote a `sine' version and the strictly positive values of m denote a cosine version when the superscript is $\mathbb{R}$. This is possible without causing any arithmetic problems.

Appendix D The spherical Bessel and Hankel functions

Definitions

For real values of the independent variable $x \geq 0$ and integers values of the degree $n \geq 0$, the solutions of the Bessel Equation are the spherical Bessel functions of the first kind [72]

$$j_n(x) = \sqrt{\frac{\pi}{2x}}\, J_{n+1/2}(x) = 2^n x^n \sum_{s=0}^{\infty} \frac{(-1)^s (n+s)!}{s!\,(2n+2s+1)!}\, x^{2s}\,, \tag{D1}$$

and the spherical Bessel functions of the second kind, also known as Neumann functions, [72]

$$n_n(x) = \sqrt{\frac{\pi}{2x}} N_{n+1/2}(x) = (-1)^{n+1} J_{-n-1/2}(x) = \frac{(-1)^{n+1}}{2^n x^{n+1}} \sum_{s=0}^{\infty} \frac{(-1)^s (s-n)!}{s!\,(2s-2n)!}\, x^{2s}\,. \tag{D2}$$

These functions have the set of positive real numbers as a co-domain and can be combined together to form the spherical Bessel function of the third kind [72]

$$h_n^{(1)}(x) = \sqrt{\frac{\pi}{2x}} H_{n+1/2}^{(1)}(x) = j_n(x) + i\, n_n(x) = \frac{(-i)^{n+1} e^{ix}}{x} \sum_{s=0}^{n} \frac{i^s (n+s)!}{s!\,(n-s)!} \frac{1}{(2x)^s}\,, \tag{D3}$$

also known as the spherical Hankel function of the first kind, and the spherical Bessel function of the fourth kind [72]

$$h_n^{(2)}(x) = \sqrt{\frac{\pi}{2x}} H_{n+1/2}^{(2)}(x) = j_n(x) - i\, n_n(x) = \bar{h}_n^{(1)}(x)\ , \tag{D4}$$

also known as the spherical Hankel function of the second kind. The capital letters ‘J’, ‘N’, and ‘H’ used in the above formulations denote the non-spherical version of the Bessel functions. Plots of these and more details about them can be seen in [71, 72, 106, 107], as well as the procedure of solving the Bessel equation.

The spherical Bessel functions of zeroth degree are given by [72]

$$j_0(x) = \frac{\sin x}{x}\,, \qquad n_0(x) = \frac{-\cos x}{x}\,, \qquad h_0^{(1)}(x) = \frac{-ie^{ix}}{x}\,, \qquad h_0^{(2)}(x) = \frac{ie^{-ix}}{x}\,, \tag{D5}$$

and for the derivatives, by [72]

$$\frac{dj_0(x)}{dx} = \frac{x\cos x - \sin x}{x^2}\,, \qquad \frac{dn_0(x)}{dx} = \frac{x\sin x + \cos x}{x^2}\,,$$
$$\frac{dh_0^{(1)}(x)}{dx} = \frac{e^{ix}(x+i)}{x^2}\,, \qquad \frac{dh_0^{(2)}(x)}{dx} = \frac{e^{-ix}(x-i)}{x^2}\,. \tag{D6}$$

Rayleigh`s formula and derivatives

The spherical Bessel functions can also be written using Rayleigh`s formulas [72]

$$j_n(x) = (-1)^{n+1}x^n\left(\frac{1}{x}\frac{d}{dx}\right)^n\left\{\frac{\sin x}{x}\right\}, \tag{D7}$$

$$n_n(x) = (-1)^{n+1}x^n\left(\frac{1}{x}\frac{d}{dx}\right)^n\left\{\frac{\cos x}{x}\right\}, \tag{D8}$$

$$h_n^{(1)}(x) = -i(-1)^n x^n\left(\frac{1}{x}\frac{d}{dx}\right)^n\left\{\frac{e^{ix}}{ix}\right\}\,, \tag{D9}$$

$$h_n^{(2)}(x) = i(-1)^n x^n\left(\frac{1}{x}\frac{d}{dx}\right)^n\left\{\frac{e^{-ix}}{ix}\right\}, \tag{D10}$$

which also allows the derivation of closed-form expression for their derivatives.

Recurrence relations

The recurrence relations between spherical Bessel functions are [72]

$$\frac{2n+1}{x}f_n(x) = f_{n-1}(x) + f_{n+1}(x)\,, \tag{D11}$$

$$\frac{df_n(x)}{dx} = f_{n-1}(x) - \frac{n+1}{x}f_n(x)\,, \tag{D12}$$

$$(2n+1)\,\frac{df_n(x)}{dx} = n\,f_{n-1}(x) - (n+1)\,f_{n+1}(x)\,, \tag{D13}$$

where the function $f_n(x)$ can be any one of j_n , n_n , $h_n^{(1)}$ or $h_n^{(2)}$.

Wronskian relations

Another set of important formulations are the Wronskian relations [72]

$$j_n(x)\frac{dn_n(x)}{dx}-\frac{dn_n(x)}{dx}j_n(x)=\frac{1}{x^2}\ , \tag{D14}$$

and

$$j_n(x)\frac{dh_n^{(1)}(x)}{dx}-\frac{dj_n(x)}{dx}h_n^{(1)}(x)=\frac{i}{x^2}\ . \tag{D15}$$

and

$$j_n(x)\frac{dh_n^{(2)}(x)}{dx}-\frac{dj_n(x)}{dx}h_n^{(2)}(x)=\frac{-i}{x^2}\ . \tag{D16}$$

Orthogonality

The orthogonality of the spherical Bessel functions of the first kind is given by the relation [72]

$$\int\limits_0^a dr\left\{r^2 j_n\left(\alpha_{nl}\frac{r}{a}\right)j_n\left(\alpha_{nl'}\frac{r}{a}\right)\right\}=\frac{a^3}{2}\ [j_{n+1}(\alpha_{nl}r)]^2\ \delta(l-l')\ , \tag{D17}$$

for a closed interval $[0;a]$ and by the relation [72]

$$\int\limits_0^\infty dr\ \{r^2 j_n(k_1 r) j_n(k_2 r)\}=\frac{\pi}{k_1^2}\delta(k_1-k_2)\ ,$$

for the open interval $[0;\infty)$, where α_{nl} represents the l-th zero of the function $j_n(x)$, not counting $j_n(0)$, and k_1 , k_2 are two arbitrary constants. δ is the Dirac delta function.

Asymptotic behaviour for small arguments

It is of interest to calculate approximations which explain how the spherical Bessel functions behave asymptotically as the argument becomes very small. This can be done with the infinite series expansions from the definitions (D1) and (D2), as they are based on positive powers of the argument. In (D3) and (D4), the spherical Hankel functions are expressed as a finite series of n negative power terms, so the term with the power of $-n$ is the leading one.

When $x \to 0$, more and more terms of the expansion become negligible, thus if only the respective leading order terms are taken into consideration, it is obtained that [72]

$$j_n(x) \sim \frac{x^n}{(2n+1)!!}, \tag{D18}$$

$$n_n(x) \sim -\frac{(2n-1)!!}{x^{n+1}}, \tag{D19}$$

$$h_n^{(1)}(x) \sim -i\frac{(2n-1)!!}{x^{n+1}}, \tag{D20}$$

and

$$h_n^{(2)}(x) \sim i\frac{(2n-1)!!}{x^{n+1}}. \tag{D21}$$

The above representations of the spherical Hankel functions are pure imaginary. This happens because the spherical Neumann functions asymptotically go to $-\infty$ as their argument goes to zero, thus they dominate in the expression of $h_n^{(1,2)}(x)$, compared to that of $j_n(x)$.

The approximations (D18) – (D21) are valid as long as the term succeeding the leading order one is negligible, or in other words, when the corresponding power of the argument dominates its coefficient in the series. Therefore, the condition of validity for (D18) and (D20) are

$$x \ll \sqrt{\frac{(2n+2)(2n+3)}{n+1}} = \sqrt{2(2n+3)}, \tag{D22}$$

and, respectively,

$$x \ll \frac{2}{n(n+1)} . \tag{D23}$$

In the case of the first derivatives of $j_n(x)$, $h_n^{(1)}(x)$, and $h_n^{(2)}(x)$ to calculate the asymptotic behaviour at small arguments, the formulations (D18) – (D21) are used in the recurrence relations described by (D12) and, then, only the leading order terms are considered in the resulting expressions. When $n \geq 1$, this leads to

$$\frac{dj_n(x)}{dx} \approx -\frac{n\,x^{n-1}}{(2n+1)!!}\ , \tag{D24}$$

and

$$\frac{dh_n^{(1)}(x)}{dx} \approx i\,\frac{(n+1)(2n-1)!!}{x^{n+2}}\ , \qquad \frac{dh_n^{(2)}(x)}{dx} \approx -i\,\frac{(n+1)(2n-1)!!}{x^{n+2}}\ . \tag{D25}$$

Asymptotic behaviour for large arguments

When considering the asymptotic behaviour of the spherical Bessel functions as the argument becomes very large, the infinite series expansions from the definitions (D1) – (D4) cannot be used because they are based on positive powers of the argument. That is why an expansion based on negative powers of the argument needs to be found for the spherical Bessel functions of the first and second kinds. The spherical Hankel functions are expressed in terms of a series with a finite number of terms that already contain negative powers. These are derived in detail in [72] and can be written as

$$j_n(x) = \frac{1}{x}\left[W_{n+1/2}(x)\sin\left(x-\frac{n\pi}{2}\right) + Q_{n+1/2}(x)\cos\left(x-\frac{n\pi}{2}\right)\right]\ , \tag{D26}$$

$$n_n(x) = \frac{(-1)^{n+1}}{x}\left[W_{n+1/2}(x)\cos\left(x+\frac{n\pi}{2}\right) - Q_{n+1/2}(x)\sin\left(x+\frac{n\pi}{2}\right)\right], \tag{D27}$$

$$h_n^{(1)}(x) = \frac{1}{x}\exp\left\{i\left(x-\frac{n\pi}{2}-\frac{\pi}{2}\right)\right\}\cdot\left[W_{n+1/2}(x) + iQ_{n+1/2}(x)\right], \tag{D28}$$

and

$$h_n^{(2)}(x) = \frac{1}{x}\exp\left\{-i\left(x-\frac{n\pi}{2}-\frac{\pi}{2}\right)\right\}\cdot\left[W_{n+1/2}(x) - iQ_{n+1/2}(x)\right], \tag{D29}$$

where the two coefficients $W_{n+1/2}(x)$ and $Q_{n+1/2}(x)$ are given by [72]

$$W_{n+1/2}(x) = \sum_{s=0}^{[n/2]} \frac{(-1)^s(n+2s)!}{s!\,(n-2s)!}\,\frac{1}{(2x)^{2s}}, \tag{D30}$$

and

$$Q_{n+1/2}(x) = \sum_{s=0}^{\left[\frac{(n-1)}{2}\right]} \frac{(-1)^s (n+2s+1)!}{s!\,(n-2s-1)!} \frac{1}{(2x)^{2s+1}} \ . \tag{D31}$$

It is important to note that $W_{n+1/2}(x)$ and $Q_{n+1/2}(x)$ represents the even and, respectively, the odd powers of the same finite series, thus the leading order term in (D26) and (D28) is of power zero and always given by $W_{n+1/2}(x)$ out of the two coefficients.

Taking the limit $x \to \infty$ and considering only the leading order term of $W_{n+1/2}(x)$ while $Q_{n+1/2}(x)$ becomes negligible, the following asymptotic approximations can be written [72]

$$j_n(x) \sim \frac{1}{x} \sin\left(x - \frac{n\pi}{2}\right), \tag{D32}$$

$$n_n(x) \sim -\frac{1}{x} \cos\left(x - \frac{n\pi}{2}\right), \tag{D33}$$

$$h_n^{(1)}(x) \sim (-i)^{n+1} \frac{e^{ix}}{x} = -i \frac{e^{i(x-n\pi/2)}}{x}, \tag{D34}$$

and

$$h_n^{(2)}(x) \sim i^{n+1} \frac{e^{-ix}}{x} = i \frac{e^{-i(x-n\pi/2)}}{x}, \tag{D35}$$

These are valid as long as the term succeeding the leading order one is negligible, or in other words, when the coefficient of the first term in $Q_{n+1/2}(x)$ is considerably smaller than its corresponding power, $1/x$. Therefore, the condition of validity for (D32) – (D35) is [72]

$$x \gg \frac{n(n+1)}{2} \ . \tag{D36}$$

In the case of the first derivatives of $j_n(x)$ and $h_n^{(1)}(x)$, to calculate the asymptotic behaviour at large arguments, the formulations (D32) and (D34) are used in the recurrence relations described by (D12), and then the terms with $1/x^2$ can be ignored in the resulting expressions. For the function $j_n(x)$, [72]

$$\frac{dj_n(x)}{dx} \sim \frac{1}{x}\cos\left(x - \frac{n\pi}{2}\right). \tag{D37}$$

which imposes $x \gg \sqrt{n+1}$ due to ignoring the $1/x^2$ terms, and for $h_n^{(1,2)}(x)$, [72]

$$\frac{dh_n^{(1)}(x)}{dx} \sim (-i)^n \frac{e^{ix}}{x}\,, \qquad \frac{dh_n^{(2)}(x)}{dx} \sim i^n \frac{e^{-ix}}{x}\,, \tag{D38}$$

which also imposes $x \gg \sqrt{n+1}$. The condition (D36) already ensures that (D32) – (D35) are valid as it is stricter than $x \gg \sqrt{n+1}$.

Appendix E Far-field mapping of the exterior solution to the Helmholtz equation

As can be observed in Appendix D, the spherical Hankel function of the second kind, $h_n(kr)$, which controls the radial dependency of the sound field, has asymptotic behaviour at low and large arguments. In other words, as $r - a$ tends to zero and the position is closer to the source distributions, the spherical harmonic terms in series expansion of the sound field have a complicated radial behaviour described by an inverse power law (see 0). This region is denoted as the 'near-field' which transitions into the 'far-field' region as $r \to \infty$. For the latter of the two the radial behaviour of the spherical harmonic terms resembles a $e^{-ikr}/(kr)$ function. It is important to note that the conditions of validity of the two asymptotic regimes of $h_n(kr)$ are governed by how large/small kr is with respect to a relation based on n. Therefore, it is not straightforward to establish analytically where the transition between near-field and far-field occurs and this result can be different depending on frequency.

Following the procedure from [74], the goal is to prove that the relation (2.27) for the far-field pressure and its respective directivity pattern (2.29), are true. Given the nature of the exterior problem, an outward propagating field towards infinity, there is no reason why the far-field pressure should not remain an analytic function. Thus, it can be expressed in terms of its own spherical harmonic expansion

$$\lim_{r\to\infty} \tilde{p}(\vec{r}) = \sum_{n=0}^{\infty} \sum_{m=-n}^{n} \tilde{\mathcal{P}}_{n,m}^{(\mathbb{C})}\, Y_{n,m}^{(\mathbb{C})}(\theta,\varphi) \ , \tag{E1}$$

where $\tilde{C}_{n,m}^{(\mathbb{C})}$ are coefficients given by

$$\tilde{\mathcal{P}}_{n,m}^{(\mathbb{C})} = \int\limits_{\Omega} d\Omega \left\{ \lim_{r\to\infty} \tilde{p}(\vec{r}) \cdot \bar{Y}_{n,m}^{(\mathbb{C})}(\theta,\varphi) \right\} \ , \tag{E2}$$

as a result of orthonormality property of the spherical harmonics. Likewise, there is the spherical harmonics expansion for the pressure field of a diverging wave,

$$\tilde{p}(\vec{r}) = \sum_{n=0}^{\infty} \sum_{m=-n}^{n} \widetilde{D}_{n,m}^{(\mathbb{C})}\, h_n(kr)\, Y_{n,m}^{(\mathbb{C})}(\theta,\varphi)$$

with the coefficients formulated as

$$h_n(kr)\ \widetilde{D}^{(\mathbb{C})}_{n,m} = \int_\Omega d\Omega \left\{ \tilde{p}(\vec{r}) \cdot \bar{Y}^{(\mathbb{C})}_{n,m}(\theta,\varphi) \right\}.$$

The integral does not depend on the value of r, so the limit can be commuted in front to obtain

$$\tilde{\mathcal{P}}^{(\mathbb{C})}_{n,m} = \int_\Omega d\Omega \left\{ \lim_{r\to\infty} \tilde{p}(\vec{r}) \cdot \bar{Y}^{(\mathbb{C})}_{n,m}(\theta,\varphi) \right\} = \lim_{r\to\infty} \int_\Omega d\Omega \left\{ \tilde{p}(\vec{r}) \cdot \bar{Y}^{(\mathbb{C})}_{n,m}(\theta,\varphi) \right\}$$

$$= \lim_{r\to\infty} h_n(kr)\ \widetilde{D}^{(\mathbb{C})}_{n,m} = \frac{e^{-ikr}}{kr} i^{n+1} \widetilde{D}^{\mathbb{C}}_{n,m}\ , \tag{E3}$$

using the asymptotic behaviour of the spherical Hankel function at large arguments. The same tactic can be applied for the acoustic particle velocity, (2.28),

$$\tilde{u}(\vec{r}) = \frac{i}{\rho_0 c_0} \sum_{n=0}^{\infty} \sum_{m=-n}^{n} \widetilde{D}^{(\mathbb{C})}_{n,m}\ h'_n(kr)\ Y^{(\mathbb{C})}_{n,m}(\theta,\varphi)\ ,$$

where

$$h'_n(kr) \widetilde{D}^{(\mathbb{C})}_{n,m} = \int_\Omega d\Omega \left\{ \tilde{u}(\vec{r}) \cdot \bar{Y}^{(\mathbb{C})}_{n,m}(\theta,\varphi) \right\},$$

Let the far-field particle velocity be expressed as

$$\lim_{r\to\infty} \tilde{u}(r,\theta,\phi) = \sum_{n=0}^{\infty} \sum_{m=-n}^{n} \tilde{\mathcal{U}}^{(\mathbb{C})}_{n,m}\ Y^{(\mathbb{C})}_{n,m}(\theta,\varphi)\ \ , \tag{E4}$$

with

$$\tilde{\mathcal{U}}^{(\mathbb{C})}_{n,m} = \int_\Omega d\Omega \left\{ \lim_{r\to\infty} \tilde{u}(\vec{r}) \cdot \bar{Y}^{(\mathbb{C})}_{n,m}(\theta,\varphi) \right\}. \tag{E5}$$

Therefore, it can be written that

$$\tilde{\mathcal{U}}^{\mathbb{C}}_{n,m} = \int_\Omega d\Omega \left\{ \lim_{r\to\infty} \tilde{u}(\vec{r}) \cdot \bar{Y}^{(\mathbb{C})}_{n,m}(\theta,\varphi) \right\} = \lim_{r\to\infty} \int_\Omega d\Omega \left\{ \tilde{u}(\vec{r}) \cdot \bar{Y}^{(\mathbb{C})}_{n,m}(\theta,\varphi) \right\}$$

$$= \lim_{r\to\infty} \frac{i}{\rho_0 c_0} h'_n(kr)\ \widetilde{D}^{(\mathbb{C})}_{n,m} = \frac{i}{\rho_0 c_0} \frac{e^{-ikr}}{kr} i^n \widetilde{D}^{(\mathbb{C})}_{n,m}\ , \tag{E6}$$

by commuting the limit in front of the integral and using the asymptotic behaviour of the first derivative of the spherical Hankel function at large arguments.

The procedure used up until these point to calculate the spherical harmonic coefficients of the far-field pressure has not relied on the fact that the variation with radial distance is given by a spherical Hankel function rather than a spherical Bessel function. In other words, the same strategy can be used if $j_n(kr)$ was present in the series expansion instead of $h_n(kr)$, as $j_n(kr)$ also has asymptotic behaviour that tends to a finite value as $r \to \infty$. However, the term far-field does not make sense in the context of an interior problem.

It is also of interest to consider what happens to the far-field pressure and particle velocity at high frequencies, in other words, both k and r tend to $+\infty$. The issue is that the limit $k \to \infty$ cannot be taken directly in the formulations (E3) and (E5), because the asymptotic behaviour of the spherical Hankel function for large arguments has already been applied once. Furthermore, this asymptotic behaviour cannot be applied individually to each terms of the spherical harmonic expansions of a diverging or converging wave solution, because it is not uniform in n [74] , thus each term might have a different rate at which the asymptote is reached.

Because of the arguments presented above, Colton`s tactic seen previously will be attempted this time for both k and r tending to $+\infty$. Also, the ultimate goal is to relate these limits to the pressure on the sphere of radius a . It is important to note that $\tilde{p}(a, \theta, \varphi)$ in these expressions is at a single frequency, but it can be considered a variable when taking the limit.

It is assumed that the limits of the pressure and particle velocity as both k and r tend to $+\infty$ remain analytic functions, because the nature of the exterior problem is such that there is no reason why this behaviour should be any different. Thus, it is written that

$$\lim_{\substack{r \to \infty \\ k \to \infty}} \tilde{p}(r, \theta, \varphi) = \sum_{n=0}^{\infty} \sum_{m=-n}^{n} \tilde{\mathcal{T}}_{n,m}^{(\mathbb{C})} \, Y_{n,m}^{(\mathbb{C})}(\theta, \varphi) \, , \tag{E7}$$

where

$$\tilde{\mathcal{T}}_{n,m}^{(\mathbb{C})} = \int_{\Omega} d\Omega \left\{ \lim_{\substack{r \to \infty \\ k \to \infty}} \tilde{p}(\vec{r}) \cdot \bar{Y}_{n,m}^{(\mathbb{C})}(\theta, \varphi) \right\} . \tag{E8}$$

The limit can be commuted in front of the integral that does not depend on k or r to get

$$\tilde{\mathcal{T}}_{n,m}^{(\mathbb{C})} = \int\limits_{\Omega} d\Omega \left\{ \lim_{\substack{r\to\infty \\ k\to\infty}} \tilde{p}(\vec{r}) \cdot \bar{Y}_{n,m}^{(\mathbb{C})}(\theta,\varphi) \right\} = \lim_{\substack{r\to\infty \\ k\to\infty}} \int\limits_{\Omega} d\Omega \left\{ \tilde{p}(\vec{r}) \cdot \bar{Y}_{n,m}^{(\mathbb{C})}(\theta,\varphi) \right\} =$$

$$= \lim_{\substack{r\to\infty \\ k\to\infty}} h_n(kr) \widetilde{D}_{n,m}^{(\mathbb{C})} = \lim_{\substack{r\to\infty \\ k\to\infty}} \frac{h_n(kr)}{h_n(ka)} \int\limits_{\Omega'} d\Omega' \left\{ \tilde{p}(a,\theta',\varphi') \cdot \bar{Y}_{n,m}^{(\mathbb{C})}(\theta',\varphi') \right\}. \quad \text{(E9)}$$

In the above relation, the ratio of the two spherical Hankel function of the same degree has a limit based on the asymptotic behaviour (D35). However, the pressure on the sphere of radius a also varies with frequency in an in an unknown way, thus no further progress can be made in this pursuit, unless the variation of $\tilde{p}(a,\theta',\varphi')$ with ω is known.

Appendix F Extracting spherical harmonic coefficients

In the same coordinate system, an equation that relates two spherical harmonic decompositions of coefficients $\tilde{\alpha}_{n,m}^{(\mathbb{C})}$ and, respectively, $\tilde{\beta}_{l,q}^{(\mathbb{C})}$, over the same domain is considered:

$$\mathcal{C}_1 \sum_{n=0}^{\infty} \sum_{m=-n}^{n} \tilde{\alpha}_{n,m}^{(\mathbb{C})}\, h_n\,(kr)\, Y_{n,m}^{(\mathbb{C})}(\theta,\varphi) = \mathcal{C}_2 \sum_{l=0}^{\infty} \sum_{q=-l}^{l} \tilde{\beta}_{l,q}^{(\mathbb{C})}\, h_l\,\ (kr)\, Y_{q,l}^{(\mathbb{C})}(\theta,\varphi)\ , \tag{F1}$$

where n, m, l, q are integers and $n \geq 0$, $|m| \leq n$, $l \geq 0$, $|q| \leq l$. $\mathcal{C}_1$, $\mathcal{C}_2 \in \mathbb{C}$ are two independent constants. The pairs of degree and order (n, m) and repectively (l, q) are also independent of each other.

Let there be a new random pair of integers n' and m' with $n' \geq 0$ and $|m'| \leq n'$. The factor $\bar{Y}_{n',m'}^{(\mathbb{C})}(\theta,\varphi)$ acts as a constant to the double summation signs in (F1) , thus multiplying both sides of the equation by the spherical harmonic $\bar{Y}_{n',m'}^{(\mathbb{C})}(\theta,\varphi)$ yields

$$\mathcal{C}_1 \sum_{n=0}^{\infty} \sum_{m=-n}^{n} \tilde{\alpha}_{n,m}^{(\mathbb{C})}\, h_n\,(kr)\, Y_{n,m}^{(\mathbb{C})}(\theta,\varphi)\, \bar{Y}_{n',m'}^{(\mathbb{C})}(\theta,\varphi)$$

$$= \mathcal{C}_2 \sum_{n=0}^{\infty} \sum_{m=-n}^{n} \tilde{\beta}_{l,q}^{(\mathbb{C})}\, h_l\,\ (kr)\, Y_{q,l}^{(\mathbb{C})}(\theta,\varphi)\ \bar{Y}_{n',m'}^{(\mathbb{C})}(\theta,\varphi)\,,$$

and then integrating both sides over the unit sphere

$$\int_0^{\pi} \sin\theta\, d\theta \int_0^{2\pi} d\varphi\, \left\{ \mathcal{C}_1 \sum_{n=0}^{\infty} \sum_{m=-n}^{n} \tilde{\alpha}_{n,m}^{(\mathbb{C})}\, h_n\,(kr)\, Y_{n,m}^{(\mathbb{C})}(\theta,\varphi)\, \bar{Y}_{n',m'}^{(\mathbb{C})}(\theta,\varphi) \right\} =$$

$$= \int_0^{\pi} \sin\theta\, d\theta \int_0^{2\pi} d\varphi\, \left\{ \mathcal{C}_2 \sum_{n=0}^{\infty} \sum_{m=-n}^{n} \tilde{\beta}_{l,q}^{(\mathbb{C})}\, h_l\,\ (kr)\, Y_{q,l}^{(\mathbb{C})}(\theta,\varphi)\ \bar{Y}_{n',m'}^{(\mathbb{C})}(\theta,\varphi) \right\}$$

From the linearity of the integral operator,

$$\mathcal{C}_1 \sum_{n=0}^{\infty} \sum_{m=-n}^{n} \tilde{\alpha}_{n,m}^{(\mathbb{C})}\, h_n\,(kr) \int_0^{\pi} \sin\theta\, d\theta \int_0^{2\pi} d\varphi\, \left\{ Y_{n,m}^{(\mathbb{C})}(\theta,\varphi)\, \bar{Y}_{n',m'}^{(\mathbb{C})}(\theta,\varphi) \right\} =$$

$$= \ \mathcal{C}_2 \sum_{n=0}^{\infty} \sum_{m=-n}^{n} \tilde{\beta}_{l,q}^{(\mathbb{C})}\, h_l\,\ (kr) \int_0^{\pi} \sin\theta\, d\theta \int_0^{2\pi} d\varphi\, \left\{ Y_{q,l}^{(\mathbb{C})}(\theta,\varphi)\, \bar{Y}_{n',m'}^{(\mathbb{C})}(\theta,\varphi) \right\},$$

and applying the orthonormal property further results in

$$\mathcal{C}_1 \sum_{n=0}^{\infty} \sum_{m=-n}^{n} \tilde{\alpha}_{n,m}^{(\mathbb{C})} \, h_n\,(kr)\, \delta_{nn'}\, \delta_{mm'} = \mathcal{C}_2 \sum_{n=0}^{\infty} \sum_{m=-n}^{n} \tilde{\beta}_{l,q}^{(\mathbb{C})} \, h_l\,\,(kr)\, \delta_{ln'}\, \delta_{qm'}\,. \tag{F2}$$

In (F2), on each side of the equals sign, the multiplication of the two Kronecker delta functions give a value of one in a single situation: when $n = n'$, $m = m'$ and, respectively, $l = n'$, $q = m'$; all other cases result in a value of zero. Because of this, the double summations end up being equal to only one term and

$$\mathcal{C}_1\, \tilde{\alpha}_{n,m}^{(\mathbb{C})} \, h_n\,(kr) = \mathcal{C}_2\, \tilde{\beta}_{l,q}^{(\mathbb{C})} \, h_l\,\,(kr)\,. \tag{F3}$$

It can be observed that the coefficients of the two, initial spherical harmonics series have now been isolated from their respective summation signs in the equation.

When defining (F1), it is possible to maintain the same indices for the order and degree of the terms in the two decompositions. In other words, allow each term from the left-hand side to correspond to a term from the right-hand side that has the same degree and the same order, effectively imposing a consistent succession of orders and degrees in the respective summations. This succession is referred to as the ‘mode-matching approach’ and yields

$$\mathcal{C}_1\, \tilde{\alpha}_{n,m}^{(\mathbb{C})} \, h_n\,(kr) = \mathcal{C}_2\, \tilde{\beta}_{l,q}^{(\mathbb{C})} \, h_n\,(kr) => \mathcal{C}_1\, \tilde{\alpha}_{n,m}^{(\mathbb{C})} = \mathcal{C}_2\, \tilde{\beta}_{l,q}^{(\mathbb{C})}\,. \tag{F4}$$

Appendix G Spherical harmonics expansion of a 3D spherical wave

The sound field generated by a point-monopole source is derived from first considering the case of a sphere of radius R whose surface is pulsating at constant normal surface velocity $\widetilde{U}_R$ (m/s). The limit is then taken as the radius R is allowed to tend to zero while keeping its volume velocity constant. The approach forms a singularity at the centre of the pulsating sphere and can be expressed mathematically as

$$\tilde{p}_m(\mathbf{r}) = ik\rho_0 c_0 \tilde{q} \frac{e^{-ik|\mathbf{r}-\mathbf{r}'|}}{4\pi|\mathbf{r}-\mathbf{r}'|}, \qquad \mathbf{r} \neq \mathbf{r}' \quad , \tag{G1}$$

is the pressure field from a point-monopole, in the frequency domain, for the $e^{+i\omega t}$ time-domain convention, where

$$\mathbf{r} = \begin{bmatrix} x \\ y \\ z \end{bmatrix} = \begin{bmatrix} r \sin\theta \cos\varphi \\ r \sin\theta \sin\varphi \\ r \cos\theta \end{bmatrix}$$

is the position vector of the evaluation point in space and

$$\mathbf{r}' = \begin{bmatrix} x' \\ y' \\ z' \end{bmatrix} = \begin{bmatrix} r' \sin\theta' \cos\varphi' \\ r' \sin\theta' \sin\varphi' \\ r' \cos\theta' \end{bmatrix}$$

is the position vector for the location of the source. The quantity $\tilde{q}$ represents the source strength based on volume velocity $(m^3 s^{-1})$ and is expressed as the product of velocity times area $\tilde{q} = \widetilde{U}_R \times 4\pi R^2$. It is important to re-emphasize that $\tilde{q}$ is maintained fixed as $R \to 0$.

The factor represented by the fraction in expression (G1) is a Green`s function of the Helmholtz equation, specifically, the causal version corresponding to a diverging wave field for the $e^{+i\omega t}$ time-domain convention. This is written in convention as

$$\tilde{G}^{(+)}(\mathbf{r}|\mathbf{r}') = \frac{e^{-ik|\mathbf{r}-\mathbf{r}'|}}{4\pi|\mathbf{r}-\mathbf{r}'|} ,$$

where the '+' superscript denoted the causality. There is also the acausal version of this function, which corresponds to a converging wave field

$$\tilde{G}^{(-)}(\mathbf{r}|\mathbf{r}') = \frac{e^{+ik|\mathbf{r}-\mathbf{r}'|}}{4\pi|\mathbf{r}-\mathbf{r}'|} .$$

Given two different position vectors $\mathbf{r}$ and $\mathbf{r}'$, the expansion into spherical harmonics of the Green`s function $\tilde{G}^{(-)}(\mathbf{r}|\mathbf{r}')$ is given by [71, 108]

$$\tilde{G}^{(-)}(\mathbf{r}|\mathbf{r}') = \frac{e^{+ik|\mathbf{r}-\mathbf{r}'|}}{4\pi|\mathbf{r}-\mathbf{r}'|} = ik \sum_{n=0}^{\infty} \sum_{m=-n}^{n} j_n(kr_<)\, h_n^{(1)}(kr_>)\, Y_{n,m}^{(\mathbb{C})}(\theta,\varphi)\, \bar{Y}_{n,m}^{(\mathbb{C})}(\theta',\varphi') \ , \tag{G2}$$

where $r_< = \min\left(|\mathbf{r}|, |\mathbf{r}'|\right)$ and $r_> = \max\left(|\mathbf{r}|, |\mathbf{r}'|\right)$.

From Euler`s formula,

$$\frac{e^{-ik|\mathbf{r}-\mathbf{r}'|}}{4\pi|\mathbf{r}-\mathbf{r}'|} + \frac{e^{+ik|\mathbf{r}-\mathbf{r}'|}}{4\pi|\mathbf{r}-\mathbf{r}'|} = \frac{2\cos(k|\mathbf{r}-\mathbf{r}'|)}{4\pi|\mathbf{r}-\mathbf{r}'|} \ . \tag{G3}$$

For $\mathbf{r}$ and $\mathbf{r}'$, the addition theorem of the spherical Bessel functions is given by [106]

$$\frac{-\cos(k|\mathbf{r}-\mathbf{r}'|)}{k|\mathbf{r}-\mathbf{r}'|} = \sum_{n=0}^{\infty} (2n+1)\, j_n(kr_<)\, n_n(kr_>)\, P_n(\hat{\mathbf{r}}\cdot\hat{\mathbf{r}}') \ , \tag{G4}$$

and the addition theorem of spherical harmonics is expressed as [72]

$$P_n(\hat{\mathbf{r}}\cdot\hat{\mathbf{r}}') = \sum_{m=-n}^{n} \frac{4\pi}{2n+1}\, Y_n^m(\theta,\varphi)\, \bar{Y}_n^m(\theta',\varphi') \,, \tag{G5}$$

where $\hat{\mathbf{r}} = \mathbf{r}/|\mathbf{r}|$ and $\hat{\mathbf{r}}' = \mathbf{r}'/|\mathbf{r}'|$ are unit vectors set in the direction outward from the origin towards the angles (θ,φ) and, respectively, (θ',φ') . Combining (G4) with (G5) and inserting everything back into (G3) leads to

$$\frac{e^{-ik|\mathbf{r}-\mathbf{r}'|}}{4\pi|\mathbf{r}-\mathbf{r}'|} + \frac{e^{-ik|\mathbf{r}-\mathbf{r}'|}}{4\pi|\mathbf{r}-\mathbf{r}'|} = -2k \sum_{n=0}^{\infty} j_n(kr_<)\, n_n(kr_>) \sum_{m=-n}^{n} Y_{n,m}^{(\mathbb{C})}(\theta,\varphi)\, \bar{Y}_{n,m}^{(\mathbb{C})}(\theta',\varphi') \,. \tag{G6}$$

The same principles used when expressing the sine and cosine functions based on Euler`s formula can be applied in the case of the spherical Bessel function of the first kind and the spherical Neumann function. Therefore,

$$j_n(x) = \frac{h_n^{(1)}(x) + h_n^{(2)}(x)}{2} \ ,$$

$$n_n(x) = \frac{h_n^{(1)}(x) - h_n^{(2)}(x)}{2i} = -i\, \frac{h_n^{(1)}(x) - h_n^{(2)}(x)}{2} \ .$$

Using the above expression for the spherical Neumann function and (G2) in (G6) yields

$$\frac{e^{-ik|\mathbf{r}-\mathbf{r}'|}}{4\pi|\mathbf{r}-\mathbf{r}'|} = -2k\sum_{n=0}^{\infty}\sum_{m=-n}^{n} j_n(kr_<)\, n_n(kr_>)\, Y_{n,m}^{(\mathbb{C})}(\theta,\varphi)\, \bar{Y}_{n,m}^{(\mathbb{C})}(\theta',\varphi') -$$

$$- ik\sum_{n=0}^{\infty}\sum_{m=-n}^{n} j_n(kr_<)\, h_n^{(1)}(kr_>)\, Y_{n,m}^{(\mathbb{C})}(\theta,\varphi)\, \bar{Y}_{n,m}^{(\mathbb{C})}(\theta',\varphi') \;=>$$

$$=> \frac{e^{-ik|\mathbf{r}-\mathbf{r}'|}}{4\pi|\mathbf{r}-\mathbf{r}'|} = ik\sum_{n=0}^{\infty}\sum_{m=-n}^{n} j_n(kr_<)\, \left[h_n^{(1)}(x) - h_n^{(2)}(x)\right] Y_{n,m}^{(\mathbb{C})}(\theta,\varphi)\, \bar{Y}_{n,m}^{(\mathbb{C})}(\theta',\varphi')$$

$$- ik\sum_{n=0}^{\infty}\sum_{m=-n}^{n} j_n(kr_<)\, h_n^{(1)}(kr_>)\, Y_{n,m}^{(\mathbb{C})}(\theta,\varphi)\, \bar{Y}_{n,m}^{(\mathbb{C})}(\theta',\varphi') \;=>$$

$$=> \frac{e^{-ik|\mathbf{r}-\mathbf{r}'|}}{4\pi|\mathbf{r}-\mathbf{r}'|} = -ik\sum_{n=0}^{\infty}\sum_{m=-n}^{n} j_n(kr_<)\, h_n^{(2)}(kr_>)\, Y_{n,m}^{(\mathbb{C})}(\theta,\varphi)\, \bar{Y}_{n,m}^{(\mathbb{C})}(\theta',\varphi')\,.$$

Therefore, the pressure of a point-monopole can be expanded into a series of spherical harmonics

$$\begin{aligned}\tilde{p}_m(\mathbf{r}) &= ik\rho_0 c_0 \tilde{q}\, \frac{e^{-ik|\mathbf{r}-\mathbf{r}'|}}{4\pi|\mathbf{r}-\mathbf{r}'|} = \\ &= k^2\rho_0 c_0 \tilde{q}\sum_{n=0}^{\infty}\sum_{m=-n}^{n} j_n(kr_<)\, h_n^{(2)}(kr_>)\, Y_{n,m}^{(\mathbb{C})}(\theta,\varphi)\, \bar{Y}_{n,m}^{(\mathbb{C})}(\theta',\varphi')\,.\end{aligned} \tag{G7}$$

Appendix H Obtaining spherical harmonic expansion of plane-wave from the one of spherical wave

The plane-wave expansion of the spherical harmonics, expression (2.34), can be obtained from that of a point-monopole, expression (2.38) by setting the position of a point-monopole to infinite distance away. As $r' \to \infty$, the following approximation can be employed

$$|\mathbf{r} - \mathbf{r}'| \simeq r' - \mathbf{n} \cdot \mathbf{r} = r' - r \ , \tag{H1}$$

where $\mathbf{n}$ is a unit vector in the direction of $\mathbf{r}$. Using this in (2.38), $r' \gg r$ holds and

$$\lim_{r' \to \infty} \left\{ \frac{e^{-ik|\mathbf{r}-\mathbf{r}'|}}{4\pi|\mathbf{r}-\mathbf{r}'|} \right\} = \frac{e^{-ik(r'-r)}}{4\pi(r'-r)} \simeq \frac{e^{-ikr'}}{e^{-ikr}} \frac{1}{4\pi r'} =$$

$$= \lim_{r' \to \infty} \left\{ -ik \sum_{n=0}^{\infty} \sum_{m=-n}^{n} j_n(kr)\, h_n^{(2)}(kr')\, Y_{n,m}^{(\mathbb{C})}(\theta, \varphi)\, \bar{Y}_{n,m}^{(\mathbb{C})}(\theta', \varphi') \right\}.$$

In the previous relation, the limit of the series expansion as $r' \to \infty$ can be determined, therefore,

$$\lim_{r' \to \infty} \left\{ -ik \sum_{n=0}^{\infty} \sum_{m=-n}^{n} j_n(kr)\, h_n^{(2)}(kr')\, Y_{n,m}^{(\mathbb{C})}(\theta, \varphi)\, \bar{Y}_{n,m}^{(\mathbb{C})}(\theta', \varphi') \right\} =$$

$$= -ik \sum_{n=0}^{\infty} \sum_{m=-n}^{n} \lim_{r' \to \infty} \left\{ h_n^{(2)}(kr') \right\} j_n(kr)\, Y_{n,m}^{(\mathbb{C})}(\theta, \varphi)\, \bar{Y}_{n,m}^{(\mathbb{C})}(\theta', \varphi') =$$

$$= -ik \sum_{n=0}^{\infty} \sum_{m=-n}^{n} \frac{e^{-ikr'}}{kr'}\, i^{n+1}\, j_n(kr)\, Y_{n,m}^{(\mathbb{C})}(\theta, \varphi)\, \bar{Y}_{n,m}^{(\mathbb{C})}(\theta', \varphi') =$$

$$= \frac{e^{-ikr'}}{r'} \sum_{n=0}^{\infty} \sum_{m=-n}^{n} i^{n}\, j_n(kr)\, Y_{n,m}^{(\mathbb{C})}(\theta, \varphi)\, \bar{Y}_{n,m}^{(\mathbb{C})}(\theta', \varphi') = \frac{e^{-ikr'}}{e^{-ikr}} \frac{1}{4\pi r'} =>$$

$$=> e^{ikr} = 4\pi \sum_{n=0}^{\infty} \sum_{m=-n}^{n} i^{n}\, j_n(kr)\, Y_{n,m}^{(\mathbb{C})}(\theta, \varphi)\, \bar{Y}_{n,m}^{(\mathbb{C})}(\theta', \varphi') = \frac{e^{-ikr'}}{e^{-ikr}} \ . \tag{H2}$$

Appendix I List of used MATLAB programs

Programs for calculating special mathematical functions

- radial_functions → MATLAB function for calculating spherical Bessel or Hankel functions of first or second kind, given an order and a vector of values as the arguments.
- radial_functions_prime → MATLAB function for calculating the first derivative of spherical Bessel or Hankel functions of first or second kind, given an order and a vector of values as the arguments.
- spherical_harmonics → MATLAB function for calculating the spherical harmonic functions for all orders m, given a degree n, a vector of values for angle θ, and a vector of values for angle φ.
- sunflower_spherical_spread → MATLAB function that receives a chosen number of points on a spherical surface and it spreads them such that each created patch between the points has the same surface area. The coordinates of the uniformly spaced points are returned.

Programs for modelling the passive behaviour of impedance sphere

- Z_rhoc_scattering_convergent_near_field → template MATLAB script for calculating the total sound pressure and scattered sound pressure due to a monochromatic plane-wave in the near-field of the modelled impedance sphere, where data is produced on a single plane parallel to the direction of travel for the plane-wave.
- scattering_directivity_Z_rhoc → template MATLAB script for calculating the directivity of the far-field scattered pressure due to a monochromatic plane-wave interacting with the modelled impedance sphere, where data is produced on a single plane parallel to the direction of travel for the plane-wave.

Programs for modelling the passive behaviour of thin spherical shell

- res_modeshapes_vac_loaded → MATLAB scripts for calculating the resonant frequencies and the modeshapes of the modelled thin spherical shell, when in vacuum or when externally loaded by the fluid.
- Jun_wat_rub_sph_shell_scatt_pow → template MATLAB script for calculating the spherical harmonic coefficients and the radiated sound power for acoustic scattering of a monochromatic plane-wave, acoustic radiation of a monochromatic point-monopole in the fluid, and acoustic radiation due to a monochromatic point-force exciting the surface, for the case of a thin spherical shell made of rubber and surrounded by water.
- Jun_air_rub_sph_shell_scatt_pow → template MATLAB script for calculating the spherical harmonic coefficients and the radiated sound power for acoustic scattering of a monochromatic plane-wave, acoustic radiation of a monochromatic point-monopole in the fluid, and acoustic radiation due to a monochromatic point-force exciting the surface, for the case of a thin spherical shell made of rubber and surrounded by air.
- Jun_wat_steel_sph_shell_scatt_pow → template MATLAB script for calculating the spherical harmonic coefficients and the radiated sound power for acoustic scattering of a monochromatic plane-wave, acoustic radiation of a monochromatic point-monopole in the fluid, and acoustic radiation due to a monochromatic point-force exciting the surface, for the case of a thin spherical shell made of steel and surrounded by water.
- Jun_air_steel_sph_shell_scatt_pow → template MATLAB script for calculating the spherical harmonic coefficients and the radiated sound power for acoustic scattering of a monochromatic plane-wave, acoustic radiation of a monochromatic point-monopole in the fluid, and acoustic radiation due to a monochromatic point-force exciting the surface, for the case of a thin spherical shell made of steel and surrounded by air.
- Jun_wat_silverA_sph_shell_scatt_pow → template MATLAB script for calculating the spherical harmonic coefficients and the radiated sound power for acoustic scattering of a monochromatic plane-wave, acoustic radiation of a monochromatic point-monopole in the fluid, and acoustic radiation due to a monochromatic point-force exciting the surface, for the case of a thin spherical shell made of ‘silver alloy’ and surrounded by water.

Programs for feedforward control with spherical harmonic coefficients

- acous_scattering_SHSC → MATLAB function for calculating the spherical harmonic coefficients corresponding to either a monochromatic acoustic plane-wave travelling in a free-field fluid, the acoustic scattering from the thin spherical shell due to a monochromatic plane-wave, the acoustic radiation of a monochromatic point-monopole in the vicinity of the thin spherical shell, or the acoustic radiation due to a monochromatic point-force exciting the surface of the thin spherical shell. Coefficients after control can be calculated with this function.
- acous_scattering_RSHS_coeff_primary → MATLAB function for calculating the spherical harmonic coefficients corresponding to the acoustic scattering from the impedance sphere due to a monochromatic plane-wave.
- acous_scattering_RSHS_coeff_secondary → MATLAB function for calculating the spherical harmonic coefficients corresponding to the acoustic radiation of a monochromatic point-monopole in the vicinity of the impedance sphere.
- RSHSC_0_0_controlled_pi_05pi → MATLAB function as template for applying feedforward power minimization based on spherical harmonic coefficients of a known primary and known secondary consisting of a single source at a specific position.
- RSHSC_05pi_05pi_05pi_05pi_controlled_pi_05pi → MATLAB function as template for applying feedforward power minimization based on spherical harmonic coefficients of a known primary and a known secondary consisting of a single source at a specific position.
- RSHSC_pi_0_0_0_controlled_pi_05pi → MATLAB function as template for applying feedforward power minimization based on spherical harmonic coefficients of a known primary and a known secondary consisting of a single source at a specific position.
- RSHSC_pi_0_controlled_pi_05pi → MATLAB function as template for applying feedforward power minimization based on spherical harmonic coefficients of a known primary and a known secondary consisting of a single source at a specific position.
- RSHSC_4_cardinal_controlled_pi_05pi → MATLAB function as template for applying feedforward power minimization based on spherical harmonic coefficients of a known primary and a known secondary consisting of four sources at specific positions.
- acous_scattering_RSHS_coeff_1controlled → MATLAB function that receives the spherical harmonic coefficients of a known primary and a known secondary consisting of a single source, as well as the optimized source parameter after control, and returns the spherical harmonic coefficients after control.

- acous_scattering_RSHS_coeff_2controlled → MATLAB function that receives the spherical harmonic coefficients of a known primary and a known secondary consisting of two sources, as well as the optimized source parameter after control, and returns the spherical harmonic coefficients after control.
- acous_scattering_RSHS_coeff_pos_3controlled → MATLAB function that receives the spherical harmonic coefficients of a known primary and a known secondary consisting of three sources, as well as the optimized source parameter after control, and returns the spherical harmonic coefficients after control.
- acous_scattering_RSHS_coeff_pos_4controlled → MATLAB function that receives the spherical harmonic coefficients of a known primary and a known secondary consisting of four sources, as well as the optimized source parameter after control, and returns the spherical harmonic coefficients after control.
- multi_channel_pmp_control_sph_scatterer_Z100 → template MATLAB function for applying the feedforward power minimization based on spherical harmonic coefficients when using multiple secondary point-monopoles that are uniformly spread on the surface of the impedance sphere.
- multi_channel_pmp_control_sph_scatterer_Z100 → template MATLAB function for applying the feedforward power minimization based on spherical harmonic coefficients when using multiple secondary point-monopoles that are uniformly spread on a virtual sphere surrounding the impedance sphere and positioned at a distance away.

Programs for feedback control with spherical harmonic coefficients

- modal_velocity_feedback → template MATLAB scripts for calculating matrices required in velocity feedback control and for modelling the outcomes of velocity feedback control.

References

[1] T. R. Neil, Z. Shen, D. Robert, B. W. Drinkwater, and M. W. Holderied, "Moth wings are acoustic metamaterials," *Proceedings of the National Academy of Sciences,* vol. 117, no. 49, p. 31134, 2020, doi: 10.1073/pnas.2014531117.

[2] Youtube user "amt253", "Ealing Film-Loops 80-244 - Diffraction and Scattering Around Obstacles in a Ripple Tank," 02:00 / 03:22 ed. Apr 9, 2017.

[3] "Pixabay.com." https://pixabay.com/ (accessed 3 June, 2021).

[4] H. Lamb, *The dynamical theory of sound*. New York: Dover (in English), 1925.

[5] G. V. Borgiotti, "The power radiated by a vibrating body in an acoustic fluid and its determination from boundary measurements," *J. Acoust. Soc. Am.,* vol. 88, p. 1884, 1990.

[6] D. M. Photiadis, "The relationship of singular value decomposition to wave-vector filtering in sound radiation problems," *J. Acoust. Soc. Am.,* vol. 88, p. 1152, 1990.

[7] S. J. Elliott and M. E. Johnson, "Radiation modes and the active control of sound power," *J. Acoust. Soc. Am.,* vol. 94, p. 2194, 1993.

[8] T. Tarvainen, B. T. Cox, J. P. Kaipio, and S. R. Arridge, "Reconstructing absorption and scattering distributions in quantitative photoacoustic tomography," *Inverse Problems,* vol. 28, no. 8, p. 084009, 2012, doi: 10.1088/0266-5611/28/8/084009.

[9] B. Peters and T. S. Olesen, "Integrating Sound Scattering Measurements in the Design of Complex Architectural Surfaces Informing a parametric design strategy with acoustic measurements from rapid prototype scale models," in *Proceedings of the eCAADe 2010 Conference : Future Cities*, Zurich, Switzerland, 1 September 2010, Zurich, Switzerland, 2010, pp. 481-491.

[10] B. Peters, N. Hoban, Y. Jay, and Z. Xian, "Improving Meeting Room Acoustic Performance through Customized Sound Scattering Surfaces," in *Proceedings of the International Symposium on Room Acoustics, ISRA 2019*, Amsterdam, Netherlands, 15-17 September 2019, Online, 2019, pp. 213-225.

[11] R. Duda and W. Martens, "Range dependence of the response of a spherical head model," *Journal of the Acoustical Society of America,* vol. 104, pp. 3048-3058, 1998.

[12] H. Xu, R. Xia, J. Li, and Y. Yan, "An improved free-field cross-talk cancellation method based on the spherical head model," *Appl. Acoust.,* vol. 123, p. 47, 2017.

[13] "Snappygoat.com." https://snappygoat.com/ (accessed 3 June 2021).

[14] P. A. Deymier, *Acoustic Metamaterials and Phononic Crystals*, First ed. Springer Berlin Heidelberg, 2013.

[15] L. Zigoneanu, B. I. Popa, and S. A. Cummer, "Three-dimensional broadband omnidirectional acoustic ground cloak," *Nat Mater,* vol. 13, no. 4, pp. 352-5, Apr 2014, doi: 10.1038/nmat3901.

[16] P. A. Kerrian, A. D. Hanford, D. E. Capone, and B. S. Beck, "Development of a perforated plate underwater acoustic ground cloak," *The Journal of the Acoustical Society of America,* vol. 146, no. 4, pp. 2303-2308, 2019, doi: 10.1121/1.5127844.

[17] V. K. Varadan, V. V. Varadan, J. H. Su, and T. A. K. Pillai, "Comparison of sound scattering by rigid and elastic obstacles in water," *The Journal of the Acoustical Society of America,* vol. 71, no. 6, pp. 1377-1383, 1982, doi: 10.1121/1.387858.

[18] K. J. Diercks and R. Hickling, "Echoes from Hollow Aluminum Spheres in Water," *The Journal of the Acoustical Society of America,* vol. 41, no. 2, pp. 380-393, 1967, doi: 10.1121/1.1910349.

[19] R. Hickling, R. K. Burrows, J. F. Ball, and M. Petrovic, "Power flow for sound incident on a solid aluminum sphere in water," *The Journal of the Acoustical Society of America,* vol. 89, no. 6, pp. 2509-2518, 1991, doi: 10.1121/1.400822.

[20] R. R. Goodman and R. Stern, "Reflection and Transmission of Sound by Elastic Spherical Shells," *The Journal of the Acoustical Society of America,* vol. 34, no. 3, pp. 338-344, 1962, doi: 10.1121/1.1928120.

[21] C. J. Partridge, *Sound wave scattering from an elastic spherical shell* (MRL technical report; MRL-TR-91-9, Accessed from https://apps.dtic.mil/sti/citations/ADA264039). Maribyrnong, Vic: Materials Research Laboratory, 1993.

[22] C. J. Partridge, *Sound wave scattering from a rigid sphere* (MRL technical report; MRL-TR-91-9, Accessed from https://nla.gov.au/nla.cat-vn1232772). Maribyrnong, Vic: Materials Research Laboratory, 1993.

[23] C. A. Rohde, T. P. Martin, M. D. Guild, C. N. Layman, C. J. Naify, M. Nicholas, A. L. Thangawng, D. C. Calvo, and G. J. Orris, "Experimental Demonstration of Underwater Acoustic Scattering Cancellation," *Scientific Reports,* vol. 5, no. 1, p. 13175, 2015, doi: 10.1038/srep13175.

[24] P. A. Nelson and S. J. Elliott, *Active control of sound*, First ed. Academic press, 1991.

[25] E. Avital, D. Neeshtha, Bholah, G. Giovanelli, and T. Miloh, "Sound Scattering by an Elastic Spherical Shell and its Cancellation using a Multi-pole Approach," *Archives of Acoustics,* vol. 42, pp. 697-705, 2017, doi: 10.1515/aoa-2017-0072.

[26] E. J. Avital and T. Miloh, "Sound scattering and its cancellation by an elastic spherical shell in free space and near a free surface," *Wave Motion,* vol. 55, pp. 35-47, 2015/06/01/ 2015, doi: https://doi.org/10.1016/j.wavemoti.2014.12.009.

[27] A. N. Norris, F. A. Amirkulova, and W. J. Parnell, "Source amplitudes for active exterior cloaking," *Inverse Problems,* vol. 28, p. 105002, 2012.

[28] A. N. Norris, F. A. Amirkulova, and W. J. Parnell, "Active elastodynamic cloaking," *Mathematics and Mechanics of Solids,* vol. 19, no. 6, pp. 603-625, 2014, doi: 10.1177/1081286513479962.

[29] J. Liu, X. Wang, M. Wu, and J. Yang, "An active control strategy for the scattered sound field control of a rigid sphere," *J. Acoust. Soc. Am.,* vol. 144, p. EL52, 2018.

[30] F. G. Vasquez, G. W. Milton, and D. Onofrei, "Exterior cloaking with active sources in two dimensional acoustics," *Wave Motion,* vol. 48, p. 515, 2011.

[31] C. House, J. Cheer, and S. Daley, "The effect of active vibration control on the sound field scattered from a flexible structure," in *Proceedings of the 28th edition of ISMA International Conference on Noise & Vibration Engineering*, Leuven, Belgium, 17-19 September 2018, Online, 2018.

[32] C. House, J. Cheer, and S. Daley, "An investigation into the performance limitations of active acoustic cloaking using an acoustic quiet-zone," in *Proceedings of Meetings on Acoustics*, 2019, vol. 39, p. 055002, doi: 10.1121/2.0001190.

[33] J. Cheer, "Active control of scattered acoustic fields: Cancellation, reproduction and cloaking," *J Acoust Soc Am,* vol. 140, no. 3, p. 1502, Sep 2016, doi: 10.1121/1.4962284.

[34] E. Friot, R. Guillermin, and M. Winninger, "Active control of scattered acoustic radiation: A real-time implementation for a three-dimensional object," *Acta Acust. Acust.,* vol. 92, p. 278, 2006.

[35] E. Friot and C. Bordier, "Real-time active suppression of scattered acoustic radiation," *Journal of Sound and Vibration,* vol. 278, no. 3, pp. 563-580, 2004, doi: 10.1016/j.jsv.2003.10.064.

[36] C. House, J. Cheer, and S. Daley, "On the use of virtual sensing for the real-time detection and active control of a scattered acoustic field," in *Proceedings of ICSV26, the 26th International Congress on Sound and Vibration*, Montreal, Canada, 7-11 July 2019, Online, 2019.

[37] C. House, J. Cheer, and S. Daley, "An Investigation into the Effect of Uncertainty on Active Acoustic Cloaking," in *Proceedings of Inter-Noise 2020*, Online, 23 - 26 Aug 2020, Online, 2020.

[38] C. Beckett, "Studies of acoustic scattering using a parametric array," PhD Thesis, University of Bath, Bath, 1992.

[39] D. Eggler, H. Chung, F. Montiel, J. Pan, and N. Kessissoglou, "Active noise cloaking of 2D cylindrical shells," *Wave Motion,* vol. 87, pp. 106-122, 2019.

[40] Y. Braikia, M. Melon, C. Langrenne, É. Bavu, and A. Garcia, "Evaluation of a separation method for source identification in small spaces," *The Journal of the Acoustical Society of America,* vol. 134, no. 1, pp. 323-331, 2013, doi: 10.1121/1.4809647.

[41] M. Melon, C. Langrenne, P. Herzog, and A. Garcia, "Evaluation of a method for the measurement of subwoofers in usual rooms," *The Journal of the Acoustical Society of America,* vol. 127, no. 1, pp. 256-263, 2010, doi: 10.1121/1.3270392.

[42] F. Ma, W. Zhang, and T. Abhayapala, "Real-time separation of non-stationary sound fields on spheres," *The Journal of the Acoustical Society of America,* vol. 146 1, p. 11, 2019.

[43] F. Ma, W. Zhang, and T. D. Abhayapala, "Active control of outgoing noise fields in rooms," *The Journal of the Acoustical Society of America,* vol. 144, no. 3, pp. 1589-1599, 2018, doi: 10.1121/1.5055217.

[44] F. Ma, W. Zhang, and T. D. Abhayapala, "Active Control of Outgoing Broadband Noise Fields in Rooms," *IEEE/ACM Transactions on Audio, Speech, and Language Processing,* vol. 28, pp. 529-539, 2020, doi: 10.1109/TASLP.2019.2960716.

[45] S. Spors and H. Buchner, "Efficient massive multichannel active noise control using wave-domain adaptive filtering," in *2008 3rd International Symposium on Communications, Control and Signal Processing*, 12-14 March 2008, pp. 1480-1485, doi: 10.1109/ISCCSP.2008.4537461.

[46] Y. I. Bobrovnitskiĭ, "Theory of the new high-efficiency absorbing and nonscattering coatings," *Acoustical Physics,* vol. 53, no. 5, pp. 535-545, 2007, doi: 10.1134/s1063771007050016.

[47] J. Cheer, C. McCormick, and S. Daley, "An active acoustic metamaterial for the control of sound transmission," in *Proceedings of ICSV23, the 23rd International Congress on Sound and Vibration*, Athens, Greece, 10-14 July 2016, Online, 2016.

[48] M. Reynolds and S. Daley, "An active viscoelastic metamaterial for isolation applications," *Smart Materials and Structures (Print),* vol. 23, no. 4, p. 10, 2014, doi: DOI:101088/0964-1726/23/4/045030.

[49] A. Preumont and K. Seto, "Active Control of Structures," 2008: Wiley, First ed.

[50] C. Fuller, S. Elliott, and P. Nelson, "Active control of vibration," 1996: Academic Press, First ed.

[51] C. Hansen, S. Snyder, X. Qiu, L. A. Brooks, and D. Moreau, "Active Control of Noise and Vibration", 2012: CRC Press, Second ed.

[52] L. Meirovitch, "Dynamics And Control Of Structures," 1990: Wiley, First ed.

[53] Y. He, S. Zhong, and X. Huang, "Extensions to the acoustic scattering analysis for cloaks in non-uniform mean flows," *The Journal of the Acoustical Society of America,* vol. 146, no. 1, pp. 41-49, 2019, doi: 10.1121/1.5115046.

[54] D. Eggler, M. Karimi, and N. Kessissoglou, "Active acoustic cloaking in a convected flow field," *The Journal of the Acoustical Society of America,* vol. 146, pp. 586-594, 07/01 2019, doi: 10.1121/1.5119225.

[55] J. W. S. Rayleigh, "Investigation of the disturbance produced by a spherical obstacle on the waves of sound," *Proc. London Math. Soc.,* vol. s1-4, p. 253, 1871.

[56] J. W. S. Rayleigh, *The theory of sound Vol. 1 & 2. Vol. 1 & 2*. New York: Dover (in English), 1945.

[57] Y. I. Bobrovnitskii, "A new solution to the problem of an acoustically transparent body," *Acoustical Physics,* vol. 50, no. 6, pp. 647-650, 2004, doi: 10.1134/1.1825093.

[58] Y. I. Bobrovnitskii, "A new impedance-based approach to analysis and control of sound scattering," *Journal of Sound and Vibration,* vol. 297, no. 3-5, pp. 743-760, 2006, doi: 10.1016/j.jsv.2006.04.030.

[59] Y. I. Bobrovnitskii, "Impedance acoustic cloaking," *New Journal of Physics,* vol. 12, no. 4, 2010, doi: 10.1088/1367-2630/12/4/043049.

[60] T. Martin and A. Roure, "Optimization of an Active Noise Control System Using Spherical Harmonics Expansion of the Primary Field," *Journal of Sound and Vibration,* vol. 201, no. 5, pp. 577-593, 1997, doi: https://doi.org/10.1006/jsvi.1996.0782.

[61] B. Rafaely, "Plane-wave decomposition of the sound field on a sphere by spherical convolution," *The Journal of the Acoustical Society of America,* vol. 116, no. 4, pp. 2149-2157, 2004, doi: 10.1121/1.1792643.

[62] M. A. Poletti, "Three-dimensional surround sound systems based on spherical harmonics," *J. Audio Eng. Soc.,* vol. 53, pp. 1004-1025, 2005. [Online]. Available: https://ci.nii.ac.jp/naid/80017719230/en/.

[63] F. M. Fazi, "Sound field reproduction," PhD Thesis, Institute of Sound and Vibration Research, University of Southampton, 2010. [Online]. Available: https://eprints.soton.ac.uk/158639/

[64] J. Daniel, R. Nicol, and S. Moreau, "Further investigations of high order ambisonics and wavefield synthesis for holophonic sound imaging," presented at the Proceedings of the 114th AES Convention, Amsterdam, Netherlands, 22-25 March, 2003, 5788. [Online]. Available: http://www.aes.org/e-lib/browse.cfm?elib=12567.

[65] M. Junger and D. Feit, *Sound, Structures, and Their Interaction*, Second ed. Cambridge, MA: MIT Press, 1986, p. 460.

[66] S. Timoshenko and S. Woinowsky-krieger, *Theory of Plates and Shells*, Second ed. United States of America: McGraw-Hill Book Company, 1959.

[67] K. A. Cunefare, M. N. Currey, M. E. Johnson, and S. J. Elliott, "The radiation efficiency grouping of free-space acoustic radiation modes," *J. Acoust. Soc. Am.,* vol. 109, p. 203, 2001.

[68] P. H. Jones, O. M. Maragò, and G. Volpe, *Optical tweezers : principles and applications*. Cambridge, United Kingdom: Cambridge University Press (in English), 2015.

[69] F. M. Fazi and P. A. Nelson, "Sound field reproduction as an equivalent acoustical scattering problem," *Journal of the Acoustical Society of America,* vol. 134, no. 5, pp. 3721-3729, 2013. [Online]. Available: https://eprints.soton.ac.uk/359103/.

[70] J. Astley, "ISVR6142 - Numerical Methods for Acoustics," M. Orita, Ed., Lecture notes ed. Southampton: University of Southampton, 2015.

[71] E. G. Williams, *Fourier Acoustics. Sound Radiation and Nearfield Acoustical Holography*. Academic Press, 1999.

[72] G. B. Arfken, H. J. Weber, and F. Harris, *Mathematical Methods for Physicists*, Sixth ed. United States of America: Elsevier Academic Press, 2013.

[73] L. Beranek, T. J Mellow, and A. J Zuckerwar, *Acoustics: Sound Fields and Transducers*, First ed. United Kingdom: Academic Press, 2013.

[74] D. Colton and R. Kress, *Inverse Acoustic and Electromagnetic Scattering Theory*, Second ed. (Applied Mathematical Sciences). New York, USA: Springer, New York, NY, 2013.

[75] O. A. Godin, "Rayleigh scattering of a spherical sound wave," *J. Acoust. Soc. Am.,* vol. 133, p. 709, 2013.

[76] S. J. Elliott, *Signal Processing for Active Control*, First ed. Academic Press, 200, p. 511.

[77] B. Rafaely, *Fundamentals of Spherical Array Processing*, Second ed. Switzerland AG 2019: Springer, Cham, 2019, pp. XII, 193.

[78] S. J. Elliott, M. Orita, and J. Cheer, "Active control of the sound power scattered by a locally-reacting sphere," *The Journal of the Acoustical Society of America,* vol. 147, no. 3, pp. 1851-1862, 2020, doi: 10.1121/10.0000843.

[79] T. S. Becker, D.-J. van Manen, C. M. Donahue, C. Bärlocher, N. Börsing, F. Broggini, T. Haag, J. O. A. Robertsson, D. R. Schmidt, S. A. Greenhalgh, and T. E. Blum, "Immersive Wave Propagation Experimentation: Physical Implementation and One-Dimensional Acoustic Results," *Physical Review X,* vol. 8, no. 3, p. 031011, 2018, doi: 10.1103/PhysRevX.8.031011.

[80] N. Börsing, T. S. Becker, A. Curtis, D.-J. v. Manen, T. Haag, C. Bärlocher, and J. O. Robertsson, "Numerical simulations of acoustic cloaking in a real laboratory that deploys immersive boundary conditions," *The Journal of the Acoustical Society of America,* vol. 144, no. 3, pp. 1758-1758, 2018, doi: 10.1121/1.5067783.

[81] D.-J. v. Manen, J. O. A. Robertsson, and A. Curtis, "Exact wave field simulation for finite-volume scattering problems," *The Journal of the Acoustical Society of America,* vol. 122, no. 4, pp. EL115-EL121, 2007, doi: 10.1121/1.2771371.

[82] D.-J. v. Manen, M. Vasmel, S. Greenhalgh, and J. O. A. Robertsson, "Broadband cloaking and holography with exact boundary conditions," *The Journal of the Acoustical Society of America,* vol. 137, no. 6, pp. EL415-EL421, 2015, doi: 10.1121/1.4921340.

[83] D. B. Ward and T. D. Abhayapala, "Reproduction of a plane-wave sound field using an array of loudspeakers," *IEEE Trans. Speech Audio Process.,* vol. 9, p. 697, 2001.

[84] S. Brown, S. Wang, and D. Sen, "Analysis of the sphericalwave truncation error for spherical harmonic soundfield expansions," in *2012 IEEE International Conference on Acoustics, Speech and Signal Processing (ICASSP)*, 25-30 March 2012, pp. 5-8, doi: 10.1109/ICASSP.2012.6287803.

[85] S. Elliott, M. Orita, and J. Cheer, "A modal approach to acoustic scattering and its active control," in *Proceedings of ICSV27, the 27th International Congress on Sound an Vibration*, Online, 11–15 July 2021, Online, 2021.

[86] A. Preumont, *Vibration Control of Active Structures: An Introduction*, Third ed. (Solid Mechanics and Its Applications). Springer, Dordrecht, 1999.

[87] S. Elliott, P. Gardonio, T. Sors, and M. Brennan, "Active vibroacoustic control with multiple local feedback loops," in *Proceedings of SPIE's 8th Annual International Symposium on Smart Structures and Materials*, Newport Beach, CA, USA, 2001, vol. 4327: SPIE.

[88] P. M. Morse and H. Feshbach, *Methods of theoretical physics*. United States of America: McGraw-Hill Book Company, Inc., 1953.

[89] S. Temkin, *Elements of Acoustics*. Wiley, 1981.

[90] L. Meirovitch, H. Baruh, and H. Oz, "A comparison of control techniques for large flexible systems," *J. Guid. Control, Dyn.,* vol. 6, p. 302, 1983.

[91] K. A. Kuo, H. E. M. Hunt, and J. R. Lister, "Small oscillations of a pressurized, elastic, spherical shell: Model and experiments," *Journal of Sound and Vibration,* vol. 359, pp. 168-178, 2015, doi: https://doi.org/10.1016/j.jsv.2015.08.021.

[92] A. Silbiger, "Nonaxisymmetric Modes of Vibration of Thin Spherical Shells," *The Journal of the Acoustical Society of America,* vol. 34, no. 6, pp. 862-862, 1962, doi: 10.1121/1.1918210.

[93] R. B. Evans, "Modal impedances for nonaxisymmetric vibrations of a thin spherical shell," *The Journal of the Acoustical Society of America,* vol. 100, no. 2, pp. 1242-1245, 1996, doi: 10.1121/1.415972.

[94] T. A. Duffey and C. Romero, "Strain growth in spherical explosive chambers subjected to internal blast loading," *International Journal of Impact Engineering,* vol. 28, no. 9, pp. 967-983, 2003, doi: https://doi.org/10.1016/S0734-743X(02)00169-0.

[95] M. E. Johnson and S. J. Elliott, "Active control of sound radiation using volume velocity cancellation," *The Journal of the Acoustical Society of America,* vol. 98, no. 4, pp. 2174-2186, 1995, doi: 10.1121/1.413332.

[96] P. Gardonio, Y.-S. Lee, and S. J. Elliott, "Analysis and measurement of a matched volume velocity sensor and uniform force actuator for active structural acoustic control," *Journal of the Acoustical Society of America,* vol. 110, no. 6, pp. 3025-3031, 2001. [Online]. Available: https://eprints.soton.ac.uk/10844/.

[97] J. Meyer and G. Elko, "A highly scalable spherical microphone array based on an orthonormal decomposition of the soundfield," in *2002 IEEE International Conference on Acoustics, Speech, and Signal Processing*, 13-17 May 2002, vol. 2, pp. II-1781-II-1784, doi: 10.1109/ICASSP.2002.5744968.

[98] J. A. Belloch, M. Cobos, A. Gonzalez, and E. S. Quintana-Ortí, "Real-time Sound Source Localization on an Embedded GPU Using a Spherical Microphone Array," *Procedia Computer Science,* vol. 51, pp. 201-210, 2015, doi: https://doi.org/10.1016/j.procs.2015.05.226.

[99] D. R. Mendat, J. E. West, S. Ramenahalli, E. Niebur, and A. G. Andreou, "Audio-Visual beamforming with the Eigenmike microphone array an omni-camera and cognitive auditory features," in *2017 51st Annual Conference on Information Sciences and Systems (CISS)*, 22-24 March 2017 2017, pp. 1-4, doi: 10.1109/CISS.2017.7926180.

[100] S. A. Cummer and D. Schurig, "One path to acoustic cloaking," *New Journal of Physics,* vol. 9, no. 3, pp. 45-45, 2007, doi: 10.1088/1367-2630/9/3/045.

[101] A. Alù and N. Engheta, "Achieving transparency with plasmonic and metamaterial coatings," *Physical Review E,* vol. 72, no. 1, p. 016623, 2005, doi: 10.1103/PhysRevE.72.016623.

[102] H. Chen and C. T. Chan, "Acoustic cloaking in three dimensions using acoustic metamaterials," *Applied Physics Letters,* vol. 91, no. 18, 2007, doi: 10.1063/1.2803315.

[103] M. D. Guild, A. Alù, and M. R. Haberman, "Cancellation of acoustic scattering from an elastic sphere," *The Journal of the Acoustical Society of America,* vol. 129, no. 3, pp. 1355-1365, 2011, doi: 10.1121/1.3552876.

[104] M. D. Guild, M. R. Haberman, and A. Alù, "Plasmonic cloaking and scattering cancelation for electromagnetic and acoustic waves," *Wave Motion,* vol. 48, no. 6, pp. 468-482, 2011, doi: https://doi.org/10.1016/j.wavemoti.2011.02.006.

[105] M. Poletti, "Unified description of ambisonics using real and complex spherical harmonics," in *Ambisonics Symp*, 2009, vol. 1, no. 1, pp. 2-2.

[106] M. Abramowitz and I. A. Stegun, *Handbook of Mathematical Functions: With Formulas, Graphs, and Mathematical Tables*. Dover Publications, 1964.

[107] G. N. Watson, *A Treatise on the Theory of Bessel Functions*. University Press, 1962.

[108] J. D. Jackson, *Classical electrodynamics*. New York: Wiley (in English), 1999.